

A11100 985357

NBS
PUBLICATIONS

NAT'L INST OF STANDARDS & TECH R.I.C.



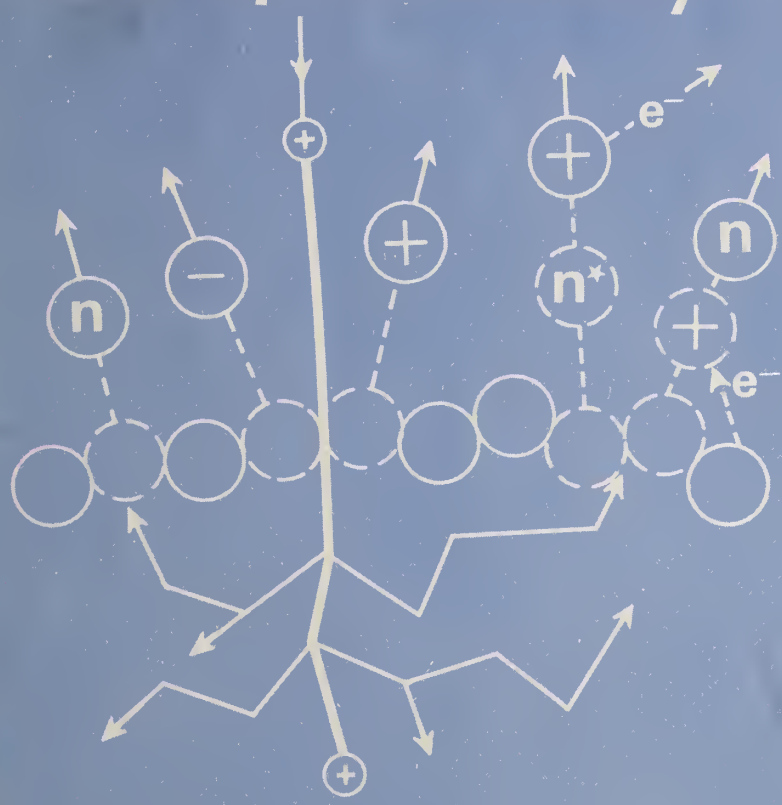
A11100985357
Workshop on Secondary Ion Mass Spectrometry
QC100 .U57 V427:1975 C.1 NBS-PUB-C 1975



NBS SPECIAL PUBLICATION 427

U.S. DEPARTMENT OF COMMERCE /National Bureau of Standards

Secondary Ion Mass Spectrometry



QC
100
.U57
no. 427
1975
C.1

NATIONAL BUREAU OF STANDARDS

The National Bureau of Standards¹ was established by an act of Congress March 3, 1901. The Bureau's overall goal is to strengthen and advance the Nation's science and technology and facilitate their effective application for public benefit. To this end, the Bureau conducts research and provides: (1) a basis for the Nation's physical measurement system, (2) scientific and technological services for industry and government, (3) a technical basis for equity in trade, and (4) technical services to promote public safety. The Bureau consists of the Institute for Basic Standards, the Institute for Materials Research, the Institute for Applied Technology, the Institute for Computer Sciences and Technology, and the Office for Information Programs.

THE INSTITUTE FOR BASIC STANDARDS provides the central basis within the United States of a complete and consistent system of physical measurement; coordinates that system with measurement systems of other nations; and furnishes essential services leading to accurate and uniform physical measurements throughout the Nation's scientific community, industry, and commerce. The Institute consists of a Center for Radiation Research, an Office of Measurement Services and the following divisions:

Applied Mathematics — Electricity — Mechanics — Heat — Optical Physics — Nuclear Sciences² — Applied Radiation² — Quantum Electronics³ — Electromagnetics³ — Time and Frequency³ — Laboratory Astrophysics³ — Cryogenics³.

THE INSTITUTE FOR MATERIALS RESEARCH conducts materials research leading to improved methods of measurement, standards, and data on the properties of well-characterized materials needed by industry, commerce, educational institutions, and Government; provides advisory and research services to other Government agencies; and develops, produces, and distributes standard reference materials. The Institute consists of the Office of Standard Reference Materials and the following divisions:

Analytical Chemistry — Polymers — Metallurgy — Inorganic Materials — Reactor Radiation — Physical Chemistry.

THE INSTITUTE FOR APPLIED TECHNOLOGY provides technical services to promote the use of available technology and to facilitate technological innovation in industry and Government; cooperates with public and private organizations leading to the development of technological standards (including mandatory safety standards), codes and methods of test; and provides technical advice and services to Government agencies upon request. The Institute consists of a Center for Building Technology and the following divisions and offices:

Engineering and Product Standards — Weights and Measures — Invention and Innovation — Product Evaluation Technology — Electronic Technology — Technical Analysis — Measurement Engineering — Structures, Materials, and Life Safety⁴ — Building Environment⁴ — Technical Evaluation and Application⁴ — Fire Technology.

THE INSTITUTE FOR COMPUTER SCIENCES AND TECHNOLOGY conducts research and provides technical services designed to aid Government agencies in improving cost effectiveness in the conduct of their programs through the selection, acquisition, and effective utilization of automatic data processing equipment; and serves as the principal focus within the executive branch for the development of Federal standards for automatic data processing equipment, techniques, and computer languages. The Institute consists of the following divisions:

Computer Services — Systems and Software — Computer Systems Engineering — Information Technology.

THE OFFICE FOR INFORMATION PROGRAMS promotes optimum dissemination and accessibility of scientific information generated within NBS and other agencies of the Federal Government; promotes the development of the National Standard Reference Data System and a system of information analysis centers dealing with the broader aspects of the National Measurement System; provides appropriate services to ensure that the NBS staff has optimum accessibility to the scientific information of the world. The Office consists of the following organizational units:

Office of Standard Reference Data — Office of Information Activities — Office of Technical Publications — Library — Office of International Relations.

¹ Headquarters and Laboratories at Gaithersburg, Maryland, unless otherwise noted; mailing address Washington, D.C. 20234.

² Part of the Center for Radiation Research.

³ Located at Boulder, Colorado 80302.

⁴ Part of the Center for Building Technology.

OCT 14 1975

not acc.
QC100
.457
no.427
1975
C.2

Secondary Ion Mass Spectrometry

Special publication, no. 427

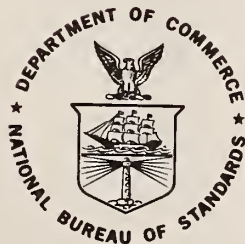
Proceedings of a Workshop on
Secondary Ion Mass Spectrometry and
Ion Microprobe Mass Analysis

Held at the National Bureau of Standards
Gaithersburg, Md., September 16-18, 1974

Edited by

K. F. J. Heinrich and D. E. Newbury

Institute for Materials Research
National Bureau of Standards
Washington, D.C. 20234



U.S. DEPARTMENT OF COMMERCE, Rogers C.B. Morton, Secretary

James A. Baker, III, Under Secretary

Dr. Betsy Ancker-Johnson, Assistant Secretary for Science and Technology

NATIONAL BUREAU OF STANDARDS, Ernest Ambler, Acting Director

U.S.
111
Issued October 1975

Library of Congress Cataloging in Publication Data

Workshop on Secondary Ion Mass Spectrometry and Ion Microprobe Mass Analysis, National Bureau of Standards, 1974.
Secondary Ion Mass Spectrometry.

(National Bureau of Standards Special Publication; 427)

"CODEN: XNBSAV."

Supt. of Docs No.: C13.10:427.

I. Mass Spectrometry—Congresses. 2. Microprobe Analysis—
Congresses. I. Heinrich, Kurt F. J. II. Newbury, D. E. III. Title.
IV. Series: United States. National Bureau of Standards. Special
Publication; 427.

QC100.U57 No. 427 [QD96.M3] 389'.08s [545'.33] 75-619223

National Bureau of Standards Special Publication 427

Nat. Bur. Stand. (U.S.), Spec. Publ. 427, 230 pages (Oct. 1975)

CODEN: XNBSAV

U.S. GOVERNMENT PRINTING OFFICE
WASHINGTON: 1975

For sale by the Superintendent of Documents, U.S. Government Printing Office, Washington, D.C. 20402
(Order by SD Catalog No. C13.10:427). Price \$3.00 . (Add 25 percent additional for other than U.S. mailing).

ABSTRACT

This book is the formal report of the Workshop on Secondary Ion Mass Spectrometry (SIMS) and Ion Microprobe Mass Analysis held at the National Bureau of Standards in September 1974. Invited and contributed papers cover a range of topics in the SIMS field: design of SIMS instrumentation; factors affecting secondary ion collection; techniques of reducing secondary ion mass spectra to yield quantitative compositional information; comparisons of SIMS with Auger electron spectroscopy (AES); techniques of obtaining elemental depth profiles and the instrumental and physical factors affecting such profiles; and applications of SIMS to the study of geological samples. The papers include both tutorial reviews and detailed reports on current research in SIMS. The volume should be of interest to all workers in the SIMS and surface analysis fields.

Key words: Auger electron spectroscopy; elemental depth profiling; ion microprobe mass analysis; ion optics; local thermal equilibrium (LTE); mineral analysis; secondary ion mass spectrometry (SIMS); surface analysis.

Certain commercial products are identified in this paper in order to specify adequately the experimental procedure. In no case does such identification imply recommendation or endorsement by the National Bureau of Standards, nor does it imply that the products identified are necessarily the best available for the purpose.

FOREWORD

The Analytical Chemistry Division of the National Bureau of Standards, Institute for Materials Research, is concerned with the development of new techniques of analysis as well as the improvement of existing methods of chemical analysis. Since one of its goals is to improve the dissemination of knowledge, the NBS Analytical Chemistry Division has sponsored a series of special conferences, symposia and workshops on various topics in analytical chemistry. The workshops normally are devoted to detailed discussions of relatively sharply defined subjects. The objective is to bring together interested scientists from throughout the world to exchange information and advance the state-of-the-art with leading workers keynoting the discussions. Because of the specific nature and recent origin of these fields, there is frequently no other satisfactory venue available for detailed discussions to take place; such discussions are often overwhelmed when attached to large international meetings which cover the gamut of analytical chemistry. Past topics of these workshops and the published proceedings include: Quantitative Electron Probe Microanalysis (NBS Special Publication 298), Aerosol Measurements (NBS Special Publication 412), and Oil Pollution Monitoring (NBS Special Publication 409). These proceedings are available from the Superintendent of Documents, Government Printing Office, Washington, D. C. 20402.

This volume contains the proceedings of another workshop in this series on the topic of Secondary Ion Mass Spectrometry (SIMS). The three-day meeting attracted seventy-five participants from the U.S., Europe and Australia. The workshop format consisted of keynote talks given by eminent workers in several specialties, followed by extensive discussion. The papers which make up this volume include papers reporting the views of the keynote speakers as well as shorter contributions based on floor discussions.

The large number of attendees to this meeting, considering the relative scarcity of SIMS instrumentation (about 50 SIMS instruments exist worldwide), indicates that this topic is rapidly growing in interest and importance. This publication should serve to characterize the current state of SIMS as an emerging measurement technology, and should be a valuable reference to workers in this field.

John D. Hoffman, Director
Institute for Materials Research
National Bureau of Standards

PREFACE

Microanalysis by means of secondary ion mass spectrometry is still in the initial phases of exploration. The observation of elements of low atomic number, the measurement of isotope ratios, and the shallow depth of sampling achievable with an ion microprobe or ion microscope are the outstandingly attractive features of this technique. They have already produced exciting results in diverse fields of application, including the study of distribution in depth of dopants and impurities in semiconductor materials, the characterization of the microscopic distribution of hydrogen and boron in alloys, and the analysis of microscopic particles. On the other hand, the experimental difficulties and instrumental limitations, the uncertainties involving theoretical models of ion-target interaction, and the serious problems in obtaining appropriate standards have vexed the analysts involved in the practice of ion probe microanalysis.

Since the cost of purchase and maintenance of the instrument is very high, the prospective user needs all the information he can obtain in order to assess the potential gains and the limitations of secondary ion mass spectrometry applied to his specific needs.

The present publication is not intended to answer all important questions on the subject. Rather, it presents a series of papers on the principles of instrumentation, theory and applications in selected fields.

There is no other book currently available that is exclusively dedicated to this subject, and we are confident that the present publication will be of interest and help to actual or potential users of secondary ion mass spectrometry.

K. F. J. Heinrich

D. E. Newbury

CONTENTS

	Page
Abstract	iii
Foreword	v
Preface	vii
 The Ion Microprobe - Instrumentation and Techniques	 1
H. Liebl	
 Looking at the Collection Efficiency Problem Through the Ion Microscope Optics	 33
G. Slodzian	
 High Mass Resolution Secondary Ion Mass Spectrometry	 63
P. Williams and C.A. Evans, Jr.	
 A Comparison of Mass Spectra from Three Ion Probes	 69
J.G. Bradley, D.Y. Jerome and C.A. Evans, Jr.	
 A Critical Discussion of the Local Thermal Equilibrium Model for the Quantitative Correction of Sputtered Ion Intensities	 79
C.A. Andersen	
 An Outline of Secondary Ion Emission Models	 121
J.M. Schroeer	
 Empirical Quantitation Procedures in SIMS	 129
J.A. McHugh	
 Application of SIMS Microanalysis Techniques to Trace Element and Isotopic Studies in Geochemistry and Cosmochemistry	 135
J.F. Lovering	

Factors that Influence an Elemental Depth Concentration Profile . . 179

J.A. McHugh

A Comparison of Auger Electron Spectroscopy (AES) and Secondary
Ion Mass Spectrometry (SIMS) 191

J.M. Morabito

Key Word Index 225

THE ION MICROPROBE-INSTRUMENTATION AND TECHNIQUES

H. Liebl

Max-Planck-Institut für Plasmaphysik
EURATOM Association
8046 Garching
Munich, Federal Republic of Germany

I. INTRODUCTION

After the success of the electron microprobe, several new methods for the microanalysis of solids have been tried and developed, and the evolution is still in progress. Setting aside special methods for particular applications like autoradiography or field desorption microscopy, there are in principle two ways of microanalysis, shown in figure 1: emission microscopy combined with spectroscopy (a), and the microprobe technique (b). In both cases the sample is induced by some primary radiation to emit some secondary radiation, characteristic of its composition, which is then analyzed. The desired lateral resolution is achieved in case (a) by forming a magnified image of the surface with appropriate optics, using the transmitted component of the secondary radiation. The image thus shows the topographical distribution of the atomic or molecular species emitting that transmitted radiation. For spot analyses the radiation is collected behind a hole in the screen and the secondary spectrum is scanned. In case (b) the lateral resolution is achieved by focusing the primary radiation to a microprobe having a diameter which depends on the desired resolution. By an x-y deflection device any spot within a certain area on the sample can be hit and thus spot analyses be made. Distribution pictures are obtained by raster scanning the sample area and using the transmitted secondary signal to modulate the intensity of an oscilloscope, the x-y deflection of which is synchronized with the primary beam raster scan.

If the primary radiation can be focused by lenses, but not the secondary radiation, the microprobe technique is the only possible way. This is the case with the electron microprobe X-ray analyzer. When the primary radiation is made up of ions, and sputtered secondary ions are used as secondary radiation, then both avenues are open and have been taken. Instruments of type (a) are appropriately called "ion microanalyzers," while instruments of type (b) should be referred as "ion microprobe analyzers" for distinction. Ion microanalyzers were built by two groups in France. Goutte and coworkers [1,2] used a "Wien filter" for mass analysis of the secondary ions. The elegant designs of

Castaing and Slodzian [3,4], which to them were, as Castaing put it [5], "a pleasant exercise in optics," led to the development of the Cameca Ion Microanalyzer [6].

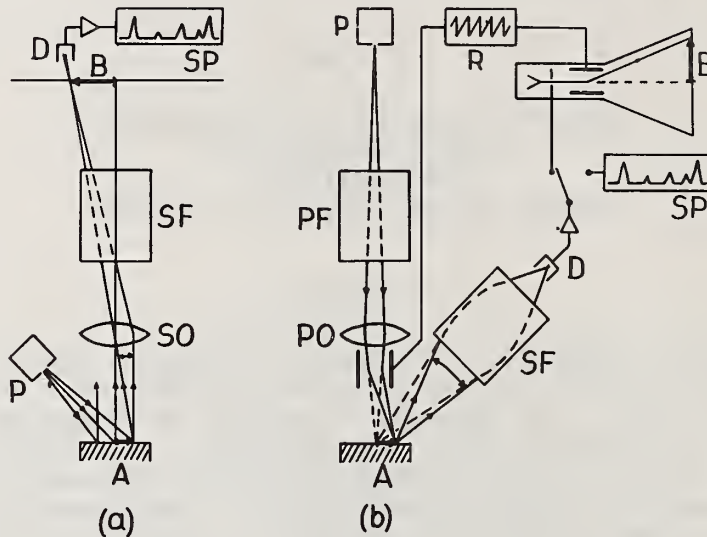


Figure 1. The two ways of microanalysis: (a) direct imaging combined with analysis, (b) microprobe method. (A, sampled area; B, image of A; P, primary source; SO, secondary optics; SF, secondary filter; D, detector; SP, spectrum; PF, primary filter; PO, primary optics; R, raster scanning).

It has been my frequently expressed opinion [7] that ion microprobe analyzers have an intrinsic advantage over ion microanalyzers on the basis of absolute sensitivity. In an ion microanalyzer the overall transmission of secondary ions from sample to detector is linked to the lateral resolution because the lens aberrations of the imaging optics impose restrictions on the solid angle and energy bandwidth utilized. On the other hand, in an ion microprobe analyzer the secondary optics can be designed to accommodate a much larger solid angle and energy bandwidth with the same mass resolution. Further, one can try to improve the lateral resolution by making finer primary beams, without degrading the transmission for the secondary ions.

Since I am obviously prejudiced in favor of ion microprobe analyzers, I am going to review only these instruments. Ion microanalyzers are the topic of a separate paper at this meeting.

Ion Microprobe Instrumentation

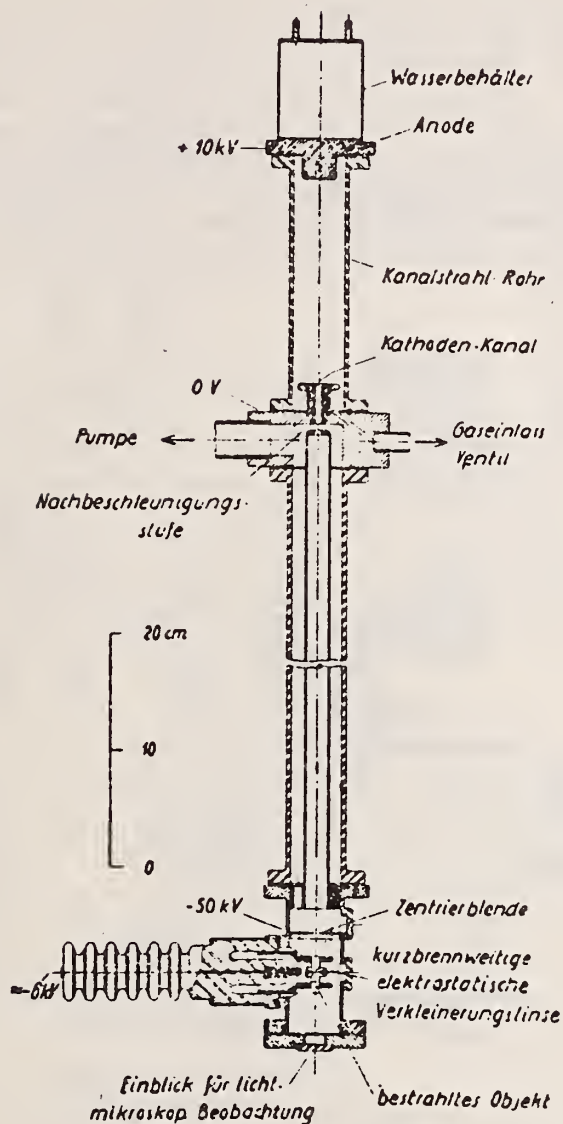


Figure 2. Early ion microprobe (v. Ardenne 1939 [9]).

II. EVOLUTION AND PRESENT INSTRUMENTATION

Ion microprobe analyzers have two groups of ancestors: Ion microprobes and secondary ion mass spectrometers. Both groups still exist separately, ion microprobes for microetching, scanning ion microscopy and ion implantation, and secondary ion mass spectrometers for bulk and surface analysis. (Not all apes evolved into humans,

either.) Both groups can be traced back about 35 years. Sloane and Press [8] studied the sputtering of negative ions upon positive ion bombardment in 1938. The first ion microprobe was published in 1939 by von Ardenne [9]. For history's sake, his setup is shown in figure 2. Here the beam from a canal-ray tube, having a large energy spread, is focused by an einzel lens to a probe of about 30 μm diameter. Figure 3, from the same publication, shows a proposed setup for micromachining, with two stage demagnification of the ion probe, and *in situ* observation of the thin sample by transmission electron microscopy. Ten

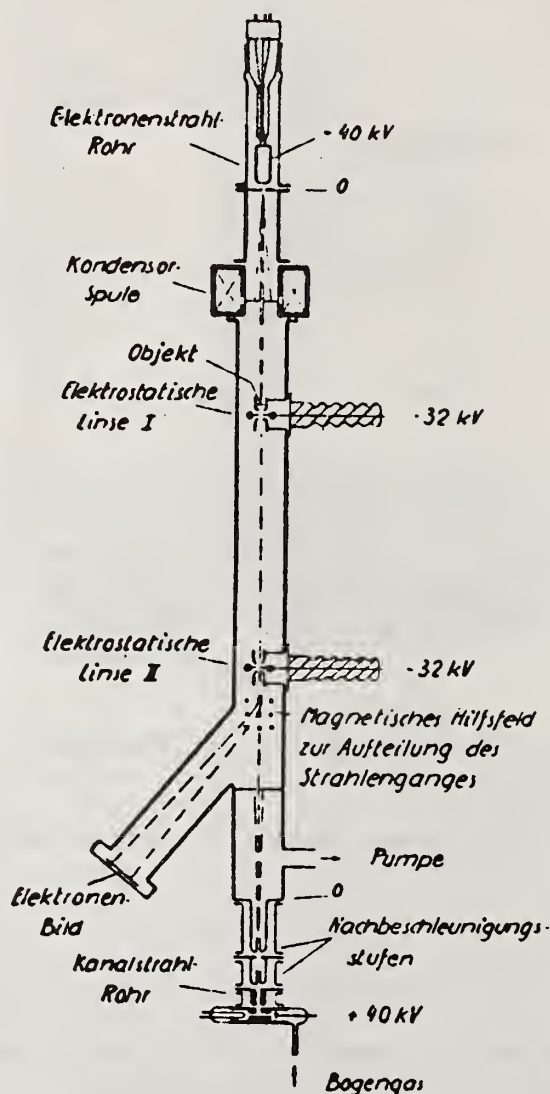


Figure 3. Ion microprobe combined with transmission electron microscope (v. Ardenne 1939 [9]).

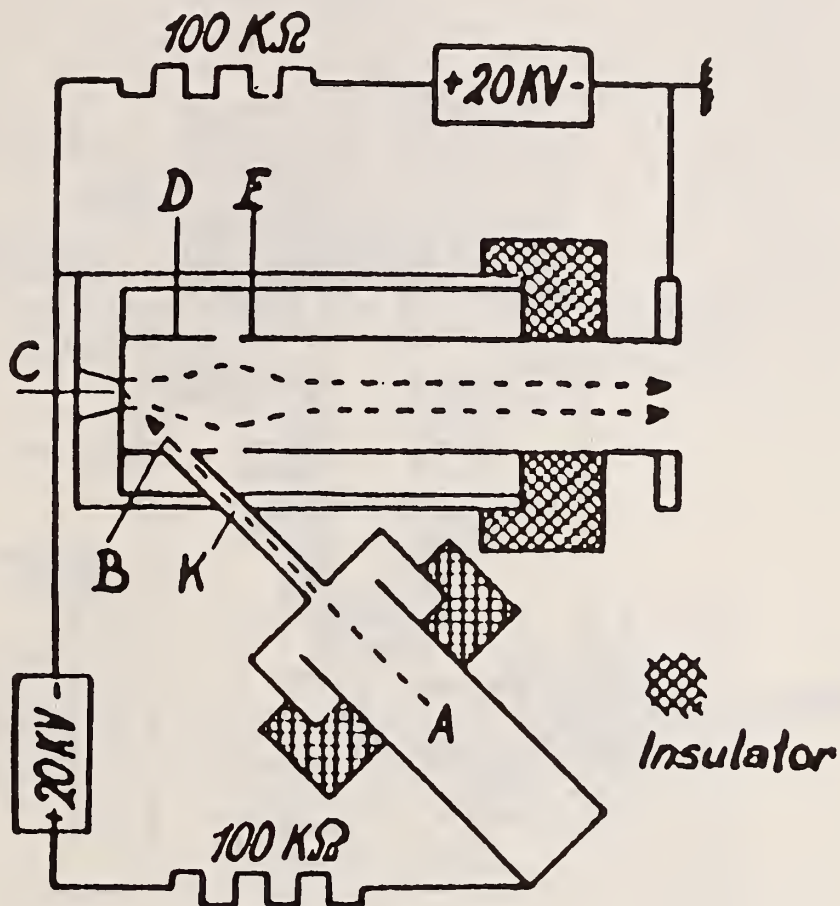


Figure 4. Sputtering ion source with primary beam from canalray tube (Herzog and Viehböck 1949 [10]).

years later Herzog and Viehböck [10] published their sputter ion source (fig. 4). They also used a canal-ray tube to generate an intense and energetic ion beam. It was guided down a long and narrow tube affording high flow resistance, so that the sputtering took place in a relatively good vacuum. In those days canal-ray tubes were the most convenient and

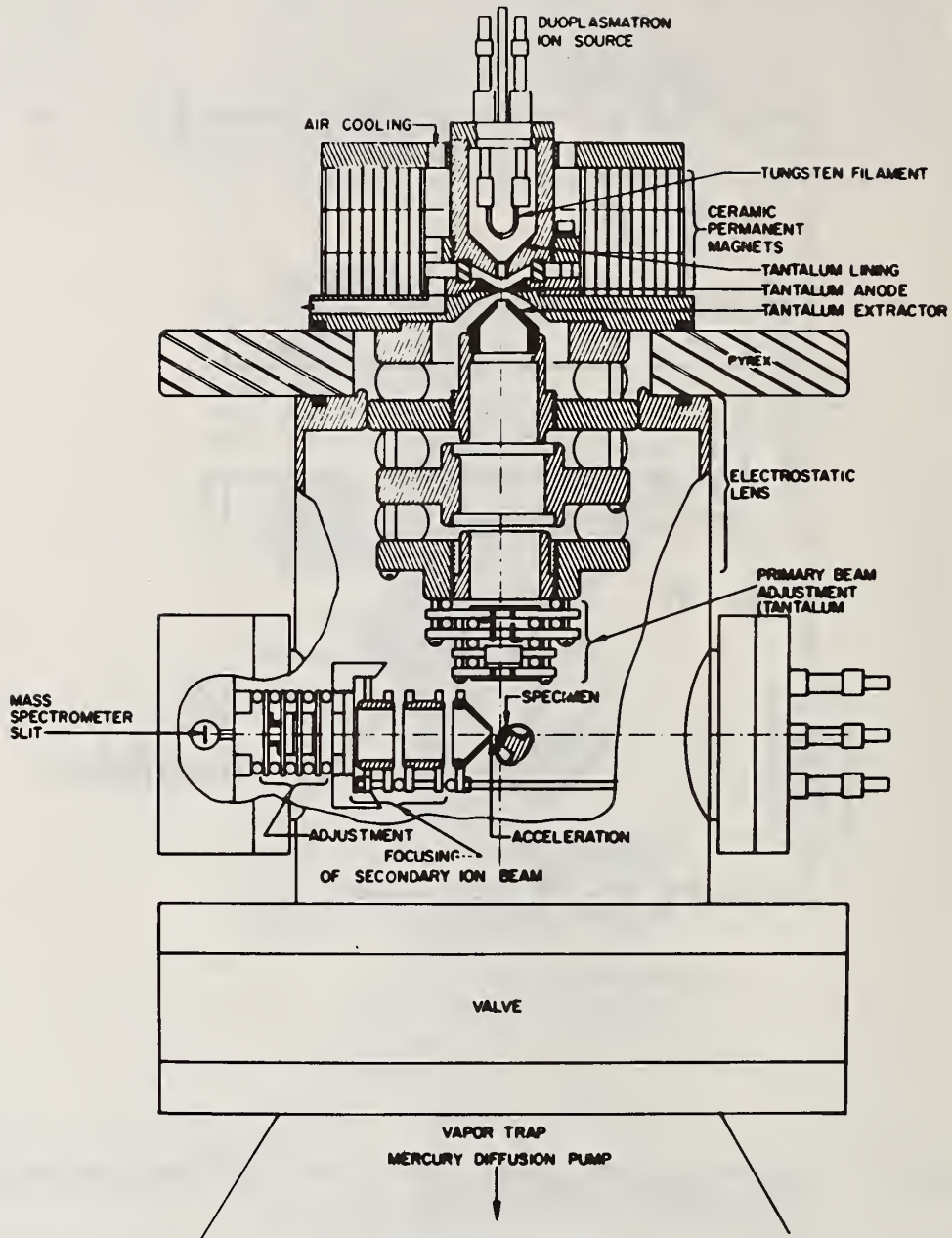


Figure 5. Sputtering ion source with focused primary beam from duoplasmatron (Liebl and Herzog 1964 [12]).

Ion Microprobe Instrumentation

widely used source of ions from gases for double-focusing mass spectrographs. In the mass spectrograms lines from the cathode material would show up, as a consequence of cathode sputtering, and this fact had been utilized to obtain mass lines from solids. But this source was the first to produce secondary ions with a primary ion beam technique. This thread was picked up again in 1961, when I worked in Herzog's group at Geophysics Corporation of America (GCA), and we had a contract for a sputtering ion source [11]. The final version [12] of the resulting device is shown in figure 5. In 1956, von Ardenne's duoplasmatron ion source had become known [13], which was superior by orders of magnitude to the old canal-ray tube with respect to gas consumption, energy spread, and brightness. The version shown in this figure was of my own design, trimmed to yield a very pure ion beam of high brightness. The use of ceramic permanent magnets instead of a coil as customary, brought certain advantages. The ion beam extracted from it had only a few electron volts of energy spread and thus could be focused very sharply with

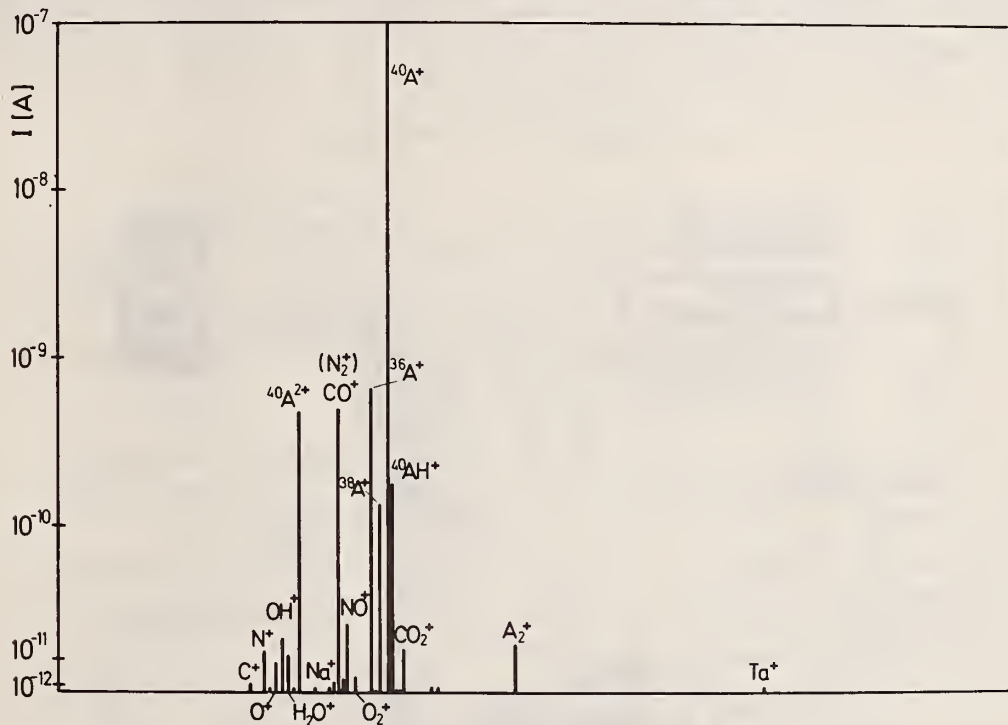


Figure 6. Mass spectrum of primary argon beam with impurities [14].

a 1:1 imaging lens onto the sample to a minimum diameter of about 300 μm , corresponding to the size of the exit hole in the anode of the duoplasmatron. For beam adjustment x-y deflection was provided. The secondary ions were extracted at a right angle to the primary beam from the tilted sample surface and focused onto the mass spectrometer entrance slit. The composition of the primary beam could be simply

checked by using the sample surface as an electrostatic mirror, thereby deflecting a fraction of the primary beam into the mass spectrometer. In the course of this work it turned out that, even with all precautions, the primary beam carried varying amounts of impurity ions, besides the doubly charged and diatomic ions of the gas used [14]. This is seen in figure 6, which shows the impurities in an argon ion beam on a logarithmic scale. It also turned out that the secondary ion yield was extremely matrix-sensitive. Therefore, when I joined Applied Research Laboratories (ARL) in 1964 and started designing the IMMA (Ion Microprobe Mass Analyzer), I decided that the primary beam had to be mass-analyzed [15]. Figure 7 shows the final layout of the IMMA [16], based on my original design, with later improvements added. The duoplasmatron is basically similar to that of figure 5, but the hot filament is replaced by a hollow cathode to allow stable operation with reactive gases. The intermediate electrode can be offset to allow extraction of negative ions, which are useful in the analysis of insulating samples (see below). The extracted ion beam is mass-analyzed by a 90° magnetic field of the wedge type, formed between plane but inclined pole faces. In such a field, the ions follow trochoidal

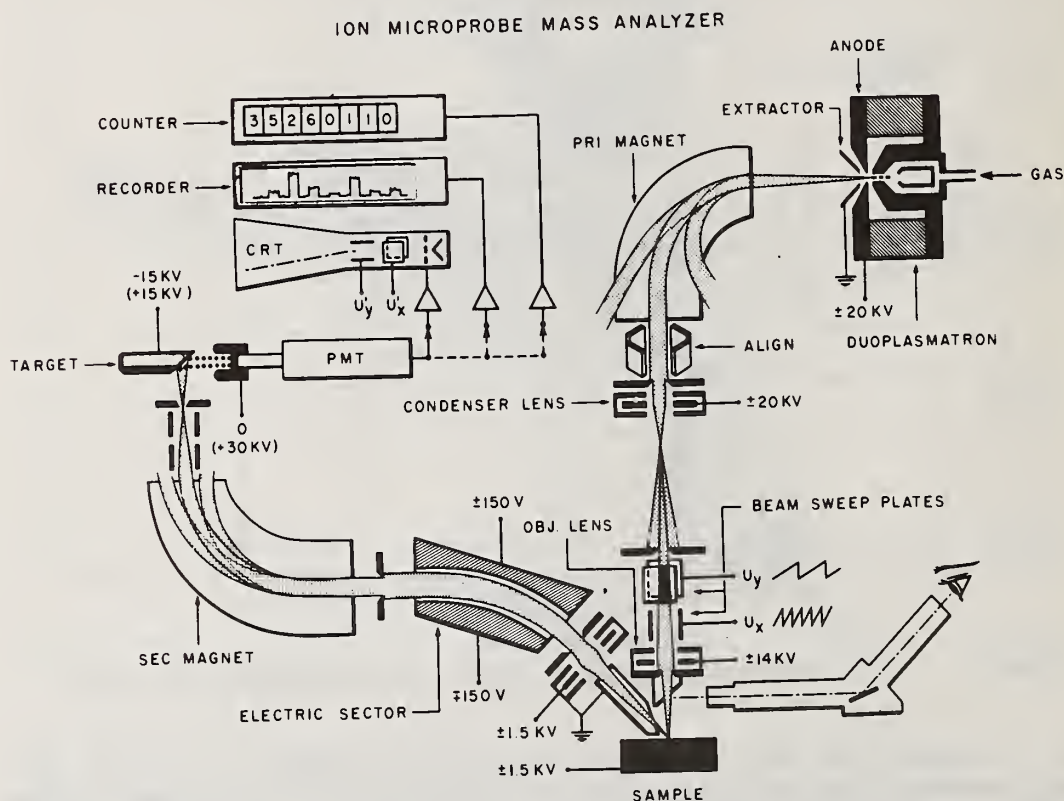


Figure 7. Final layout of IMMA (ARL) [15,16].

Ion Microprobe Instrumentation

trajectories. The merits of this choice are two-directional focusing and no second order angular aberration with a geometrically simple setup. The mass-analyzed emerging beam is focused with two stage demagnification by einzel lenses onto the sample. The secondary ions are accelerated into a mass spectrometer, designed to provide particularly high transmission. It consists of an einzel lens, a 45° spherical condenser, and a wedge magnet of the same type as for the primary beam analysis. The detector is an ion-electron converter plus scintillator and photomultiplier. Positive or negative secondary ions can be detected with equal sensitivity. Between the magnet and the exit slit two pairs of deflection plates are placed which can be used to switch in rapid sequence between two neighboring masses. This "peak switch" is most useful for isotopic ratio measurements.

The IMMA prototype was in operation two years after it was started and I presented the first secondary ion micrographs at the 1967 ASTM meeting on mass spectrometry in Denver, Colorado [17]. During the assembly of the IMMA, Long of Cambridge University published a thorough feasibility study of an ion microprobe analyzer [18], shown schematically in figure 8. His intended application was isotopic ratio

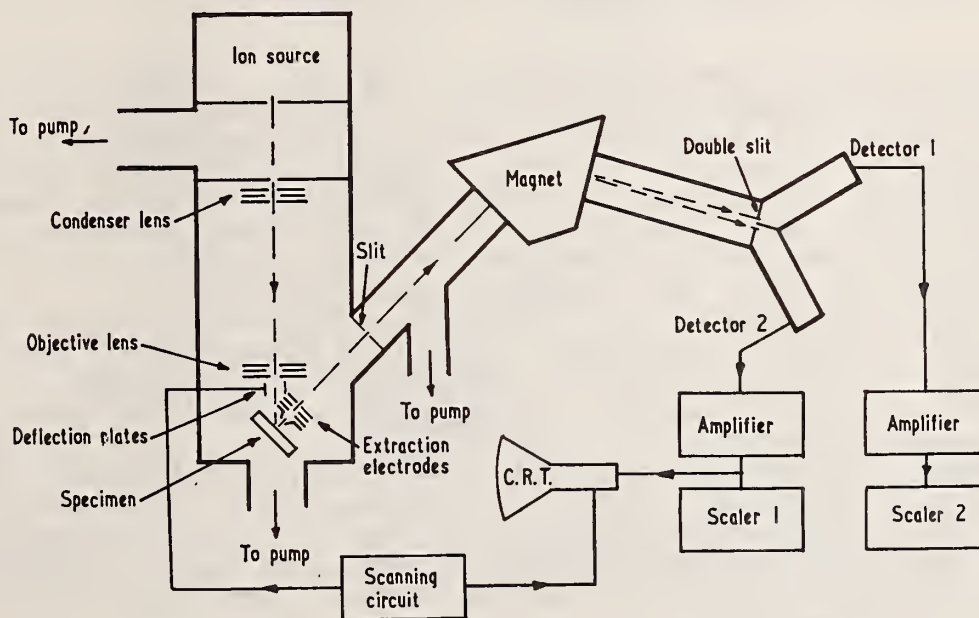


Figure 8. Proposed ion microprobe analyzer (Long 1965 [18]).

measurements on geological samples. A student of his, Drummond, started construction, and in 1967, they published scanning ion micrographs, obtained with secondary electrons, showing about 0.5 μm resolution [19]. Figure 9 shows their primary beam column [20] with a duoplasmatron, a symmetric einzel lens as condenser, and an asymmetric einzel lens as

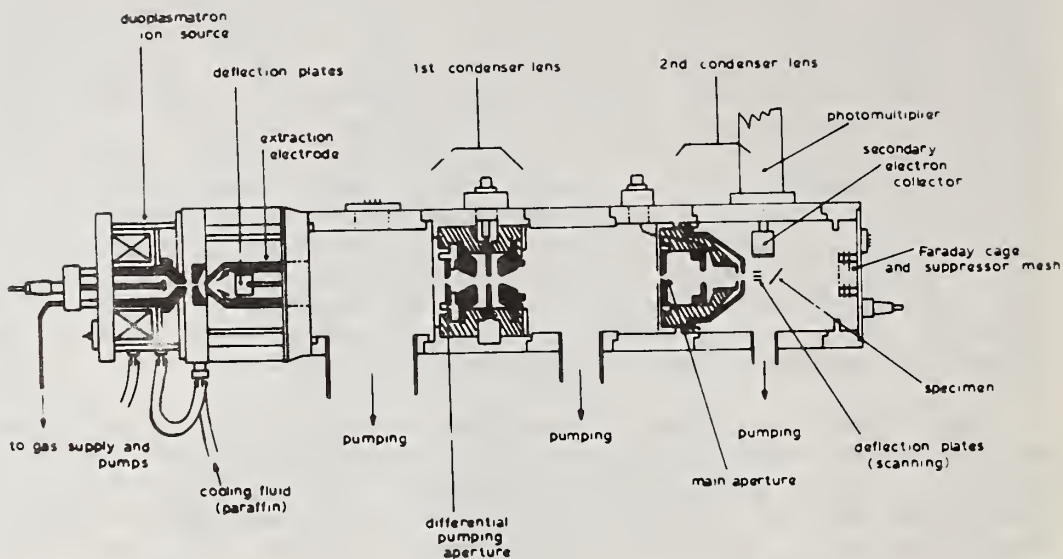


Figure 9. Scanning ion microprobe (Drummond and Long 1967 [19]).

objective lens. Such an asymmetric lens has a reduced spherical aberration compared to symmetric lenses, if the working distance is made very short [21]. At this condition, Long and Drummond reported a probe diameter of only $0.2 \mu\text{m}$. Recently, Long and Coles [22] have published applications with the completed instrument. Essential design features of figure 9 were incorporated into the primary beam column which was developed subsequently by Associated Electrical Industries, Ltd. as an accessory to their MS7 mass spectrometers [23] (fig. 10). The main changes are a hollow cathode in the duoplasmatron and the addition of a magnet. The mass spectrometer is of the Mattauch-Herzog type with optional electric or photoplate detection and a mass resolution up to 10000. The third commercial ion microprobe analyzer on the market was developed by Hitachi, and first announced in 1969 at the Mass Spectrometry Conference in Kyoto [24]. The latest version [25] is shown in figure 11. A point of interest is the placement of a multiplier close to the sample, which facilitates scanning ion microscopy by secondary electrons, with the sample biased negatively. In a recent installation of this instrument a Wien filter was inserted in the primary column for mass separation [25].

Besides the commercially available ion microprobe analyzers, there are now several laboratory instruments in operation. Figure 12 shows the combined ion and electron microprobe (UMPA), which I started in 1968 at the Max-Planck-Institut für Plasmaphysik near Munich [7]. It was conceived as a research instrument, suited not only for bulk analysis with high lateral resolution, but also for surface research. Therefore, the apparatus is built in UHV-technology to reach pressures under 10^{-8} torr. As the primary beam, not only ions can be used but also

Ion Microprobe Instrumentation

electrons. The secondary analyzer can be used as an energy spectrometer or as a mass spectrometer, both with two-directional focusing. For the primary beam focusing "hybrid lenses" are used, which are made by fitting a nonmagnetic aperture electrode into the gap of a conventional magnetic lens. Such a lens can act as magnetic lens for electrons, as an einzel lens for ions or electrons, and as a combined lens for ions and

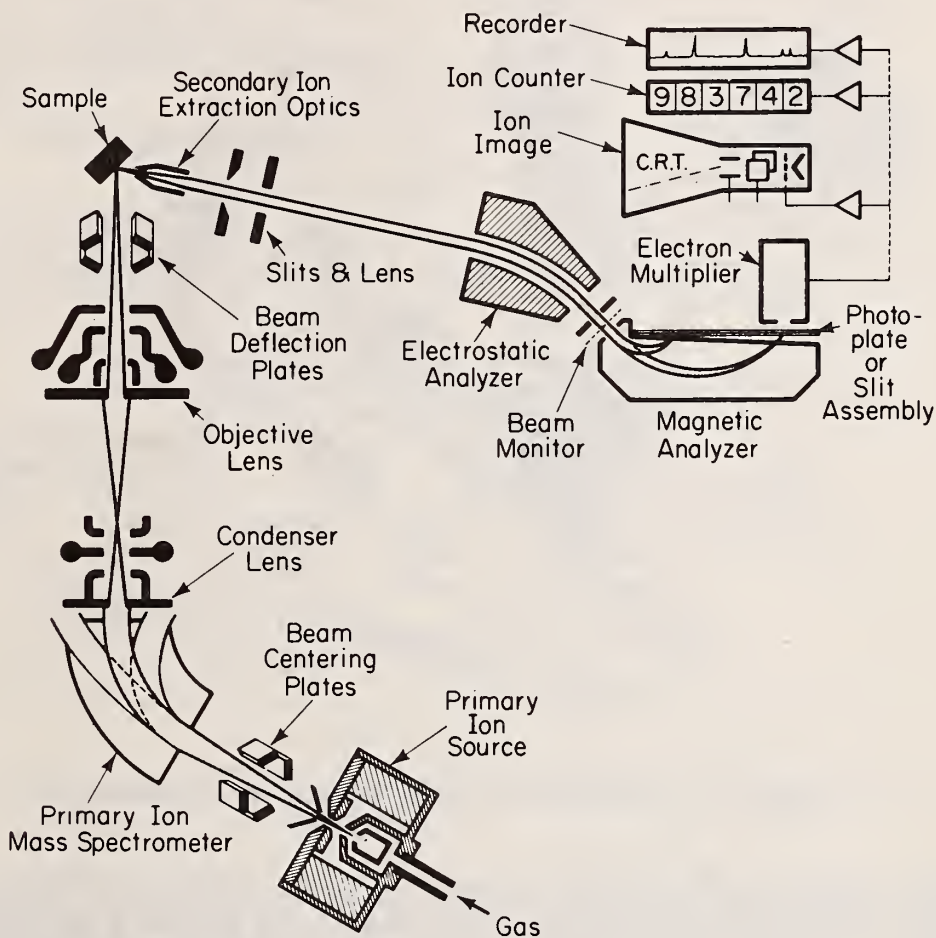


Figure 10. AEI ion microprobe analyzer (drawing from C. A. Evans, Jr., Anal. Chem. 44 (1972) 67A).

electrons simultaneously. The idea behind the 180° primary ion magnet is shown in figure 13. Sector magnets as well as the Wien filter perform in addition to the mass separation an energy dispersion, resulting in an elongation of the focused spot, especially at lower beam energies. Here the beam is made to enter the 180° magnet parallel, the mass separating slit is placed in the middle, and the ions leave the magnet as a parallel beam, only slightly broadened due to their energy spread. At the condenser lens focus, no lateral energy dispersion is

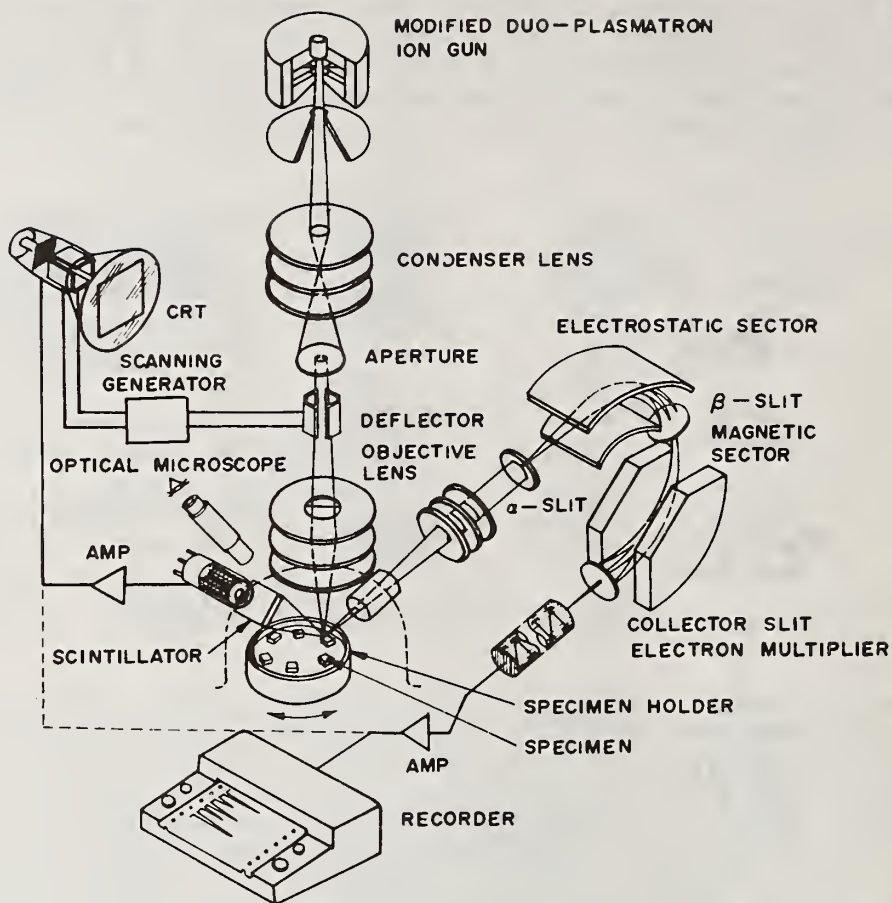


Figure 11. Hitachi IMA-2 ion microprobe analyzer [25].

left; the focus is round. Another advantage is that the ion acceleration voltage and the magnetic field need not be extremely constant. We are in the process of attaching an energydispersive X-ray spectrometer, which will facilitate conventional electron analysis.

Another prototype instrument, based on this design, has been built by Meier at Varian MAT in Bremen [27]. A scheme of it is shown in figure 14. The primary magnet is turned to the other side to make more room around the sample stage for various attachments such as a residual gas analyzer and a backscattered electron detector, or an energy dispersive X-ray spectrometer. This instrument is also built using UHV-technology. At the Austrian research site Seibersdorf near Vienna, Rüdener and Steiger recently finished assembly of another UHV-ion microprobe analyzer [28] (fig. 15). The primary column is rather conventional with duoplasmatron and two asymmetric einzel lenses, but without mass analysis. The secondary mass spectrometer is rather

Ion Microprobe Instrumentation

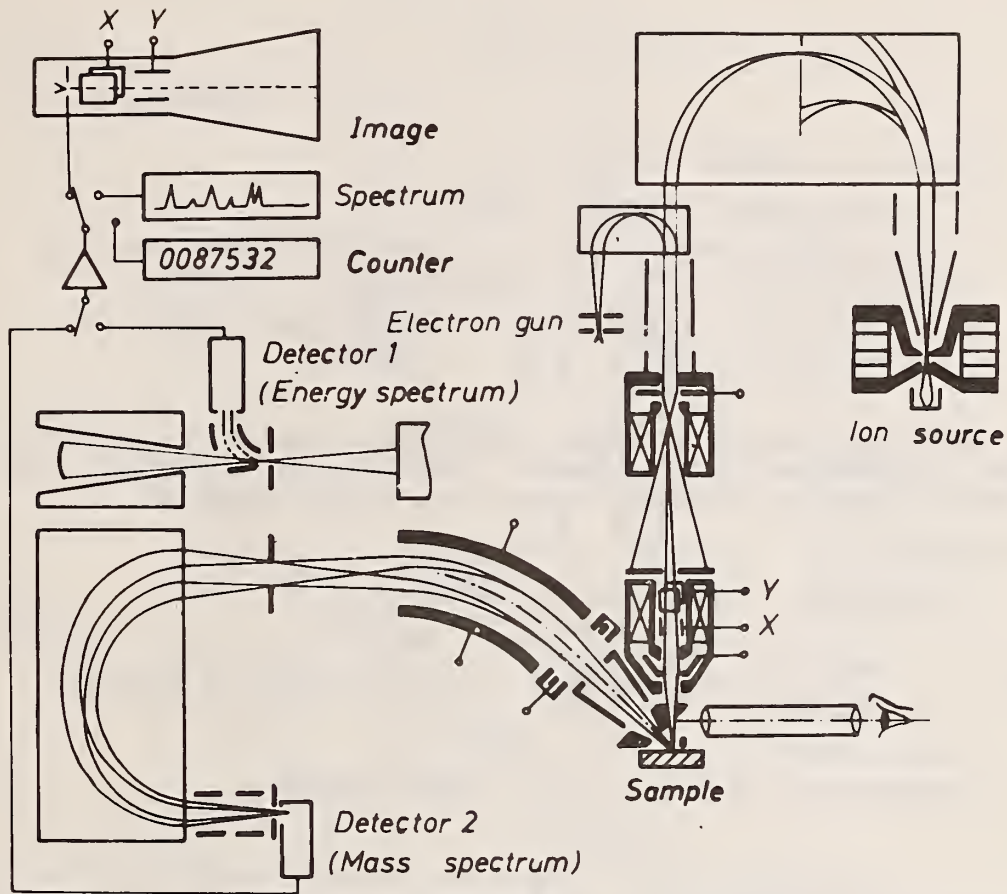


Figure 12. Combined ion and electron microprobe analyzer (UMPA) [7].

unusual in that it actually consists of two double focusing mass spectrometers in tandem. The first one has an energy-dispersed intermediate focus. The first mass spectrum is formed at a slit inside a 180° uniform field magnet, serving as entrance slit of the second mass spectrometer. This arrangement is distinguished by great abundance sensitivity because of the virtual elimination of the scattered ion background from the major peaks.

Now I am going to talk about some instrumental details worthy of closer consideration. One crucial design feature is the effective secondary ion collection from the sample, because it enters directly into the total transmission and therewith into the absolute sensitivity. The relation between the consumed sample volume and the number of ions collected at the detector, which stem from a monoisotopic constituent present with the atomic concentration C in a matrix of atom density N (atoms/cm³) is given by

$$n = CN a \Delta z \gamma \eta \quad (1)$$

with a = samples area (cm^2)
 Δz = depth interval (cm)
 γ = ionization ratio of detected ionic species
 (sputtered ions/sputtered particles)
 η = total transmission factor from sample to
 detector.

In order to measure a minimum concentration C_{\min} with a precision of $\pm 10\%$, 100 ions have to be collected. Taking $N = 6 \times 10^{22} \text{cm}^{-3}$ as an average figure, we obtain the volume which has to be eroded

$$a \Delta z \approx 1.6 \times 10^{-21} / \gamma \eta C_{\min} \quad (2)$$

For a $1 \mu\text{m}^2$ area, the eroded depth interval Δz becomes

$$\Delta z \approx 1.6 \times 10^{-13} / \gamma \eta C_{\min} \quad (3)$$

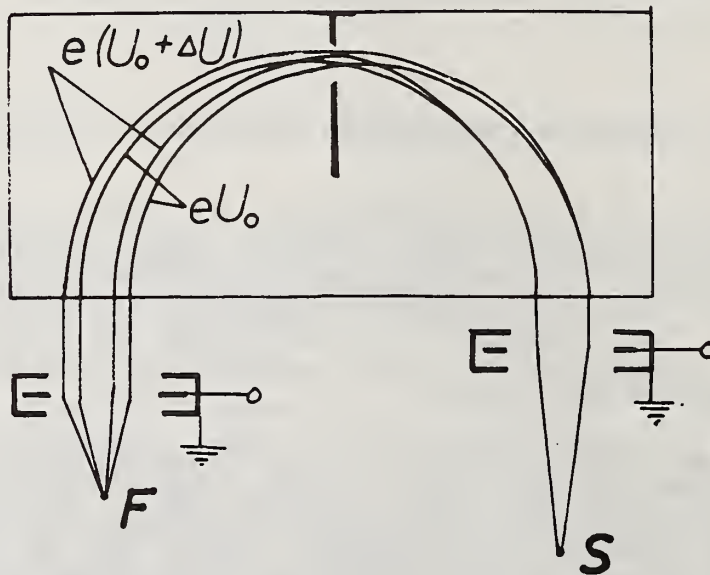


Figure 13. Mass separation without energy dispersion (primary beam of UMPA) [7].

Ion Microprobe Instrumentation

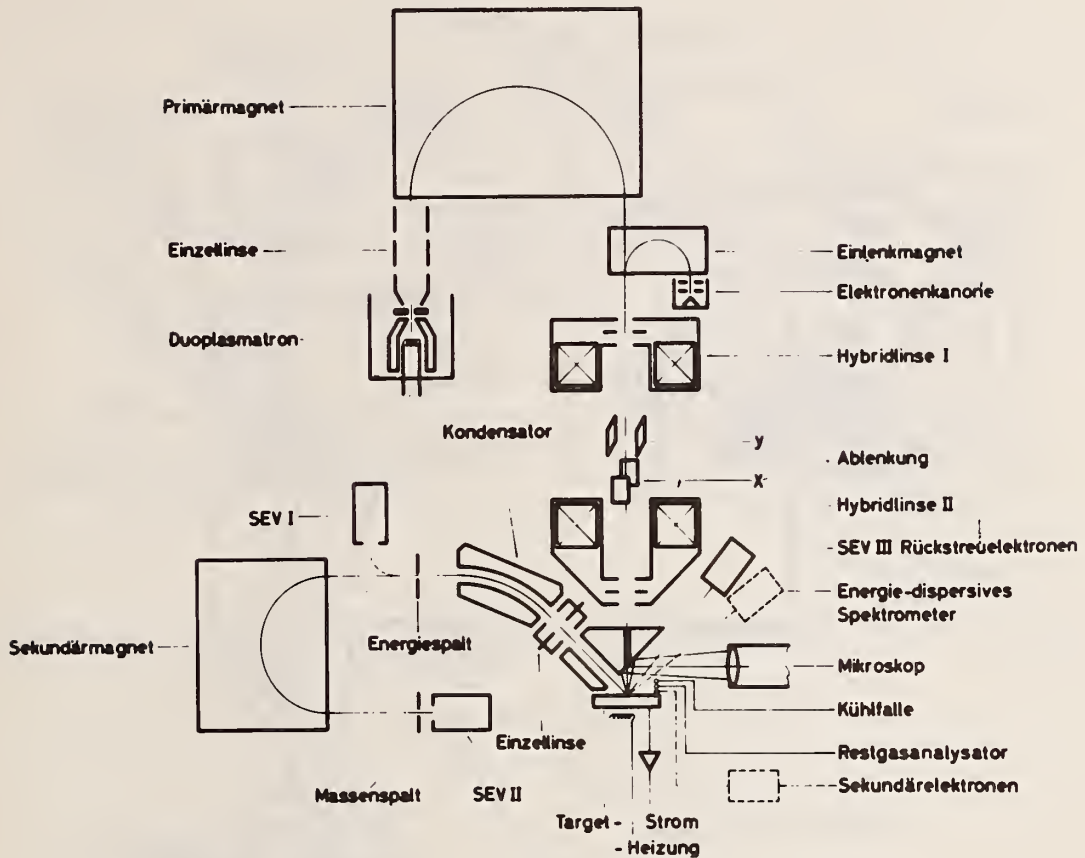


Figure 14. Layout of Varian MAT prototype ion and electron microprobe analyzer [27].

Assuming for example an ionization ratio of 10^{-2} and a transmission of 10%, the depth interval required for $C_{\min} = 100$ ppm comes out to be 160 \AA . This would also be about the depth interval required to make one scanning image of that low concentration constituent. For one scanning image of the matrix ($C = 1$), Δz comes out to be $1.6 \times 10^{-2} \text{ \AA}$, which means that only 0.006 monolayers are required. With a transmission of 0.1% instead of 10%, these erosion figures are 100 times as large, *i.e.*, 1.6 \mu m in the one case and 0.6 monolayers in the other. These examples demonstrate the importance of effective secondary ion collection. Figure 16 shows the arrangements used with IMMA [16] and UMPA [7]. Both afford high collection efficiency owing to appropriate shaping of the acceleration field. In both cases *in situ* microscopic observation with a numerical aperture as high as 0.25 is possible over a metal mirror having a central hole for passage of the primary beam. In case (b) the objective lens can be placed somewhat closer to the sample, which for a given beam brightness yields a higher current in the spot. On the other hand, the displacement of the spot due to the secondary acceleration field is larger than in case (a). Another scheme worth mentioning was

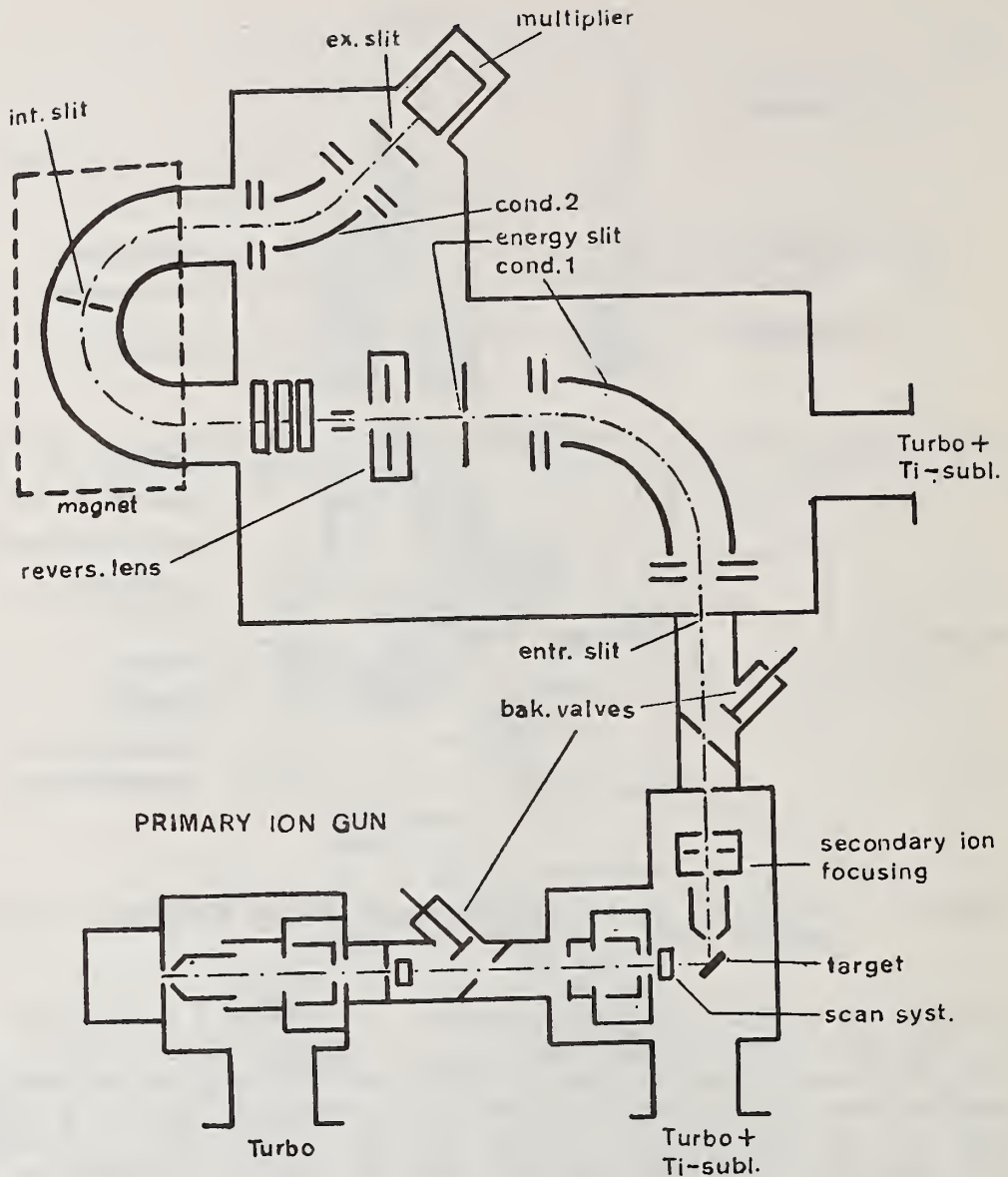


Figure 15. Ion microprobe analyzer of Rüdener and Steiger [28].

proposed by Goutte *et al.* [29] (fig. 17). Here the secondary ions were to be accelerated over a short distance and then deflected out by a little electrostatic prism, the outer plate of which is perforated for passage of the primary beam. Another point of interest is the secondary ion analysis by a quadrupole mass filter, which had been done first by Krohn in SIMS work [30] but has not been used in ion microprobes yet.

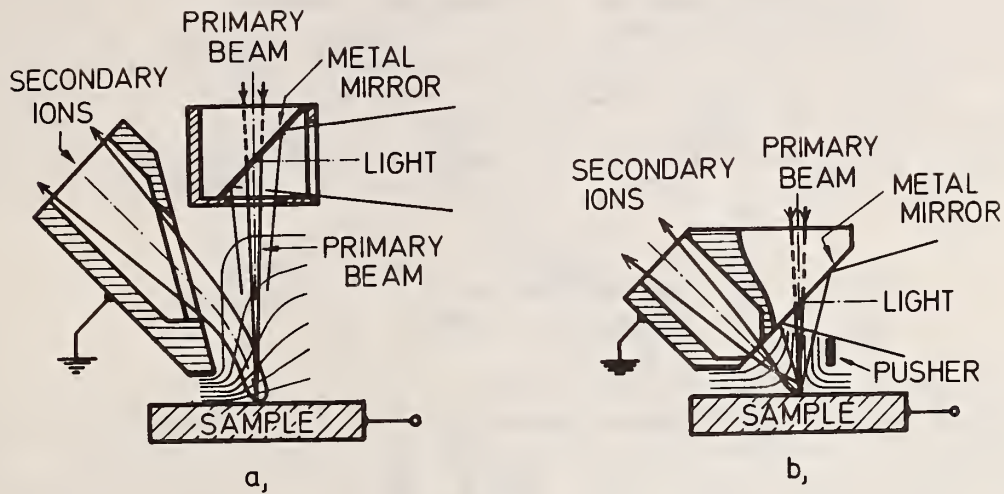


Figure 16. Secondary ion acceleration with (a) IMMA (Fig. 7) and (b) UMPA (Fig. 12).

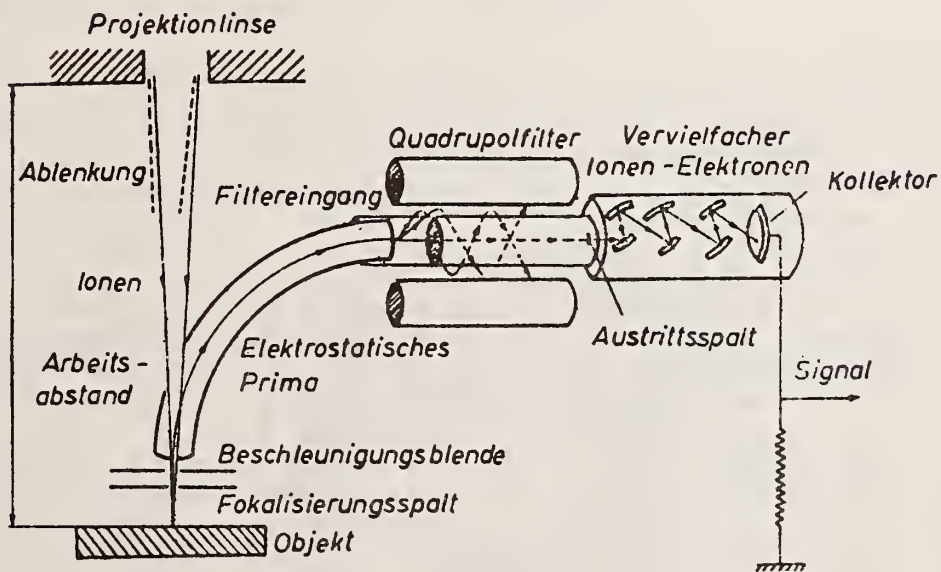


Figure 17. Secondary ion acceleration through apertures, deflection of electrostatic prism, and analysis by quadrupole mass filter (Goutte *et al.* [29]).

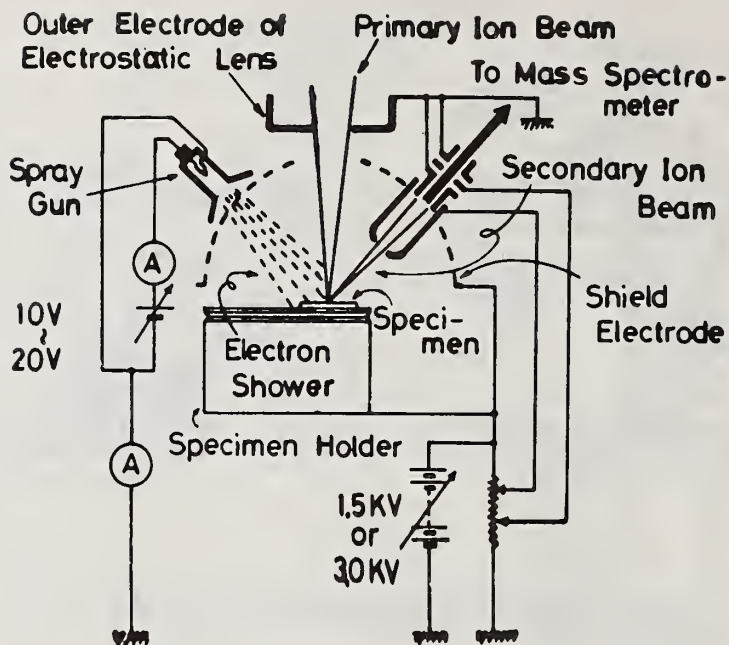


Figure 18. Hitachi IMA-2 sample stage [31].

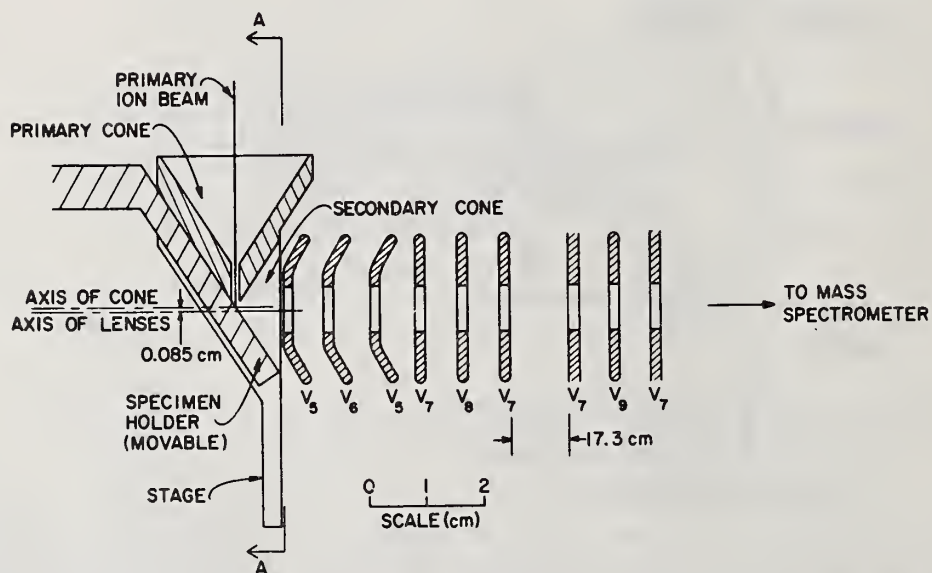


Figure 19. Secondary ion collection system for ANL 100-inch mass spectrometer (Krohn and Ringo [35]).

Figure 18 shows the sample stage arrangement of the Hitachi IMA-2 [31]. A point of interest here is the electron spray gun used to prevent charge-up of insulating samples. This method had also been used with the sputter ion source of figure 5 by Herzog and co-workers [32]. Andersen, Roden and Robinson [33] have demonstrated the usefulness of using a negative primary beam to alleviate the charge-up problem. The combined ion and electron microprobes (fig. 12 and 14) offer the additional possibility of using a positive ion beam plus an electron beam simultaneously.

III. CURRENT DEVELOPMENT

The mass spectrometers of the ion microprobe analyzer described so far are designed for higher transmission and medium resolution, save the AEI instrument. Since they are all double-focusing instruments, transmission can be traded for higher resolution. But there is a recognized need for a high transmission (10%) - high resolution (10,000) instrument, particularly for geochemical [34] and biochemical [35] applications. One step in that direction has been made by Krohn and Ringo [35] at ANL. They are developing a microprobe attachment for the Argonne 100-inch mass spectrometer. Figure 19 shows their secondary ion collection system, developed to achieve optimal matching with the acceptance phase space of their mass spectrometer. It is made up of three einzel lenses, but the crucial feature is the division of the specimen stage into sections of different potentials.

I have mentioned above that the current into a given spot becomes larger if the distance from the objective lens to the sample can be made the shorter. Figure 20 shows calculated diameters of the beam focus for different beam currents as a function of the convergence angle. A beam of typical brightness and energy spread from a duoplasmatron is assumed. The curves are the RMS values of the combined contributions from Gaussian diameter (d_g), spherical aberration (d_s), and chromatic aberration (d_c) [36,37]. The values of the aberration constants C_s and C_c used here are typical of the objective lenses used in IMMA [15] or UMPA [7] (3 to 4 cm focal length). The optimum convergence angles, to be defined by the final aperture, are where these curves have minima. Figure 21 shows similar plots, but for an objective lens of only 0.5 cm focal length. It shows that it should be possible to obtain a spot of less than 2000 Å diameter with 10^{-11} A beam current. These plots apply for a 10 keV beam with a 10 eV energy spread. Using a higher beam energy would increase the brightness and therefore move the d_g -lines down, and it would further decrease the relative energy spread $\Delta U/U$ and therefore move the d_c -lines down. So the minima of the curves would be lower, too. But higher beam energies should not be used with respect to undesirable effects upon the samples. Hill [38] has reported a 0.3 μm diameter spot with a 30 keV Ar^+ beam of 5×10^{-10} A current, and Drummond and Long have reported a 0.2 μm diameter spot with a 20 keV Ar^+ beam [20] (current not reported).

From the above consideration on sample consumption, it is clear that striving for submicron spot sizes would make sense, even though the required depth interval will be increased, provided that the secondary ion transmission can be made high. It is obvious that the secondary ions cannot be extracted sideways from the sample, if it is very close to the objective lens. I have figured out a way to overcome this problem [39]. Figure 22 shows the solution: The secondary ions are extracted back through the objective lens. The same set of electrodes is used as objective lens for the primary beam and for secondary ion acceleration. The problem here is that the primary beam has to be confined by a small aperture to obtain the optimum convergence angle, but the secondary ion collection should be efficient. This is accomplished by choosing the potentials in such a way that the primary beam is focused by the two lens fields onto the sample, while the secondary beam has a crossover in the aperture fitted inside the middle electrode, and leaves the assembly as a parallel beam (fig. 23). Figure 24 shows the incorporation of a Schwarzschild-type microscopic objective for viewing the sample *in situ*. The secondary beam is separated from the primary beam by a deflection condenser having a bore in the outer

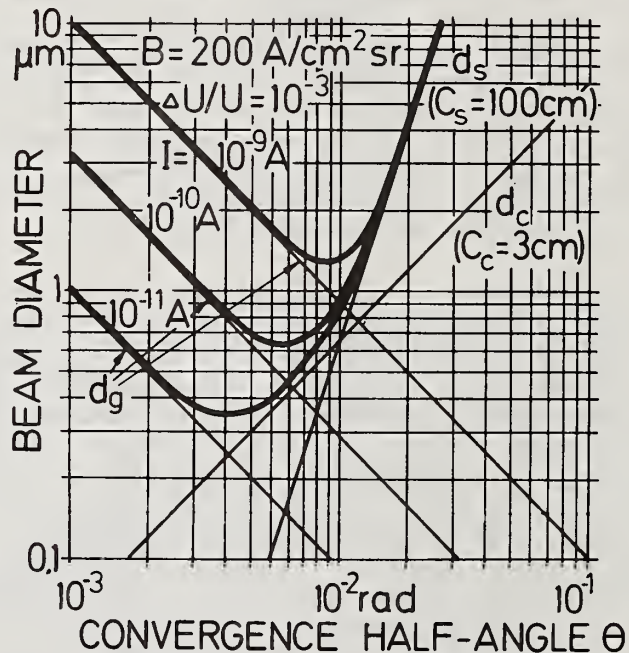


Figure 20. Calculated diameters of focused ion beam vs. convergence angle obtainable with einzel lens of 3 cm focal length. Contributions; d_g , Gaussian diameter; d_s , spherical aberration, d_c , chromatic aberration.

shell (visible at the upper rim of fig. 24). A complete ion microprobe analyzer with this lens, called the COALA (Combined Objective and Anode-Lens Analyzer), is presently under assembly.

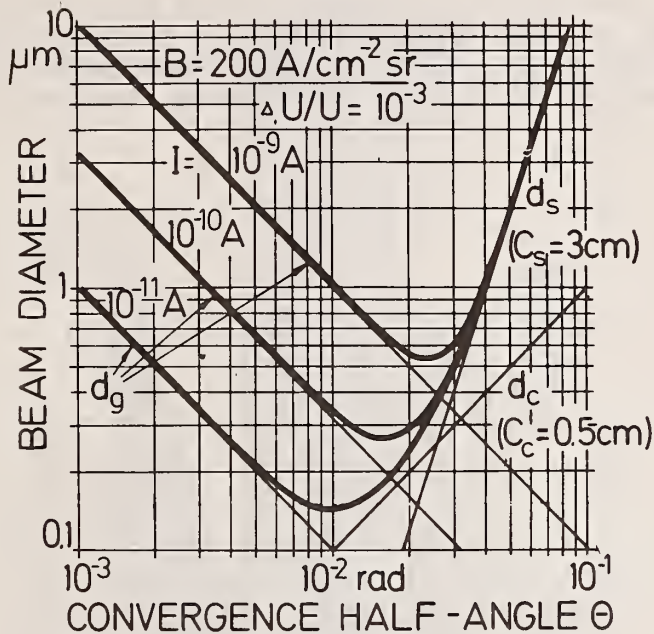


Figure 21. Beam diameters like Fig. 20, but with einzel lens of 0.5 cm focal length.

IV. DEPTH PROFILING

One of the most important applications of ion microprobe analyzers is the measurement of concentration profiles [40]. While the lateral resolution is about 1 μm for the present instruments, the depth resolution can be 100 times better, around 100 Å. With an ion microprobe analyzer, a concentration in-depth profile can be taken from a very small area. In order to obtain even erosion without sloping walls, several methods can be used. The simplest way (fig. 25a) is to use an unfocused beam hitting the final aperture. Since the current density across the aperture is then uniform, a flat-bottomed crater with very steep walls will result. Higher current densities and therefore erosion rates can be obtained, if such a uniform beam is weakly focused by the objective lens (fig. 25b). The current density will stay uniform, as long as the lens aberrations are still negligible. Although the erosion progresses evenly, in these two cases, there will be a contribution to the secondary ion current from the narrow rim zone, amounting to perhaps a few percent of the total current.

It depends on the problem at hand whether this is tolerable or not. Even this small contribution is eliminated with the so-called "electronic aperture" scheme [16] (fig. 26). The focused primary beam is raster scanned across the area under investigation. The scaler counting the mass-analyzed secondary ions is electronically gated by

signals derived from the scan voltages, so that only the ions from the central portion of the rastered area are counted. Figure 27 shows optical micrographs of an erosion area obtained by raster scanning [43]. The interferometric micrograph demonstrates how evenly the erosion progresses.

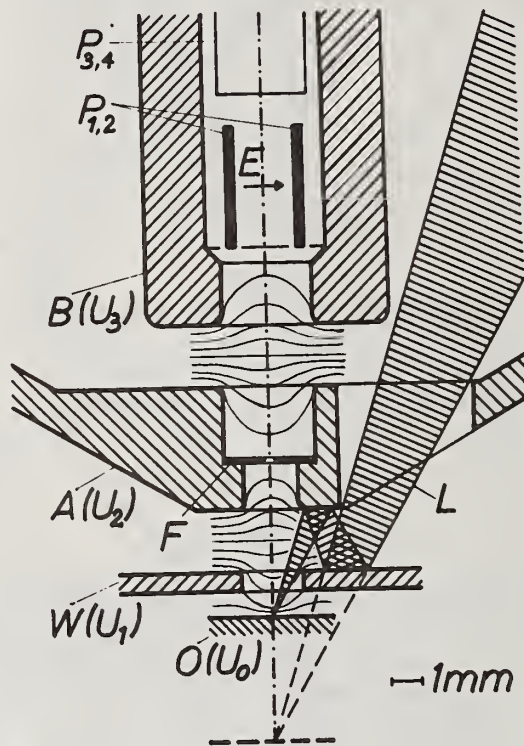


Figure 22. Combined objective and anode lens of COALA (Combined Objective and Anode Lens Apparatus). O, Sample; W, Wehnelt; A, anode; B, grounded electrode; $P_{1,2}$ and $P_{3,4}$, deflection plates; L, light cone [39].

Tamura *et al.* [44] at Hitachi have used the so-called stop-scan method, where the beam raster scans for erosion and in between is directed to any desired spot for analysis. They also have used the energy stop of the mass spectrometer as mechanical aperture to suppress ions from the rim zone, by making it smaller than the image of the rastered area.

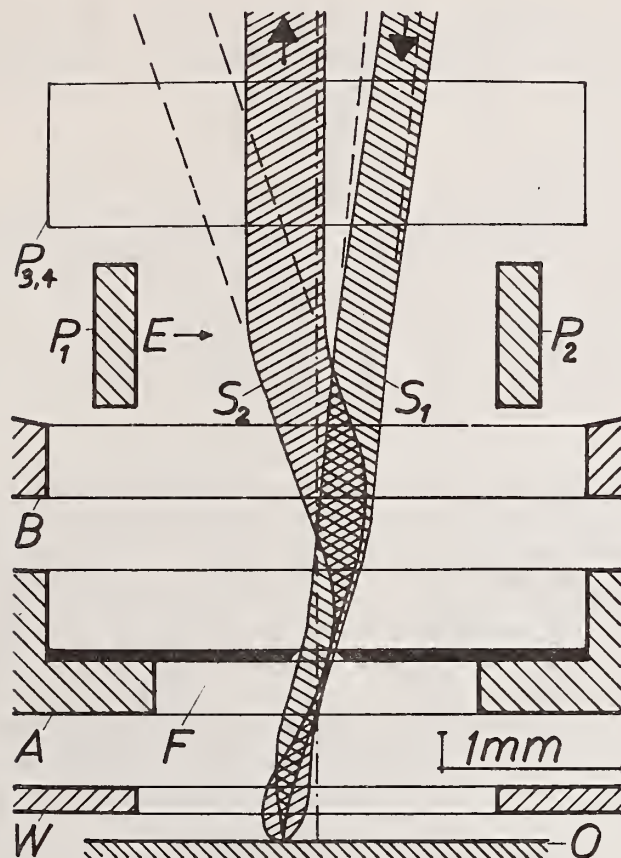


Figure 23. Primary (S_1) and secondary (S_2) beams in COALA lens in an off-axis scan position.

V. ION MICROPROBE ANALYSIS BY OTHER TECHNIQUES

The analysis of secondary ions is not the only method for bulk or surface characterization by application of ion beams. Other techniques are: Low-energy noble ion scattering spectroscopy (ISS), Rutherford-backscattering of high energy light ions, nuclear reactions induced by high energy light ions, and ion-induced X-ray emission. Cookson and Pilling [55] at Harwell have built a magnetic quadrupole quadruplet capable of focusing light ions up to 3 MeV energy to a spot of $4 \mu\text{m}$ diameter, and have reported measurements using these techniques (except ISS) with a microbeam.

Another effect which has also been utilized for surface characterization by ion microprobe techniques is the so-called "ionoluminescence." A significant fraction of the sputtered neutrals and ions come off the surface in excited states, and subsequently relax

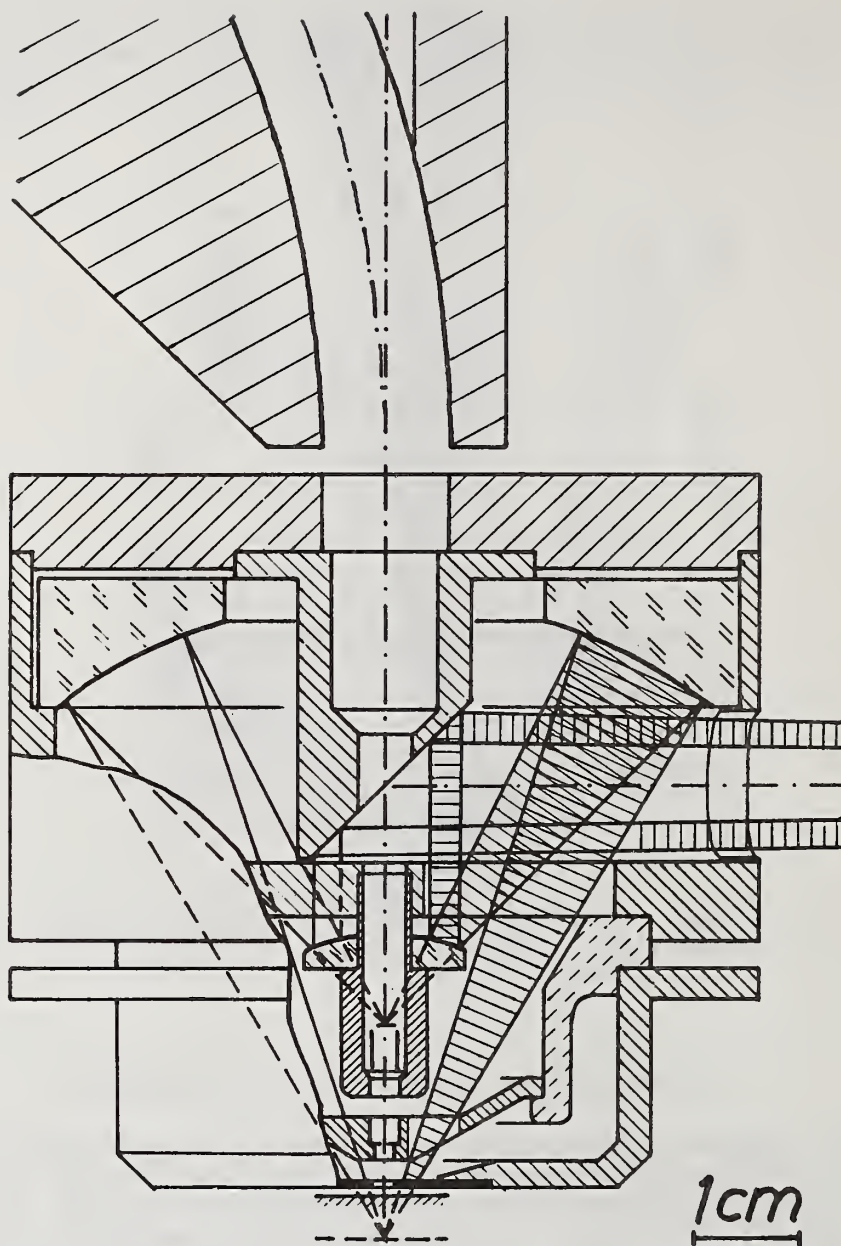


Figure 24. COALA lens with microscopic mirror optics. Separation of beams by deflection condenser (upper rim of figure).

under photon emission. Whoever has worked with intense heavy ion beams has seen the glow above a bombarded target. Figure 28 shows an arrangement published by Goutte *et al.* [29] in 1967. A beam of alkali ions from a thermionic hairpin ion source is focused by a single einzel

Ion Microprobe Instrumentation

lens onto the sample. The emitted light is focused by a concave mirror into a photomultiplier. Interference filters were used for analysis.

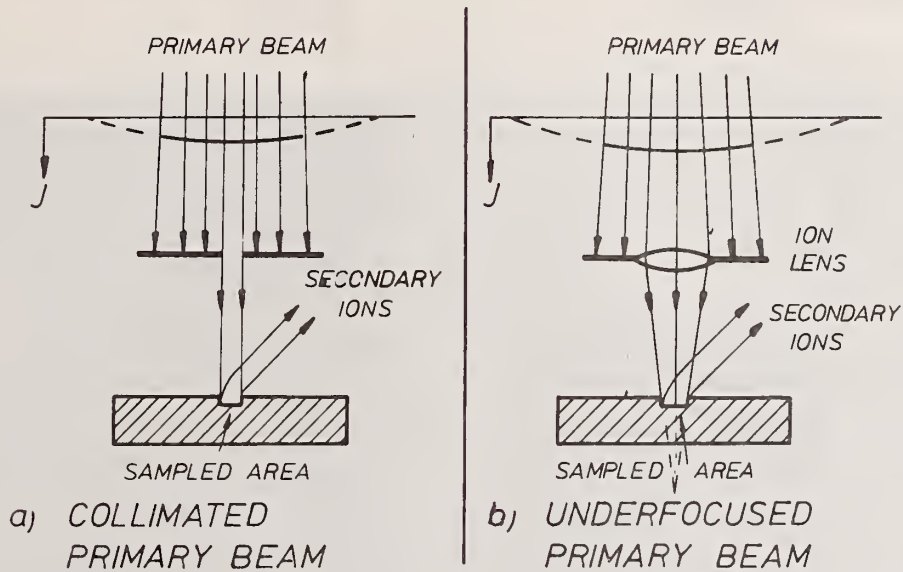


Figure 25. Even erosion obtained with (a) collimated primary beam (b) underfocused primary beam.

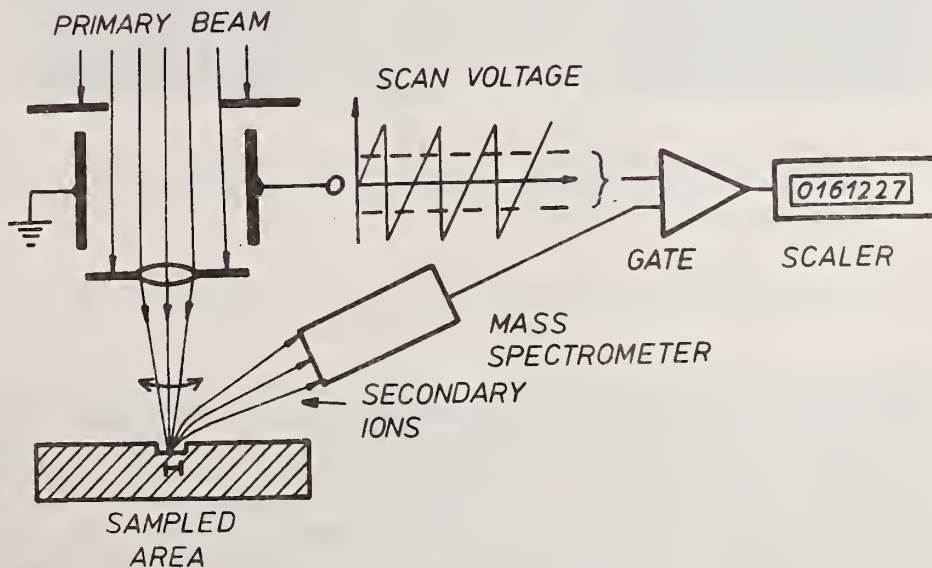


Figure 26. Scheme of electronic aperture.

Figure 29 shows scanning micrographs obtained by this technique. Several groups now have been working to investigate the ionoluminescence [45,46]. It seems that it may find more application in ion microprobe analysis.

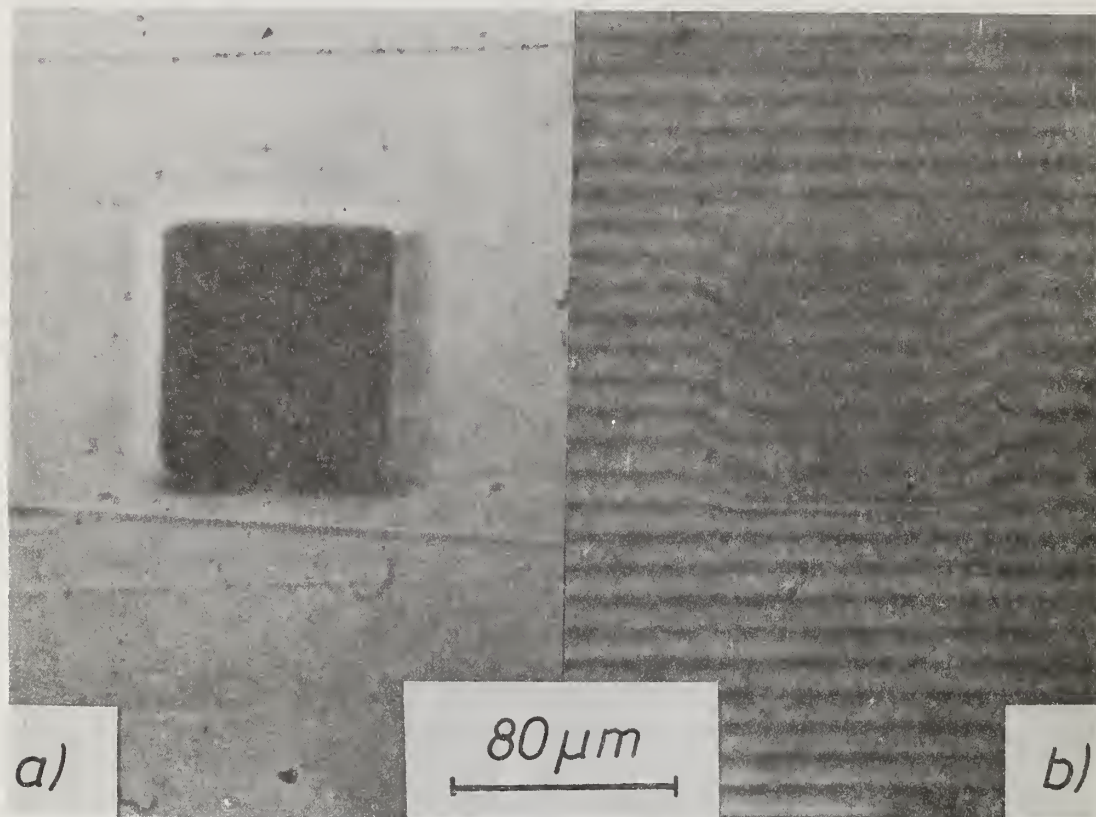


Figure 27. Optical micrographs of raster eroded area. Sample: 2000 Å Al on (111) Si surface. Beam: 10 μm diameter, 10 keV Ar⁺. Erosion depth: 2600 Å.

VI. ION SOURCES

The duoplasmatron-type source has proven to be a good workhorse ion source, affording high brightness, low energy spread, and versatility as a source for a variety of ionic species. After the benefits of using reactive species instead of the commonly used argon had been demonstrated by Andersen [47] following a suggestion of mine, the replacement of the hot filaments by hollow cathodes made stable operation with reactive gases possible. In the plots of beam diameters (fig. 20 and 21) the positions of the Gaussian beam size (d_g) lines for different beam currents depend on the brightness of the ion gun. A

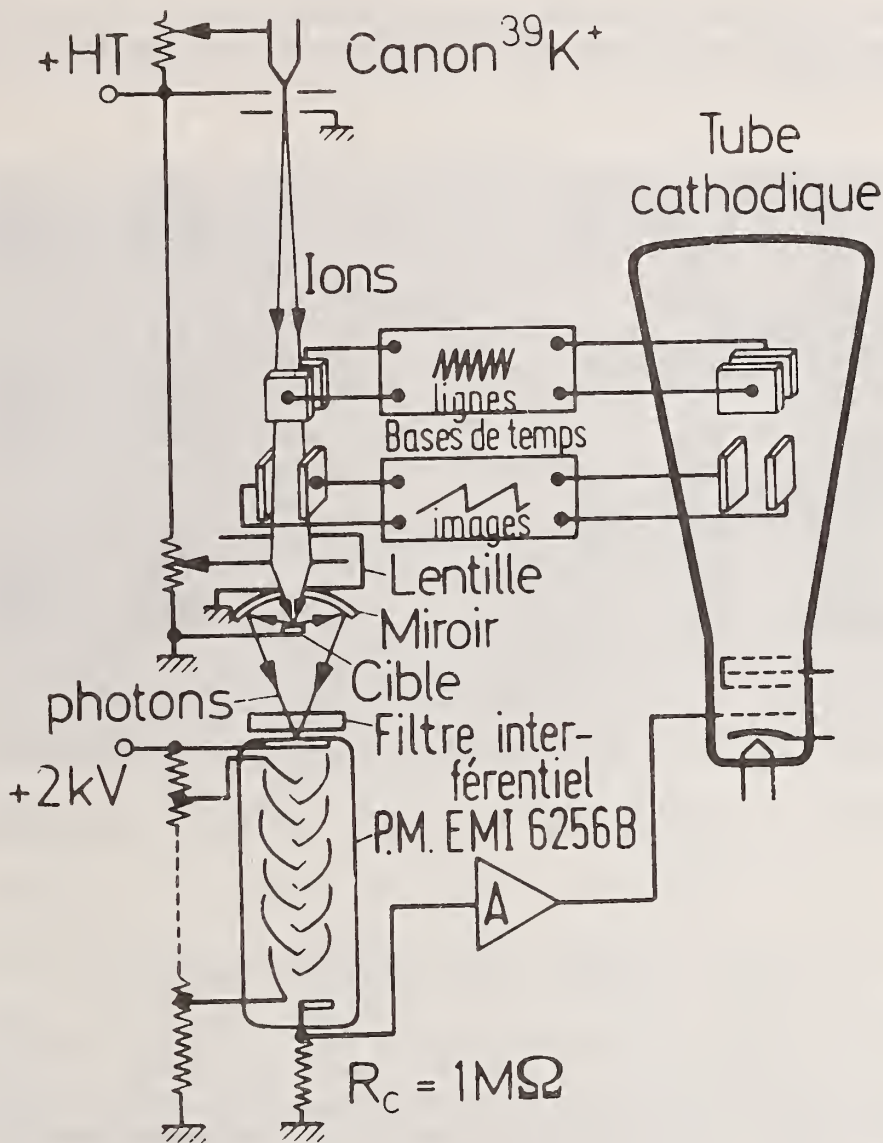


Figure 28. Scanning ion microprobe using iono-luminescence (Goutte *et al.* 1967 [29]).

higher brightness value moves the d_g line for a given beam current down toward smaller spots. The only ion source with higher brightness values than duoplasmatrons are field ionization and field evaporation sources [48-51]. These might have a future in ion microprobes, especially field evaporation sources operated with liquid alkali metals, since alkali ions have been found to have a similar beneficial effect on the production of negative secondary ions as ions of electronegative gases on the production of positive secondary ions [30,52]. However, because

of the particular emission characteristics of field ion sources, completely different ion optics would have to be used for microprobe formation [53].

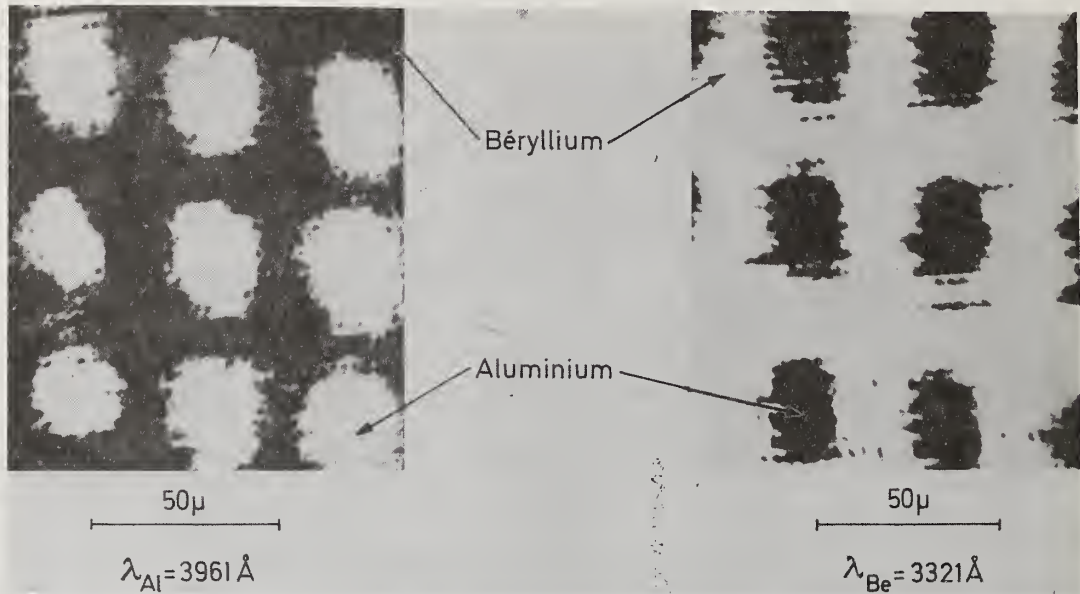


Figure 29. Iono-luminescence micrographs obtained with instrument of Fig. 28.

VII. COMPLETE THREE-DIMENSIONAL ANALYSIS

In most ion microprobe analyzers only one of the secondary ionic species can be detected at a time; the others are wasted. An exception is the AEI-instrument, if used with photoplate detection, since the Mattauch-Herzog mass spectrograph produces a simultaneous complete mass spectrum. But photoplate detection has its drawbacks, especially the limited dynamic range. One way out could be multiple electric detection, facilitating on-line data acquisition.

Another possibility to record all masses of an eroded volume would be to use digital scanning with a pulsed primary beam, to analyze each burst of secondary ions with a time-of-flight mass spectrometer, which records the different masses successively, and to store the output information. This way, a complete mass spectrum from each volume element of the eroded volume would be on record and could be displayed in whichever way one wished. A novel type of time-of-flight mass spectrometer which is energy-focusing and, therefore, appears well suited to accommodate the rather large energy spread of sputtered ions, has been developed by Poschenrieder [54].

It seems that the ion microprobe analyzer has established itself as a valuable new tool for the analytical laboratory, but that there is room for improvement of its instrumental and analytical capabilities.

VIII. REFERENCES

1. Bernard, R. and Goutte, C. R., Acad. Sci. 246, 2597-99 (1958).
2. Goutte, R., Guillaud, C., Javelas, R., and Mériaux, J. Microscopie 3, 473-82 (1964).
3. Castaing, R., and Slodzian, G., J. Microscopie 1, 395 (1962).
4. Castaing, R., Proc. 4th Int. Conf. on X-Ray Optics and Microanalysis, 48, Hermann, Paris (1966).
5. Castaing, R., Proc. 6th Int. Conf. on X-Ray Optics and Microanalysis, 399-407, Univ. Tokyo Press (1972).
6. Rouberol, J.-M., Guernet, J., Dechamps, P., Dagnot, J.-P. and Guyon de la Berge, J.-M., Proc. 5th Int. Conf. on X-Ray Optics and Microanalysis, 311-18, Springer (1969).
7. Liebl., H., Int. J. Mass Spectrom. Ion Phys. 6, 401-12 (1971).
8. Sloane, R. H., and Press, R., Proc. Roy. Soc. A. 168, 284-301 (1938).
9. Ardenne, M. v., Z. Techn. Phys. 20, 344-46 (1939).
10. Herzog, R. F. K. and Viehböck, F. P., Phys. Rev. 76, 855-56 (1949).
11. Liebl, H. J. and Herzog, R. F. K., J. Appl. Phys. 34, 2893-96 (1963).
12. Liebl, H. J. and Herzog, R. F. K., 12th Ann. Conf. Mass Spectrom. Allied Topics, ASTM E-14, 393-97, Canada (1964).
13. Ardenne, M. v., Tab. d. Elektronenphysik, Ionenphysik und Übermikroskopie, Vol. I, p. 544, VEB Deutsch. Verlag d. Wissensch., Berlin, Germany (1956).
14. Herzog, R. F. K., Liebl, H. J., Poschenrieder, W. P., and Barrington, A. E., NASA Report N 65-23741.
15. Liebl, H., J. Appl. Phys. 38, 5277-83 (1967).
16. Whatley, T. A., Slack, C. B., and Davidson, E., see Ref. 5, p. 417-22.

17. Liebl, H., 15th Ann. Conf. Mass. Spectrom. All. Top., ASTM E-14, Paper 160, Denver, Col. (1967).
18. Long, J. V. P., Brit. J. Appl. Phys. 16, 1277-84 (1965).
19. Drummond, I. W., Long, J. V. P., Nature 215, 950-52 (1967).
20. Drummond, I. W., and Long, J. V. P., Proc. 1st Int. Conf. on Ion Sources, 459-68, Saclay, France (1969).
21. Septier, A., CERN Report No. 60-39.
22. Coles J. N., and Long, J. V. P., Phil. Mag. 29, 457-71 (1974).
23. Banner, A. E., Bateman, R. H., Halliday, J. S., and Wildig, E., AEI New Product Information (1972).
24. Tamura, H., Kondo, T., Doi, H., Omura, I. and Taya, S., in Recent Developments in Mass Spectroscopy, 205-9, Univ. Tokyo Press (1970).
25. Tamura, H., Kondo, T., Hirano, T., see ref. 5, 423-29.
26. Matsumoto, R., Sato, K., and Suzuki, K., 6th Int. Vac. Congr., Kyoto (1974).
27. Meier, S., 7. Koll. Arbeitskr. ED0, June 1974, Frankfurt/Main, Germany.
28. Rüdener, F. G., and Steiger, W., 6th Int. Vac. Congr., Kyoto (1974).
29. Goutte, R., Guillaud, C., Javelas, R., and Meriaux, J.-P., Optik 26, 574-81 (1967).
30. Krohn, V. E., J. Appl. Phys. 33, 3523-25 (1962).
31. Nakamura, K., Aoki, S., Tamura, H., and Doi, H., see ref. 5, 447-54.
32. Herzog, R. F. K., Poschenrieder, W. P., Rüdener, F. G., and Satkiewicz, F. G., see ref. 17, paper 93.
33. Andersen, C. A., Roden, H. J., and Robinson, C. F., J. Appl. Phys. 40, 3419-20 (1969).
34. Lovering, J. F., Comments on Earth Sciences: Geophysics (1973) (in press).
35. Krohn, V. E., and Ringo, G. R., Rev. Sci. Instr. 43, 1771-72 (1972).

36. Wilson, R. G., and Brewer, G. R., Ion Beams with Applications to Ion Implantation, Wiley, New York (1973).
37. Seliger, R. L., and Fleming, W. P., J. Appl. Phys. 45, 1416-22 (1974).
38. Hill, A. R., Nature 218, 202-3 (1968).
39. Liebl, H., Vacuum 22, 619-21 (1972).
40. Liebl, H., J. Vac. Sci. Technol. (in press).
41. Tamura, H., Kondo, T., and Doi, H., Adv. Mass Spectrom. 5, 441-443 (1971).
42. Blewer, R. S., and Guthrie, J. W., Surf. Sci. 32, 743-47 (1972).
43. Staudenmaier, G., Liebl., H., and Hofer, W. (unpublished).
44. Tamura, H., Kondo, T., Konomata, I., Nakamura, K., and Nakajima, J., 6th Int. Vac. Congr., Kyoto (1974).
45. Martel, J. G., and Olson, N. T., Nucl. Instr. Method. 105, 269-75 (1972).
46. Tolk, N. H., Simms, D. L., Foley, E. B., and White, C. W., Rad. Eff. 18, 221-20 (1973) (for more references on iono-luminescence see ref. 45, 46).
47. Andersen, C. A., Int. J. Mass Spectrom. Ion Phys. 2, 61-74 (1969).
48. Müller, E. W., and Tsong, T. T., Field Ion Microscopy, Elsevier, New York (1969).
49. Mahoney, J. F., Yahiku, A. Y., Daley, H. L., Moore, R. D., and Perel, J., J. Appl. Phys. 40, 5101 (1969).
50. Evans, C. A., Jr. and Hendricks, C. D., Rev. Sci. Instr. 43, 1527 (1972).
51. Krohn, V. E., J. Appl. Phys. 45, 1144 (1974).
52. Andersen, C. A., Int. J. Mass. Spectrom. Ion Phys. 3, 413 (1970).
53. Heil, H., and Guckenberger, R., Proc. Symp. Ion Sources and Form. Ion Beams, Rep. No. BNL-50310, 183 (1971).
54. Poschenrieder, W. P., Int. J. Mass Spectrom. Ion Phys. 3, 357 (1972).
55. Cookson, J. A., and Pilling, F. D., Thin Solid Films 19, 381 (1973).

LOOKING AT THE COLLECTION EFFICIENCY PROBLEM THROUGH THE ION MICROSCOPE OPTICS

G. Slodzian
University of Paris
Orsay, France

I. INTRODUCTION

Secondary ion emission is used in various instruments to provide for elemental and isotopic analysis of solid samples over small areas or in thin surface layers. In addition, many people have been studying the processes of ion emission. However, it seems that not enough attention has been paid to the data collecting procedure, that is, to the energy and angular discriminations introduced by the collecting optics coupled with the energy and mass spectrometers. This paper is an attempt to cast some light on these problems. Although it specifically deals with the ion microscope optics, the principles here invoked are thought to be general enough to provide us with conclusions which will hold in other situations, possibly with minor alterations.

When a primary ion beam is directed against the target surface, each "point" of the surface becomes a source of sputtered secondary ions. The question is how to use this localized emission so as to obtain a localized analysis. One way is to look for a focusing system which would make the beam emerging from each point source converge on a corresponding image point. Two preliminary and obvious remarks can be made:

- The secondary ions exhibit an energy distribution with a maximum of several eV and a tail extending to several hundred eV. In order to reduce the energy dispersion and to handle the secondary beam more easily, it appears convenient to accelerate the ions as they leave the target.
- Magnetic lenses are too weak to focus ions and, therefore, we have to use electrostatic lenses. It is known that ions accelerated by the same voltage will follow trajectories which are independent of the ratio e/m (e and m are the charge and the mass of the ions respectively) (fig. 1).

Thus, we see that the focusing system will necessarily comprise two stages: an acceleration stage and an electrostatic focusing stage. In addition, since the magnification of the ion image will be the same regardless of the particular ion species used, from a geometrical point of view, the focusing system acts like a device which would reconstruct a kind of expanded thin layer of the target made of the material sputtered from the target. If the laws of secondary emission were simple,¹ the ion image would faithfully reproduce the composition of the sample, except for aberrations which might give some blurring of the image.

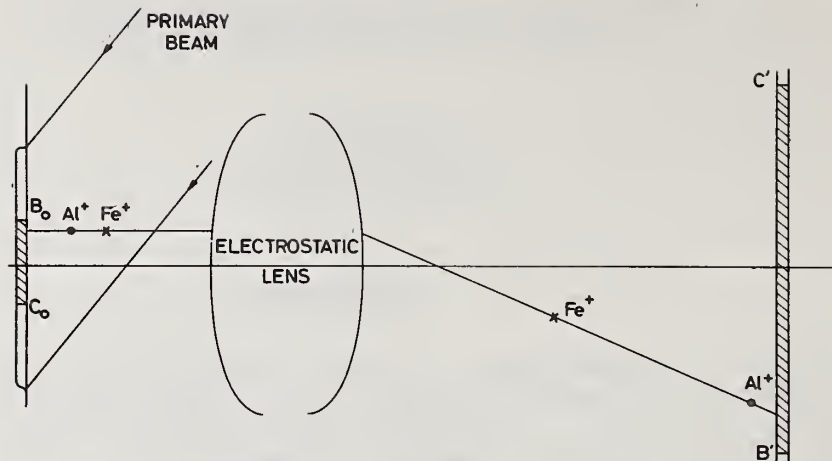


Figure 1 Schematic view of the general action of the objective lens in an ion microscope. A thin layer C_0B_0 in diameter is "reconstructed" in the image plane into an enlarged ion image $C'B'$.

Once the enlarged image is obtained, it has to be split into as many elemental images as there are different elements (or isotopes). This can be done by a combination of sector fields² similar to those used in mass spectrometry which allow an ion image made up of a given species to be filtered out. Then the filtered ion image is converted into an equivalent electron image. This latter image is either observed on a fluorescent screen or directly recorded on a photographic film. In addition, direct measurements can be performed on a specified limited area selected by aperturing at the electron image.

First, let us look at the properties of the focusing system (often called an emission or immersion lens) in some detail.

II. EMISSION LENS

(1) Secondary ion characterization

The secondary ions released at the surface are defined both by their kinetic energy ϕ_0 (in electron volts) and their velocity direction (α_0, ψ_0) where α_0 and ψ_0 are the emergence angle (colatitude) and the azimuthal angle (fig. 2) respectively. When a layer of a thickness dz over an area $d\sigma_0$ has been sputtered away, d^6N_i ions of a given species (M^+ , for instance)³ are ejected with their kinetic energy ϕ_0 in the range $d\phi_0$, and their direction (α_0, ψ_0) within the solid angle $d\Omega_0$:

$$d^6N_i = f_0(\phi_0, \alpha_0, \psi_0) d\Omega_0 d\phi_0 d\sigma_0 dz \quad (1)$$

Ion Collection Efficiency

where $f_0(\phi_0, \alpha_0, \psi_0)$ is a function which depends on emission parameters (nature of the target, angle, energy and nature of the primary ions, relative orientation of the target, surface reactions); for the sake of simplicity we assume the sample to be homogeneous.

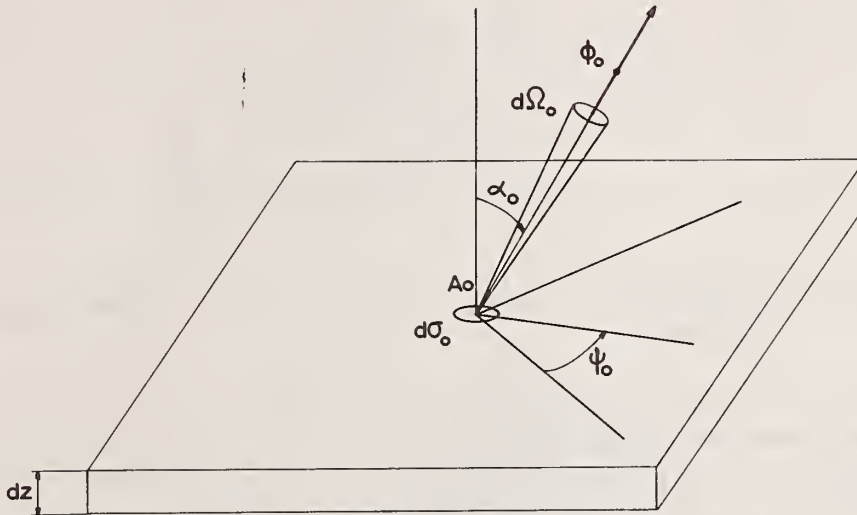


Figure 2 Characterization of the secondary ions as they are emitted: energy ϕ_0 expressed in electron volts, direction of their velocity (α_0, ψ_0), and geometrical parameters ($d\Omega_0$ solid angle, $d\sigma_0$ emitting area).

(2) Acceleration space

The ions are accelerated by the uniform electrostatic field E_0 set between the target M (at the voltage V) and the electrode N (at ground potential). In the electrode N, there is a round hole through which the ions leave the acceleration space. Near the hole, the field is no longer uniform and the equipotential surfaces are curved, having cylindrical symmetry around the Z-axis of the hole (fig. 3). This curvature of the equipotential surfaces induces focusing effects. The combination of acceleration and passage through the hole can be approximated in the following way:

- Up to the plane of the electrode N, the field is assumed to be uniform so that the trajectories between "M" and "N" are segments of parabolas.
- At the plane N there is an abrupt change in the electrostatic field which goes from the value E_0 to zero. Since the flux is conserved, an infinitely strong radial field must appear. This radial field has a divergent effect but it is acting only over an infinitesimal distance.

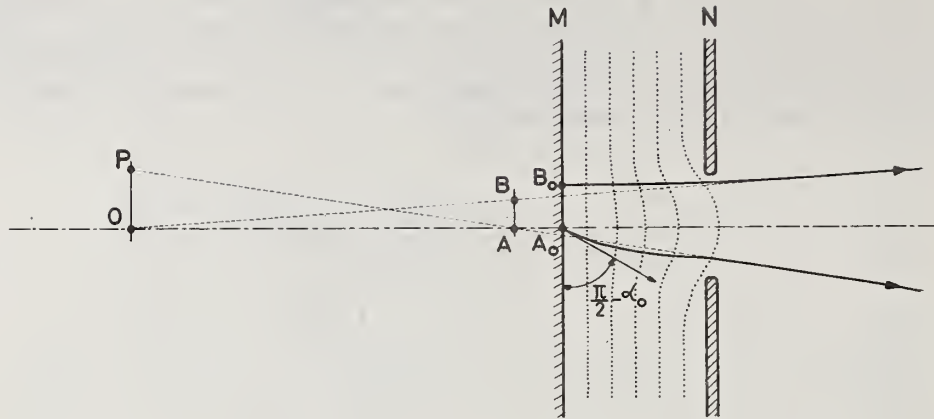


Figure 3 Acceleration space; section of the curved equipotential surfaces.

It can be shown [1] that, under these conditions, the passage through the hole does not change the distance r from the axis $z'z$ at which a trajectory pierces the plane of N , but that it changes the meridian component, $r' = dr/dz$, of the trajectory direction:

$$\Delta r' = \frac{r}{4} \cdot \frac{E_0}{V + \phi_0 \cos^2 \alpha_0} = \frac{r}{4D} \cdot \frac{1}{1 + \frac{\phi_0}{V} \cos^2 \alpha_0} \quad (2)$$

where D is the distance between M and N . Thus, the hole is acting as if it were a divergent lens placed in the plane N with its optical axis coinciding with $z'z$ and with a focal length $4D(1 + (\phi_0/V) \cos^2 \alpha_0)$. The term containing ϕ_0 describes the chromatic effect of such a lens, and if $\phi_0/V \ll 1$, it can be neglected in a first approximation.⁴ It is easy to show that, just before entering the divergent lens, the trajectories which are followed by ions which left point A_0 look as if they were coming from a virtual point A situated at a distance D behind M (fig. 4). Of course, the relation between A and A_0 or B and B_0 is the same for any point of the surface.

The effect of the uniform field alone is to produce a virtual image at a magnification of one. Further, an ion $(\phi_0, \alpha_0, \psi_0)$ leaving a point A_0 situated on $z'z$ for instance, will look as if it came from \hat{A} with the energy $V + \phi_0 \approx V$ and its velocity will have the direction $(\hat{\alpha}, \psi_0)$ where $\hat{\alpha}$ is given by

$$\sqrt{\phi_0} \sin \alpha_0 = \sqrt{V + \phi_0} \sin \hat{\alpha}, \quad \text{or} \quad \hat{\alpha} \approx \sqrt{\phi_0/V} \sin \alpha_0 \quad (3)$$

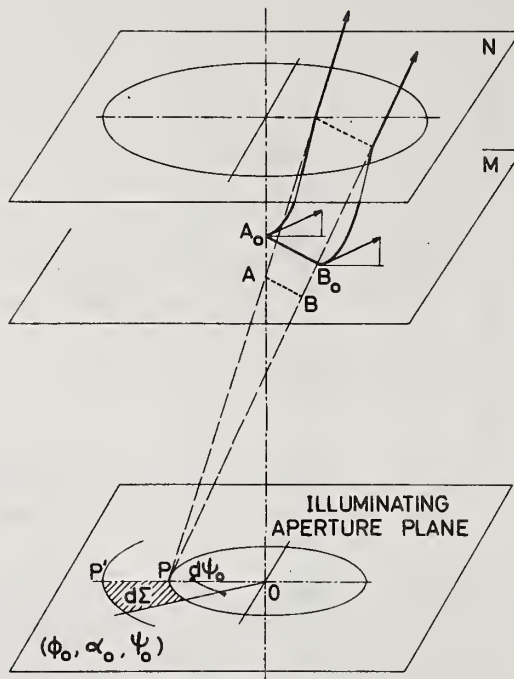


Figure 5 Three-dimensional views of ion trajectories, with the same energy and ejection direction. In the illuminating aperture plane. $\overline{OP} = p$, $\overline{PP'} = dp$, $d\Sigma = \rho d\rho d\psi_0$.

As the image [A] and the illuminating aperture [O] (which is often termed "cross-over") are virtual, it is necessary to add a lens or a combination of lenses (transfer optics) in order to obtain real images of the target surface and the cross-over. These real images can be apertured by metal diaphragms which will limit the viewing field to the diameter \overline{CB} and the illuminating aperture to the diameter $\overline{JK} = 2a$ (fig. 6). The limitation applied on the cross-over diameter implies that, for each energy ϕ_0 , the ions emitted with an angle α_0 greater than α_{0m} are not collected:

$$a \approx 4D\sqrt{\phi_0/(V+\phi_0)} \sin \alpha_{0m} \quad (4)$$

In other words, all the ions emitted with an energy lower than ϕ_{0m} are collected: $a \approx 4D\sqrt{\phi_{0m}/V}$.

The radius of the aberration spot around \hat{A} is about $\lambda_a \approx (D\phi_0/V)^{1/2} \sin \alpha_0 (1 - \cos \alpha_0)$. Because of the limitations on the cross-over, λ_a will reach a maximum for $\phi_0 = \phi_{0m}$ and $\alpha_0 = \pi/2$. Thus

the resolving spatial limit is of the order of $\lambda = (\mu \phi_{0m}/E_0)$ where μ is a dimensionless coefficient between 1 and 2⁻¹.

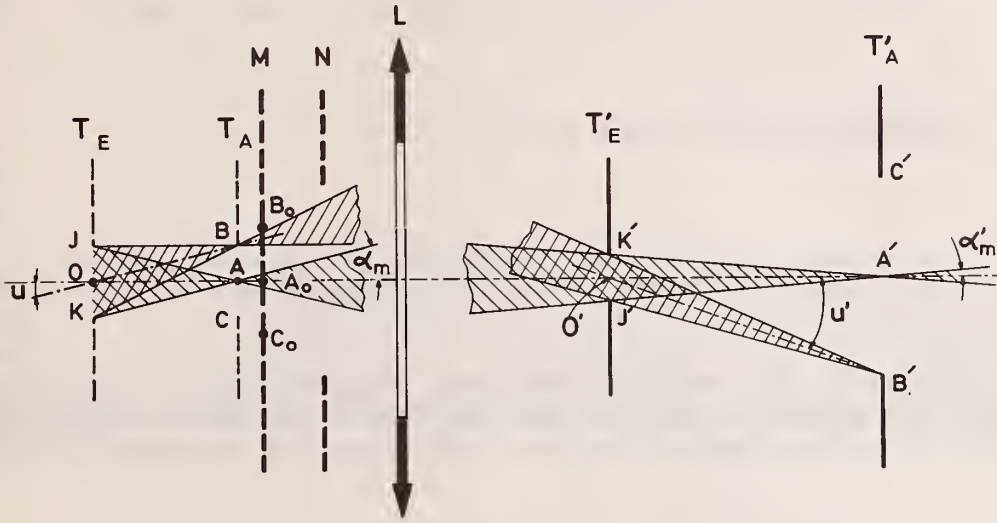


Figure 6 Objective lens; collecting optics coupled with a transfer optics reduced to one electrostatic lens.

(3) Illumination of the virtual object

The virtual image [A] plays the part of a virtual object for the transfer optics which will produce the real images actually observed. It is therefore necessary to correlate the illumination of this virtual object and the emission function $f_0(\phi_0, \alpha_0, \psi_0)$.

Let us take a small area $d\sigma$ surrounding the point A, and a solid angle $d\Omega$ around the direction (α, ψ) (fig. 7). The number of ions emitted with the initial energy ϕ_0 in the range $d\phi_0$, as a thickness dz is sputtered away, is given by:

$$d^6 N_i = f(\phi_0, \alpha, \psi) d\Omega d\sigma d\phi_0 dz \tag{5}$$

From the Lagrange-Helmholtz relation (or the equivalent Abbe's aplanatic sines relation) we know that:

$$\sqrt{\phi_0} \sin \alpha_0 \sqrt{d\sigma_0} = \sqrt{\phi_0 + V} \sin \alpha \sqrt{d\sigma} \tag{6}$$

and by differentiation against α_0 and rearranging the expressions we get:

$$\phi_0 \sin \alpha_0 \cos \alpha_0 d\alpha_0 d\sigma_0 = (\phi_0 + V) \sin \alpha \cos \alpha d\alpha d\sigma \quad (7)$$

In addition, we know that⁵ $\psi = \psi_0$.

Thus:

$$\phi_0 d\Omega_0 d\sigma_0 \cos \alpha_0 = (\phi_0 + V) d\Omega d\sigma \cos \alpha \quad (8)$$

Quantities like $d\Omega d\sigma \cos \alpha$ measure what may be termed the "geometrical extent" of the beam emerging from $d\sigma$ in the solid angle $d\Omega$ around a direction making an angle α with respect to the normal to $d\sigma$.

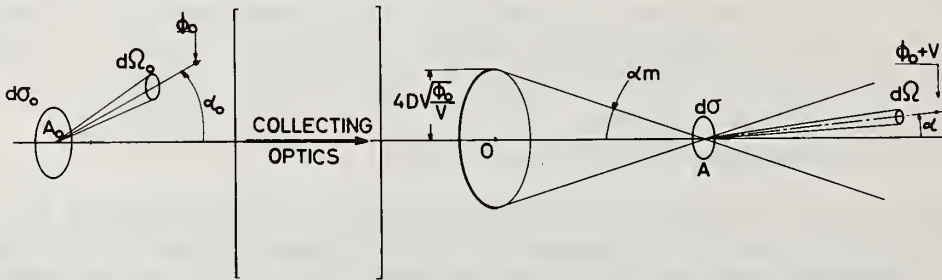


Figure 7 Schematic diagram of the effects of the collecting optics.

Let us start with d^6N_i ions emitted by $d\sigma_0$ in the solid angle $d\Omega_0$ and in the energy range $d\phi_0$ (fig. 7). When these ions leave the acceleration space, they look as if they were emerging from a surface area $d\sigma$, in a solid angle $d\Omega$ and in an energy range $d\phi_0$. Therefore, we may deduce that:

$$\frac{f_0}{\phi_0 \cos \alpha_0} = \frac{f}{(V + \phi_0) \cos \alpha} \quad (9)$$

Now, we wish to introduce some averaging because the variations of $f_0(\phi_0, \alpha_0, \psi_0)$ with ψ_0 and α_0 may be very complicated.⁶ Let us take a function $F_0(\phi_0, \alpha_0)$ such that (fig. 7):

$$\int_0^{\pi/2} f_0(\phi_0, \alpha_0, \psi_0) \sin \alpha_0 \, d\alpha_0 = \frac{1}{2} F_0(\phi_0, \psi_0) \quad (10)$$

If the emission of secondary ions followed Lambert's law for a fixed value of ψ_0 , f_0 would be equal to $F_0 \cos \alpha_0$. Although we know that it is not in general the case, we shall make the approximation by which $F_0 \cos \alpha_0$ replaces f_0 ; this approximation is valid as long as we are only looking for integral contribution to ion currents. Along these lines, we can make one step further and introduce a function $\overline{F}_0(\phi_0)$ defined by:

$$\int_0^{2\pi} F_0(\phi_0, \psi_0) \, d\psi_0 = 2\pi \overline{F}_0(\phi_0) \quad (11)$$

Here again, we will make the approximation that $F_0 = \overline{F}_0$.

This approximation and the former one are justified as long as we are interested in the total illumination of the area $d\sigma_0$ and not in the details of the angular distribution of the ions.

In summary, the number d^6N_i ions is given by the expressions:

$$d^6N_i = \overline{F}_0(\phi_0) \sin \alpha_0 \cos \alpha_0 \, d\alpha_0 \, d\psi_0 \, d\sigma_0 \, d\phi_0 \, dz \quad (12)$$

and

$$d^6N_i = \overline{F}(\phi_0) \sin \alpha \cos \alpha \, d\alpha \, d\psi \, d\sigma \, d\phi_0 \, dz \quad (13)$$

The expression for $\overline{F}(\phi_0)$ can be deduced in the following way:

$$f(\phi_0, \alpha, \psi) = \frac{V + \phi_0}{\phi_0} \cdot \frac{f_0(\phi_0, \alpha_0, \psi_0)}{\cos \alpha_0} \cos \alpha \quad (14)$$

$$= \frac{V + \phi_0}{\phi_0} F_0(\phi_0, \psi_0) \cos \alpha \quad (15)$$

Thus, it is possible to put down:

$$f(\phi_0, \alpha, \psi) = F(\phi_0, \psi) \cos \alpha \quad (16)$$

Then, by averaging according to the same procedure as previously:

$$2\pi \bar{F}(\phi_0) = \int_0^{2\pi} F(\phi_0, \psi) d\psi \quad (17)$$

It should be noted that

$$F(\phi_0, \psi) = \frac{V + \phi_0}{\phi_0} F_0(\phi_0, \psi_0), (\psi_0 = \psi) \quad (18)$$

- Because of the limitation of the illuminating aperture at a diameter $2a$, the angle α_0 cannot be greater than α_{0m}

$$\text{if } \phi_0 > \phi_{0m} \text{ with } \sqrt{\phi_0 / (V + \phi_0)} \sin \alpha_{0m} = a/4D \quad (19)$$

If $\phi_0 < \phi_{0m}$, all the ions are collected.

(4) Illumination of the illuminating aperture

The illuminating aperture, located in the plane [0], contains much experimental information on ion emission. Indeed, all the ions $(\phi_0, \alpha_0, \psi_0)$ emitted by an area σ_0 look as if they were emerging from a point $P(\rho, \psi_0)$ (fig. 5), where

$$\rho = \overline{OP} = 4D \sqrt{\phi_0 / (V + \phi_0)} \cdot \sin \alpha_0 \quad (20)$$

Near point P, over an area $d\Sigma = \rho d\rho d\psi_0$, the ion density is given by the expression:

Ion Collection Efficiency

$$\frac{d^4N_i}{d\Sigma} = \frac{V + \phi_0}{\phi_0} \cdot \frac{f_0}{16 D^2 \cos \alpha_0} \cdot \sigma_0 d\phi_0 dz \quad (21)$$

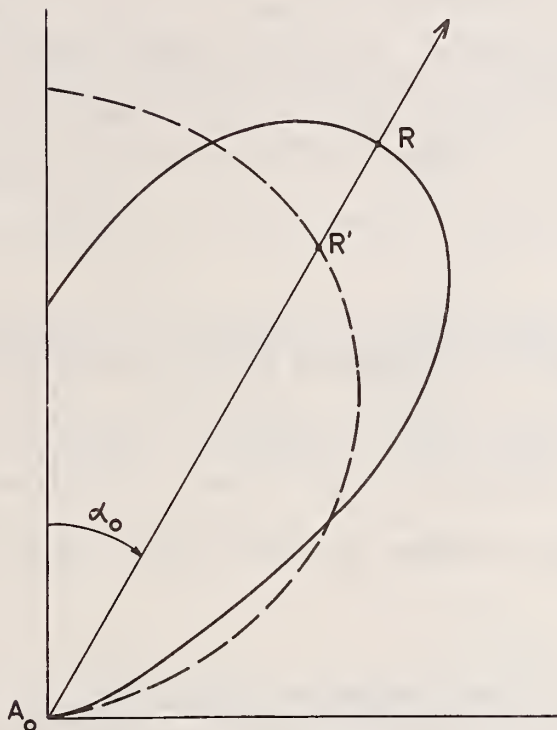


Figure 8 The continuous line gives a polar graph of the emission function $\overline{OR} = f_0(\phi_0, \alpha_0, \psi_0)$ for given ψ_0 and ϕ_0 ; the broken line gives a polar graph of the function $\overline{OR}' = F_0(\phi_0, \psi_0) \cos \alpha_0$.

If, with proper transfer optics, we produce a real image of the illuminating aperture, it becomes possible to have direct access to $f_0(\phi_0, \alpha_0, \psi_0)$; that is, to the emission pattern of the sample.

(5) Transfer Optics

The purpose of the transfer optics is to allow a better fit between the collecting optics and the mass spectrometer in order to meet specific requirements. For instance, after the spectrometer has been set to give a higher mass resolution, the transfer optics can be adjusted so as to maintain the same useful yield but this can only be achieved over a smaller analyzed field. At this stage, the size of the primary beam has no importance at all since:

- the spatial resolving limit is determined by the objective aberrations.
- the analyzed field is apertured by diaphragm T'_A .
- the useful yield is determined by the magnification of the illuminating pupil at the plane T'_E .

From the illuminating aperture on, the target and the collecting system will be replaced by the virtual object [A] and its illuminating aperture [O]. The transfer optics has to transform the virtual objects [A] and [O] into real images [A'] and [O']. It may consist of a single electrostatic lens as shown in fig. 6,7 or be composed of several lenses.

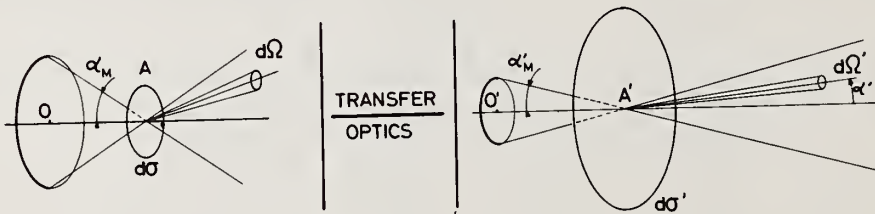


Figure 9 Schematic diagram of the general effects of the transfer optics.

Let us examine the illumination of [A'] (fig. 9). Again, from the Lagrange-Helmholtz (or aplanatic) relation, we may deduce that:

$$V \sin \alpha \cos \alpha \, d\alpha \, d\sigma = V' \sin \alpha' \cos \alpha' \, d\alpha' \, d\sigma' \quad (22)$$

but here, $V = V'$ since before and after the transfer optics, the particles are moving in regions which are at the same potential. Therefore, the quantity $\sin \alpha \cos \alpha \, d\alpha \, d\sigma$ is invariant, no matter how complicated the transfer optics is.

The geometrical extent of the beam

$$dU = \sin \alpha \cos \alpha \, d\alpha \, d\psi \, d\sigma \quad (23)$$

is also invariant since $\psi = \psi'$.

In order to average the emission pattern, it is then possible to define functions like $f'(\phi_0, \alpha', \psi')$, $F'(\phi_0, \psi')$ and $\bar{F}'(\phi_0)$. And it is not difficult to show that:

Ion Collection Efficiency

$$F(\phi_o, \psi) = F'(\phi_o, \psi') = \frac{V + \phi_o}{\phi_o} F_o(\phi_o, \psi_o) \quad (24)$$

If the transfer optics is reduced to one lens, the system formed by the collecting and the transfer optics is called an immersion lens (or emission lens) and it plays the part of an objective lens in a microscope.

III. INFLUENCE OF THE FILTERING OPTICS

We do not intend to enter into details; we just need to characterize the filtering optics by features pertinent to our problem:

- The filtering optics will accept an ion beam with a given geometrical extent ΔU_s and let through ions in a given energy band pass $\Delta\phi_o$.
- Since we are dealing with images, we choose a filtering optics which has a cylindrical symmetry. Nevertheless, this point is not essential; it would be possible to come to similar conclusions with any kind of filtering optics.

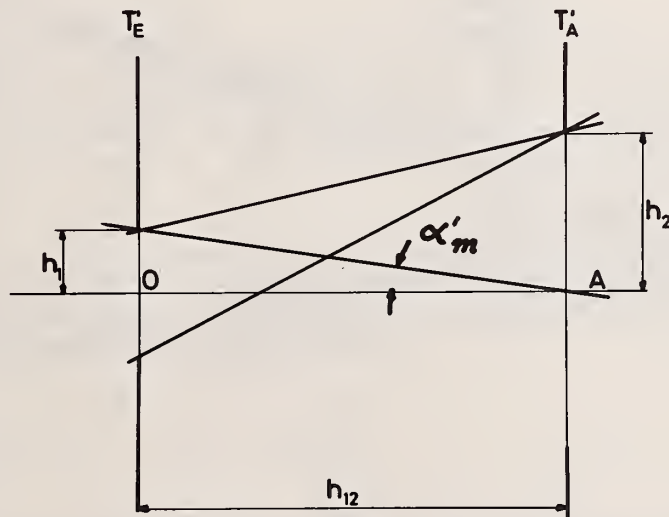


Figure 10 Characterization of the geometrical parameters of the spectrometer.

The accepted beam is physically defined by two diaphragms T'_E and T'_A aligned on the axis of the transfer optics and separated by a distance h_{12} ; h_1 and h_2 are the radii of T'_E and T'_A respectively. Usually, h_1 and h_2 are much smaller than h_{12} , so that $\alpha'_m \ll 1$ (fig. 10).

At $[A']$, the number of ions arriving on $d\sigma'$, in a solid angle $d\Omega'$, is:

$$d^6N_i \approx \bar{F}^T(\phi_0) \cos \alpha' d\Omega' d\sigma' d\phi_0 dz \quad (25)$$

$\cos \alpha' d\Omega' d\sigma'$ is the geometrical extent of the beam and $\bar{F}^T(\phi_0) d\phi_0 dz$ is equivalent to brightness in light optics. With simple geometry, it is easy to show that any plane perpendicular to the axis will have the same brightness $\bar{F}^T(\phi_0) d\phi_0 dz$. Therefore, if $[O']$ and $[A']$ are not, for instance, in coincidence with T'_E and T'_A , the total number of accepted ions will not be reduced. However, once more, using simple geometrical arguments, one can see that there are some inconveniences to a situation where $[O']$ and $[A']$ do not coincide with T'_E and T'_A . On figure 11 which represents one among many possible situations, essentially two remarks are to be made:

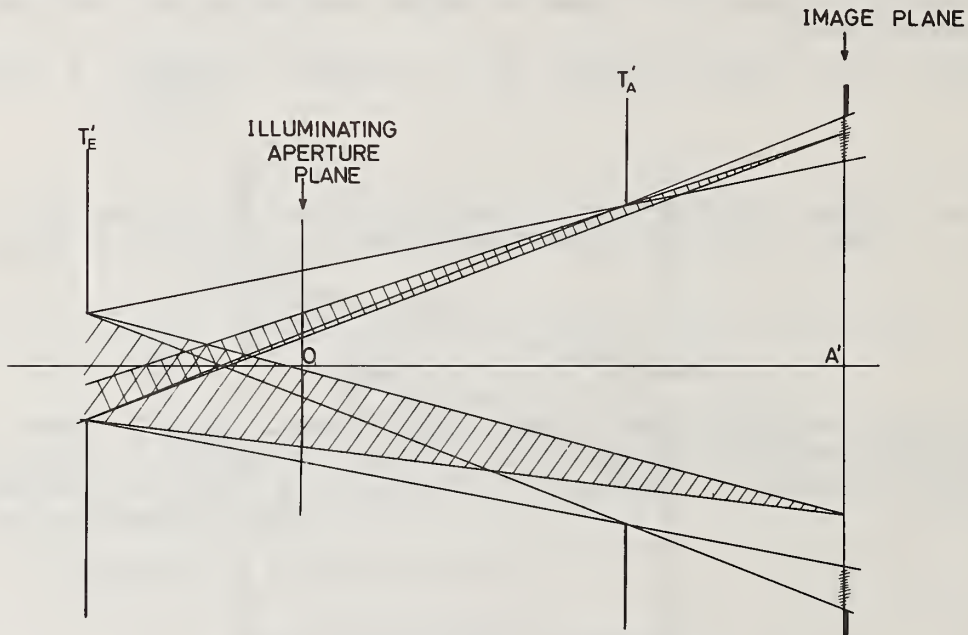


Figure 11 "Shadow effects." In the image plane, the hatched lines show the "half-light" region, the thick continuous line shows the "full-shade" region, the light continuous line shows the "full-light" region. In the illuminating aperture plane, the thick continuous line gives the part of the illuminating aperture which contributes to the illumination of a given point in the "full-light" region.

Ion Collection Efficiency

- Part of the analyzed area will be in "full light," another part will be in "half light" (hatched regions on the figure); the illumination of this latter region continuously decreases towards the edges. Thus, localized analysis should be restricted to the fully illuminated region.

- Different points of the analyzed field in the fully illuminated region will receive ions which are not coming from exactly the same location inside the illuminating aperture. Therefore, the analysis of each micro-area is not made with exactly the same type of ions.

Henceforth, we shall assume that the transfer optics is adjusted in such a way that [O'] and [A'] coincide with T'E and T'A respectively.⁸

Let us compute the number d^2N_i of ions accepted by the spectrometer in the energy range $d\phi_0$. Since α' is small the total geometrical extent of the beam accepted by the spectrometer is

$$\Delta U_s \approx \pi^2 \frac{h_1^2 h_2^2}{h_{12}^2} \quad (26)$$

$$d^2N_i = F^T(\phi_0) d\phi_0 dz \Delta U_s. \quad (27)$$

IV. THE USEFUL YIELD

(1) Definition

The destructive nature of the analysis implies the necessity to sputter a given volume of material in order to get N_i (M^+) ions of type M^+ to the detector. During the sputtering process, a volume v has been removed, which contained N_0 atoms among which one could find $N(M) = N_0 C(M)$ atoms of the element M , where $C(M)$ is the atomic concentration.

There is a close connection between the geometrical localization (the volume being analyzed) and the sensitivity limit⁹ (being defined as the smallest concentration detectable with a given precision in a given volume). Let us define a "useful yield":

$$\tau_u = \frac{N_i (M^+)}{N (M)} \quad (28)$$

To achieve a precision of $p/10^2$ in a measurement, it is necessary to produce a number N_i ions at least equal to $10^4/p^2$ and therefore to sputter away a volume $v = (1/nC)(10^4/p^2\tau_u)$ where n stands for the number of atoms per unit volume.

It should be noted that the shape of the volume is left unspecified so that the arguments given here are valid for micro-areas and for in-depth analysis as well.

Ion Collection Efficiency

It is clear that there is an imperative need for getting the best yield possible. This yield will depend upon basic ionization and sputtering processes which control the emission function $f_0(\phi_0, \alpha_0, \psi_0)$ of M^+ ions, but will also depend on instrumental parameters.

(2) Influence of the transfer optics on the useful yield

Because of the coincidence between T'_E , T'_A and $[0']$, $[A']$, the illuminating aperture $[0]$ and the analyzed field area of the target will be respectively restricted to diameters $2a$ and d_0 ($\sigma_0 = \pi d_0^2/4$). The number of ions accepted by the spectrometer in the range $d\phi_0$ is:

$$d^2 N_i = \overline{F^+}(\phi_0) d\phi_0 dz \Delta U_s = \frac{V + \phi_0}{\phi_0} \overline{F^-}(\phi_0) d\phi_0 dz \Delta U_s \quad (29)$$

Further, from the Lagrange-Helmholtz relation integrated over the geometrical extent of the beam ΔU_s , we may deduce:

$$\pi \phi_0 \sin^2 \alpha_{om} \sigma_0 = (V + \phi_0) \Delta U_s \approx V \Delta U_s \quad (30)$$

We have to examine two cases:

$$\underline{\phi_0 > \phi_{om}}; \quad \phi_{om} \approx \frac{a^2}{16 D^2} V, \quad a \approx 4D \sqrt{\phi_0/V} \sin \alpha_{om} \quad (31)$$

$$\Delta U_s = \frac{\pi \phi_0}{V} \sin^2 \alpha_{om} \sigma_0 = \frac{\pi a^2 \sigma_0}{16 D^2} \quad (32)$$

$$d^2N_i = \pi \sigma_o \sin^2 \alpha_{om} F_o(\phi_o) d\phi_o dz = \frac{V}{\phi_o} \cdot \frac{\pi a^2}{16D^2} \sigma_o F_o(\phi_o) d\phi_o dz \quad (33)$$

$$= \pi \frac{\phi_{om}}{\phi_o} \cdot \sigma_o F_o(\phi_o) d\phi_o dz \quad (34)$$

$$\underline{\phi_o \leq \phi_{om}}; \quad 4D\sqrt{\phi_o/V} \leq a \quad (35)$$

$$d^2N_i = \pi \sigma_o F_o(\phi_o) d\phi_o dz \quad (36)$$

Thus, in principle, it is possible to compute dN_i :

$$dN_i = \pi \sigma_o dz \left[\int_0^{\phi_{om}} F_o(\phi_o) d\phi_o + \phi_{om} \int_{\phi_{om}}^{\phi_{om} + \Delta\phi_o} \frac{F_o(\phi_o)}{\phi_o} d\phi_o \right] \quad (37)$$

Since the volume $\sigma_o dz$ contains $n.C(M) \sigma_o dz$ atoms M, we get the following expression:

$$\tau_u = \frac{\phi_{om}}{nC} K_\ell \quad (38)$$

where:

$$K_{\ell} = \pi \left[\frac{1}{\phi_{om}} \int_0^{\phi_{om}} F_o(\phi_o) d\phi_o + \int_{\phi_{om}}^{\phi_{om} + \Delta\phi_o} \frac{F_o(\phi_o)}{\phi_o} d\phi_o \right] \quad (39)$$

For a given sample (where n and C are known), the useful yield can be obtained experimentally by measuring the number of ions M^+ produced by the sputtering of a layer of thickness z . The expressions of τ_u and dN_j are useful if one wishes to evaluate how these quantities are evolving when instrumental parameters are changed as we shall see a little further.

In other respects, it should be noticed that the diaphragms T'_E and T'_A do not exactly play the same role:

- τ_u does not change if the diameter of T'_A is reduced (that is, if the analyzed field is reduced) since N_j and N_o are reduced in the same proportion.

- τ_u decreases if the diameter of T'_E is reduced (that is, if the diameter of the illuminating aperture is reduced). But we have to keep in mind that if some emission anisotropy occurs, the illumination of the diaphragm T'_E will not be uniform and consequently the number of ions of a given species accepted by the spectrometer may not be proportional to the open area of T'_E .

For a given experimental setup, as far as emission anisotropy can be neglected, τ_u is a well defined number essential to determine what performance one should expect. Let us take an example and put in some numbers.

A tantalum oxide film formed by anodic oxidation in an aqueous solution of ammonium citrate is bombarded with an argon beam. The measured useful yield of Ta^+ ions is about $2 \cdot 10^{-3}$. The area analyzed with this particular instrument [2] is $1.25 \times 10^4 \mu m^2$. Since n is known, it is easy to compute that for a precision of $\pm 5\%$, a layer of at least 100 Å thick must be sputtered away in order to detect an impurity which would have the same τ_u as tantalum and be present in the concentration range of 0.1 ppm. But, as already mentioned, besides the instrumental factors, the ionization processes play an important role in the values obtained for τ_u . For instance, $\tau_u(Ta^+)$ is 10^3 times smaller when pure tantalum is bombarded with argon ions, than when Ta_2O_5 is bombarded under the same conditions.

Let us make some additional remarks:

- We have not taken into account the chromatic aberrations given by the transfer optics which might slightly change the former results.

- Some care should be taken to make sure that no diaphragms other than T'_E and T'_A are stopping the ions supposed to be accepted by the spectrometer (electrode N for instance).

- τ_u is dependent on the "brightness" $(V/\phi_0)\bar{F}_0(\phi_0)$ seen by the spectrometer, on ΔU_s and on $(\Delta\phi_0/V)$. $\bar{F}_0(\phi_0)$ is related to the ionization processes so that when everything possible has been done to increase the ionization efficiency (bombardment with reactive primaries, surface reactions, . . .), the only thing which remains to be done is to increase the accelerating voltage V . We already know that, at a given voltage V , all ions of which the energies are $\phi_0 \leq \phi_{om}$, are collected; consequently a further increase of V will not change the collection efficiency for these ions since it is already 100%; it will just increase the brightness $(V/\phi_0)\bar{F}_0(\phi_0)$. This increase in brightness is not followed by an increase in ion current because the ions $\phi_0 \leq \phi_{om}$ are now filling a beam which has geometrical extent smaller than ΔU_s allowed by the spectrometer. This is another way of saying that all these ions are already completely collected, which incidently shows that if for some reasons we wish to discard the ions $\phi_0 \geq \phi_{om}$, it would be possible to improve the mass resolution without reducing the sensitivity obtained with the ions $\phi_0 \leq \phi_{om}$. Furthermore, any increase of V will also increase ϕ_{om} , so that ions with higher energies will now be collected with 100% efficiency. For those ions which are only partially collected because their energies are still higher than the new setting of ϕ_{om} , an increase of V has the effect of increasing the solid angle of emission in which they are collected: Their total contribution to the secondary ion current, provided $\phi_0 < \Delta\phi_0$, is increased. From the "spectrometer point of view," this increase is due to a higher brightness combined with a complete filling of the diaphragms T'_E and T'_A ; there is also, to a lesser degree, some contribution of the band pass since our assumption is that the ratio $\Delta\phi_0/V$ only is fixed.

It is worthwhile to note that the contribution of ions like $\phi_0 > \phi_{om}$ in a range $\delta\phi_0$ is proportional to the voltage V , but this is a direct consequence of using a Lambert's law to average the emission function. Later on, we will come back to these points.

V. SOME CONSEQUENCES

A. Bombarding Modes

Until now, none of our arguments about τ_u and the image illumination included the bombarding mode of the sample. Thence, it is obvious that the results are valid for both a broad uniform primary beam and a localized spot of primary ions (probe) which may eventually be scanned over the field to be analyzed.

Ion Collection Efficiency

However, between the two bombarding modes, a fundamental difference appears when one asks for local analysis on the micrometer scale:

- With a broad primary beam, an adequately apertured objective lens is necessary in order to obtain images with the required resolving limit.

- With a narrow primary beam, the objective lens plays the part of a collecting system only, and the resolving limit is entirely depending on the size of the primary spot.

(1) Broad primary beam

The resolving limit is on the order of $\ell = (\phi_{om}/V) D$. From the expression for τ_u it is easy to deduce that any improvement of the spatial resolution will cost a decrease of τ_u . Moreover, the relative band pass $\Delta\phi_0/V$ of the spectrometer cannot be too large because of the chromatic aberrations of the objective lens.

Let us look for the relationships existing between ℓ and τ_u . We already know that ℓ and τ_u depend on ϕ_{om} and that, through T'_E , ϕ_{om} itself depends on the radius "a" of the illuminating aperture [0]. Let $(\tau_u)_\ell$ be the useful yield for a given "a".

$$(\tau_u)_\ell = \frac{\phi_{om}}{nC} K_\ell, \quad \ell = \frac{\phi_{om}}{V} D = \frac{a^2}{16D} \quad (40)$$

Thus:

$$(\tau_u)_\ell = \frac{\ell V}{nCD} \cdot K_\ell = \frac{a^2}{16nCD^2} \cdot K_\ell \quad (41)$$

When "a" is changed into "a'", ℓ and $(\tau_u)_\ell$ will be changed into ℓ' and $(\tau_u)_{\ell'}$ respectively, and it is easy to see that:

$$\frac{(\tau_u)_\ell}{(\tau_u)_{\ell'}} = \frac{a^2 K_\ell}{(a')^2 K_{\ell'}} = \frac{\ell K_\ell}{\ell' K_{\ell'}} \quad (42)$$

If we just need a rule of thumb, we may assume to a first (and very crude) approximation that K_ℓ does not depend on ϕ_{om} :
 $(\tau_u)_\ell \approx (\ell/\ell') (\tau_u)_{\ell'}$. Therefore, with only one experimental measurement of $(\tau_u)_\ell$, we are able to get an estimate of $(\tau_u)_\ell$ for any value of a.¹⁰

Now, let $\ell^2 z$ be the minimum volume that must be sputtered in order to obtain a measurement with a given statistical fluctuation $\pm p/100$:

$$\ell^2 z = \frac{1}{nC} \cdot \frac{10^4}{p^2 (\tau_u)_\ell} , \quad \ell^3 z = \frac{10^4}{p^2} \frac{D}{VK_\ell} \quad (43)$$

If we make use of the former approximation and choose $\ell' = 1\mu\text{m}$, $(\tau_u)_{\ell'} = (\tau_u)_1$; then:

$$\ell^3 z \approx \frac{1}{nC} \cdot \frac{10^4}{p^2 (\tau_u)_1} \quad (44)$$

where all the lengths are in micrometers. According to this expression, we can estimate the minimum thickness required to make an analysis over an area ℓ^2 with a given precision. We can also estimate the "ultimate resolving limit"¹¹ which will be reached when z equals ℓ :

$$\ell^4 \approx \frac{1}{nC} \cdot \frac{10^4}{p^2 (\tau_u)_1} \quad (45)$$

It is remarkable that ℓ depends on $(\tau_u)_1$ (measured when the optics is adjusted so as to give $\ell = 1\mu\text{m}$) according to a power $(-1/4)$ only. It suggests that even wide changes in the useful yield from one element to another should not affect too much the ultimate resolving limit.

(2) Localized bombardment

Localized analysis can also be obtained by reducing the size of the bombarding beam to a small spot. For instance, let us imagine that a probe of one micrometer diameter strikes the sample and that the optics is adjusted in such a way that the emission lens gives an image with a resolving limit of one micrometer. As the spatial resolving limit does not depend on the chromatic aberrations of the objective lens, it is possible to take a larger band pass $(\Delta\phi_0)_s$. The increase of τ_u then comes from the increase of K_ℓ since the total current of ions M^+ is:

$$dN_i = \phi_{om} K_\ell \sigma_o dz. \quad (46)$$

It is well known that $F_0(\phi_0)$ presents a maximum around several electron-volts and depends on elements and ionization processes. Let us take an example which is known to favor the emission of high energy versus low energy ions: a polycrystalline nickel sample bombarded by

Ion Collection Efficiency

argon ions. The angle of incidence is about 60° , the energy of the primaries when they strike the target is 6.2 keV, the secondary Ni^+ ions are accelerated at 3.8 kV and the objective lens is set to collect all the ions up to ϕ_{om} approximately equal to 0.7 eV. From the energy distribution curve (3) it is easy to deduce the following table of the increments of $(1/\pi)(\phi_{om} K_\ell)$ where the arbitrary value 100 has been given to $(1/\pi)(\phi_{om} K_\ell)$ for $\Delta\phi_0 = 200$ eV:

ϕ_0	5	10	20	40	60	100	200
$\frac{(\phi_{om} K_\ell)}{\Delta \pi}$	50	15	11.5	10	5	4.2	4.3

From the above table one can see that an energy band $\Delta\phi_0$ as small as 10 eV would contribute 65 percent to the total current that could be obtained with a band pass of 200 eV. Of course, if for some reason or another the low energy ions are discriminated, the relative contribution of high energy ions is more important and the total current is more sensitive to the width of the band pass.

Attention should be paid to the fact that, in general, the previous numbers are only rough estimates because $\bar{F}_0(\phi_0)$ may depend on many factors. But, as far as ionization processes are concerned, we think that when "chemical emission"¹² is involved, these numbers underestimate the contribution of low energy ions.

VI. PLAYING WITH THE TRANSFER OPTICS

(1) Increasing τ_u

Let us start with an accelerating voltage V and a spectrometer characterized by $\Delta\phi_0/V$ and ΔU_s , which lead to a given mass resolving power $M/\Delta M$. For given adjustments of the transfer optics, let us assume that we have a , ℓ , $M/\Delta M$ and d_0 fixed.

Now, just by changing the adjustments of the transfer optics, we may obtain (since $\Delta U_s = \pi a^2 \sigma_0 / 64 D^2$):

$$a' = k a, \ell' = k^2 \ell, \frac{M}{\Delta M}, d' = \frac{d_0}{k}, \phi'_{om} = k^2 \phi_{om} \quad (47)$$

where k is a dimensionless factor.

We have to find out what is the value of $(K_\ell)'$ in order to estimate the increase of τ_u . Again, this estimate can only be obtained through a numerical integration of $\bar{F}_0(\phi_0)$ and $\bar{F}_0(\phi_0)/\phi_0$. But we can understand

the physical reason which leads to an increase of τ_u : the secondary ions are collected in a greater emission solid angle. As k increases, ϕ'_{om} increases and consequently the energy range in which ions are collected with 100 percent efficiency becomes larger. A further increase of k will widen the energy band of ions collected with 100 percent efficiency and increase the emission solid angle of ions which are only partly collected.

Let us try to make an estimate on the example already given. The transfer optics is now set to allow ions with $\phi'_{om} = 10$ eV to be completely collected. (With that specific instrument used, it would lead to $l' \approx 10 \mu\text{m}$ and $d'_o \approx 65 \mu\text{m}$ if we had started with $\phi_{om} \approx 0.7$ eV, $l \approx 0.7 \mu\text{m}$ and $d_o \approx 250 \mu\text{m}$.) From the energy distribution curve corrected for Lambert's law, the following table can be drawn up (with the same convention as previously).¹³

ϕ_o	10	20	40	60	100	200
$\frac{\Delta(\phi'_{om} K'_l)}{\pi}$	41	21	16	6.5	7	8.5

The ratio between $\phi'_{om} K'_l$ and $\phi_{om} K_l$ is close to 8 (both measured in the range $\Delta\phi_o = 200$ eV). Thence, $\tau'_u \approx 8 \tau_u$ when $k^2 \approx 14.3$, which gives a ratio $dN'_i/dN_i \approx 0.56$ because the analyzed field area is reduced by a factor $1/k^2$.¹⁴ But again, this is just an example to show how the things work and from one situation to another the results may be somewhat different.

As we are seeking higher useful yields, on one hand the size of the analyzed field is reduced ($d'=d_o/k$) and on the other hand the spatial resolving limit of the objective lens is deteriorated ($l'=k^2 l$). If a resolving limit lower than l' is needed, then we must reduce the size of the primary beam and match it (as far as possible) to the localization we wish to get. But it should be noted that, because the size of the analyzed field is now reduced, an image over a greater area can only be obtained if the sample is mechanically scanned or if the primary beam is rastered over the sample and the ion image scanned synchronously in front of the diaphragm T'_A . The objective lens will then essentially play the part of a collecting system. If we keep increasing k , τ_u will keep increasing but it will be less and less rewarding because $F_o(\phi_o)$ decreases with d'_o and because the chromatic aberrations will lower the expected gain. The limit will be reached as l' becomes of the order of d' .

However, before we run into such difficulties, there is room for improvement, and for this purpose the ion microscope optics coupled with a transfer optics is a tool which seems very adequate. The adequacy partly is due to the fact that it should not be difficult to switch from an ion image with a spatial resolving limit better than one micrometer,

and well adapted for surveying the sample, to the measurement of secondary ions coming from a selected area, with the best possible adjustment of the transfer optics giving the highest τ_u consistent with the specific analytical problem treated. Of course, depending on the size of the analyzed field area, the reduction of the spatial resolving power¹⁵ may or may not require a localized primary beam (the position of the probe could be adjusted and observed directly on the ion image for instance). But in all these questions, one should keep in mind that there is a close connection between spatial localization, sensitivity and concentration.

Another point has to be considered. For a given spectrometer and collecting geometry, there must be a given analyzed field area σ_0 .¹⁶ As a layer of thickness z is sputtered, this area will produce a given number N_i of ions M^+ (at a fixed voltage V). We have shown that an increase of τ_u leads to a decrease (in the example previously cited) or let us say at a stationary value of N_i . However, since low energy and higher energy ions are differently affected,¹⁷ it might happen that the ratio of the emission currents of two different elements would significantly depend on the setting of the transfer optics which controls ϕ_{om} . But at the present stage, such guesses (although not completely irrelevant) need more experimental support. However, if we are in a case where emission anisotropy is significant, it looks worthwhile to collect the emission in as large a solid angle as possible in order to improve the reproducibility of the measurements.

(2) Improving mass resolution over small areas

To improve the mass resolution, we have to reduce the entrance and the aperture diaphragm T'_E and T'_A . This will reduce ΔU_S , the geometrical extent of the beam accepted by the spectrometer.¹⁸

To improve the mass resolution by a factor of λ , we must divide h_1 by λ and h_2 by $\sqrt{\lambda}$ (because the angular aberrations are depending on h_2^2).¹⁹ The geometrical extent becomes $\Delta U'_S = (1/\lambda^3)(\Delta U_S)$. Now, let us adjust the transfer optics in order to keep the same value for "a," that is the same τ_u . Since $\Delta U'_S = (\pi a^2 \sigma'_0 / 64 D^2)$, this implies that the new diameter of the field is $d' = d_0 / (\lambda^{3/2})$.

Thus, any improvement of the mass resolution which maintains unchanged τ_u , will reduce the analyzed field. Inside this field, the resolving limit will also remain constant. However, the total signal will be reduced by a factor λ^3 since $\sigma' = \sigma_0 / \lambda^3$.

Here, we reach the interesting conclusion: wherever a small area has to be analyzed with a high mass resolution, the transfer optics may be adjusted to fulfill this requirement with no loss of signal provided σ' is greater than the analyzed area.

Of course, it is also possible to adjust the transfer optics in order to combine the effects described in (1) and (2) this section and obtain a higher τ_u and a better mass resolving power over a reduced

area. But in this case, according to the analytical requirements (localization, concentration, sensitivity . . .), the use of a probe (coupled with an ion microscope type optics) may or may not ultimately become desirable.

In order to make an estimate, let us start with the conditions already mentioned, $\ell = 1 \mu\text{m}$, $d_0 = 270 \mu\text{m}$, $M/\Delta M \approx 330$ and τ_U . If we choose $\lambda = 9$ and if we make the proper adjustments, we can get $d' \approx 10 \mu\text{m}$, $(M/\Delta M)' \approx 3000$ and leave ℓ and τ_U unchanged. Therefore, if on a grain of $10 \mu\text{m}$, we had to perform either trace analysis or isotopic ratio measurements and if on both we had to avoid mass interferences, it would be possible to do it without reducing τ_U , that is without losing sensitivity (on this specific grain), and still keep a spatial resolving limit of the order of $1 \mu\text{m}$. Thus, generally, the transfer optics allows one to maintain the same collection efficiency at high mass resolution as that obtained at lower mass resolution, but at the cost of a reduction in the field of view.

Furthermore, as already mentioned, if we accept to reduce the analyzed field, we may try to increase τ_U . For instance if we play with the factor k and take $k' = k\sqrt{2}$, then $d'' \approx 7 \mu\text{m}$, $\ell'' \approx 2 \mu\text{m}$, $\tau_U'' \approx 2\tau_U$; $(M/\Delta M)'$ stays unchanged. Taking into account the aberrations of the objective lens, we may then expect that the ions emitted from an area of $5 \mu\text{m}$ in diameter are collected with a 100 percent efficiency up to 2 eV (the contribution of ions over 2 eV being dimmed by a factor $2/\phi_0$ instead of $1/\phi_0$) and the mass resolving power is still of the order of 3000.

Once more, these numbers are given here just to show how the things work and to show with practical examples that what is really needed, in local analysis, is to have an instrument that one could adjust to his specific problem.

VII. CONCLUSION

Looking at the collection efficiency problem from a very general point of view, we have discussed the importance of the transfer optics and of the different modes of bombardment.

However, one point has been left to discussion: the information that might be present in an ion microscope. Let us imagine that we are looking at viewing field of $250 \mu\text{m}$ in diameter with a spatial resolution of one micrometer. The image contains $5 \cdot 10^4$ points of information of a square micrometer. To record such an image on a photographic plate with an optical density $d = 0.7$ will take a time t (seconds) and will require from each square micrometer 1000^{20} (which already has a statistical fluctuation of ± 3 percent). In order to get $5 \cdot 10^4$ points of information with the same statistics using a one micrometer probe with the same primary density as the former bombardment, would require a time $t_S = 5 \cdot 10^4 t [\tau_U/(\tau_U)_S]$. If, as we have already discussed, the ratio of the useful yields in both situations is about $3/5$, then $t_S \approx 3 \cdot 10^4 t$. Even if something was wrong by a factor of ten, in our estimates, t_S would

Ion Collection Efficiency

only be 3.10^3 times higher than t . Therefore, one second exposure time with an ion microscope would have to be compared to nearly one hour with a scanning probe. Moreover, with "channel plates," it will probably be possible to gain at least a factor of 10 on the exposure times. Then, each square micrometer will have to release 40 ions to produce the same optical density (thus the statistical fluctuation limit will soon be reached).

This example was given to show why a microscope is so useful: it allows a very easy and fast survey work on a sample. This way, many unexpected features can be observed, saving a lot of time and preparing the path for more precise measurements if necessary. That means that when the precision of densitometry measurements on the ion micrographs is not suitable for a given problem, any specific well located and limited area can be apertured at the ion image (or at the converted electron image) and the ion currents emitted by this area can be directly recorded. Particularly, from what has been set forth throughout this paper, no reason appears that would prevent the measurements made with the collecting optics of an ion microscope to be less suitable for subsequent operation to render the analysis quantitative. On the contrary, having a better (although approximate) knowledge of the categories of collected ions, it should be possible to investigate more deeply the influence that the instrumental factors undoubtedly have on the quantitation tests.

Moreover, we have shown how the use of a probe could benefit from the optics of the ion microscope. So we don't see any basic contradiction between "ion microscopy" and "ion probing," provided each one is used properly in order to meet the particular analytical requirements. In that respect, the transfer optics plays a key role and it should bring a great flexibility into the analytical practical operations, and allow more sophisticated analysis, such as for instance trace analysis, avoiding interference problems on small grains, or maybe precise measurements of isotopic ratios on small grains.

VIII. REFERENCES

- [1] Zworykin, V. K., Morton, G. A., Ramberg, E. G., Hillier, J., and A. W. Vance, *Electron Optics and the Electron Microscope*, Wiley, New York (1949).
- Grivet, P., *Electron Optics*, Pergamon Press (Oxford 1965).
- Magnan, C., *Traité de Microscopie Electronique (Vol. I)* Hermann Paris (1961).
- Slodzian, G., *Ann. Phys. (Paris)* 9 (1964) 591.
- [2] Hernandez, R., Lanusse, P., Slodzian, G. and Vidal, R., *Recherche Aérospatiale (Paris)* 6 (1972) 313.
- [3] Blaise, G. and Slodzian, G., *Rev. Phys. Appl. (Paris)* 8 (1973) 247.

Footnotes

1. The emission processes prevent this from being true. These processes will not be discussed in this paper.
2. The optics of filtering systems is too involved to be discussed here.
3. It could be M^- or any other kind of ion.
4. Of course, the higher the accelerating voltage V the better the approximation. But it should be mentioned that some workers are using a field-free region followed by an acceleration space. In this case, if V and D are still the acceleration voltage and distance; the change in slope $\Delta r'$ is of the order of $(r/4D)(V/\phi_0 \cos^2 \alpha_0)$ as the particle enters the acceleration space. Here, it is a convergent effect which might introduce some energy discrimination essentially at low energies.
5. This statement is obvious for meridian trajectories like, for instance, trajectories leaving point A. For ions coming from points such as B and following skew trajectories (fig. 5), the statement remains true provided the azimuthal angle is measured in a frame of reference where the z'z axis is now placed along OB. Anyway, whatever the emission point, all the ions $(\phi_0, \alpha_0, \psi_0)$ are coming from the point P of the illumination aperture (fig. 5) (aberrations being neglected).
6. The complications come from emission anisotropy: sometimes surface relief effects could also play some part.
7. Figure 6 is included just as an example; particularly the relative position of [O'] and [A'] could be inverted if necessary.
8. It should be noted that the relative positions of [O] and [A'] could as well be inverted.
9. The term "sensitivity limit" here defined is an ultimate sensitivity which could only be achieved if one had a perfect detector and if there were no "background ions" or other spurious effects of that kind. What is termed "detectability" is the practical sensitivity actually achieved with a given instrument on a given sample for a given element or isotope.
10. This approximation is acceptable if $\phi_{om} \ll \Delta\phi_0$, provided that the contribution of $\bar{F}_0(\phi_0)$ to the integrals is small at very low energies and thence if we are looking for situations where $a < a'$.
11. It was already mentioned that the spatial resolving limit λ_a is not equal to λ but the coefficient μ is difficult to estimate because it depends partly on $\bar{F}_0(\phi_0)$. Moreover, it should not be forgotten

that we are here dealing with approximate trajectories. Anyway, introducing λ_a , the expressions here computed would become:

$$\lambda_a^2 \lambda_z \approx \frac{1}{nC} \cdot \frac{10^4}{p^2(\tau_\mu)_1} \quad (48)$$

and:

$$\frac{1}{nC} \cdot \frac{10^4}{p^2(\tau_\mu)_1} \approx \lambda_a^2 \lambda^2 = \frac{\lambda_a^4}{\mu^2} \quad (49)$$

Even if μ were of the order of 2, the "ultimate spatial revolving limit" would only be multiplied by a factor of $\sqrt{2}$: $\lambda_a \rightarrow \lambda\sqrt{2}$.

12. "Chemical emission": emission process occurring either when the sample is bombarded with reactive primary ions, when a reactive gas is blown on the surface during the bombardment, or when an oxide, a halide or any other ionic compound is sputtered.
13. The experimental procedure may introduce some systematic errors. Indeed, what is measured is the contribution of ϕ_0 energy ions in the range $\delta\phi_0$ emitted in a solid angle $2\pi(1 - \cos\alpha_{om})$ so that the averaging which leads to $\bar{F}_0(\phi_0)$ actually takes into account the values of $f_0(\phi_0, \alpha_0, \psi_0)$ for α_0 included in the range $(0, \alpha_{om})$ instead of $(0, \pi/2)$.
14. The ratio dN_i'/dN_i is only relevant for thin-film analysis. Of course, for an area $\sigma_a < \sigma'$, the sputtering of a given thickness z would lead to a ratio $N_i'/N_i = (\tau_u)'/\tau_u$.
15. It could also very well be that, for a specific problem, what is rather needed is a better resolving power whatever value τ_u takes and this could also be achieved with such an experimental setup.
16. Which can eventually be extended by proper scanning methods as we have already mentioned.
17. It can be seen from the two tables given in this paper.
18. Eventually, $\Delta\phi_0$ also would have to be slightly reduced. But we shall not examine here which effect it may have on τ_u . It will be a small effect anyway.
19. In fact, the real situation is more complicated because the complete configuration of second order aberrations of the spectrometer has to be taken into account. Particularly, since the filtering optics is not Gaussian (although it may be stigmatic) the aberrations do not have cylindrical symmetry. Therefore, the shape of the diaphragms (round hole versus rectangular slits) have to be adjusted properly. Only a detailed study of these aberrations can

Ion Collection Efficiency

help to determine the best aperturing which will lead to a given improvement in mass resolution and to the best useful yield. The estimates made here show that such a goal is attainable.

20. These experimental numbers are obtained in the following way: The ion currents emitted from an area of $60 \mu\text{m}$ in diameter are measured directly after a proper aperturing at the ion image. Then, micrographs are taken with different exposure times. From optical density measurements on each micrograph it is easy to draw the calibration curve—optical density versus number of ions emitted per square micrometer. It is worthwhile to note that if we had to get an image with an optical density $d = 0.7$ from a one square micrometer area containing an element at the atomic concentration of 1 percent and presenting a useful yield $= 10^{-3}$, it would require the removal of 10^8 atoms. Such a number would correspond to the sputtering of a layer thickness of approximately 20\AA . If the primary beam density was set to give a sputtering rate of $10\text{\AA}/\text{sec}$, it should take 2 seconds to record the image of the given area and to get, with no extra effort, the images of 5×10^4 adjacent areas of one micrometer square. Moreover, from this example it can be seen that the only influence of the sputtering rate is to determine the exposure time.

HIGH MASS RESOLUTION SECONDARY ION MASS SPECTROMETRY

Peter Williams and C. A. Evans, Jr.

Materials Research Laboratory
University of Illinois
Urbana, IL 61801, U.S.A.

Ion bombardment of a solid surface produces a variety of secondary ionic species. In addition to the analytically important singly charged monatomic ions, polyatomic and multiply charged ions are produced which can complicate the qualitative and quantitative interpretation of secondary ion mass spectra. The polyatomic ions can result from the ionization of hydrocarbons or other residual gases, either in or on the sample, from clusters of the matrix atoms, and from clusters formed by the bombarding ion with the matrix atoms. Such ions can occur at the same nominal mass as the ions of analytical interest, causing a mass spectral interference.

A variety of techniques has been used to circumvent the mass spectral interference problem. Good vacuum and sample handling techniques can reduce the hydrocarbon levels. Discrimination against ions of low initial kinetic energy can improve atomic to molecular ion ratios, although this technique reduces the intensity of both [1]. Other techniques to reduce or eliminate cluster formation at the mass of interest include changing the mass and chemical nature of the primary ion or the polarity of the secondary ions. Alternatively, the mass spectrum can be treated as the superimposition of spectra from a multicomponent mixture. If the individual spectrum of each component is known and the combined spectrum contains at least N peaks for an N -component mixture, the contribution of the major components may be obtained by standard mathematical techniques. A limitation of this last technique for low abundance components is the statistical noise on the multicomponent peaks.

The one common feature of all the above techniques is that they leave a degree of ambiguity in the analysis. Thus none of these techniques allow the analyst to state with certainty the identity of an ion. He can only state that the contributions of possible interferences have been reduced.

High mass resolution techniques have been used in combination with both large-beam [2,3] and micro-beam [4] ion probes to improve the analytical capabilities of SIMS. Two significant benefits result from the use of high mass resolution. The first is the obvious separation,

in a number of cases, of the analytical ion from the interfering species permitting accurate and unambiguous intensity measurement. Second, and more important, high mass resolution mass spectrometers permit precise mass determination of the secondary ions and thus unequivocal qualitative identification of the ion species. The value of this aspect of high resolution cannot be overemphasized since there are generally several possible atomic compositions for ions at a given mass number, and precise mass determination is the only technique capable of making an unambiguous identification.

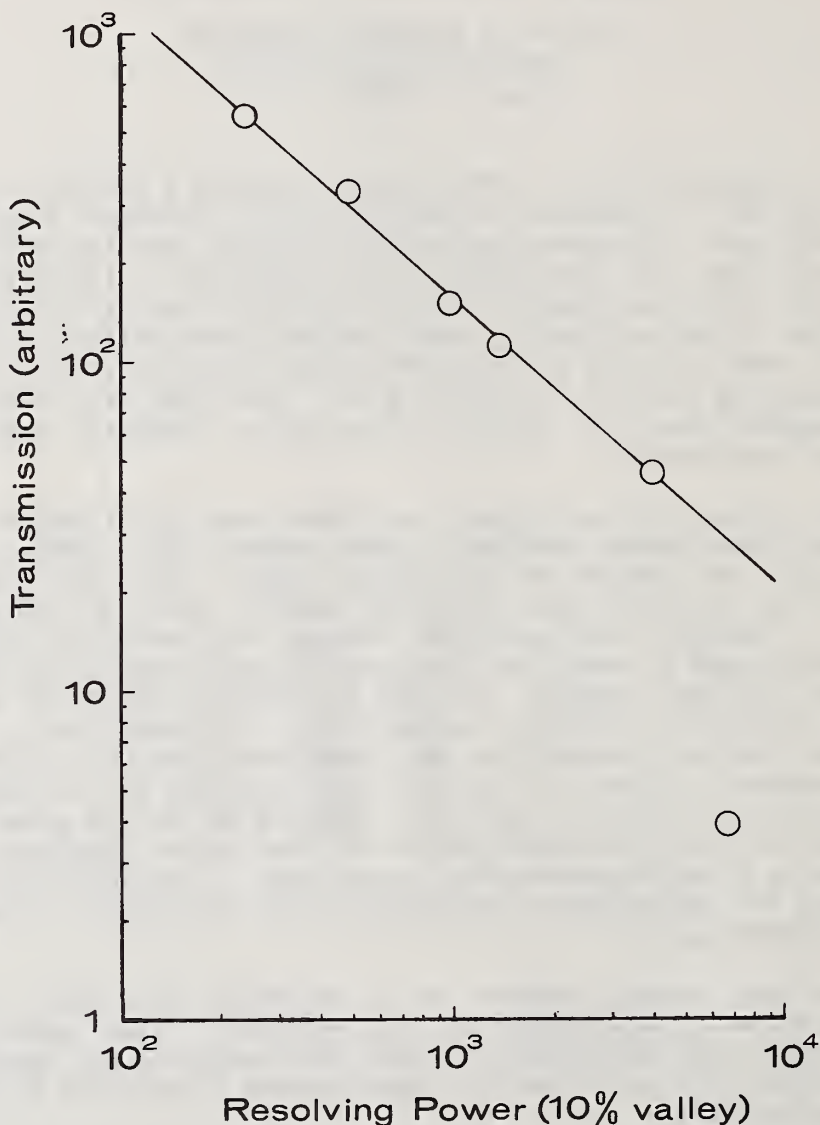


Fig. 1 Variation of transmission with resolving power on AEI-IM20 ion microprobe.

To date only modified spark-source mass spectrometers have been used for high resolution SIMS [2-4]. Such instruments have smaller angular (α) acceptance than the specially designed, low resolution microprobe [5] and have no z-focusing (where z is the long axis of the entrance slit) in the mass spectrometer. However, the use of high secondary ion accelerating potentials and the proper phasematching optics in the ion source makes the transmission of these instruments, used at low resolution, comparable in theory and practice with the high transmission, low resolution microprobe. Transmission decreases, of course, as resolution is increased -- approximately linearly for a well-focused mass spectrometer. The transmission-resolution behavior of the AEI-IM20 ion microprobe at the University of Illinois is shown in figure 1.

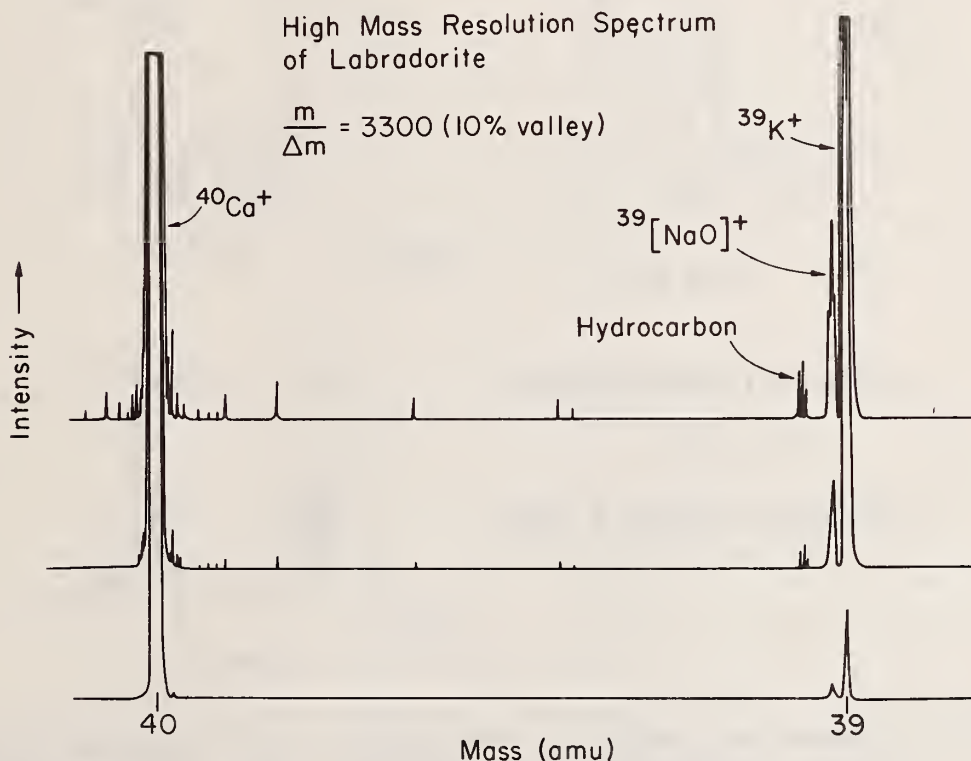


Fig. 2 Labradorite sample -- Potassium region.

At the lowest resolving power attainable with this instrument, the sensitivity for ^{56}Fe from an iron sample is 8×10^5 counts/sec/nA of primary beam. This corresponds to a measured transmission (resolved ion current/secondary ions produced) of 1 percent. The loss of transmission at high resolution is offset to some degree by the higher abundance sensitivity (fewer ions scattered from neighboring peaks into the analytical peak) of a mass spectrometer operated at high resolution.

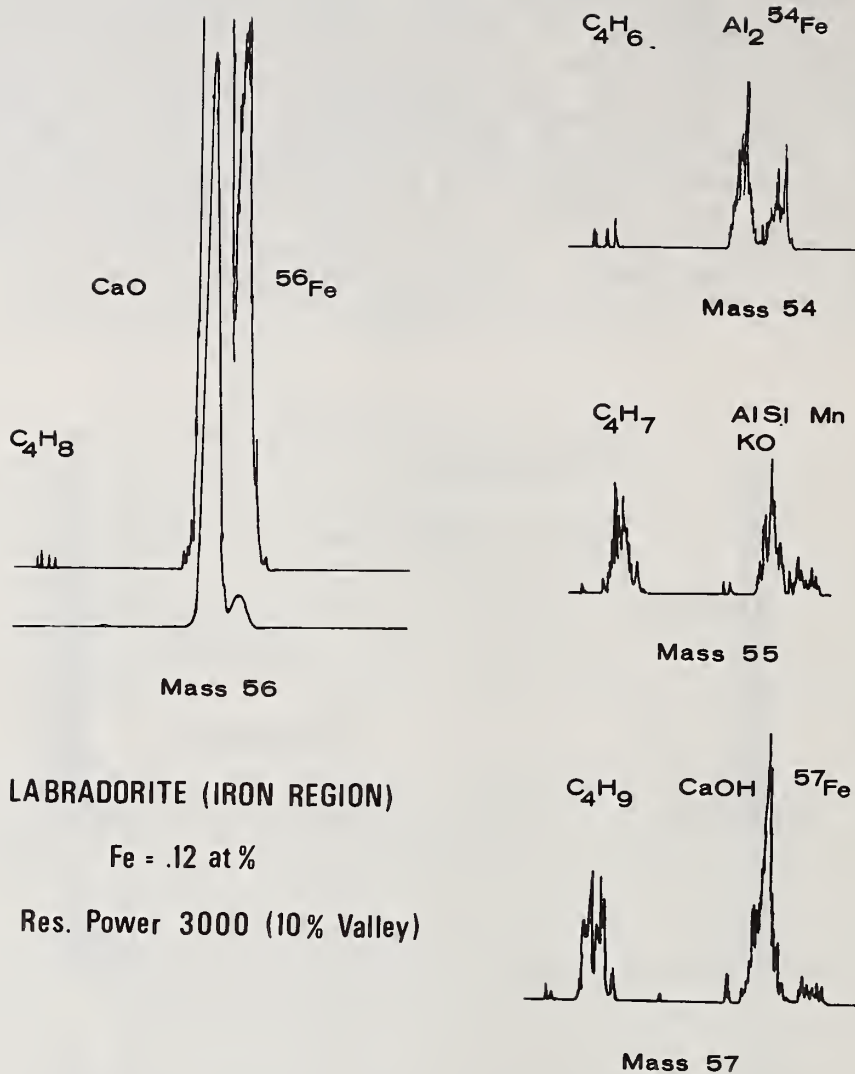


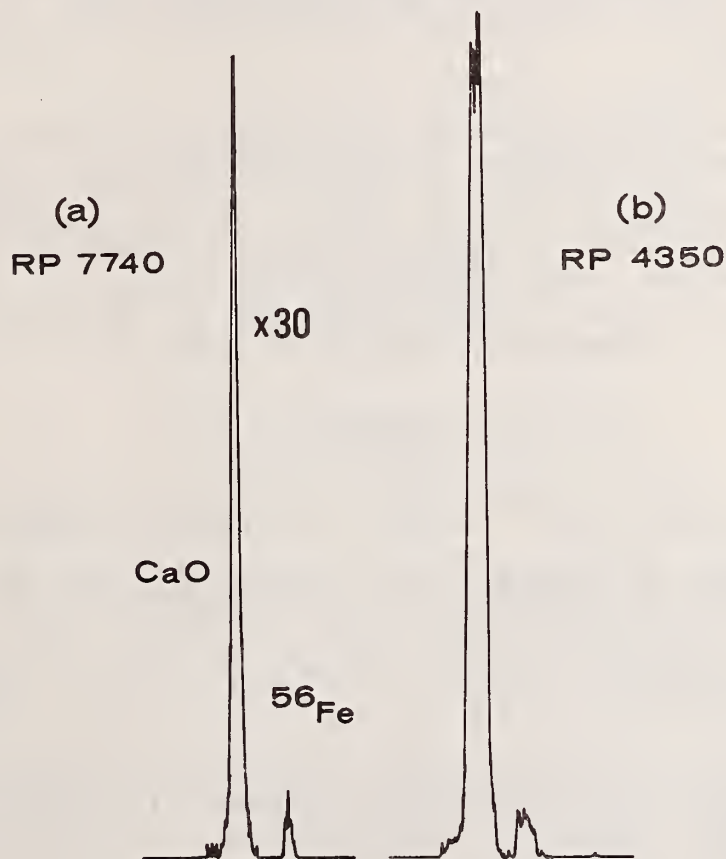
Fig. 3 Labradorite sample -- Iron region. Mass assignments of the polymer species to within ± 1 millimass unit (± 18 ppm) were made from direct measurement of peak position from the chart. Exact masses of monomer species and hydrocarbons were used for calibration.

Two modes of usage of high mass resolution ion microprobe mass spectrometry are shown in figure 2 and 3. These show spectra taken from Lake County Oregon Labradorite using the AEI-IM20 ion microprobe. High mass resolution may be used simply to check on the "purity" of specific peaks -- to check, for example, whether the vacuum techniques used have adequately suppressed hydrocarbon interferences, or whether peaks due to

High Mass Resolution SIMS

monoisotopic species are interference-free. (Interferences in the peaks of multi-isotopic species can frequently be detected through anomalous isotope ratios.) Figure 2 shows this mode of usage. Here the problem was to determine whether the $^{39}\text{K}^+$ peak was significantly contaminated with $^{23}\text{Na}^{16}\text{O}^+$. Since little $^{23}\text{Na}^{16}\text{O}^+$ was present, low resolution measurements would suffice to determine $^{39}\text{K}^+$ abundance.

A more complex situation is shown in figure 3. Here the ions of interest are iron and manganese, and it may be seen that not only the manganese peak, but also all the iron isotope peaks are masked by interferences. A resolving power (R.P.) of 3000 (10 percent valley) permits the separation, qualitative identification (via precise mass



High Resolution SIMS

Labradorite (Fe = .12 at %)

Fig. 4 High resolution performance of AEI-IM20 microprobe.

determination) and quantitative determination of Fe and Mn in the presence of interfering polymeric species. Simple measurement directly from the chart recording is adequate to determine masses to within about 1 millimass unit in a multiplet. The assignment of precise masses then allows the identification of the ion species. Although they act as interferences at low resolution, the hydrocarbon peaks become invaluable mass markers at high resolution. Judicious use of isotopic abundance data can aid identification. Thus $^{28}\text{Si}_2$ and $^{40}\text{Ca}^{16}\text{O}$ would not be resolved, but it may be estimated that $^{28}\text{Si}_2$ is less than about 10 percent of the CaO signal from the absence of $^{28}\text{Si}^{29}\text{Si}$ at mass 57 where it would be almost resolved from CaOH. ^{55}Mn is estimated to be about 40 ppma (by comparison with ^{57}Fe). Note that ^{57}Fe (20 ppma) is clearly resolved and detectable (at about 20 counts/second). A detection limit for iron in this sample is estimated to be 10 ppma. This limit is dictated by the large CaO interference and the magnitude of the secondary signal.

That sensitivity is still respectable at the highest resolving power of the mass spectrometer is demonstrated by the mass spectrum of figure 4a, taken on the same sample. ^{56}Fe (1000 ppma) is still detectable (~ 20 counts/second) at 7740 R.P. (10 percent valley). If the collector slit width is increased, without increasing the source slit width, essentially flat-topped peaks are obtained at 4300 R.P. facilitating ion counting on the top of a peak for accurate quantitative measurements or isotope ratio determinations (fig. 4b).

REFERENCES

1. Herzog, R. F. K., Poschenrieder, V. P., and Satkiewicz, F. G., GCA Corp., Bedford, Mass., for NASA, NASA-Cr89326 (N67-39205) (1967).
2. Hernandez, R., Lanusse, P., Slodzian, G., and Vidal, G., La Recherche Aerospatiale No. 1972-6, 313 (1972).
3. Blattner, R. J., Baker, J. A., and Evans, C. A., Jr., Anal. Chem. 46, 2171 (1974).
4. Bakale, D. K., Colby, B. N., and Evans, C. A., Jr., "High Mass Resolution Ion Microprobe Mass Spectrometry of Complex Matrices," Anal. Chem. (accepted for publication).
5. Liebl, H. J., J. Appl. Phys. 38, 5277 (1967).

This research was supported in part by the National Science Foundation under Grants DMR-7203026 and GP-43220X.

A COMPARISON OF MASS SPECTRA FROM THREE ION PROBES

James G. Bradley*., Dominique Y. Jerome**,
and Charles A. Evans***

*Charles Arms Laboratory
Division of Geologic and Planetary Sciences
California Institute of Technology
Pasadena, California 91125

**Laboratoire de Mineralogie et de Cristallographie
Associé au CNRS
Université de Paris VI
4 Place Jussieu
75230 Paris-Cedex 05, FRANCE

***Materials Research Laboratory
University of Illinois
Urbana, IL 61801, U.S.A.

An intercomparison of the major element mass spectra from an Applied Research Laboratories' Ion Microprobe Mass Analyzer (ARL), the Cameca Ion Analyzer IMS-300 (Cameca) and the AEI Scientific Apparatus MS-702 Ion Probe (AEI) has been made using a natural mineral [1]. The comparisons are on the basis of the relative detected intensities of $^{23}\text{Na}^+$, $^{27}\text{Al}^+$, $^{28}\text{Si}^+$ and $^{40}\text{Ca}^+$ secondary ions (SI's). The work was done with the intent of determining the feasibility of doing quantitative analyses of mineral samples for the major and minor cations on the three machines and to determine the extent to which the three instruments provide a common result that can be used to advance the theory of quantitative secondary ion mass spectroscopy (SIMS).

The intercomparison was done on samples of Lake County Oregon Labradorite (LC) [2,3]. Lake County is a crystalline feldspar of low potassium content so that it is a plagioclase feldspar, and its sodium and calcium content is such that it is classified as labradorite. Its major element composition as determined by electron probe analysis at NASA-JSC is given in Table 1 [4]. This analysis is in good agreement with the wet chemical analysis found in reference 2. Lake County has proven to be a particularly useful microanalytical standard for SIMS comparisons because it possesses four major cations with no

significant interferences for secondary ion mass spectrometry, it is quite homogeneous from sample to sample and within a given sample there are very large volumes without foreign inclusions. This mineral has also been used as a trace element standard [5]. (Warning: no particular sample of Lake County or other mineral should be assumed to be chemically homogeneous or the same as any other sample without detailed checks made by accurate and precise analytical techniques.)

Table 1: Composition of Lake County Labradorite

Element	Atomic percent concentrations
Si	18.1
Al	12.7
Ca	5.0
Na	2.5
K	0.062
Fe	0.12
O	61.6

All the data presented for the ARL and AEI instruments and some preliminary Cameca data (not presented here) were obtained from analysis of a single sample of Lake County Labradorite. This is the same sample whose analysis is given in Table 1. The sample was extensively checked for inclusions and sodium-calcium zoning with the electron probe and was found to be homogeneous within counting statistics. The data presented for the Cameca instrument were obtained from analysis of a separate sample. An extensive check of this sample with an electron probe found it to be free of inclusions and zoning and homogeneous in major elements within counting statistics. The major element compositions of the two samples agree within a fraction of a percent.

The differences in the mass spectra of the instruments are illustrated in figure 1. In section A are plotted the true abundances of silicon, aluminum, calcium, and sodium in the sample, assuming 61.5% oxygen. In sections B through E the data represent the relative intensities of the detected calcium, silicon, aluminum, and sodium secondary ion beams with the sum of intensities adjusted to give a total of 38.5%. For example the data for silicon as plotted is the result of the calculation

$$F_{Si} = \frac{[^{28}Si^+]/0.9921}{[^{40}Ca^+]/.9697 + [^{28}Si^+]/0.9221 + [^{27}Al^+] + [^{23}Na^+]} \cdot 38.5\%$$

Spectra Comparison

where $[nM^+]$ is the actual detected secondary ion intensity in counts/second or amperes. The factor 38.5% reflects the fact that the non-oxygen elements of the true bulk composition represent about 38.5% of all the sample atoms. The introduction of this factor makes easier the comparison of true versus ion probe compositions although there is no reason to believe that any ion probe raw analysis should agree with the true composition. No predictive data reduction scheme (such as CARISMA) has been used on any of the data presented here.

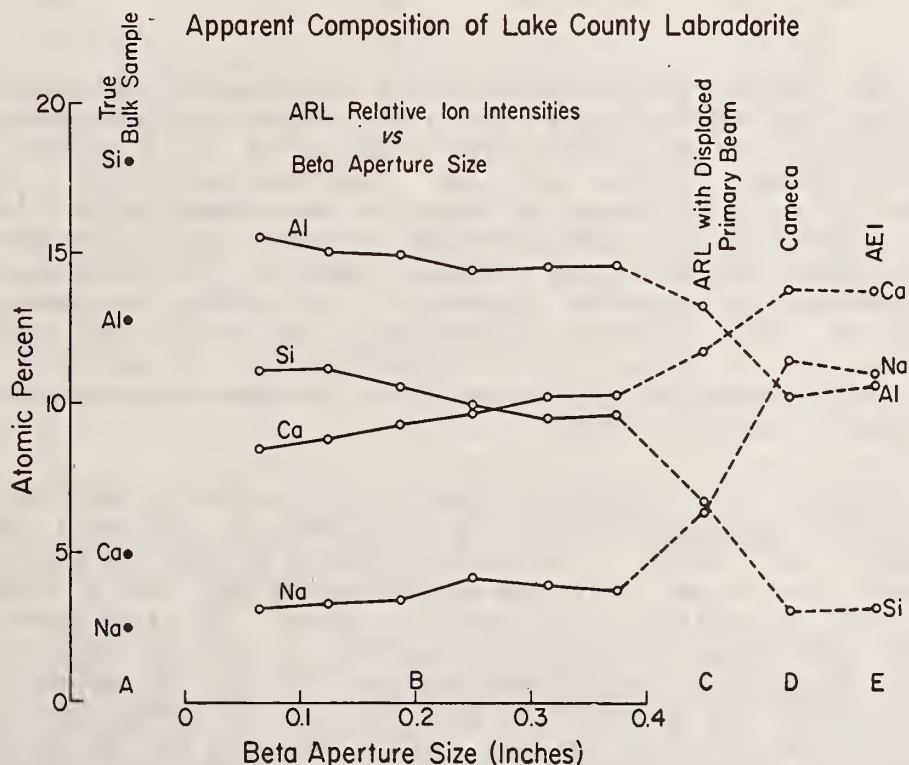


Figure 1. True bulk composition of Lake County Labradorite (section A) and the composition as indicated by relative ion intensities (sums adjusted to 38.5%) are displayed as measured by ARL, Cameca and AEI ion probes (sections B-E).

Section B represents the relative secondary ion intensities in the ARL instrument as the beta aperture diameter was varied. The analyzed spot was kept in its nominal on-axis design standard position. "Normal" operation is at a beta aperture diameter of 0.31 inches. The alpha aperture was kept at its normal diameter of 0.25 inches.

Section C represents the relative secondary ion intensities in the ARL instrument with the analyzed sample spot moved about 300 microns toward the secondary ion pickup electrode relative to its standard on-axis position. The alpha aperture diameter was 0.25 inches. The beta aperture diameter was 0.31 inches.

Sections D and E represent the relative secondary ion intensities as measured on the Cameca and AEI ion probes under their "normal" operating conditions.

The ARL data were obtained with a pulse counting detector and so have been corrected for dead time. The Cameca and AEI data were obtained as analog signals from the output of a scintillation-photomultiplier detector and an electron multiplier detector respectively. In all cases the data from measurement of the $^{28}\text{Si}^+$ and $^{40}\text{Ca}^+$ intensities have been corrected for their isotopic abundances to give total silicon and calcium signals. The secondary mass spectrometers and detection systems of all three instruments may introduce a mass dependent discrimination for certain ions; no effort has been made to correct for this discrimination. It should be noted that analog detection systems typically show more mass discrimination than pulse counting systems.

Section B of figure 1 shows the variation in the relative ion intensities as measured in the ARL instrument as the beta aperture diameter was varied. The beta aperture is between the electric and magnetic sectors and limits the angular spread and energy spread of the ions transmitted to the magnetic sector. The alpha aperture was set at 0.25 inches for these measurements. In the ARL instrument, the alpha aperture is an entrance aperture limiting the maximum angular divergence of the secondary ion beam that can be transmitted to the electric and magnetic sectors. Before measuring the ion intensities at each aperture setting, the sample bias voltage was adjusted in accordance with the ARL recommended procedure. That is, the sample voltage was increased somewhat beyond that required for maximum secondary ion transmission in order to qualitatively flatten the top of a peak displayed on the console oscilloscope (in this case $^{40}\text{Ca}^+$). It is likely that this procedure serves to position the secondary ion beam so that the highest energy ions do not pass through the beta aperture.

The trends in relative secondary ion intensities (section B, fig. 1) should be considered rather subtle, as the average secondary ion intensity increased a factor of 30 in going from the narrowest to the widest aperture. The repeatability at any one aperture is rather poor because of the qualitative tuning procedure. For example, the details of the $^{23}\text{Na}^+$ trend are not repeatable and probably meaningless.

Spectra Comparison

Section C of figure 1 shows the relative secondary ion intensities that were measured with the primary ion beam deflected to move its impact point on the sample approximately 300 micrometers closer to the secondary ion pickup electrode than it would be in the "design standard configuration." The sensitivity for aluminum (counts per second per nanoampere of primary ion beam) increased approximately a factor of two with deflection of the primary beam. Deflecting the primary ion beam apparently caused the secondary mass spectrometer to transmit more of the same "kind" of ions that increasing the beta aperture diameter caused it to transmit.

Sections D and E display the relative secondary ion intensities detected in running LC in the Cameca and AEI instruments. The similarity of Cameca and AEI relative intensities is quite striking. The relative ion intensities detected by the ARL under normal operating conditions (fig. 1, section B; alpha aperture 0.25 inches diameter, beta aperture 0.31 inches diameter and primary beam on axis) are strikingly different from those of AEI and Cameca. The similarities and dissimilarities between the spectra produced by the three instruments may reflect some "universal" genuine property of SI's emitted from an O^- bombarded LC sample or the relationships may be entirely due to combinations of the widely different parameters and characteristics of the three instruments.

The O^- primary ions in the Cameca strike the sample with an energy of about 14.5 keV at an angle of about 45° to the sample surface; the SI's are drawn off perpendicular to the sample surface and sent through a single focusing mass spectrometer at an energy of 4.5 keV. The SI's in the Cameca are detected by a scintillation-photomultiplier detector with the ion to electron conversion occurring at an impact energy of about 55 keV.

The O^- primary ions in the AEI instrument strike the sample with an energy of 35 keV at an angle of 73° to the sample surface; the SI's are drawn off the sample surface by an electrode arrangement that bends them through an angle of about 60° with respect to a normal to the sample surface and sends them through a double focusing secondary mass spectrometer at an energy of 10 keV. The SI's are detected by an electron multiplier with the impact energy on the conversion dynode of about 13 keV.

In the ARL instrument, the O^- primary ions strike the sample normal to the surface with an energy of 21.5 keV; the SI's are drawn off the sample surface by an electrode arrangement that bends them through an angle of 45° and sends them through a double focusing secondary spectrometer at an energy of 1.5 keV. The ions are detected by a scintillation-photomultiplier detector with ion to electron conversion occurring at an energy of 16.5 keV.

The dissimilarity of the ARL compared to the Cameca and AEI spectra cannot be due only to different primary ion impact energy

since its 21.5 keV impact energy is between that of the Cameca (15 keV) and AEI (35 keV). It cannot be due to some simple property of the ARL secondary ion pickup geometry or to its double focusing secondary spectrometer, since the AEI instrument is similarly configured. The normal incidence of the primary ions in the ARL is a possible explanation but seems unlikely because the primary beam impact in the AEI is only 17° away from the normal. Mass discrimination can be ruled out since even a strong discrimination (inversely proportional to the square root of ion mass) in any instrument is qualitatively of the wrong nature as well as of insufficient magnitude to bring about better agreement between the ARL spectrum and the others.

It seems likely that the source of the disagreement of the ARL spectrum with the others lies in which ions are being transmitted. The secondary ion pickup electrode arrangement in each instrument is capable of discriminating against ions of different initial energies and angles of emission.

The rather simple Cameca pickup geometry permits calculation of its energy discrimination properties. A normally equipped Cameca instrument will not transmit SI's with more than about 0.5 eV of velocity parallel to the sample surface. Hence the more energetic SI's will be strongly discriminated against although those few ions of higher energy, say more than about 5 eV above sample voltage, which are directed almost normal to the sample surface will still enter the mass spectrometer. The mass spectrometer further discriminates against high energy ions because the electrostatic mirror will not reflect ions of energy more than about (in the case of these experiments) 20 eV above sample voltage. Further, since the mass spectrometer is single focusing the mass peak shape for a particular ion is distorted according to the proportion of ion energies present. A typical peak shape (at mass resolution approximately 300) is shown in figure 2. The occurrence of the maximum on the low mass side of the peak represents a high production of low energy ions and/or high transmission for low energy ions. The presence of a low tail on the high mass side represents a reduced secondary ion production and/or low transmission for energetic ions. Hence the ratio of the low energy peak to the high energy tail at the 20 eV mirror cutoff is some crude measure of the degree to which high energy ions are produced at the sample surface. This peak to tail ratio was measured for each of the four ions dealt with here; the results are listed in Table 2. Unfortunately the peak to tail ratio was not measured for molecular ions. The points to note are that there are rather few high energy sodium and calcium ions, rather many higher energy aluminum and silicon ions and that the Cameca peak heights as reported here represent essentially the intensities of the lower energy ions.

The secondary ion pickup geometry of the AEI instrument can also discriminate against certain ion energies. The bending of the secondary ions through an angle of 60° causes a spatial separation of the trajectories of ions of different energies. Hence only a finite

Spectra Comparison

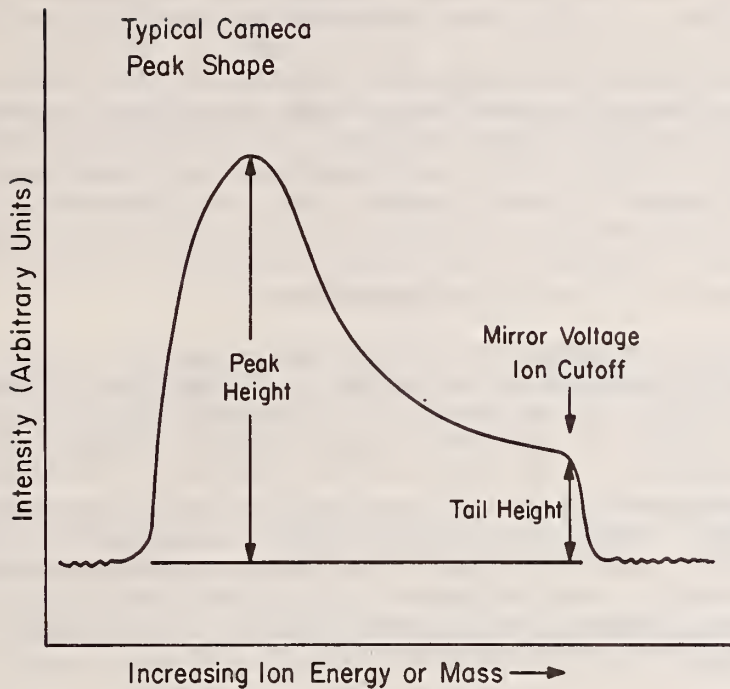


Figure 2. The typical shape of a single-mass peak. (at a mass resolution of about 300) from the singlefocusing Cameca ion probe as displayed by magnetic scanning.

Table 2: Relative low energy peak to high energy tail ratios as measured on the Cameca ion probe.

Ion	$\frac{\text{peak}}{\text{tail}}$ Ratio
$^{40}\text{Ca}^+$	73
$^{28}\text{Si}^+$	7.4
$^{27}\text{Al}^+$	15
$^{23}\text{Na}^+$	240

energy spread can be transmitted through the apertures of the pickup electrode. There is a secondary ion steering repeller over the sample region that allows maximizing of the detected ion intensities. If the greatest production of secondary ions occurs at low energies then maximizing of intensities will occur with low energy ions transmitted preferentially and only some fraction of the higher energy ions transmitted. If only the low energy ions are transmitted or if an insignificant number of high energy ions are produced, then the relative ion intensities determined by the AEI peak heights will be the same as that produced by the Cameca instrument despite the double focusing character of the AEI spectrometer.

The ARL instrument can discriminate against ions of certain energies for the same reason as the AEI, but the ARL pickup system does not include a secondary ion steering repeller to permit adjustment of which ion energies are transmitted through the pickup electrode apertures. The trend of ARL relative ion intensities with increasing beta aperture is consistent with an increasing transmission of low energy ions (those represented in the Cameca and AEI peak heights) due to a sample voltage adjustment procedure which always sets approximately the same upper limit on the energy of transmitted ions and hence decreases the low energy limit as the beta aperture size increases.

The increase in aluminum (and other ion) sensitivity and alteration of relative ion intensities with displaced primary ion bombardment position in the ARL (fig. 1, section C) are consistent with improved transmission of the more abundant low energy ions, since the alteration of the relative intensities is such that the improved transmission is for the same type ion represented in the Cameca (and AEI) peak heights. The greater magnitude of relative intensity changes with spot position change (versus beta aperture changes) indicates that most of the discrimination is occurring in the pickup electrode.

If for the moment the spectral differences can be ruled out as due to differences in sputtering conditions, the data seem to indicate that the ARL machine discriminates against the transmission of low energy ions and that the low energy ions are dominant in the sputtered spectrum. Also the data are consistent with the Cameca and AEI discriminating against higher energy ions, the AEI only if the low energy ions are dominant in the secondary ion energy spectra.

It is felt that the results presented here truly represent instrumental characteristics as determined under the specified operating conditions and with the instruments otherwise tuned by experienced operators, but the measurements should be confirmed in other laboratories. The systematic effects of varying sputtering and tuning conditions need to be studied within each instrument to determine the extent that each can yield altered relative ion intensities. Measurements on other multiple element standards would be

Spectra Comparison

helpful in revealing the systematics of an elemental discrimination based on sputtered ion energy differences.

The similarities and dissimilarities of the relative secondary ion intensities as measured by various instruments must be understood, particularly in so far as they reflect only instrumental differences, before the data from any instrument can be used to establish the validity of any theory for the quantification of secondary ion mass spectroscopy.

Acknowledgements

Bradley was supported by a National Research Council Research Associateship during the work at NASA-JSC. His initial work in France was generously made possible by a travel grant from Centre National de la Recherche Scientifique of France.

Bradley and Jerome acknowledge valuable and stimulating discussions with Professor Georges Slodzian in whose laboratory the Cameca measurements were done.

The work at the University of Illinois was supported by the National Science Foundation Grants GP-42330X and DMR-7203026.

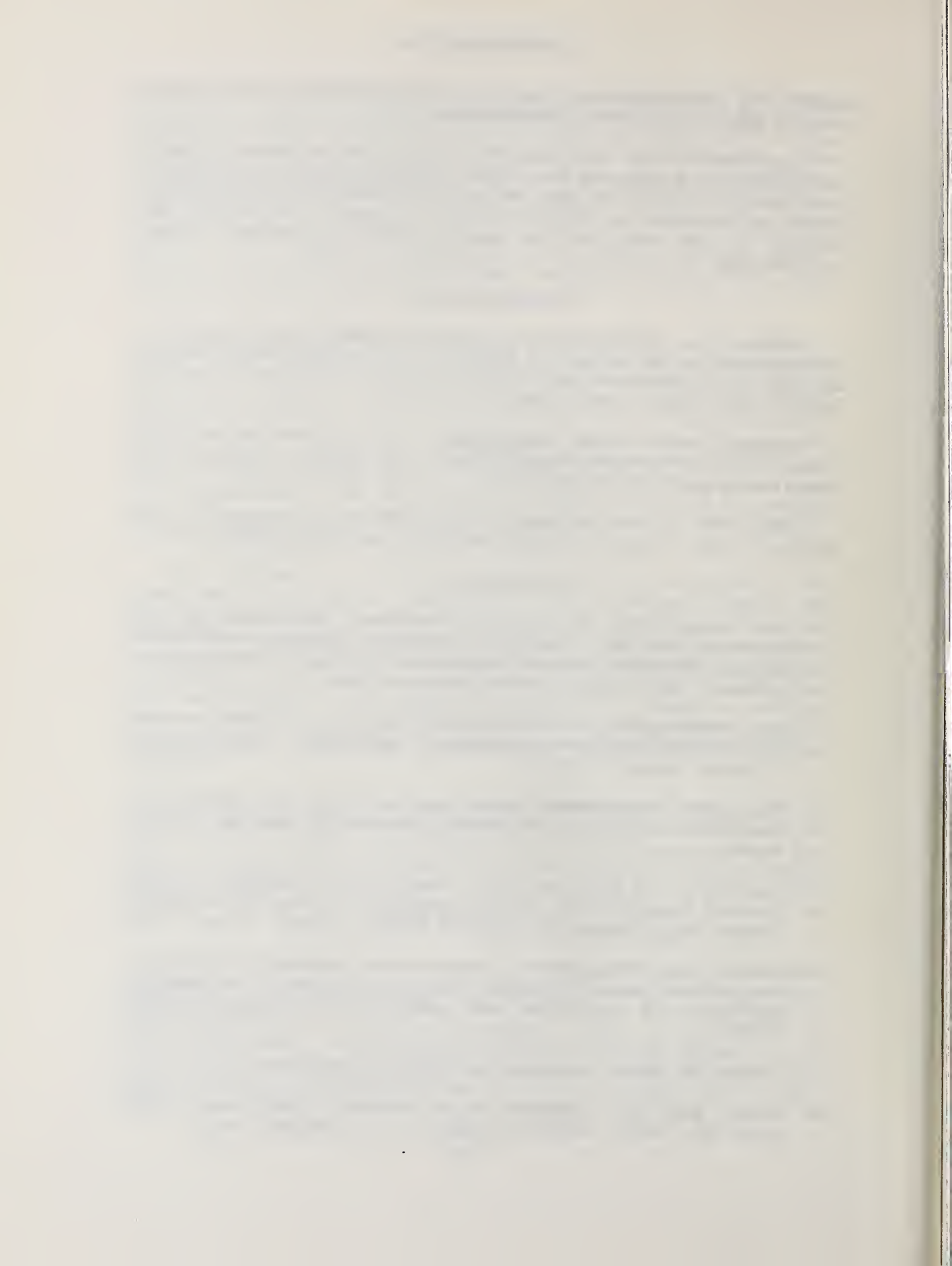
References

1. The measurements on the ARL instrument were done on the instrument of the Geochemistry Branch, Planetary and Earth Sciences Division, National Aeronautics and Space Administration, Lyndon B. Johnson Space Center, Houston, Texas.

The measurements on the AEI instrument were done on the instrument of the Materials Research Laboratory, University of Illinois, Urbana, Illinois.

The Cameca measurements were made on the instrument of the Laboratoire de Physique des Solides, Université Paris-Sud, Orsay, France.

2. Stewart, D. B., Walker, G. W., Wright, T. L., and Fahey, J. J., Physical properties of calcic labradorite from Lake County, Oregon, Amer. Mineral. 51, 177-197 (1966).
3. Limited quantities of this mineral can be obtained by writing to the National Museum of Natural History, Smithsonian Institution, Washington, D. C. 20560 and referring to the sample number 115900.
4. Analyst Roy Brown, Lockheed Electronics Corporation.
5. Meyer, C., Jr., Anderson, D. H., Bradley, J. G., Proc. Fifth Lunar Sci. Conf., Geochim. Cosmochim. Acta, Pergamon Press.



A CRITICAL DISCUSSION OF THE LOCAL THERMAL
EQUILIBRIUM MODEL FOR THE QUANTITATIVE CORRECTION
OF SPUTTERED ION INTENSITIES

C. A. Andersen

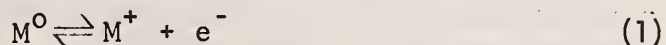
Hasler Research Center
Applied Research Laboratories
95 La Patera Lane
Goleta, California 93017

I. INTRODUCTION

Over the past few years we have developed an analytical method for the quantitative interpretation of sputtered ion intensities. On the basis of experimental observations, it has been postulated that the production of sputtered ions is a function of the electronic properties of the surface of the sample which, in turn, are related to the surface chemistry. We have learned that we can control the electronic properties of the sample surface and enhance and stabilize the yield of secondary sample ions through control of the chemistry of the surface by the proper selection of the primary bombarding ion beam. The emission of positive ions is enhanced by the increased electronic work function created by bombarding with an electronegative gas such as oxygen [1], while the emission of negative ions is enhanced by the decreased work function created by bombarding with an electropositive gas such as cesium [2].

The quantitative model that has been developed [3] to convert the enhanced and stabilized ion yields to atomic concentrations is based on a local thermal equilibrium (LTE) model. This working hypothesis states that the majority of sputtered ions, atoms, molecules, and electrons are in thermal equilibrium with each other and that these equilibrium concentrations can be predicted through the use of the proper Saha equations [4].

The ionization process postulated in this model can be thought of as an equilibrium dissociation reaction such as that given in equation 1.



The equilibrium constant for this reaction is simply written as the concentrations of the products over the concentrations of the reactants, as given in equation 2.

$$K_n^+ = \frac{n_m^+ \cdot n_e^-}{n_{M^0}} \quad (2)$$

At thermal equilibrium the equilibrium constant can be calculated according to the Saha-Eggert ionization equation [5], as given in equation 3:

$$\left(\frac{2\pi kT}{h^2} \cdot \frac{m_e \cdot m_{M^+}}{m_{M^0}} \right)^{3/2} \frac{B_{M^+} B_{e^-}}{B_{M^0}} e^{-E/kT} \quad (3)$$

where h is Planck's constant, k is Boltzmann's constant, T is the absolute temperature in $^{\circ}K$, m is the mass, B the internal partition function, and E the dissociation energy of the species in question (in this case it is the first ionization potential of the atom). A practical logarithmic form of equation 3 is given in equation 4 and shows that the ratio of positive ions to neutral atoms of an element is a function of the temperature and electron density of the assemblage:

$$\log(n_{M^+}/n_{M^0}) = 15.38 + \log 2(B_{M^+}/B_{M^0}) + 1.5 \log T - \frac{5040(I_p - \Delta E)}{T} - \log n_{e^-} \quad (4)$$

where n_{M^+} and n_{M^0} are the numbers of atoms of element M in two adjacent charge states, B_{M^+} and B_{M^0} are the internal partition functions of these charge states, 2 is the partition function of a free electron, I_p is the ionization potential depression due to Coulomb interactions of the charged particles, and n_{e^-} is the number of electrons per cm^3 .

It can be seen from equation 4 that, given the partition functions and the ionization potential, the ratio of the number of singly charged ions to neutral atoms of an element is predicted by the temperature and electron density of the assemblage. This is the basis for a quantitative method since the singly charged ions are directly observed in the mass spectrum. Therefore, from the predicted ratio of singly charged to neutral atoms, the total number of atoms of an element present in the sputtering assemblage can be calculated. If all the elements observed in the mass spectrum are treated in this way, the atomic composition of the sample is derived.

The sputtering assemblage is assumed to be basically a dense plasma of coexisting positive and negative atomic and molecular ions, electrons, and neutral atoms and molecules. Under the present experimental ion-bombardment conditions, most of the particles are neutral atoms and singly charged positive ions. There are, however, for elements of high electron affinity and high oxygen affinity, significant numbers of negative ions and oxide molecules in equilibrium with the positive ions and neutral atoms. The equilibrium concentrations of these species can be calculated with the appropriate Saha equations, as will be shown shortly, and the intensities of the positive ions corrected for their abundance. All the observed intensities of singly charged positive ions in the mass spectrum are corrected in this way to give the total atomic composition of the sputtering plasma, which is directly related to that of the solid. We have previously demonstrated [4] that such a correction procedure generally works well.

A substantial degree of success using this model has also been reported: by R. Shimizu *et al.* [6] using an Ar⁺ beam and a Hitachi IMA-2 to analyze a steel standard; by F. G. Rudenauer and W. Steiger [7] using an Ar⁺ beam and a specially designed ion microprobe with tandem mass spectrometers to analyze a steel sample; by A. Lodding *et al.* [8] using an O⁻ beam and a CAMECA IMS 300 ion analyzer to analyze known apatite samples; by C. Meyer *et al.* [9] using an O⁻ beam and an ARL IMMA to analyze plagioclase standards; by J. Schroerer [10] using an O₂⁺ beam and an AEI ion microprobe attachment to the MS 702 to analyze several NBS steel standards; by D. Simons [11] using the same equipment and an O⁻ beam to analyze a plagioclase standard (Lake County); and by J. Lovering [12] using an O⁻ beam and an ARL IMMA to analyze many different mineral standards. J. F. Bradley [13] has also reported element intensity ratios for Lake County plagioclase obtained with a CAMECA IMS 300 and an O⁻ bombarding ion beam that appear to be identical to those reported by Simons [11]. In addition Z. Jurela [14] has proposed, and demonstrated with a good deal of success, a similar thermodynamic model which differs from that discussed here in that it stresses a nonequilibrium state. An independent evaluation [10] of Jurela's nonequilibrium model using several NBS steel standards, however, indicated that it did not account for the observed ion intensities with as good accuracy as did the local thermal equilibrium model.

Based on the apparent successful application of the method by several investigators using different instruments to many different types of samples, it is appropriate to critically discuss the LTE model in terms of the confirming and negating evidence and also in terms of a possible physical basis.

II. CONFIRMING EVIDENCE FOR LTE

There are six main observational indications that local thermal equilibrium exists between the electrons, ions, atoms, and molecules of the sputtering assemblage. These are:

1. Positive Ions in Equilibrium with Neutral Atoms

Equation 4 was developed to describe thermal ionization and is taken as one of the validity criteria for the establishment of local thermal equilibrium [15]. An example of the application of this equation to sputtered positive ion data obtained from a well-characterized mineral standard is given in figure 1. In this case, the effective temperature and electron density of the sputtering region were obtained by solving the Saha-Eggert ionization equations for the best fit of the observed singly charged ion intensities to the known concentrations of the elements in the sample. The symbols II and I refer to the singly charged ion and neutral atom, respectively. ΔE in this case

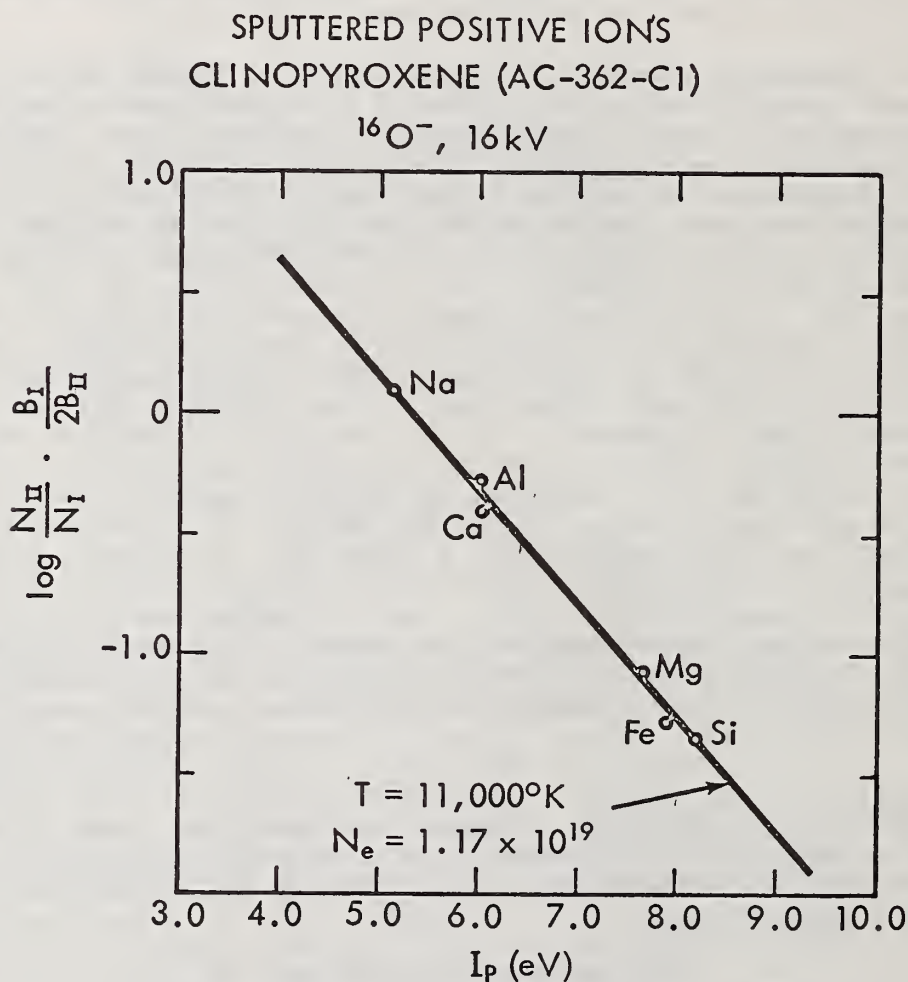
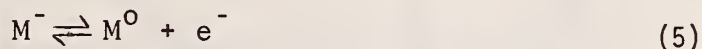


FIGURE 1: Saha-Eggert ionization equation applied to sputtered positive ion data from a mineral standard bombarded with $^{16}\text{O}^-$ at 16 keV.

is 0.66 eV. Equation 4 is basically a linear equation in two unknowns, T and n_{e^-} . The values for two observed singly-charged-to-neutral atom ratios, therefore, permit a solution for the temperature and electron density of the sputtered region. In practice, the neutral atom intensities are not observed but the composition of the sample is known and the ratio of the corrected ion intensities thereby established. The fit of the data to the Saha-Eggert ionization equation indicates that the singly charged ions in the sputtering assemblage are in thermal equilibrium with the neutral atoms and that the equation can be used to predict this ratio.

2. Negative Ions in Equilibrium with Neutral Atoms

The electron attachment process under equilibrium conditions can be written as:



The dissociation constant of this reaction can be written in a form analogous to equation 2 and evaluated according to a Saha equation analogous to equation 3. A practical logarithmic form of the latter equation is given in equation 6:

$$\log(n_{M^-}/n_{M^0}) = -15.38 + \log(g_{M^-}/2g_{M^0}) - 1.5 \log T + \frac{5040E_a}{T} + \log n_{e^-} \quad (6)$$

where E_a is the electron affinity of the neutral atom of element M , and g represents the statistical ground state of the negative ion or the neutral atom.

Experimental confirmation that sputtered negative ion yields fit such a relationship at elevated temperatures is given in figure 2. Here the ratios of the number of negative ions to neutral atoms for three elements from a mineral standard are plotted versus the electron affinity of the atom. The statistical weights of the ions and atoms have not been included because they are unknown. This simplification is discussed in another paper [4]. The effective temperature and electron density were obtained from the experimental data using equation 6, setting the statistical weights equal to one, and the known atomic concentrations of the elements in the sample. Again, there seems to be evidence of local thermal equilibrium between negative ions and neutral atoms.

In this example the temperature is noticeably lower than that observed for the positive ion data of figure 1. The significance of this difference is not fully appreciated at this time because of a

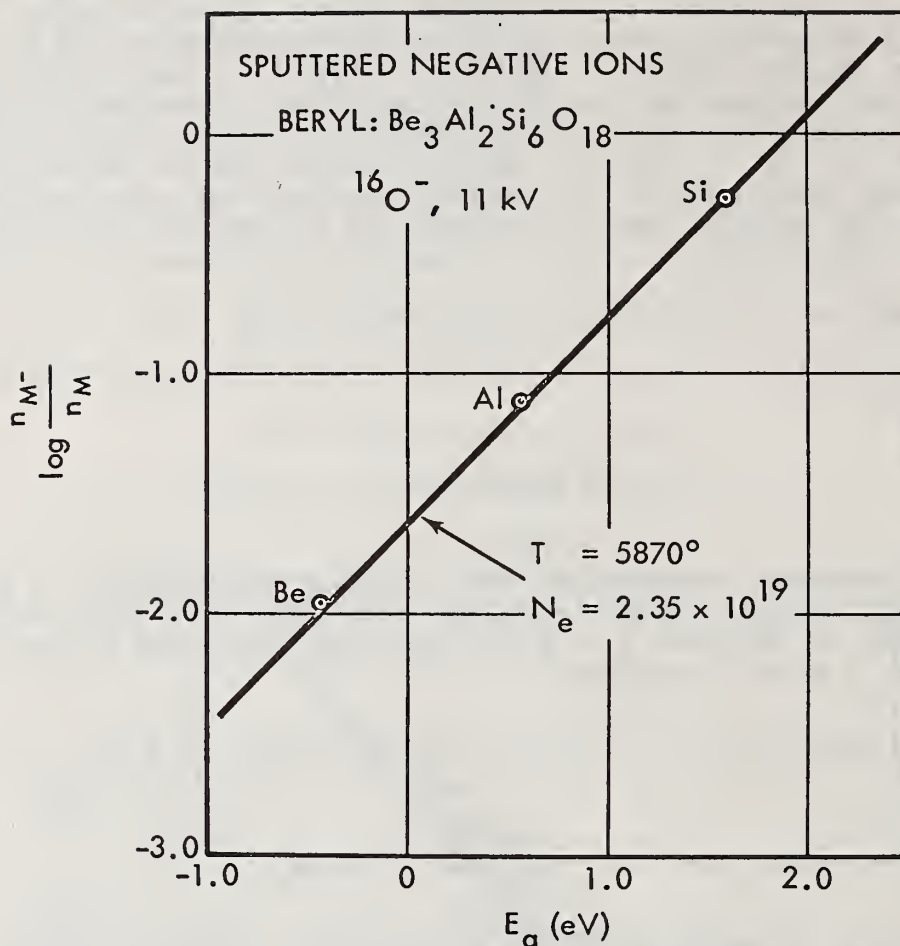


FIGURE 2: Saha equation applied to sputtered negative ion data from a mineral standard bombarded with $^{16}\text{O}^-$ at 11 keV.

general paucity of negative ion data. It is thought, however, that the relatively high electron density at this lower temperature is significant. More work with negative ions is earnestly needed.

3. Molecular Ions in Equilibrium with Atomic Ions

The molecular and atomic species under conditions of local thermal equilibrium are related through dissociation reactions such as:



where the superscript refers to neutral particles. Similar equations could be written for the dissociation of charged molecules to charged atoms. The dissociation constant of this reaction can be written in a form analogous to equation 2 and evaluated according to a Guldberg-Waage equation that is analogous to Saha equation 3. Using an approximation for the partition function of the diatomic molecule [16], the latter equation is given in equation-8.

$$K_{n_1^0} = 2.70 \times 10^{20} \frac{B^0 e}{g^0} \left[\frac{m_M m_O}{m_{MO}} \right]^{3/2} X \quad (8)$$

$$B_{MO} B_O T^{1/2} \left[1 - 10 \exp \left(\frac{-0.625 \omega^0}{T} \right) \right] 10 \exp \left(\frac{-5040 V_{d^0}}{T} \right)$$

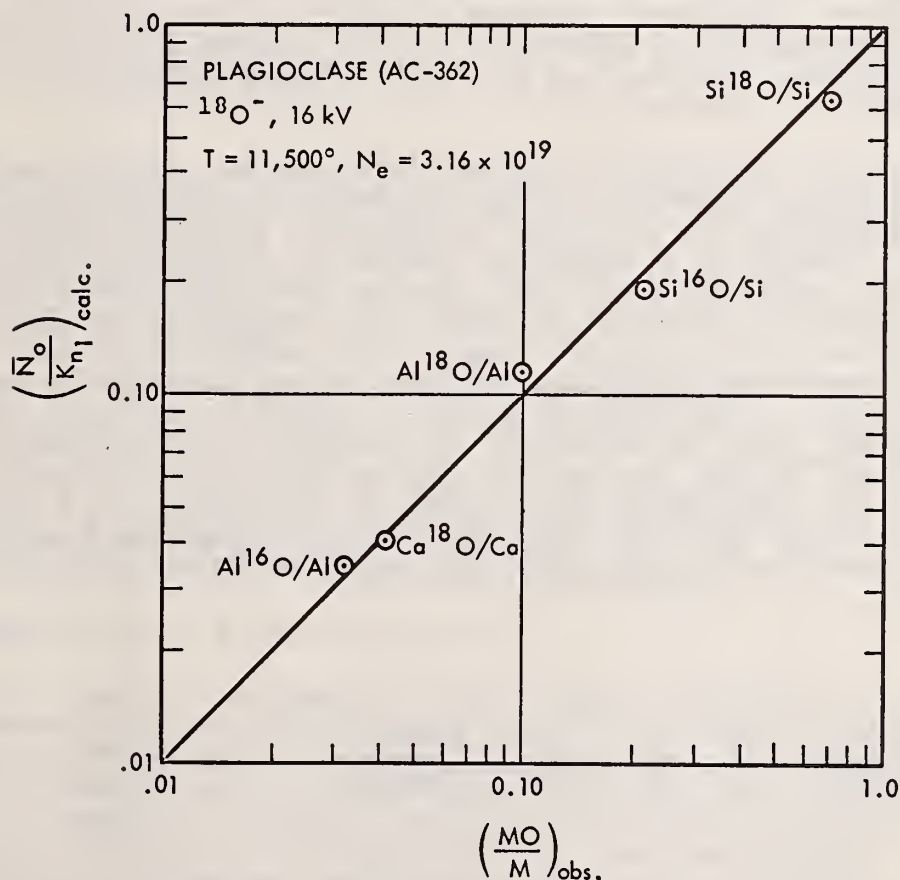


FIGURE 3: Observed positive atomic and monoxide ion intensities (corrected for degree of ionization) as a function of the calculated dissociation constant and the average concentration of free oxygen. Data from a mineral standard bombarded with $^{18}\text{O}^-$, at 16 keV.

where B_e^0 is the rotational constant for the electronic state referred to a vibrationless condition, ω^0 is the vibrational constant, g^0 is the statistical weight of the electronic ground state, and v_d^0 is the dissociation energy of the neutral molecule. Equation 8 can be used to determine the neutral molecular monoxide-to-metal atom ratio if the concentration of neutral free oxygen is known [4].

The accuracy of this approach is illustrated in figure 3 where data obtained from a silicate mineral standard bombarded with a pure beam of $^{18}O^-$ are shown. The observed positive atomic and molecular ion intensities of both $M^{16}O$ and $M^{18}O$ have been corrected for their degree of ionization and plotted as a function of the calculated neutral molecular dissociation constant and the average concentration of neutral free ^{16}O or ^{18}O in the sputtering region. The average concentration of neutral free oxygen, \bar{N}_O , was determined from the experimental data to be the average value calculated using the observed MO^+/M^+ intensity ratios (corrected for their degree of ionization) of each of the molecule and atom pairs illustrated in figure 3. The fit of the data demonstrates that the molecular ions observed in the mass spectrum are the products of equilibrium reactions and that their relative concentrations can be calculated with equation 8.

Another indication of the equilibrium between molecules and atoms that is implied in the data discussed above can be obtained by comparing the temperatures derived from the molecules to that derived from the atoms. As explained in subsection 1 above, a temperature is derived from the sputtered atomic ion data by using the LTE model (CARISMA) [3,4] to match the observed sputtered ion intensities to the known composition of the standard sample. This temperature is known as the CARISMA temperature and relates the ratio of ions to atoms of a specific element at a given electron density. It is also possible to derive a temperature from the molecular ion spectra, without knowing the composition of the sample, by forming the ratio of molecular ion intensities (corrected for their degree of ionization) of a pair of molecules, MO and $M'O$, and using equation 9. Equation 9 is simply a ratio formed from equation 8 for two oxide molecules with different cations.

$$\frac{n_M \cdot n_{MO'}}{n_{MO} \cdot n_{M'}} = \frac{B_e}{B_e'} \cdot \frac{g}{g'} \cdot \frac{B_M}{B_{M'}} \cdot \left[\frac{m_M m_{MO'}}{m_{MO} m_{M'}} \right]^{3/2} \quad (9)$$

$$\frac{1-10 \exp\left(\frac{-0.625\omega}{T}\right)}{1-10 \exp\left(\frac{-0.625\omega'}{T}\right)} \cdot 10 \exp\left(\frac{-5040}{T}(v_d - v_d')\right)$$

ANDESINE ($^{18}\text{O}^-$): T(°K)

kV	$T\left(\frac{\text{Si}}{\text{Si}^{18}\text{O}} : \frac{\text{Al}}{\text{Al}^{18}\text{O}}\right)$	$T\left(\frac{\text{Si}}{\text{Si}^{16}\text{O}} : \frac{\text{Al}}{\text{Al}^{16}\text{O}}\right)$	T (CARISMA)
18	10200	9700	11480
16	10550	10075	13560
14	10850	10440	14600
11	11375	11225	14280
8	12050	12150	16740

TABLE I: LTE (CARISMA) temperatures compared to temperatures derived from molecular oxide data from a silicate bombarded at different energies.

Table I gives the results of such a comparison based on data derived from a mineral standard bombarded with $^{18}\text{O}^-$ at several different accelerating potentials. Two sets of Si and Al monoxide molecular ion data, one incorporating natural ^{16}O from the sample and the other incorporating implanted ^{18}O from the bombarding beam, were compared to the CARISMA temperatures.

It can be seen that, although the temperatures don't match perfectly, they are of the same order and trend in the same direction as the accelerating potential is changed. (This important inverse relationship will be returned to later.) The temperature differences noted may be real or may be related to errors in the physical constants required to solve the equations. In any case the data again support local thermal equilibrium between atoms and molecules.

4. Perfect Mixing of Reaction Particles

The internal consistency of the data for molecules formed from metal atoms of the sample with both natural ^{16}O from the sample and with bombardment-introduced ^{18}O , shown in both the above data and those of figure 3, demonstrates that (under these experimental conditions) the molecules observed in the mass spectrum are not directly related to the molecular structure of the solid but are the reaction products of a collection of implanted atoms and sample atoms interacting at an elevated temperature. The perfect mixing implied is an indication of equilibrium among the particles.

A further indication of the perfect mixing of atoms, observed in the sputtered ion data discussed above, is obtained by determining the

ratio of the implanted to natural oxygen for the different pairs of atoms and molecules. The atom ratio of $^{18}\text{O}/^{16}\text{O}$ can be determined: (1) directly from the sputtered ion intensity ratio of these two isotopes; (2) from the ratio of $\text{Si}^{18}\text{O}/\text{Si}^{16}\text{O}$ according to equation 10a-f; and (3) from the ratio of $^{18}\text{O}_2/^{16}\text{O}_2$ according to equation 11a-f. The equations are self-explanatory, being analogous to equations 2 and 3, and the results of the analysis are given in Table II.

ANDESINE ($^{18}\text{O}^-$): $n_{^{18}\text{O}}/n_{^{16}\text{O}}$

kV	$(n_{^{18}\text{O}}/n_{^{16}\text{O}})$	$(n_{^{36}\text{O}}/n_{^{32}\text{O}} \times 0.838)^{1/2}$	$(n_{^{28}\text{Si}^{18}\text{O}}/n_{^{28}\text{Si}^{16}\text{O}} \times 0.896)$
18	2.68	2.64	2.70
16	2.78	2.50	3.78
14	2.62	2.21	2.87
11	2.65	2.52	2.58
8	2.54	-	2.83

TABLE II: The ratio of implanted ^{18}O to sample ^{16}O gas derived from atomic and molecular oxide data from a silicate bombarded at different keV.

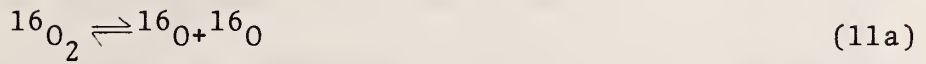


$$K_{n_{\text{MO}}} = \frac{n_{\text{M}} \cdot n_{\text{O}}}{n_{\text{MO}}} \quad (c)$$

$$K_{n_{\text{MO}}} = \left(\frac{2\pi kT}{k^2} \cdot \frac{m_{\text{M}} \cdot m_{\text{O}}}{n_{\text{MO}}} \right)^{3/2} \frac{B_{\text{M}}^{16}\text{O}}{B_{\text{MO}}} \cdot e^{-V_d/kT} \quad (d)$$

$$\frac{n_{18O}}{n_{16O}} = \frac{n_{M18O}}{n_{M16O}} \cdot \frac{K_{nM18O}}{K_{nM16O}} \quad (e)$$

$$\frac{n_{18O}}{n_{16O}} = \frac{n_{M18O}}{n_{M16O}} \left(\frac{m_{18O} \cdot m_{M16O}}{m_{16O} \cdot m_{M18O}} \right)^{3/2} \quad (f)$$



$$K_{n,16O_2} = \frac{n_{16O} \cdot n_{16O}}{n_{16O_2}} = \frac{(n_{16O})^2}{n_{16O_2}} \quad (b)$$

$$n_{16O} = \left(n_{16O_2} \cdot K_{n,16O_2} \right)^{1/2} \quad (c)$$

$$\frac{n_{18O}}{n_{16O}} = \left[\frac{n_{18O_2}}{n_{16O_2}} \cdot \frac{K_{n,18O_2}}{K_{n,16O_2}} \right]^{1/2} \quad (d)$$

$$\frac{n_{18O}}{n_{16O}} = \left[\frac{n_{18O_2}}{n_{16O_2}} \left(\frac{(m_{18O})^2 \cdot m_{16O_2}}{(m_{16O})^2 \cdot m_{18O_2}} \right)^{3/2} \right]^{1/2} \quad (e)$$

$$\frac{n_{18O}}{n_{16O}} = \left(\frac{n_{16O_2}}{n_{18O_2}} \times 0.838 \right)^{1/2} \quad (f)$$

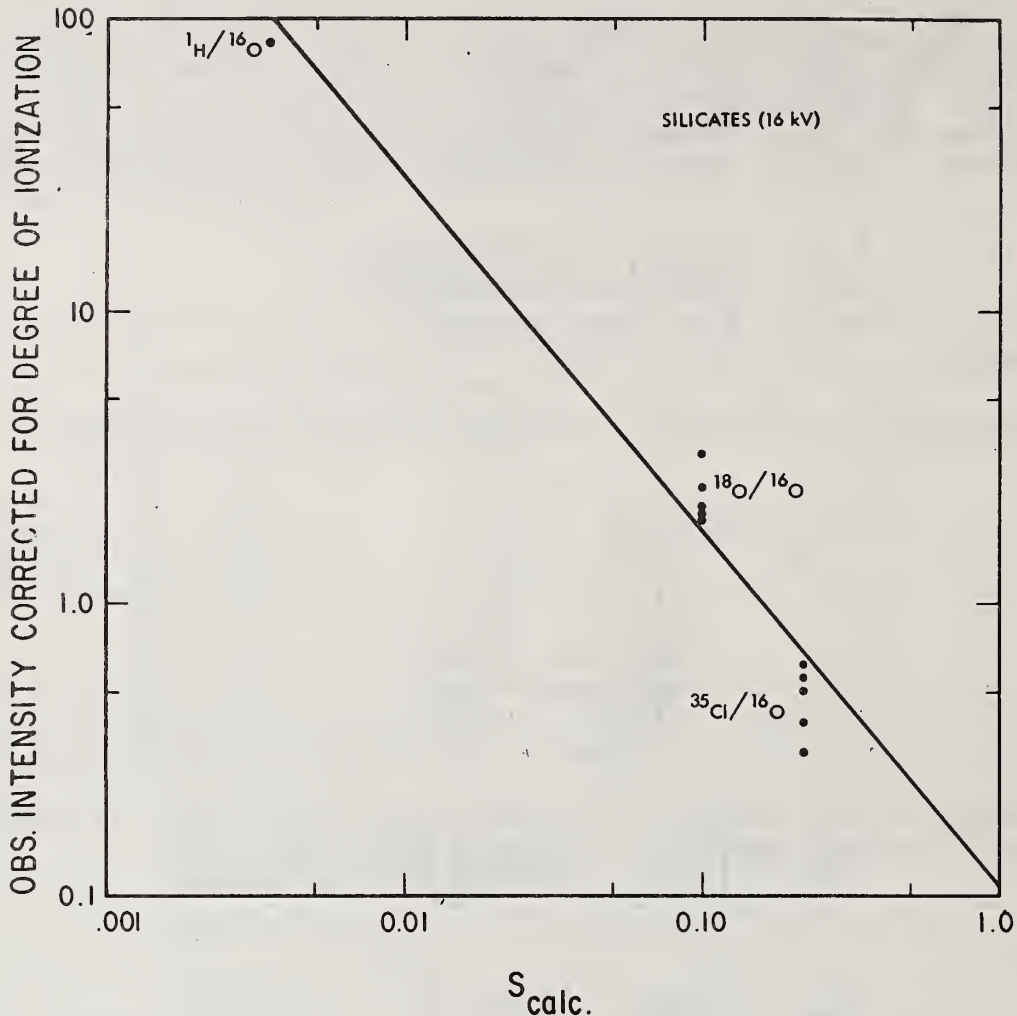


FIGURE 4: Ratio of implanted to sample gas as a function of the calculated sputtered atom yield for silicates bombarded with $^1\text{H}^-$, $^{18}\text{O}^-$, and $^{35}\text{Cl}^-$ at 16 keV.

It can be seen in Table II that the $^{18}\text{O}/^{16}\text{O}$ ratios obtained from all three combinations of atoms and molecules are essentially equivalent, indicating that the ^{18}O and ^{16}O atoms are equally distributed among the oxygen and silicon monoxide molecules. The differences noted are probably the results of errors in the data.

It is also interesting to note that the ratio of $^{18}\text{O}/^{16}\text{O}$ is approximately constant with accelerating potential and that it has a value of about 2.6. This indicates that there are about 2.6 times as many implanted ^{18}O atoms in the sputtering assemblage as there were ^{16}O atoms originally in the solid sample. Since the mineral was originally

about 62 percent oxygen, the new oxygen content of the sputtering assemblage must be about 85 percent. This would appear to be a large amount of entrapped gas for the solid to contain.

Figure 4 shows the fairly consistent $^{18}\text{O}/^{16}\text{O}$ ratio measured in five different mineral types at an accelerating potential of 16 kV plotted as a function of the calculated [2] sputtered atom yield (in relative units). The sputtered atom yield was chosen because it had previously been shown [17] that the amount of inert gas trapped in a metal was inversely proportional to this function. Also shown on the plot are the ratios of implanted to sample gas obtained when mineral specimens are bombarded with ^1H and ^{35}Cl beams. The inverse relationship appears to hold and it can be seen that as the sputtering yield drops the amount of entrapped bombarding gas increases greatly with the ratio of bombarding gas to sample gas approaching 100 in the case of H bombardment.

5. Electrons in Equilibrium with the Sample Surface

We have recorded the temperatures and electron densities that have been derived from the analysis of several hundred standard samples using the described [4] LTE model and have noted a definite relationship between these two parameters [18]. This functional relationship may be interpreted by returning to the dissociation reaction given in equation 2 where it is noted that the equilibrium constant of the reaction is given in terms of the concentrations of the ions, atoms and electrons. It is important to understand, however, that it is not necessary to assume that in this equation the electrons come only from the ionization of the atoms [19]. Some, or the majority, of the electrons, required to explain the degree of ionization observed, could arise from other processes. A possible source, for example, could be thermally emitted electrons coming from a hot spot on the surface of the bombarded sample such as might be associated with the postulated local plasma.

Electron emission from a hot surface can generally be described by Richardson's equation [20].

$$I = A_R T^2 e^{-\phi_0/kT} \quad (12)$$

where I is the electron yield of the surface in A/cm^2 , A_R is Richardson's constant, T is the absolute temperature of the surface, k is Boltzmann's constant, and ϕ_0 is the work function of the surface at absolute zero temperature. This formulation gives the electron emission in terms of the electronic work function and the temperature of the surface. N_e , the electron concentration per cubic centimeter, required for the dissociation equation can be obtained from I , the electron emission per square centimeter, by using the relationship given in equation 13 [19]:

$$N_e = 4.034 \times 10^{13} \cdot T^{-1/2} I \quad (13)$$

Richardson's equation can thus be tested to see if it gives the dependence noted in the observed relationship between temperature and electron density. A satisfactory result will be considered to be a straight line fit of the temperature and electron density data on a Richardson plot and a reasonable electronic work function for the materials derived from the slope of that line.

This test has been made in the next two figures where the LTE-derived electron densities have been plotted against the LTE-derived temperatures according to Richardson's equation. Figure 5 represents 163 silicate analyses [4]. It should be noted that these are the analyses of known standard reference materials and that the temperatures and electron densities plotted are obtained independently of each other by simply allowing a computer using an LTE model (CARISMA) to pick the temperatures and electron densities that best explain the observed sputtered ion intensities with respect to the known sample compositions. The heavy line through the points is a least squares fit that gives better than 95 percent correlation. Richardson's relation on the basis of these data would predict an average electronic work function for the emitting surfaces of 11.18 volts, defined at absolute zero temperature. This value may be slightly higher than expected but is not entirely inconsistent with known band gaps of insulators [21]. The temperature coefficient of the work function is negative and about 4×10^{-4} eV/°K, which is also of about the right magnitude [22]. The light dashed line on the plot is related to our experience with metals analysis which is given in figure 6.

Figure 6 is similar to figure 5 except here the heavy line is a least squares fit through 60 metal alloy analyses we have made [4]. The points were derived from the LTE model using CARISMA in exactly the same way as those shown in figure 5. The average work function of the electron emitting surfaces using these data is now predicted by Richardson's equation to be 8.54 volts at absolute zero. The correlation is in excess of 90 percent and the temperature coefficient of the work function is nearly identical to that observed for the silicates. The work function again might seem a little high but probably is not excessive for an oxygen-saturated metal surface [19]. The lower dashed line is that derived from the silicate analyses of figure 5. The upper dashed line is given for comparison and represents the actual electron emission with temperature of a heated tungsten filament [23]. It is interesting to note here the temperature and electron density observed by Shimizu *et al.* [6] using an LTE model to interpret the results of their analysis using an argon beam. The temperature reported (6000°-6500°K) is very similar to those we have noted on similar materials but their electron density ($N_e = 5.6$ - 5.2×10^{18} e⁻/cm³) is much larger indicating, according to the Richardson equation, a considerably lower electronic work function of the bombarded surface. This is exactly the result to be expected when bombarding a

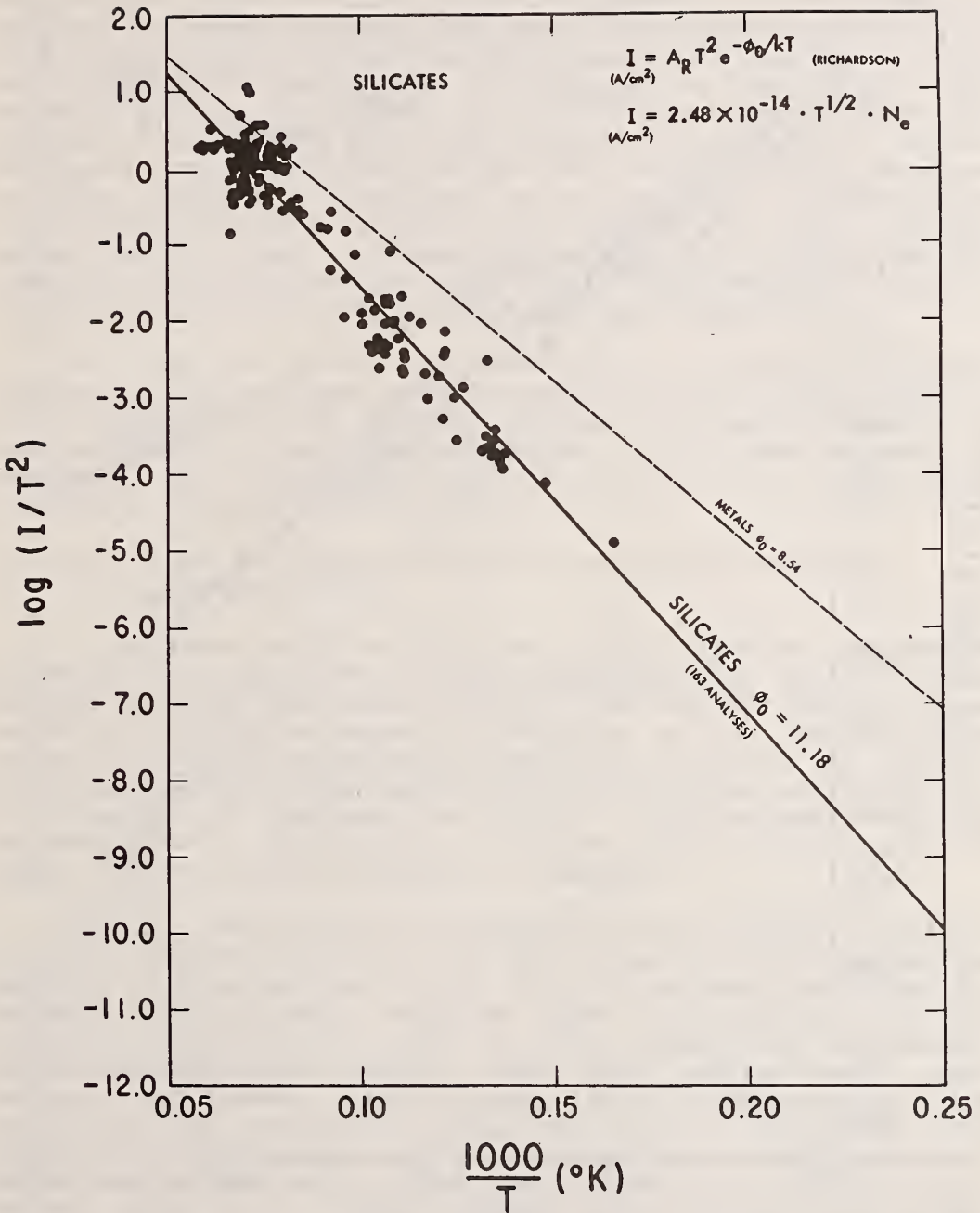


FIGURE 5: Richardson plot of LTE derived electron densities and temperatures for 163 metal analyses.

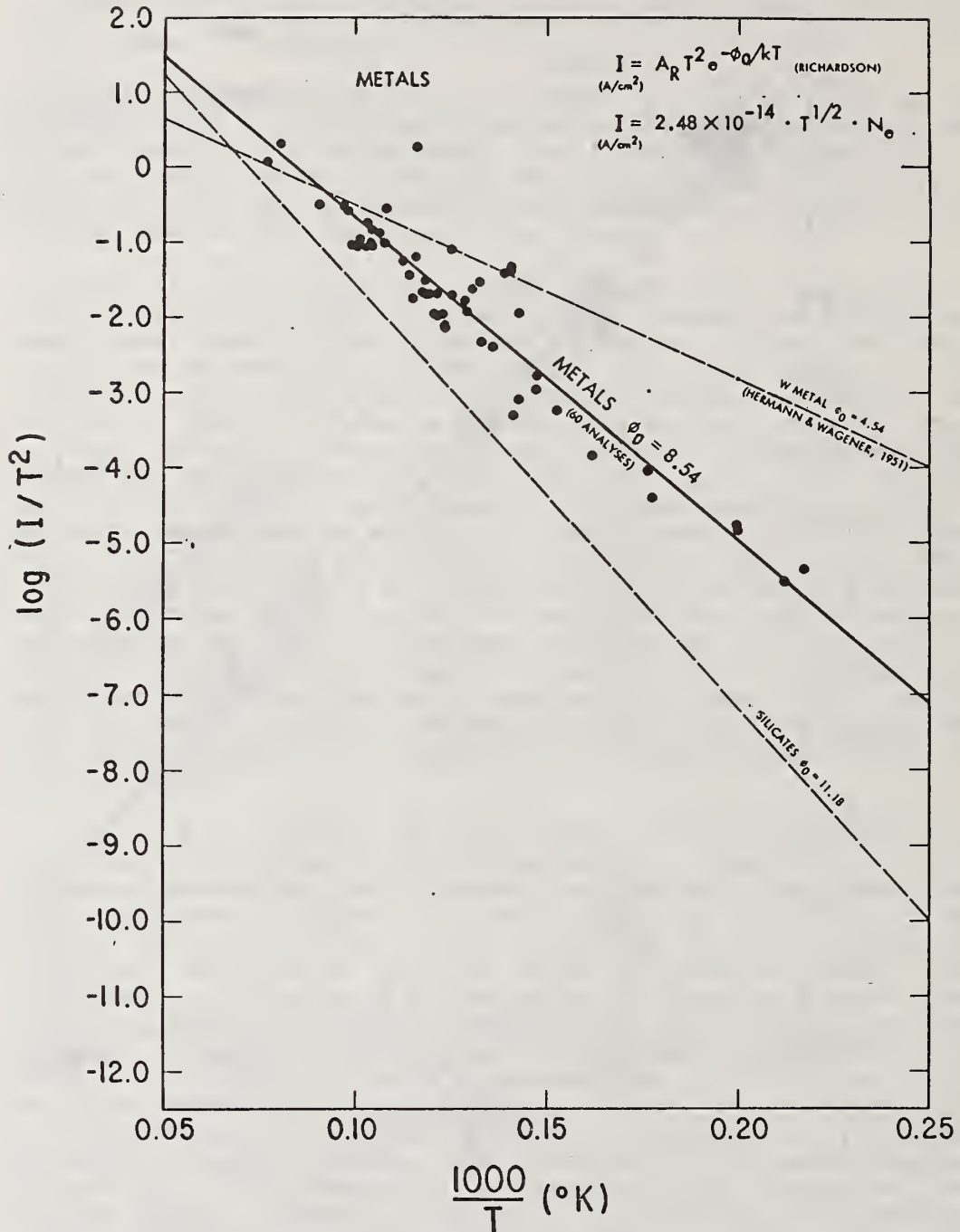


FIGURE 6: Richardson plot of LTE derived electron densities and temperatures for 60 metal analyses.

metal with an inert gas such as argon as opposed to an electronegative reactive gas such as oxygen [1]. The increased work function created when bombarding with the reactive gas decreases the electron emission and consequently the electron density of the local plasma which increases the absolute sputtered ion yield, see equation 4. This same effect, of course, can be realized by analyzing a sample or a point on the sample that naturally has a higher work function. This phenomenon is often observed in sputtered ion micrographs of polycrystalline samples where both bright and dark grains of a material with a constant composition are seen. Prolonged bombardment with an oxygen beam will eventually overcome the natural work function differences and produce an image of equal intensity for grains of equivalent composition.

The good fit of the LTE-derived data to Richardson's equation, coupled with the derivation of a reasonable electronic work function for the surfaces, indicates that the electrons are in equilibrium with the surface which is at an elevated temperature. This further suggests, by inference, that all the sputtered particles are in equilibrium with a hot spot on the surface of the sample.

6. Equivalence of Temperatures Derived from Optical Emission and Sputtered Ion Data

The emission of ultraviolet and visible radiation from samples subjected to energetic (few keV) ion bombardment has generally been observed by many investigators [24-30]. The behavior they have noted concerning the relative changes in intensity of the radiation with respect to oxygen coverage of the sample and with respect to insulator versus metal is exactly analogous to the behavior noted previously for the intensity of sputtered ions [2,3]. This indicates that the processes governing the emission of radiating excited particles are the same as those that govern sputtered ion emission.

Recently, Shimizu and his colleagues [31] have spectrally analyzed the optical radiation generated from aluminum and aluminum oxide samples bombarded with argon ions at 14 keV. Using Saha's relationships, according to the LTE model, they have found the radiation from the sputtered excited neutral atoms to yield temperatures of several thousand degrees Kelvin ($\sim 5000^\circ\text{K}$). They found similar results when analyzing the spectral data of Kerkow [32]. The temperatures of the insulator (Al_2O_3) were generally higher than those of the metal (Al), again paralleling sputtered ion relationships [4]. These temperatures, they emphasized, are similar to the temperatures they had previously derived, using an LTE model, in their analysis of sputtered ion data obtained from iron samples bombarded under similar experimental conditions (6). They were also able to dramatically change the shape of the optically emitting region above the surface of an Ar-bombarded tantalum sample by simply applying a weak magnetic field to the sample [33].

These results are consistent with an LTE model and indicate that the sputtered neutral atoms exhibit degrees of excitation equivalent to

the high temperatures derived from the sputtered ion data. The results also indicate that the radiating excited neutral atoms interact and exchange charges with the sputtered ions above the surface of the sample, as demonstrated by the effect of the superposed magnetic field.

III. ACCURACY OF THEORETICAL CALCULATION METHOD

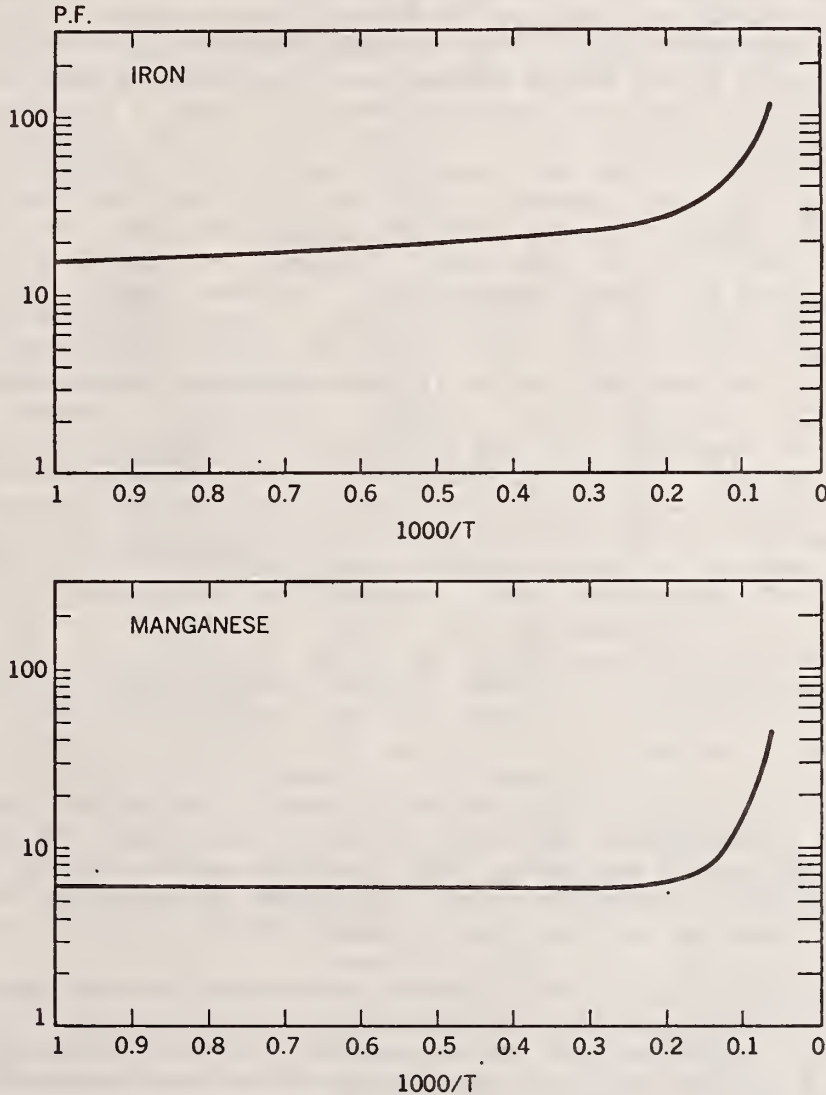
Before discussing the negating evidence for the LTE model, it would be well to analyze the inherent accuracy of the equations and constants being used in our calculations (CARISMA) to test the model. Table III lists the physical constants required to solve the LTE equations according to our particular approach (CARISMA), their source in the literature [4], and an estimate of the accuracy with which each constant is known.

CONSTANTS FOR ANALYTICAL CALCULATIONS		
PARAMETER	COMMENTS	SOURCES
ISOTOPIIC COMPOSITION	ACCURACY <1 — 5%	F. A. WHITE (1968)
IONIZATION POTENTIAL (IP)		
• ELEMENT	ACCURACY <1 — 15%	SAMSONOV (1968)
• OXIDE	FOR 25 ELEMENTS ONLY	VEDENEYEV (1966) AND OTHERS
• DIOXIDE	FOR 13 ELEMENTS ONLY	"
PARTITION FUNCTION (B)		
• NEUTRAL ATOM	FOR 72 ELEMENTS, <7000° K	DeGALAN (1968)
AND	FOR 25 ELEMENTS, >7000° K	DRAWIN AND FELENBOK (1965)
POSITIVE ION	(Fe, >7000° K)	SPARKS AND FISCHEL (1971)
• MONOXIDE	ASSUMED EQUAL TO ATOM VALUE	
MONOXIDE		
• ROTATIONAL CONSTANT (B_0^2)	FOR 78 ELEMENTS	ROSEN (1971) and EXTRAPOLATION
• VIBRATIONAL CONSTANT (ω^2)	"	"
• STATISTICAL WT. GROUND STATE (g^0)	"	"
• DISSOCIATION ENERGY (V_0^2)	" (ACCURACY 5-30%)	ROSEN (1971) AND OTHERS
DIOXIDE DISSOCIATION ENERGY	ACCURACY 10-30%	VEDENEYEV (1966)
ELECTRON AFFINITY (EA)	ACCURACY ~1 - 20%	VEDENEYEV (1966), SAMSONOV (1968), PAGE AND GOODE (1969), GRAY (1965), AND OTHERS
STATISTICAL WT. ATOM GROUND STATE	NOT PRESENTLY USED	

TABLE III: Physical constants used in CARISMA, their limitations and sources.

The most important part of the correction applied to the positive ion intensities of most elements is that given by equation 4 which predicts the ratio of the number of singly charged positive ions to neutral atoms of an element. In fact for the purposes of illustration in figure 1, the positive ion intensities corrected for the atomic concentration of the elements have been plotted as a function of equation 4 only, and the molecular oxide and negative ion contributions have been neglected. Generally, the molecular oxide and negative ion

corrections become significant only at lower temperatures and at higher values of the electron density respectively. Equation 4 depends on the ionization potential of the neutral atom and on the internal partition functions of the singly charged positive ion and of the neutral atom. In this respect, the limitations imposed by the available physical constants set the maximum upper limit of our program (CARISMA) at 17000°K, mainly because of a lack of the partition functions of the neutral atoms of the elements at higher temperatures.



STEIGER AND RUDENAUER (1974)

FIGURE 7: Partition functions of the neutral atoms of iron and manganese as a function of temperature (ref. 34).

The second most important part of the correction to be applied to test the LTE model involves the calculation of the number of metal atoms that appear as molecules (generally as oxides when bombarding with oxygen) rather than as atoms. The remaining parts of the correction, *i.e.* for negative ions and for dioxide molecules, are usually not of significant proportions and are discussed in more detail in reference 4.

An illustration of this problem is given in figure 7, taken from Steiger and Rüdener [34], where the partition functions of the neutral atoms of Fe and Mn are shown as functions of temperature. The partition functions vary only slowly in the low temperature range (<5000°K) but change rapidly in the higher temperature range where we generally work. We use partition functions that have been calculated as functions of ΔE by Drawin and Felebok [35], wherever possible, and extrapolate their data to 17000°K, if their data are not given in this temperature range. For most of the other elements we use partition functions from De Galan *et al.* [36]. Their data stop at 7000°K and we use the ratio of the partition functions of the singly charged to neutral atom at this temperature for all higher temperatures. For some elements such as U and Th, we have to be satisfied with a single value for this ratio established at 5000°K [37]. The effect of these limitations on the accuracy of the computed results is unknown because the inaccuracies in the partition functions are unknown. The effect, however, scales directly in magnitude and is probably considerable for some of the elements that are in the group known only in the low temperature region.

In addition to the internal partition functions the other important constant required in the calculation of equation 4 is the ionization potential of the neutral atom. An example of the variability that can be found in the literature for what might be thought to be a well established physical parameter is given in Table IV. The reported ionization potential of U is seen to have varied by about 25 percent in the last ten years. Errors in the ionization potential scale exponentially (see equation 3) and can lead to very large errors in the calculation of the positive-ion to atom ratio (10 percent error can result in a change by a factor of two or more). We (CARISMA) have been using the 1968 Samsonov [38] value in our calculations. The appearance of the value by Avni and Klein [39] questions the validity of that choice and possibly bears on some of the errors we have experienced with our U and Th analysis, as will be discussed shortly.

As stated above, the molecular oxide terms are only important at lower temperatures and high concentrations of oxygen. This correction is mainly influenced by the exponential dissociation energy term of equation 8. The dissociation energies and molecular constants of the neutral monoxide molecules of most of the elements can be found in the literature. The accuracies of these data, however, are quite variable and lead to variable accuracies in the final calculations. The dissociation energies and the vibrational, rotational and electronic constants used for the neutral monoxide molecules are generally taken from a compilation on diatomic molecules by Rosen [40] supplemented mainly by data from Gaydon [41]. In general, many of the ionization

THORIUM AND URANIUM IONIZATION POTENTIAL

SOURCE	Th	U
*Avni and Klein (1973)	7.5 + 0.3 eV	6.3 + 0.3 eV
Mann (1964)		6.11 + 0.05
Bakulina and Ionov (1959)		6.08 + 0.08
DeMaria (1960)		5.4 + 0.3
Gingerich and Lee (1964)		4.9
Samsonov (1968)	6.95	5.65

*Spectrochimica Acta, 28B, p. 331.

TABLE IV: Variation in the ionization potentials of Th and U found in the literature.

potentials of the neutral monoxide molecules are missing. To overcome this situation the final correction equation in CARISMA [4] has been written so as to be independent of the ionization potential of the molecule. In order to accomplish this, however, the rather drastic approximation is made that the dissociation constants of the positive and negative molecular ions are equal to those of the neutral molecules. The errors generated by these assumptions are discussed more fully in reference 4 but generally lead to errors of unknown magnitude in the final correction. The errors could be large, however, because of their exponential dependence. With these inadequacies in the test procedure in mind we can proceed to examine the negating evidence for LTE.

IV. NEGATING EVIDENCE FOR LTE

There are three lines of observational data which indicate that the sputtering assemblage of electrons, ions, atoms, and molecules are not in local thermal equilibrium or at least not in exact LTE. These are:

1. Apparent Non-Equilibrium of Heavy Molecular Oxide Components

As was discussed in reference 4, the group of elements that have the largest molecular oxide components tend to show significant errors in their calculated concentration values when corrected according to our LTE (CARISMA) model. This is shown in figure 8 where CARISMA-corrected ion microprobe results for several elements of this group are shown compared to the "true" values established by several other analytical techniques [4]. The heavy lines represent a perfect one-to-one correspondence and each line has its own concentration scale as indicated. The samples analyzed are coded in the legend. As illustrated, the general result is that the ion microprobe results are too small compared to the true values, *i.e.* at the temperature required by the lighter atomic ion data CARISMA predicts the ratio of monoxide molecular components to elemental components for the elements illustrated in figure 8 that are much smaller than what are actually

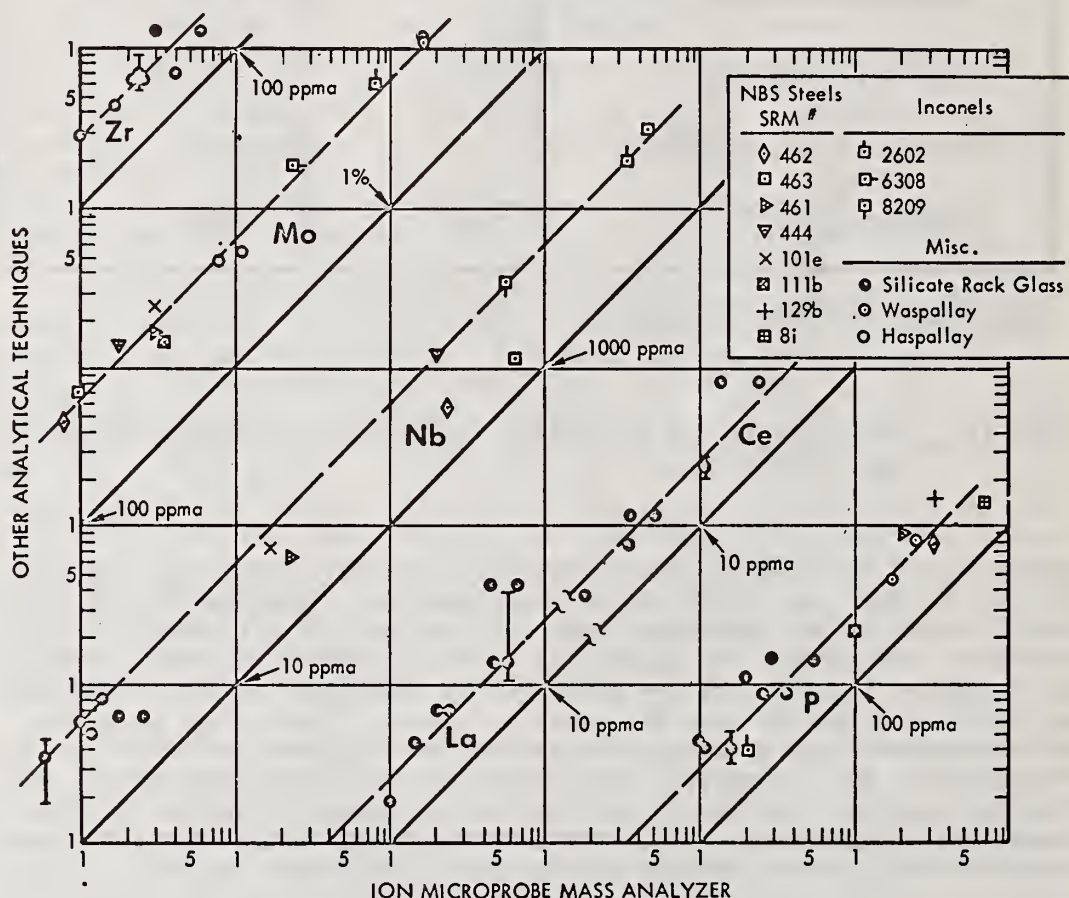


FIGURE 8: Comparison of the analyses using the LTE model (CARISMA) with those of other analytical techniques for Zr, Mo, Nb, La, Ce and P in metal and silicate matrices.

observed in the mass spectra. The observed intensities of the molecular oxide ions of the heavy atomic weight elements of high oxygen affinity, in fact, often exceed the intensities of their component metallic atomic ions.

Our preliminary results [4] indicated that the errors, although of unknown origin, were constant in many different samples as shown by the dashed line in figure 8. Recent work, however, indicates that this simple conclusion is probably not valid. It now appears that the errors found for a particular element can be quite variable. This is best demonstrated by looking at an extreme case. The errors of largest

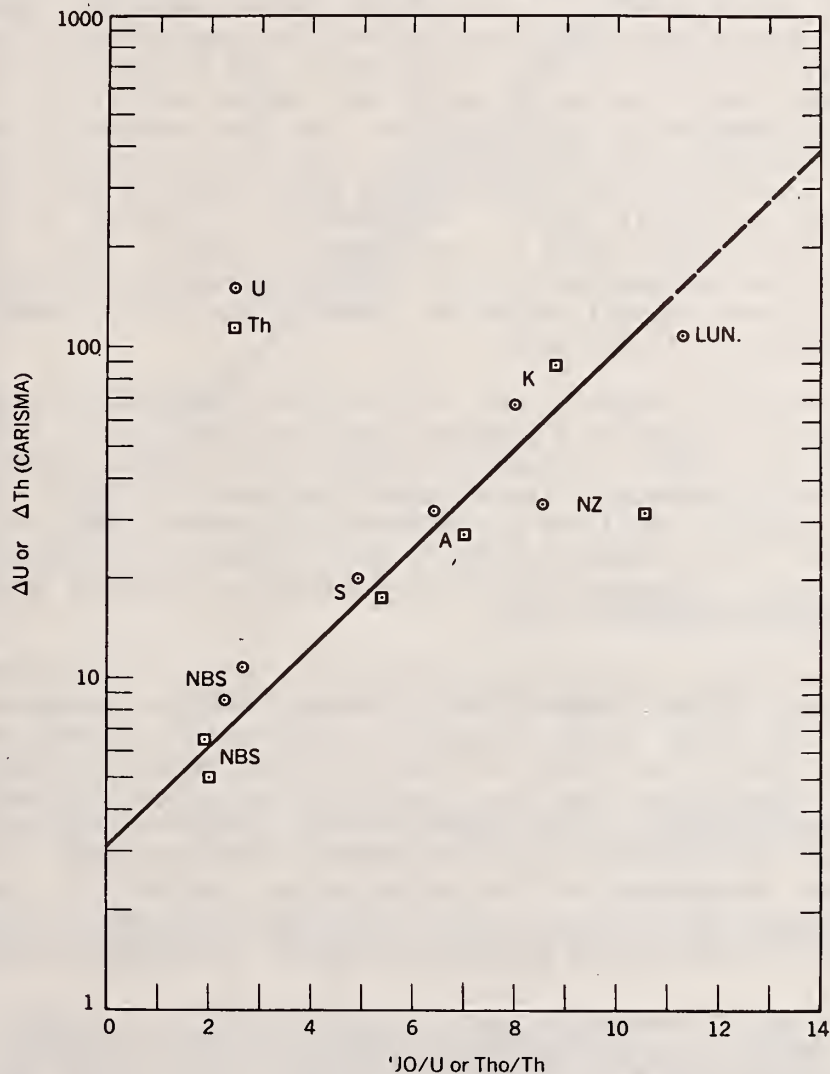


FIGURE 9: Error factors by which the LTE model (CARISMA) derived U and Th concentration values must be multiplied to obtain the true values as a function of the observed UO^+/U^+ and ThO^+/Th^+ ratios.

magnitude encountered using our LTE (CARISMA) model are found for U and Th. Figure 9 shows the errors recently determined for these elements in a set of zirconolite mineral samples [42] and in the NBS glass standard SRM 612. The factors (ΔU or ΔTh) by which the CARISMA calculated concentration value must be multiplied to obtain the true concentration, are plotted versus the observed UO/U or ThO/Th ion ratios respectively. The molecular oxide to atomic ion ratio, MO/M, is chosen because it represents an internal thermometer that can be used to judge the temperature of the sputtering assemblage [4]. These results indicate that as the temperature decreases (increasing MO/M ratio), the error increases. The generally good correspondence of the errors with the MO/M ratio, which is directly observed in the mass spectrum, leads to an extremely simple empirical correction that has been effectively used to quantitatively analyze uranium in radiometric age dating work [43]. It is apparent that the errors can be very large; much larger, in fact, than can be generated by possible errors in the ionization potential such as discussed in Table IV (*i.e.*, changing the uranium ionization potential from 5.65 to 6.3 decreases the error factor by only about 20 percent in a typical case). The effects of errors in the other constants discussed in Table III are probably equally small, but the effect of the assumption as to the equivalence of the positive and negative ion and neutral molecular oxide dissociation constants is unknown and may be significant.

The errors, however, are not instrument dependent (assuming the instrument is operated in a standard analytical mode) as is illustrated in figure 10. Figure 10 shows the CARISMA error factors determined for the rare earth elements by two different operators [44] using the same set of standards [45] and two different ion probes (IMMA) of the same manufacture. It is apparent that the error factors are essentially the same in each laboratory for these elements as indicated by the solid one-to-one correspondence line.

As mentioned earlier, the molecular oxide ions are expected to be most important at low temperatures, assuming a constant concentration of oxygen. The large oxide components observed in the mass spectrum, therefore, lead to the conclusion that the heavy molecular oxides are at a lower temperature than are the lighter atoms and electrons of the sputtering assemblage. It is possible to calculate this apparent lower temperature by assuming that the total observed error is in the temperature dependence of the dissociation constant of the heavy molecule (see equation 8). This was done for the set of zirconolite mineral and NBS glass data discussed above and the results are given in Table V.

In Table V, T_e represents the CARISMA temperature determined from the ion intensity data of the major elements, ΔU and ΔTh are the errors in the U and Th analyses at that temperature, and T_g is the temperature required for the molecule in order to obtain the true U or Th concentration. ΔT is the apparent temperature drop of the heavy molecule. It can be seen that the relative temperature decrease ($\Delta T/T_e$) is fairly constant in these samples, showing less than a 30 percent

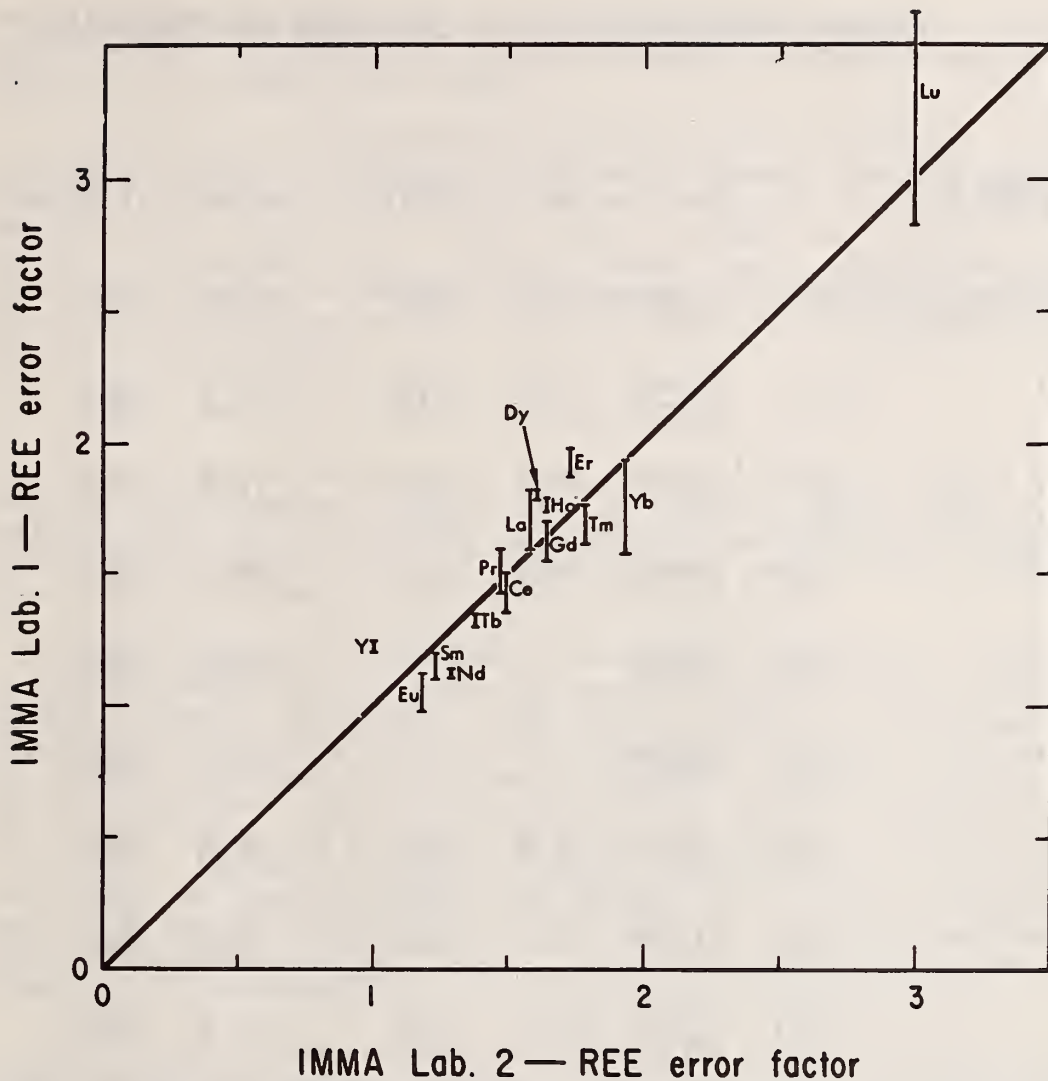


FIGURE 10: Error factors for the rare-earth elements derived by two different ion microprobe laboratories (ref. 44).

total variation (standard deviation of 10 percent or less) although the error factors, themselves, range over factors of ten.

At present, it is not known if this improvement is fortuitous or actually indicates a lower temperature for the heavy molecular oxides. The errors seem to be related only to the heavy atoms that have large oxide molecules such as U and Th and those elements mentioned in reference 4. Pb which has nearly the same mass as U has only a small molecular oxide and a very much smaller error. The error also generally decreases with atomic weight. Significant errors only begin to appear

TEMPERATURE DIFFERENCE OF ELECTRONS AND MOLECULES

SAMPLE		T_E	ΔU	$\Delta T/T_E$	ΔT_H	$\Delta T/T_E$
ZIRCONOLITE(K)		11960	66.8	.540	87.8	.507
"	(A)	13720	31.9	.519	27.1	.461
"	(S)	14200	20.2	.500	17.5	.444
"	(NZ)	14500	33.4	.517	31.3	.476
"	(5A)	12960	-	-	28.9	.452
"	(5C)	11520	-	-	27.0	.427
"	(6B)	13900	34.8	.511	34.9	.496
"	(7A)	11160	40.4	.453	35.1	.418
"	(7C)	12180	36.1	.474	27.5	.450
"	(8A)	10000	-	-	27.7	.380
NBS	(GCE)	13640	8.7	.447	5.00	.380
"	(H)	15480	10.9	<u>.470</u>	6.48	<u>.380</u>
				0.492±.032		0.437±.048

TABLE V: Error factors for Th and U in several LTE-corrected mineral analyses listed with their CARISMA temperatures (T_e) and the possible reduction in the temperature (ΔT) required to obtain the true analysis.

around atomic number 40 and above. The lighter molecular oxides generally have the temperature (T_e) established by CARISMA for the atoms and ions of the sample, see figure 3.

Finally, it is possible that the observed errors are related to the abnormally large energy spreads (up to several hundred electron volts) observed [46] to be associated with the metallic atomic ion component of these molecular oxides. The large energy spreads may result in a physical discrimination by the ion probe itself against the total integrated intensity of the atomic ion species, or may indicate a second ion generating process that is not controlled by LTE. More work is in progress on this subject.

2. Apparent Non-Equilibrium of Multiply Charged Ions

The LTE model appears to fail in its ability to predict the observed ratio of multiply charged ions to singly charged ions and, possibly, also in its ability to predict the correct ratio of singly charged ions to neutral atoms for those elements which have a large first ionization potential, *e.g.*, fluorine ($I_p=17.4$ eV).

An illustration of this behavior for multiply charged ions is given in figure 11 where data collected from several analyses of three similar silicate minerals are shown. This graph is similar to that given in figure 1 and is actually a plot of the Saha-Eggert ionization equation. The ratios of the singly charged ions to neutral atoms modified by their partition functions are plotted versus the first ionization potential of the element ($\Delta E = 0.55$ eV) using the method described in the discussion of figure 1. The doubly charged to singly charged ion ratios (++) and the triply to doubly charged ion ratios (+++) are those actually observed in the mass spectra. They are modified by their partition functions and are plotted versus the second and third ionization potentials of the element ($\Delta E = 1.10$ and 1.65 eV, respectively).

The slope of the line on such a plot gives the temperature of the assemblage and the absolute position of the line gives the electron density. It can be seen that the slopes of the two lines drawn through the singly and doubly charged ratio data are identical, within experimental uncertainty, but that the doubly charged data lie above the singly charged data. This indicates that, although the doubly charged ions are at essentially the same temperature as the singly charged ions and neutral atoms, they exist in a region of approximately 50 times lower electron density. This result was noted earlier [4] and leads to a problem in directly using the observed ratios of doubly to singly charged ions of a pair of elements for obtaining the electron density appropriate to the sputtered singly charged ions and neutral atoms. The electron density is too low by a rather large, but seemingly constant, factor. As can be seen in figure 11, the triply charged data appear to be at even a lower electron density.

The reason for this apparent violation of LTE is not understood at present. Possibly it is related to the relative velocities of the

different charged species and the probability for an electronic transition between the ion and the surface. In the mode of analysis used to acquire the data of figure 11, a positive bias of about 1500

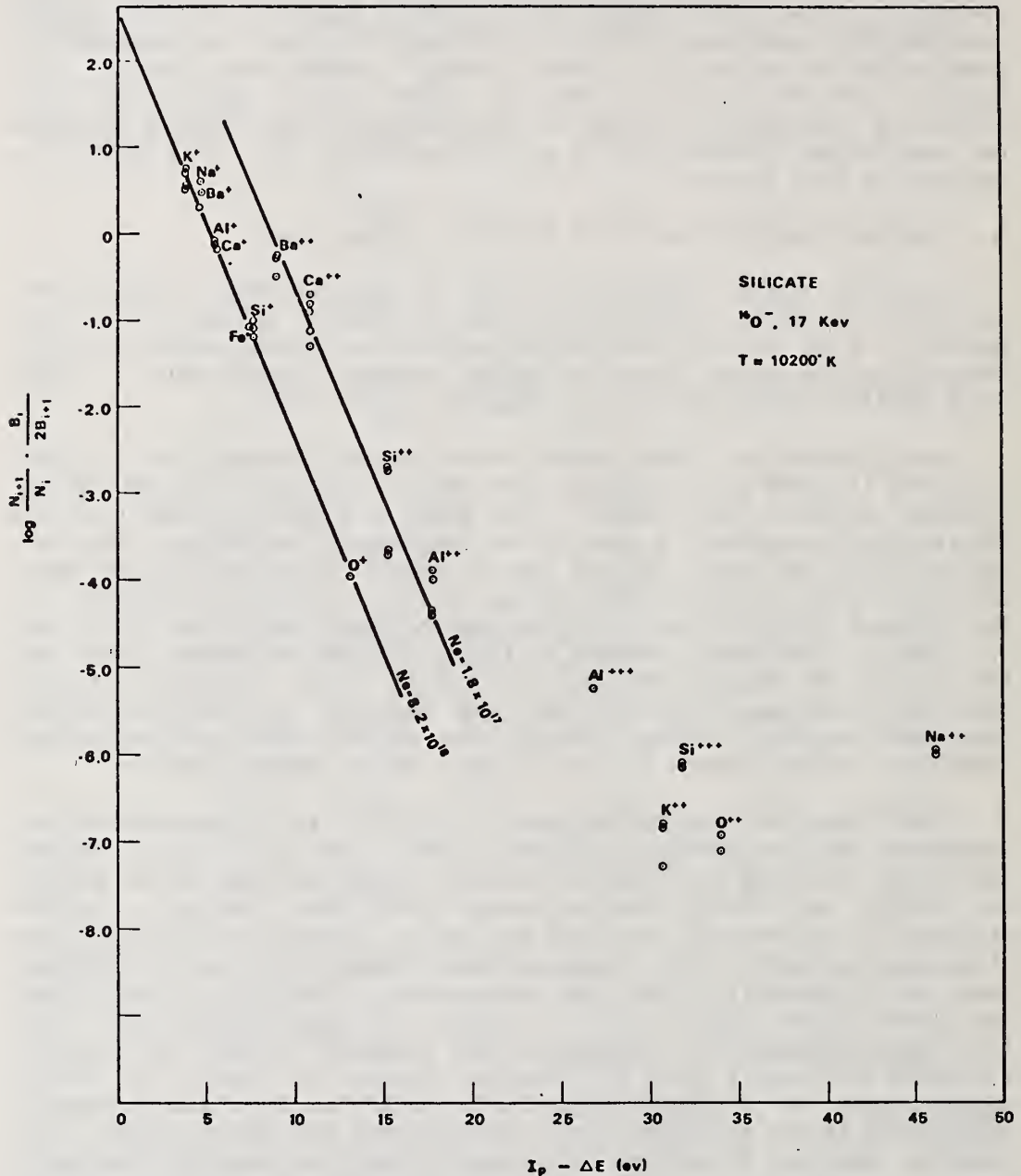


FIGURE 11: Saha-Eggert ionization equation applied to singly, doubly, and triply charged positive ions sputtered from silicate standard with $^{16}\text{O}^+$ at 17 keV.

volts is applied to the surface of the sample. According to the discussion of van der Weg and Rol [47] this could lead to a greater probability of escape without an electronic transition to a given distance from the surface of the sample for the multiply charged ions of an element because of their larger velocities in the applied field. The observed data would then indicate that an electron density gradient exists which decreases away from the positively charged surface of the sample.

It is also quite possible that some completely different mechanism controls the production of the majority of the multiply charged ions. This possibility is consistent with the observations of Joyes [48] who notes a strong kinetic character in the emission of Al^{++} and Al^{+++} but only a very small kinetic character in the emission of the low energy Al^+ ions which, of course, represent the great majority of the sputtered Al ions.

Figure 11 also shows that the data for doubly-charged ions of very high ionization potential appear to be at even lower electron densities. It may also be true that singly-charged ions of high ionization potential, such as fluorine, do not exhibit the same electron density as that shown by the elements of lower ionization potential. Fluorine generally has ion abundances that are too large, sometimes apparently by as much as an order of magnitude or more, with respect to the ion abundances of the lower ionization potential elements in the same sample. The reason for this is not understood and more work needs to be done.

We are presently performing our quantitative analysis of the high ionization potential elements by using working curves constructed from many different samples of the same general chemistry [49]. This approach must be carefully checked when a substantially different sample composition is analyzed. For example, Hinthorne [50] showed that the slope of the fluorine working curve changed by 30-40 percent between silicates and phosphates. The working curves are also very instrument-dependent and extreme care should be taken when attempting to transfer so-called sensitivity factors between instruments of different design. For example, the slope of the F working curve ($F^+/P^+ \times P\%$ versus $F\%$) in a phosphate matrix was found to be 6.5 in an Applied Research Laboratories Ion Microprobe Mass Analyser (IMMA) [50] and 0.136 in a CAMECA Ion Microscope (IMS) [8].

3. Non-Maxwellian Energy Distribution of the Sputtered Ions

The LTE model also appears to fail when the energy distributions of sputtered particles are considered. The particles of a thermal equilibrium assemblage are expected to exhibit a Maxwellian energy distribution characterized by a common temperature. An example of the observed energy distributions of singly charged Al and Si ions sputtered from a glass sample is given in figure 12 [51]. The long, high energy tails observed do not appear to be Maxwellian in character and the energy distributions are found to have different shapes for two

different elements from the same sample. The peaks of the energy distributions are also found to be at fairly high values (~ 6 eV) compared to the temperatures calculated for these ions using the LTE model.

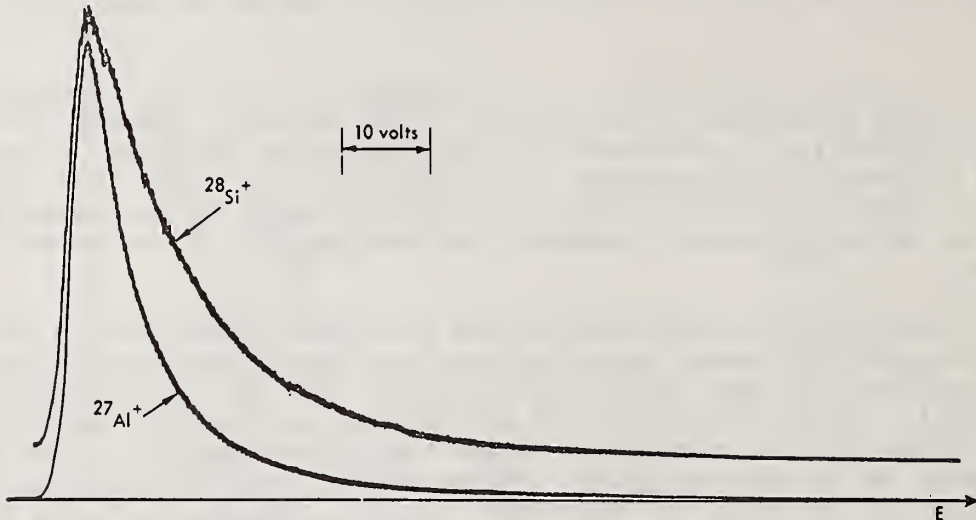


FIGURE 12: Energy distributions of positive aluminum and silicon ions sputtered from a glass standard with $^{16}\text{O}^-$ at 8 keV (ref. 51).

In general, the lower sputtered-ion energies (< 20 eV), which contain the great majority of the sputtered ions, can be fit to a Maxwellian energy distribution. The temperature coefficients of these distributions are, however, very large ($\sim 7 \times 10^4$ K in the present example). In fact, Maxwellian energy distributions for low-energy sputtered ions have been reported by Stanton [52] and by Coswell and Smith [53]. Secondary electrons generated under ion bombardment also display energy distributions that contain the majority ($> 95\%$) of the electrons in the low energy region (< 20 eV) [54].

The higher-energy ions, however, are observed to deviate from the Maxwellian distributions by a generally continuously increasing factor as energy increases. Sometimes small bumps are noticed in the very high energy regions of the distributions [55]. The reasons for these deviations are not understood at present, but have been ascribed by Stanton [52] to a changing amplitude function in the Maxwellian distribution and used by Jurela [55] as evidence for a second mechanism for the generation of sputtered ions.

It is obvious that much more work needs to be done in this area for a proper understanding of the meaning of the energy distributions. It should be remembered that these charged particles exist in the presence of a static electric field and its effect on the overall shape of the energy distribution curves must be taken into account [56]. Another important modifying influence on the shape of the energy distribution curve may be the potential barrier at the surface of the sample, or the binding energy of the atom to the surface of the sample, which must be overcome in order for the atom to be sputtered [57,58].

V. POSSIBLE PHYSICAL MECHANISM

An obvious question to be asked at this point is whether or not there is a physical mechanism that can possibly explain the apparent LTE conditions postulated in this work. The most likely candidate for this purpose would appear to be the thermal spike model originated by Seitz and Koehler [59] and discussed by Thompson and Nelson [60] and Vinegard [61]. A thermal spike is pictured as a local volume of a target crystal wherein the majority of the atoms are temporarily in motion as the result of an atomic collision cascade initiated by the process of high energy ion bombardment. To satisfy our data requirements we would imagine this collision cascade as intersecting the surface of the sample. The phenomenon of thermal spikes has been used to interpret sputtering data [62,63] and has also been proposed by Jurela [14] to be the possible source of the high temperatures encountered in his model of secondary sputtered ion emission.

An exhaustive review of thermal spike theory will not be made here, but rather the predictions of a recent preliminary theoretical study by Sigmund [64] will be used to examine its possible application to our data. Sigmund's study predicts the time constant of the spike, the lifetime of the cascade (the slowing down time of the projectile atom), and the effective maximum energy density (energy per atom) within the spike as functions of the energy and mass of the bombarding ion beam and the mass of the target sample. An important conclusion drawn by Sigmund is that a tendency towards local thermal equilibrium exists in the spike which is dependent on how much the time constant of the spike (τ) exceeds the lifetime of the cascade (τ_0). These times and the effective energy per atom have been calculated according to Sigmund's model [64] and the results are given in Table VI.

Table VI lists experimental data obtained from silicate standard samples ($Z \approx 10$) bombarded with $^1\text{H}^-$, $^{18}\text{O}^-$, and $^{35}\text{Cl}^-$ and from a heavy metal standard (Waspalloy, $Z \approx 29$) bombarded with $^{18}\text{O}^-$, all at 15 keV. The LTE temperatures obtained from these data according to CARISMA are listed for comparison with effective energies per atom and the times calculated according to Sigmund's model. It is obvious that the calculated spike energy approaches that predicted by the LTE model only in the case of the heavy matrix. The very light bombarding ion (H) would appear to result in only a very small value for the effective energy per atom compared to that apparently predicted by the LTE model.

THERMAL SPIKE PARAMETERS*

15 KEV	TIME CONSTANT	CASCADE LIFETIME		MAX. ENERGY DENSITY	TEMP. SPIKE	TEMP. CARISMA
ION/SAMPLE	T (SEC)	To (SEC)	T/To	E (EV)	T(°K)	T(°K)
¹ H/SILICATE	2.4×10^{-9}	3.7×10^{-14}	6.5×10^4	.002	23	14160
¹⁸ O/SILICATE	5.7×10^{-11}	1.2×10^{-13}	4.8×10^2	.05	580	14500
³⁵ CL/SILICATE	2.3×10^{-11}	1.7×10^{-13}	1.4×10^2	.10	1160	14300
¹⁸ O/WASPALLOY	1.0×10^{-11}	1.2×10^{-13}	8.3×10^1	.52	5990	8500

*P. SIGMUND, APPL. PHYS. LETT., 25, 169, 1974, (USING $m = 1/3$).

TABLE VI: Comparison of LTE (CARISMA) temperatures with the effective maximum energy density per atom, the atomic cascade lifetime, and the thermal spike time constant derived from Sigmund's model (ref. 64).

These calculations were made using $m = 1/3$ in the elastic scattering power potential [64]. The calculation of the effective energy per atom is very sensitive to the choice of this exponent and although it is probably a good choice for low keV oxygen bombardment [65], it may not apply as well to bombarding ions or targets of greatly different mass.

The time constant of the spike according to this model is generally on the order of 10^{-11} seconds and exceeds the lifetime of the cascade by about two orders of magnitude. This is about 100 periods of atomic vibration and would appear to be within the range where concepts of thermal equilibrium have some validity [66]. The calculated time constant for the H gas bombardment experiment is exceedingly long which may be related to the problem of the choice of the power potential exponent discussed above.

Another important conclusion from Sigmund's model is that the effective energy per atom in the spike should decrease in a simple linear relationship with increasing bombarding ion energy. This unsuspected inverse relationship was observed earlier in the data given in Table I. Experiments performed by bombarding a silicate (andesine) and a heavy matrix (Waspalloy) with ¹⁸O⁻ ion beams of different energy had previously yielded data which the LTE model interpreted to be

decreasing temperatures with increasing bombardment energy. These data are given in Table VII as a function of the true bombarding beam potential (the primary accelerating potential plus 1.5 kV of additional extraction potential at the sample).

<u>keV</u>	<u>ANDESINE</u> <u>eV/Å (z=0)</u>	<u>T_{CARISMA}</u> <u>°K</u>	<u>WASPALLOY</u> <u>eV/Å (z=0)</u>	<u>T_{CARISMA}</u> <u>°K</u>
9.5	35.2	16740	36.5	14940
12.5	31.6	14280	33.8	12360
15.5	28.1	14640	31.2	9260
17.5	25.7	13560	29.4	7760
19.5	23.4	11480	-	-

TABLE VII: Comparison of LTE (CARISMA) temperatures with the energy lost in the surface of samples bombarded at different keV using the data of figures 14 and 15 (ref. 68).

The data are plotted in figure 13 as an inverse function of the bombarding ion energy according to the model of Sigmund [64]. The general correlation is apparent.

Earlier, T. Ishitani and his colleagues used their Monte Carlo simulation program [67] to calculate the energy loss of the bombarding oxygen beam with depth in the sample for andesine and Waspalloy as a function of energy [68]. These simulations are shown in figures 14 and 15. It is instructive to note that the relative difference of the deposited energy at some depth in the sample (such as, for example, that associated with the mean of the energy loss distribution with energy) does not reflect the observed CARISMA temperature differences. This is especially obvious in the Waspalloy data where the two sets of data actually trend in the opposite manner. It is the energy losses in the first collisions at the very surface that reflect the trend of the CARISMA temperatures. This again indicates that the hot zone we are sampling involves only the uppermost surface layers of the sample. In order to illustrate this, the energy losses at ρZ equal to zero depth were taken from the figures and are listed in Table VII (the units of eV/Å were chosen for convenience). The data are also plotted in figure 16. The correlation of the CARISMA temperatures with the energy deposited in the surface layer according to a Monte Carlo simulation is apparent.

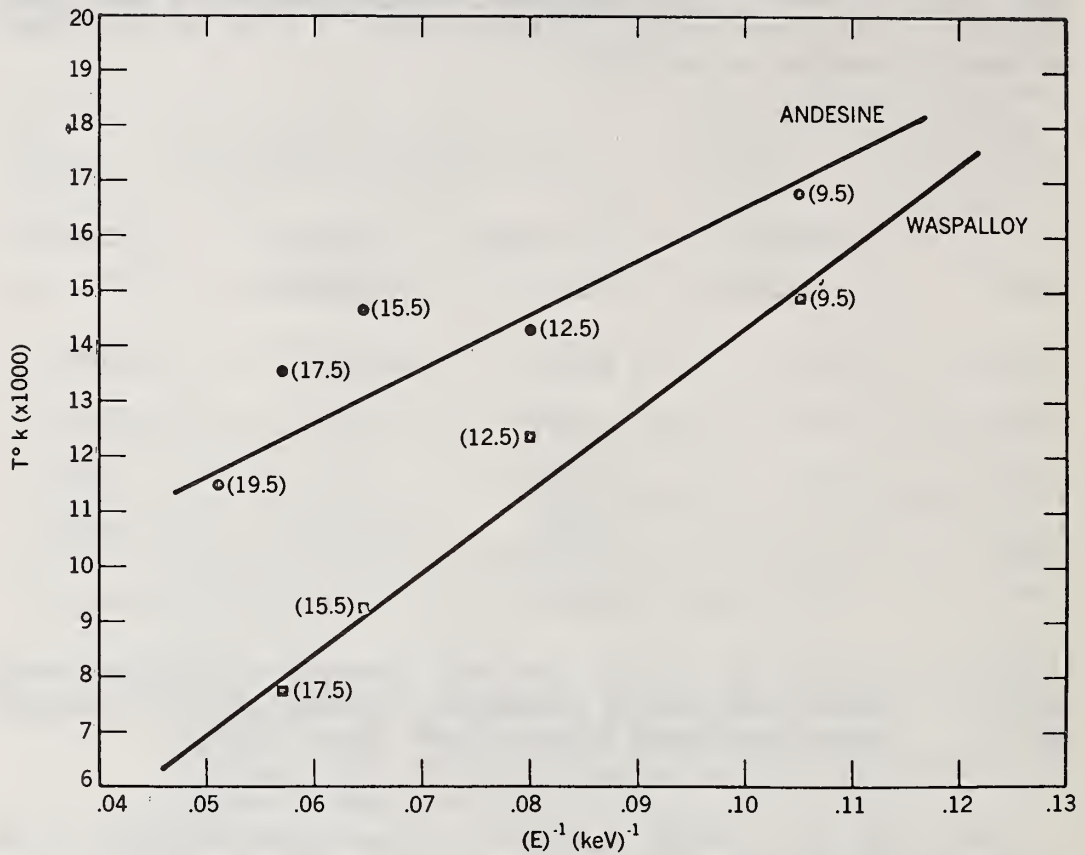


FIGURE 13: LTE (CARISMA) derived temperatures for a silicate (andesine) and heavy metal alloy (Waspalloy) bombarded with $^{18}\text{O}^-$ at different energies as a function of the inverse of the bombarding beam accelerating potential.

It would appear that there is some hope of interpreting the apparent high temperatures indicated by the LTE model through either the thermal spike model directly or a computer simulation of the energy loss of the bombarding ion beam and the dissipation of this energy among the affected atoms.

VI. CONCLUSION

In conclusion it can be said that there is a good deal of experimental evidence that a simple model based on the concept of local thermal equilibrium of the sputtering assemblage can be used to interpret sputtered ion yields with good accuracy. The practicality of the model for quantitative elemental analysis of a wide variety of

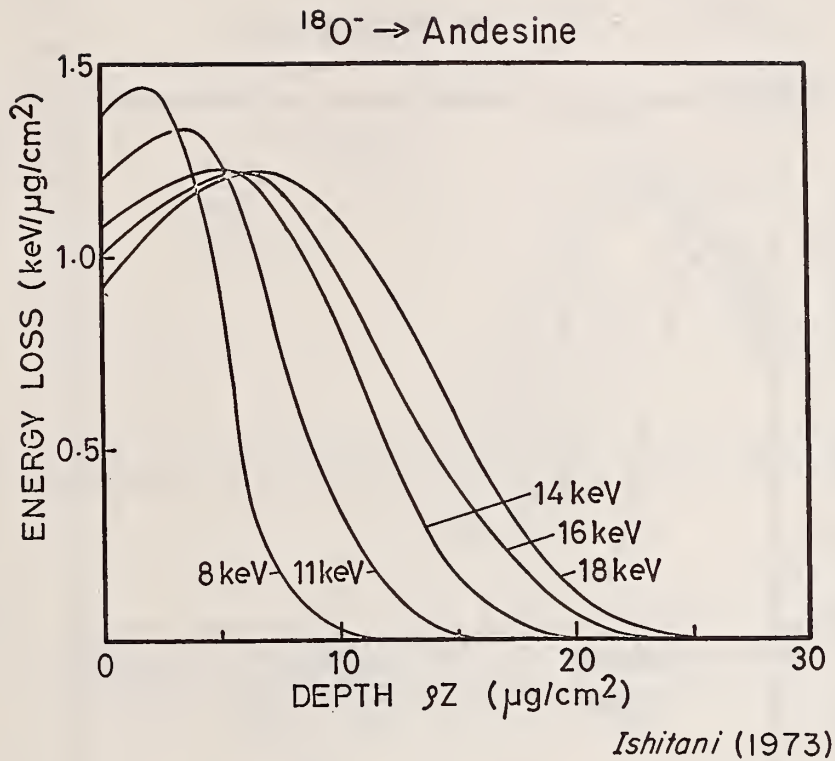
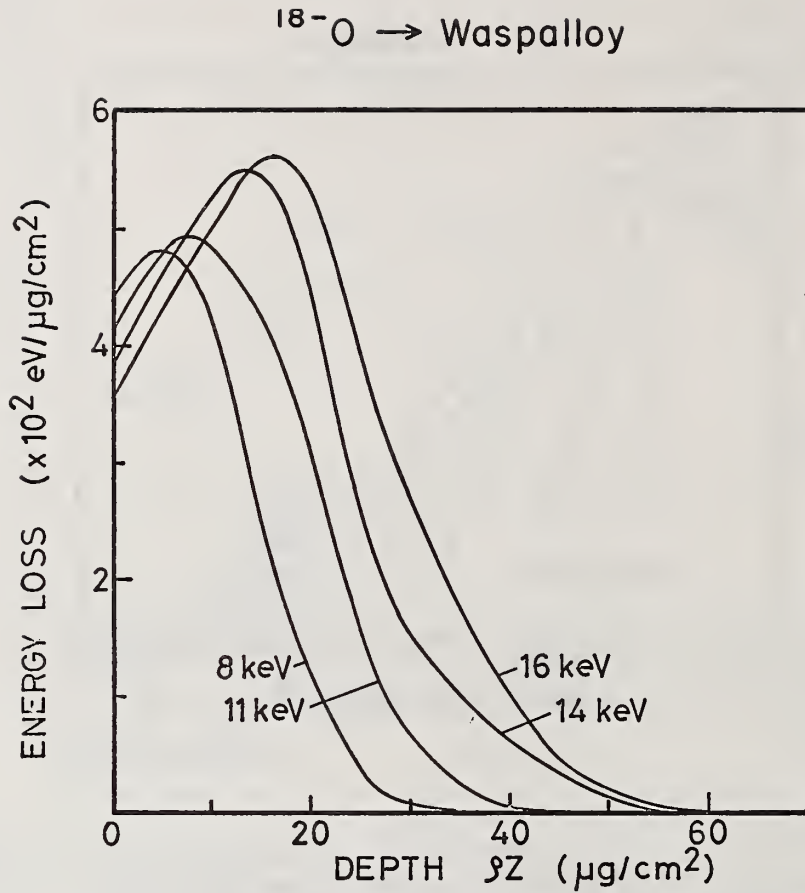


FIGURE 14: Monte Carlo simulation of the energy loss of a bombarding $^{18}\text{O}^-$ beam as a function of depth in andesine for different energies (ref. 68).

samples with many different instrument designs is generally confirmed. The physical basis of the model, however, is very much an area of speculation with the particular aspects of the very high temperatures predicted, possibly exceeding the critical temperature [69] of the sample [14b], and of the establishment of equilibrium between the atoms and the electrons being questions of particular concern.



Ishitani (1973)

FIGURE 15: Monte Carlo simulation of the energy loss of a bombarding $^{18}\text{O}^-$ beam as a function of depth in Waspalloy for different energies (ref. 68).

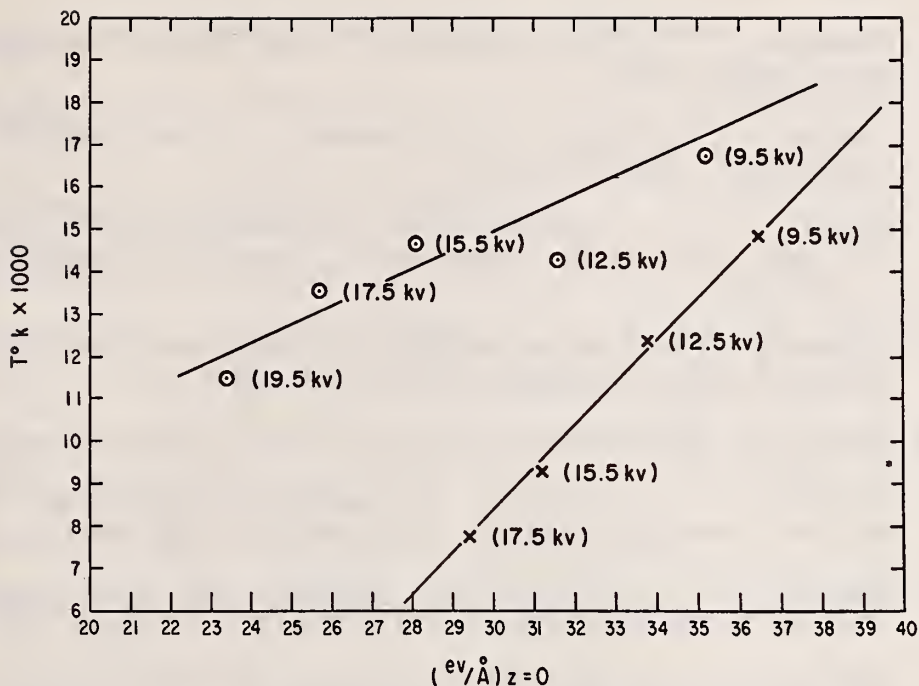


FIGURE 16: Energy loss ($\text{eV}/\text{Å}$) at the surface ($\rho z=0$) of samples using data given in figure 14 and 15 as functions of the LTE (CARISMA) derived temperatures.

VII. REFERENCES

1. Andersen, C. A., Third Natl. Electron Microprobe Conf. Chicago, IL, 1968; *Int. J. Mass Spectrom. Ion Phys.* 2, 61 (1969).
2. Andersen, C. A., Fourth Natl. Electron Microprobe Conf. Pasadena, CA, 1969; *Int. J. Mass Spectrom. Ion Phys.* 3, 413 (1970).
3. Andersen, C. A., Fifth, Sixth, and Seventh Natl. Electron Microprobe Conf. New York, 1970; Pittsburgh, 1971; San Francisco, 1972.
4. Andersen, C. A. and Hinthorne, J. R., *Analytical Chem.*, 45, 1421 (1973).
5. Saha, M. N., *Phil. Mag.*, 40, 472 (1920); *Z. Phys.*, 6, 40 (1921); and Eggert, J., *Z. Phys.*, 20, 570 (1919).
6. Shimizu, R., Ishitani, T. and Ueshima, Y., *Jap J. Appl. Phys.*, 13, 250 (1974).

7. Rüdener, F. G. and Steiger, W., Proc. 6th Intl. Vacuum Cong., Kyoto, Japan, 1974.
8. Lodding, A., Gourgout, J. M., Petersson, L. G. and Frostell, G., Z. Naturforsch., 29a, 897 (1974).
9. Meyer, C., Jr., Anderson, D. H., and Bradley, J. G., Proceedings 5th Lunar Science Conf., Supplement 5, Geochim. et Cosmochim. Acta, 1, 685 (197).
10. Schroerer, J., Workshop on Secondary Ion Mass Spectrometry, National Bureau of Standards, Gaithersburg, 1974, paper 6.
11. Simons, D., University of Illinois (Urbana), private communication.
12. Lovering, J. F., Workshop on Secondary Ion Mass Spectrometry, National Bureau of Standards, Gaithersburg, 1974, paper 8.
13. Bradley, J. G., Workshop on Secondary Ion Mass Spectrometry, National Bureau of Standards, Gaithersburg, 1974, paper 4.
14. Jurela, Z., (a) Radiation Effects, 13, 167 (1972) and (b) Int. J. Mass Spectrom. Ion Phys., 12, 33 (1973).
15. Boumans, P. W. J. M., *Theory of Spectrochemical Excitation*, Plenum Press, N. Y., 1966, p. 80.
16. Herzberg, G., *Molecular Spectra and Molecular Structure, I. Spectra of Diatomic Molecules*, D. van Nostrand, Princeton, N. J., 1950, pp. 123, 125, 467.
17. Almen, O., and Bruce, G., Nucl. Instr. Methods, 11, 257 (1961).
18. Andersen, C. A., Hinthorne, J. R., Eighth Natl. Electron Microprobe Conf., New Orleans, 1973.
19. Langmuir, I., and Kingdon, K. H., Proc. Royal Soc., A107, 61 (1925).
20. Dekker, A. J., *Solid State Physics*, Prentice-Hall, Englewood Cliffs, N. J., 1962, p. 220.
21. Shankland, T. J., Science, July, 51 (1968).
22. Haas, G. A., and Thomas, R. E., *Measurement of Physical Properties*, Ed. E. Passaglia, Interscience Publ., N. Y., 1972, p. 91.
23. Hermann, G., and Wagener, S., *The Oxide Coated Cathode*, Chapman and Hall, London, 1951, Vol. 2, p. 74.
24. Snoek, C., van der Weg, W. F., and Rol. P. K., Physica, 30, 341 (1964).

25. Tsong, I. S. T., Phys. Stat. Sol.(a), 7, 451 (1971).
26. White, C. W., Simms, D. L., and Tolk, N. H., Science, 177, 481 (1972).
27. Tolk, N. H., Simms, D. L., Foley, E. B., and White, C. W., Radiation Effects, 18, 221 (1973).
28. Kerkdijk, C., and Thomas, E. W., Physica, 63, 577 (1973).
29. Thomas, G. E., and de Kluizenaar, E. E., Le Vide, 167, 190 (1974).
30. Tsong, I. S. T., and McLaren, A. C., Nature, 248, 43 (1974).
31. Kato, M., Shimizu, R., and Ishitani, T., Techn. Reports of Osaka Univ., 24, No. 1199, 451 (1974).
32. Kerkow, H., Phys. Stat. Sol.(a), 10, 501 (1971).
33. Shimizu, R., Kato, M., and Ishitani, T., Jap. J. Appl. Phys., 13, 1477 (1974).
34. Steiger, W., and Rüdener, F. G., J. Mass Spectrom. Ion Phys., 13, 411 (1974).
35. Drawin, H. W., Felenbok, P., *Data for Plasmas in Local Thermodynamic Equilibrium*, Gautheir-Villars, Paris, 1965.
36. De Galan, L., Smith, R., and Winefordner, J. D., Spectrochim. Acta, 23B, 521 (1968).
37. Corlin, C. H., J. Astrophys. 136, 916 (1962).
38. Samsonov, G. V., *Handbook of the Physicochemical Properties of the Elements*, IFI/Plenum, N. Y., 1968, p. 20.
39. Avni, R., and Klein, F. S., Spectrochim. Acta, 28B, 331 (1973).
40. Rosen, B., *Spectroscopic Data Relative to Diatomic Molecules*, Pergamon Press, N. Y., 1970.
41. Gaydon, A. G., *Dissociation Energies and Spectra of Diatomic Molecules*, 3rd ed., Chapman and Hall, London, 1968.
42. Lovering, J. F., Dept. Geology, Univ. Melbourne, Australia. Personal communication.
43. Hinthorne, J. R., Andersen, C. A., and Conrad, R. L., to be submitted to Geochimica et Cosmochimica Acta (1975).
44. Lovering, J. F., In press, Comments on Earth Sciences: Geophysics (1975).

45. Duke, M. J., Center for Volcanology, Univ. Oregon, Eugene, Oregon. Personal communication.
46. Fralick, R. D., and Roden, H. J., Applied Research Laboratories, Goleta, CA, personal communication.
47. van der Weg, W. F., and Rol, P. K., Nucl. Instr. Methods, 38, 274 (1965).
48. Joyes, P., Radiation Effects, 19, 235 (1973).
49. Hinthorne, J. R., and Andersen, C. A., Am. Mineral., 60, 143 (1975).
50. Hinthorne, J. R., 26th Pittsb. Conf. on Analytical Chem. and Appl. Spect., Cleveland, 1975.
51. Roden, H. J., Fralick, R. D., 26th Pittsb. Conf. on Analytical Chem. and Appl. Spect., Cleveland, 1975.
52. Stanton, H. E., J. Appl. Phys., 31, 678 (1960).
53. Cowell, G. K., and Smith, H. P., Jr., J. Appl. Phys. 43, 412 (1972).
54. Lonchet, F., Viel, L., Benazeth, C., Fagot, B., and Colombie, N., Radiation Effects, 14, 123 (1972).
55. Jurela, Z., *Ion Surface Interaction, Sputtering and Related Phenomena*, Eds. R. Behrisch, W. Herland, W. Poschenrieder, P. Staib and H. Verbeek, Gordon and Breach Science Publ., London, 1973, p. 161.
56. Blaise, G., and Slodzian, G., Revue de Physique Appliquée, 8, 105 (1973).
57. Miyagawa, S., J. Appl. Phys., 44, 5617 (1973).
58. Harrison, D. E., Jr., Moore, W. L., Jr., and Holcombe, H. T., Radiation Effects, 17, 167 (1973).
59. Seitz, F., and Koehler, J. S., *Solid State Physics*, Eds. F. Seitz and D. Turnbull, Academic Press, N. Y., 1956, Vol. 2, p. 305.
60. Thompson, M. W., and Nelson, R. S., Phil. Mag., 7, 2015 (1962).
61. Vineyard, G. H., Faraday Soc. London, Discussion, 31, 7 (1961).
62. Anderson, H. H., and Bay, H. L., Radiation Effects, 19, 139 (1973).
63. Kelly, R., and Lam, N. Q., Radiation Effects, 19, 39 (1973).

64. Sigmund, P., Appl. Phys. Letters, 25, 169 (1974).
65. Sigmund, P., H. C. Orsted Institute, Copenhagen, personal communication.
66. Dienes, G. J., and Vineyard, G. H., *Radiation Effects in Solids*, Interscience Publ., N. Y., 1957, p. 36.
67. Ishitani, T., Shimizu, R., and Murata, K., Jap. J. Appl. Phys., 11, 125 (1972); and Phys. Stat. Sol.(b), 50, 681 (1972).
68. Ishitani, T., and Shimizu, R., Dept. of Appl. Phys., Osaka Univ., Osaka, Japan, personal communication.
69. Gates, D. S., and Thodos, G., A. I. Ch. E. Journal, 6, 50 (1960) and D. A. Young and B. J. Alder, Phys. Rev. A, 3, 364 (1971).

1. The first part of the document discusses the importance of maintaining accurate records of all transactions.

2. It is essential to ensure that all entries are supported by proper documentation and receipts.

3. Regular audits should be conducted to verify the accuracy of the records and identify any discrepancies.

4. The second part of the document outlines the procedures for handling cash and credit transactions.

5. All cash receipts should be recorded immediately and deposited in a secure bank account.

6. Credit sales should be recorded at the time of sale, and the corresponding receivables should be tracked.

7. The third part of the document provides guidelines for managing inventory and stock levels.

8. Inventory should be counted regularly to ensure that the recorded quantities match the actual stock.

9. The fourth part of the document discusses the importance of maintaining accurate financial statements.

10. These statements should be prepared on a regular basis and reviewed by management to assess the company's financial health.

11. The fifth part of the document outlines the procedures for handling payroll and employee benefits.

12. Payroll records should be maintained accurately, and all payments should be made on time.

13. The sixth part of the document discusses the importance of maintaining accurate tax records.

14. All tax-related documents should be organized and retained for the required period.

15. The final part of the document provides a summary of the key points and emphasizes the importance of consistent record-keeping.

AN OUTLINE OF SECONDARY ION EMISSION MODELS

Juergen M. Schroeer

Department of Physics
Illinois State University
Normal, Illinois 61761

I. Types of Models

The models for the emission of secondary ions can be classified as follows:

A. Emission of Atomic Ions:

1. Thermodynamic Models

- a) Saha-Langmuir
- b) Andersen-Hinthorne
- c) Jurela

2. Quantum-mechanical Models

- a) Schroeer
- b) Sroubek
- c) Van der Weg and Bierman, Benninghoven
- d) Joyes (Paris group)
- e) Rüdener *et al.*
- f) MacDonald

B. Emission of Molecular Ions:

- a) Benninghoven (dissociation) and Slodzian (chemical ionization)
- b) Valence model of Plog, Wiedman, and Benninghoven
- c) Fingerprint model of Werner

II. Definitions

Total sputtering yield:

$$S = \frac{(M^+) + (M^*) + (M^0) + (M^-) + \text{molecules}}{(A^+)}, \quad (1)$$

where +, -, and 0 refer to the charge of the sputtered particle, * is excited neutral, M is the sputtered metal atom, A⁺ is the bombarding ion, and (M⁺) is the number of sputtered positive metal atoms, etc.

Secondary ion yield:

$$S^+ = \frac{(M^+)}{(A^+)} \quad (2)$$

Probability of ionization:

$$R^+ = \frac{(M^+)}{(M^+) + (M^*) + (M^0) + \dots} = \frac{S^+}{S} . \quad (3)$$

If we make the simplifying assumption that we are dealing with a matrix m of a single element, in which various impurities i with concentrations c_i are dissolved, then the apparent secondary ion yield for the impurities is

$$Y_i^+ = c_i S_i^+ = c_i S_m R_i^+ . \quad (4)$$

In (4) we made the further assumption, that after equilibrium has been reached, the total sputtering yield for the impurities is the same as for the matrix atoms, *i.e.*, $S_i = S_m$. Also,

$$Y_m^+ = c_m S_m R_m^+ = S_m R_m^+ , \quad (5)$$

since $c_m \sim 1$. So,

$$c_i = \frac{R_m^+ Y_i^+}{R_i^+ Y_m^+} = \frac{Y_i^+}{R_{rel}^+ Y_m^+} . \quad (6)$$

The spectroscopist measures the Y 's, and wants the c 's. He needs to know R_{rel}^+ .

III. Langmuir-Saha Equation [1]

The Langmuir-Saha equation

$$R^+ \propto \exp \left(- \frac{I - \phi}{kT} \right) , \quad (7)$$

where I is the ionization energy and ϕ the work function, holds if we have thermal equilibrium between a surface at temperature T and the evaporated atoms, ions and electrons. Equation (7) is applicable to thermal desorption, but does not work for sputtering.

IV. Model of Andersen and Hinthorne [2]

The model assumes a plasma "at the surface" where there is local thermal equilibrium between atoms, ions and electrons, such as



The equilibrium constant is described by the Saha-Eggert equation

$$\frac{(M^+) N_e}{(M^0)} = (2\pi m_e k T)^{3/2} \frac{2 B^+(T)}{B^0(T)} \exp\left(-\frac{I - \Delta E(N_e, T)}{kT}\right), \quad (9)$$

where T is the plasma temperature, B the partition functions (tabulated in the literature), ΔE the reduction in the ionization energy due to the plasma, N_e the electron concentration, and m_e the electron mass. This model works very well for the bombardment of alloys and minerals with oxygen or other reactive gases at energies around 10 keV. $T \sim 5000$ to $15,000$ K. T and N_e are fitting parameters. [3] $R^+(\text{rel})$ can be calculated [2,4] from (9). If $(M^+) \ll (M^0)$, then

$$R^+(\text{rel}) = \text{constant} \frac{B_i^+(T)}{B_i^0(T)} \exp\left(-\frac{I_i}{kT}\right). \quad (10)$$

V. Model of Jurela [5]

Jurela uses the Dobretsov equation which deals with surface ionization through non-equilibrium thermodynamics:

$$R^+ = \frac{B^+(T)}{B^0(T)} \exp\left(-\frac{I_c - \phi}{k T}\right), \quad (11)$$

where T is the local surface temperature, and $I_c = I - \Delta I$. ΔI is the image potential energy at a critical distance from the surface, which is approximately equal to one-half of a lattice constant. The model was tested by bombarding many pure elements with 8 and 40 keV argon ions. Solving for the temperature, he found values between 2000 and

5000 K, which he feels are more reasonable than the temperatures in the model of Andersen and Hinthorne.

VI. Model of Schroeer

He assumes that the sputtered atoms leave the surface in a neutral, unexcited state and are subsequently ionized by a quantum-mechanical transition of the atoms' valence electrons to the top of the conduction band of the metal. The ionization probability is calculated using the adiabatic approximation, giving

$$R^+ = \left[\frac{A}{I - \phi} \right]^2 \left[\frac{\hbar v}{a (I - \phi)} \right]^n, \quad (12)$$

where A is the surface binding energy of the sputtered atom, \hbar is Planck's constant divided by 2π , v its velocity, n a fitting parameter (~ 2.5), a is about one-half the surface layer thickness and is used as a fitting parameter ($\sim 1.5 \text{ \AA}$). The model has been tested with reasonable success [4,6,7] by bombarding pure metals with 12 keV argon ions. Limited success has been obtained for the analysis of alloys. [8]

VII. Model of Sroubek [9]

Sroubek's basic approach is the same as Schroeer's, but he makes use of molecular orbital calculations to evaluate the quantum-mechanical transition probabilities. Depending on the mathematical approximations made, he obtains

$$R^+ \approx \left[\frac{A}{I - \phi} \right]^2 \left[\frac{\hbar v}{a (I - \phi)} \right]^2, \quad (13)$$

or

$$R^+ \sim \frac{3}{2\pi} \left[\frac{\hbar v}{a (I - \phi)} \right]^3 \quad (14)$$

When he considers the possibility of level crossings between the electron levels of the solid and those of the sputtered atom, then

$$R^+ \sim \left[\frac{\hbar v}{a(I - \phi)} \right]^{1/2} \quad (15)$$

Experimental tests are very limited so far. [9]

VIII. Model of van der Weg and Bierman, [10] and Benninghoven [11],

They assume that the sputtered particle leaves the surface as an ion and is subsequently neutralized by electrons from the solid through resonance tunneling and Auger transitions,

$$R^+ \sim \exp\left(-\frac{ca}{v}\right), \quad (16)$$

with $a \approx 2 \text{ \AA}$, $c \approx 4 \times 10^{14} \text{ sec}^{-1}$. This was tested for the excitation of Cu under 80 keV argon bombardment. [10]

IX. Model of Joyes *et al.* [12]

They assume that the atoms are sputtered as neutrals, but with an inner electron excited to an outer electron shell. Upon de-excitation, the available energy is given to a valence electron which is ejected (this is called auto-ionization). The mathematics is very complex; tests have been limited so far to the bombardment of a few transition elements by argon. [13]

X. Model of Rüdener *et al.* [4,14]

They take Schroeer's ionization model, combine it with Sigmund's sputtering theory, and apply it to the secondary ion emission from alloys.

XI. Model of MacDonald [15]

He finds an empirical expression for $R^+(v)$ by measuring $S^+(v)$ and $S(v)$ separately:

$$R^+(v) = S^+(v)/S(v), \quad (17)$$

where v is the velocity of the sputtered atom. He feels that the experimental results are consistent with the assumption that we have auto-ionization from an excited state, at least, for the sputtering of Cu by 10 keV argon.

XII. Molecular Ions

Atomic and molecular ions can be produced through the breaking of bonds of chemical compounds on the surface: dissociative [11] or chemical [16] ionization. The secondary ion spectrum depends on the atomic and molecular species present on the surface, and on the condition of the surface, such as its state of oxidation.

The empirical valence model of Plog *et al.* [17] quite successfully accounts for the relative intensities of ions in series such as M^+ , MO^+ , MO_2^+ , etc., emitted from oxidized metal surfaces and from oxides.

The fingerprint model of Werner [18] tries to explain the secondary ion spectrum of an unknown surface (such as oxidized Cr) as a superposition of the secondary ion spectra characteristic of known compounds (such as Cr_2O , Cr_2O_2 , Cr_3O , etc.).

XIII. Acknowledgements

Financial support through a Faculty Research Award from Illinois State University is gratefully acknowledged. A sabbatical leave at the Physikalisches Institut der Universität Münster made me aware of some very recent work, which I could therefore include in this written summary:

XIV. References

- [1] Dresser, M. S., J. Appl. Phys. 39 (1968) 338, Zemel; J., J. Chem. Phys. 28 (1958) 410.
- [2] Andersen, C. A. and Hinthorne, J. R., Anal. Chem. 45 (1973) 1421.
- [3] Shimizu, R., Ishitani, T. and Ueshima, Y., Jap. J. Appl. Phys. 13 (1974) 250.
- [4] Rüdener, F. G., Steiger, W. and Portenschlag, R., Mikrochimica Acta (Wien), Suppl. 5 (1974) 421.
- [5] Jurela, Z., Int. J. Mass Spectr. and Ion Phys. 12 (1973) 33.
- [6] Schroer, J., Rhodin, T. and Bradley, R., Surface Science 34 (1973) 571.
- [7] Wittmaak, K., - "Energy Dependence of the Secondary Ion Yield of Metals and Semiconductors," to be published.
- [8] Schroer, J., Vacuum 22 (1972) 603.
- [9] Sroubek, Z., Surface Science 44 (1974) 47.

Ion Emission Models

- [10] Van der Weg, W. F. and Bierman, D. J., *Physica* 44 (1969) 177 and 206.
- [11] Benninghoven, A., *Z. Physik* 220 (1969) 419.
- [12] Joyes, P., *J. Physique* 29 (1968) 774, and 30 (1969) 243 and 365, Castaing, R. and Hennequin, J.-F., *Adv. in Mass Spectrometry* 5 (1971) 419, and Joyes, P., *Radiation Effects* 19 (1973) 235.
- [13] Blaise, G. and Slodzian, G., *J. Physique* 31 (1970) 93.
- [14] Gries, W. and Rüdener, F. G., "A Quantitative Model for the Interpretation of Secondary Ion Mass Spectra of Dilute Alloys," to be published in *Int. J. Mass Spectrometry and Ion Physics*.
- [15] MacDonald, R. J., *Surface Science* 43 (1974) 653.
- [16] Castaing, R. and Hennequin, J.-F., *Adv. in Mass Spectrometry* 5 (1971) 419 and Slodzian, G. and Hennequin, J.-F., *Compte rendus heb. des séances Acad. Sci. (Paris) Serie B* 263 (1966) 1246.
- [17] Plog, C., Wiedmann, L. and Benninghoven, A., "Empirical Model for the Calculation of Secondary Ion Intensities from Oxidized Metal Surfaces and Metal Oxides," to be published in *Surface Science*.
- [18] Werner, H. W., de Grefte, H. A. M. and van den Berg, J., *Adv. in Mass Spectrometry* 6 (1974) 673.

The first part of the report deals with the general situation of the country and the progress of the war. It is noted that the war has been a long and hard one, and that the country has suffered greatly. The report then goes on to discuss the various departments of the government and the work they have done during the year.

The Department of the Interior has been particularly busy, and has done much to improve the condition of the public lands. It has also been successful in securing the passage of several important laws.

The Department of the Army has also done much to improve the condition of the army, and has been successful in securing the passage of several important laws.

The Department of the Navy has also done much to improve the condition of the navy, and has been successful in securing the passage of several important laws.

The Department of the Treasury has also done much to improve the condition of the treasury, and has been successful in securing the passage of several important laws.

The Department of the State has also done much to improve the condition of the state, and has been successful in securing the passage of several important laws.

The Department of the War has also done much to improve the condition of the war, and has been successful in securing the passage of several important laws.

The Department of the Justice has also done much to improve the condition of the justice, and has been successful in securing the passage of several important laws.

The Department of the Education has also done much to improve the condition of the education, and has been successful in securing the passage of several important laws.

The Department of the Agriculture has also done much to improve the condition of the agriculture, and has been successful in securing the passage of several important laws.

The Department of the Commerce has also done much to improve the condition of the commerce, and has been successful in securing the passage of several important laws.

The Department of the Labor has also done much to improve the condition of the labor, and has been successful in securing the passage of several important laws.

The Department of the Public Health has also done much to improve the condition of the public health, and has been successful in securing the passage of several important laws.

The Department of the Social Welfare has also done much to improve the condition of the social welfare, and has been successful in securing the passage of several important laws.

The Department of the Veterans Affairs has also done much to improve the condition of the veterans affairs, and has been successful in securing the passage of several important laws.

The Department of the Indian Affairs has also done much to improve the condition of the Indian affairs, and has been successful in securing the passage of several important laws.

The Department of the Insular Affairs has also done much to improve the condition of the insular affairs, and has been successful in securing the passage of several important laws.

The Department of the Territories has also done much to improve the condition of the territories, and has been successful in securing the passage of several important laws.

The Department of the District of Columbia has also done much to improve the condition of the district of Columbia, and has been successful in securing the passage of several important laws.

The Department of the District of Columbia has also done much to improve the condition of the district of Columbia, and has been successful in securing the passage of several important laws.

EMPIRICAL QUANTITATION PROCEDURES IN SIMS

J. A. McHugh

General Electric Company
Knolls Atomic Power Laboratory
Schenectady, New York 12301

The secondary ion yield is very sensitive to the state of the surface, the matrix, and the effects induced by the primary ion beam. Therefore, the ratio of secondary ion intensities of an element from various points on a surface is not always a measure of relative element concentration. Caution must be exercised especially when interpreting ion images of the surface. Such a case is illustrated in the ion micrographs of a nickel base alloy [1] shown in figure 1. The Ni, Fe, and Cr content of each grain is the same, yet the absolute ion yield of an element shows considerable variation (as much as a factor of 3). The variation is brought about by effects dependent on the chemical nature and the crystal structure of the material, and the relative orientation of the grains in the plane of the surface; such effects are primary ion channeling, radiation-induced recrystallization, differences in the concentration of implanted oxygen and differences in the angular distribution of secondary ions ejected from the various grain orientations. The relative changes in ion intensity between grains are approximately equal for all elements, and if the intensities are referenced to the ion intensity of a major constituent at each point, the differences between grains are reduced or eliminated. One concludes from observations of this type that any quantitation procedure is better based on relative ion yields from a point of analysis rather than on an absolute yield.

The precision or reproducibility of relative ion yield measurements by SIMS is quite satisfactory (< 5 percent, under controlled conditions). It would not be worthwhile to attempt quantitation of SIMS data if reasonable precision did not exist. Considering the complexity of secondary ion emission and the basic differences in SIMS instruments, it is difficult to envision a purely theoretical model applicable to all SIMS instruments, samples and analysis conditions. For example, SIMS instruments do not collect all the secondary ions produced at the sample, nor do they transmit the same representative fraction of ions. This results from inherent differences in transmission efficiency as a function of secondary ion initial energy. Therefore, any practical quantitation approach must reduce variables to a minimum and be adaptable to any SIMS instrument. The most straightforward approach is an empirical method.

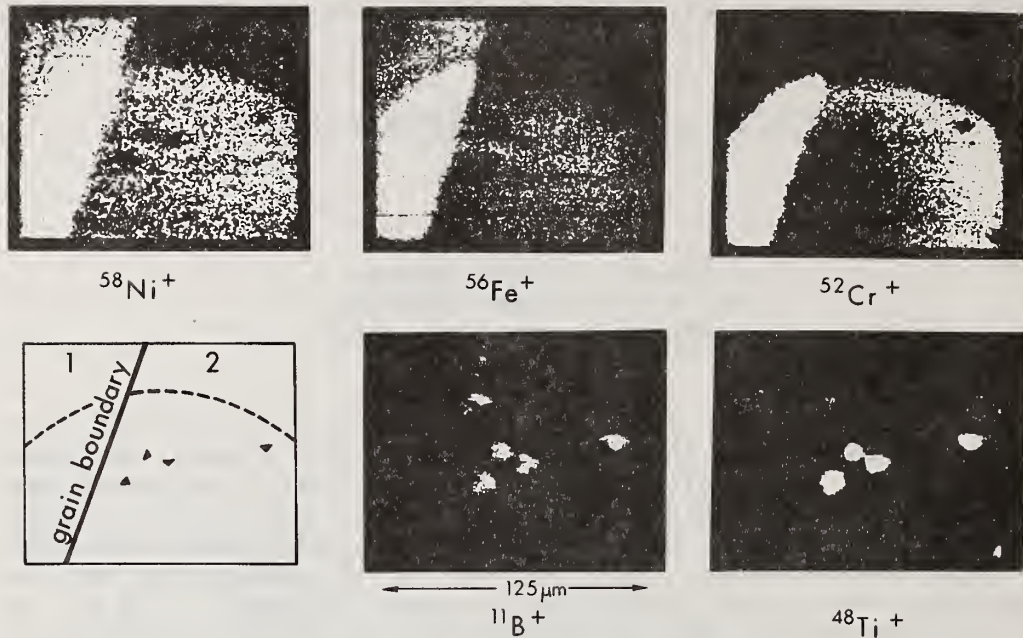


Figure 1 Ion micrographs from a grain boundary region of an Inconel sample that previously had been bombarded with a large-diameter 18.5 keV $^{16}\text{O}^-$ beam (periphery of the bombarded region is shown by the dotted line in the figure, along with the position of the grain boundary -- the solid line, and the Ti-rich inclusions -- the small triangles). Enhanced secondary ion emission is noted from grain 1 compared to grain 2. (From McHugh [1])

The basic ingredients of a useful empirical method are:

1. A set of homogeneous standards representing a wide variety of matrix types,
2. Standardized instrument operating conditions.
3. Relative elemental sensitivity factors (S_A) derived from standards, and
4. Methods to extend S_A to other matrices.

Empirical Quantitation

The foundation of any empirical method is a set of good standards which represent a variety of matrix types. The standards must be homogeneous on a micro-scale and should not be susceptible to surface and bulk element fractionation caused by sputtering and ion implantation effects. To achieve success with a quantitation method based on calibration with standards, it is important to standardize instrument operating parameters — primary ion species, energy and current density, sample environment, detector efficiency, and the energy band-pass of the secondary ion analyzer. Once one fixes these conditions, meaningful sample analyses are possible with relative elemental sensitivity factors derived from standards of the same or similar composition to the sample.

The relative elemental sensitivity factor, S_A , is defined by the following equation:

$$S_A = \frac{i_A^+ C_A^{-1}}{i_{\text{ref}}^+ C_{\text{ref}}^{-1}} \quad (1)$$

where i_A^+ = secondary ion signal for element "A" (sum of all isotopic components)

C_A = atomic concentration of element "A"

S_A = relative elemental sensitivity factor for element "A."

The relative ion yields from a standard are normalized to a common reference element. The secondary ion signals of an element "A" and the reference element are divided by their respective atomic concentrations in the standard to provide a common concentration base for comparison.

Once a set of relative elemental sensitivity factors, S_A , has been generated, the measured secondary ion signals of the unknown sample of similar composition to the standards can be reduced to relative atomic concentration by employing the following relationship.

$$(i_A^+ / i_{\text{ref}}^+) S_A^{-1} = C_A / C_{\text{ref}} \quad (2)$$

The absolute ion signals or relative ion signals, when divided by S_A , form a set of values proportional to the atomic concentration of the element in the sample. The set of relative atomic concentrations can be normalized to 100 percent and the result will be the composition of the matrix in atomic percent provided the SIMS instrument is operating

at a sensitivity sufficient to detect all major constituents of the matrix. In a well-behaved matrix, quantitative accuracies of 10 percent can be achieved with this approach. However, such an approach places great demands on the standards and on sample homogeneity.

A standard for every matrix that one could encounter is an unreasonable requirement. Therefore, empirical methods are needed to extend and adjust sensitivity factors from a few known standards to any desired matrix. The sensitivity factor will show a dependency on a parameter (let us call it ϵ_S) that characterizes the electronic properties of the secondary-ion emitting surface. The general behavior of S_A as a function of ϵ_S will follow the pattern shown in figure 2. The type of information given in this figure is derived from standards that differ widely in matrix composition, but possess a common reference element. The simplest approach for defining ϵ_S is to choose two elements that have matrix-sensitive sensitivity factors (e.g., S_1 and S_7 from fig. 2), and let $\epsilon_S = kS_1/S_7$ where k is an arbitrary constant. Other types of information present in the secondary ion spectra that could characterize ϵ_S are the secondary ion ratios M^{++}/M^+ , MO^+/M^+ and MN^+/M^+ . The ratios M^{++}/M^+ and under the proper circumstances MO^+/M^+ and MN^+/M^+ are to a first approximation independent of concentration, and therefore, are the most direct path for establishing ϵ_S for an unknown matrix or surface condition. The practical value of these ratios in defining ϵ_S has not been demonstrated as yet.

Once we obtain the function $S_A(\epsilon_S)$ for all elements we can attempt the quantitation of secondary ion signals from an unknown matrix provided our detection sensitivity is sufficiently high to detect all the major constituents. Our first task is to establish ϵ_S for the matrix or sample being analyzed. This can be done in one of three ways: one method is to use information present in the secondary ion spectra—information such as M^{++}/M^+ , MO^+/M^+ , MN^+/M^+ or any other secondary ion ratio sensitive to ϵ_S . Such a method is the most preferable because no knowledge about sample composition is required; however, at present we lack the needed information to use this method effectively. Another method depends on establishing ϵ_S from the relative ion signals and the known concentration of two or more constituents in the matrix that possess a matrix-sensitive S_A/S_B ratio. This method is quite useful for trace element analyses in a well-characterized matrix. The final method is to choose ϵ_S solely from analytical experience and judgment. Such an approach is not as undesirable as one might expect. At least the extremes are defined and a better estimate of S_A can be obtained (see fig. 2).

The analysis of solids with an oxygen primary ion beam and the methods outlined above have given favorable results. In fact, a single set of sensitivity factors gives accuracies for elemental concentrations much better than a factor of 2 for most elements in a number of quite different matrices— Al_2O_3 and Zr, Fe and Ni base alloys. Therefore, any model that applies a matrix-sensitive correction to relative sensitivity factors could only improve the results. The attractive features of the

Empirical Quantitation

approach described above are: the model is simple, should be applicable to any instrument, is not dependent on theoretical or physical constants, and is based solely on standards and measurements within the instrument.

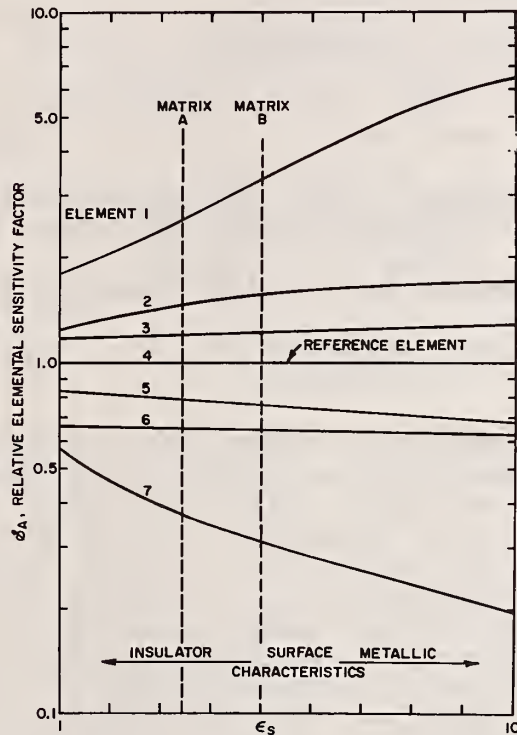


Figure 2 The dependence of the relative elemental sensitivity factor on the character of the sample surface. Information of the type illustrated in this figure can be derived for any SIMS instrument from a set of standard samples. Establishing ϵ_s for a given matrix determined the S_A values required for quantitating relative secondary ion yield data, *e.g.*, compare the set of S_A values for elements 1 through 7 in matrices A and B.

The accuracy of any quantitation procedure not involving a direct sample-standard comparison depends on the susceptibility of the matrix to surface [2-5] and bulk element fractionation caused by sputtering and ion implantation effects. Element fractionation in the primary ion implant zone depends on the characteristics of the matrix, the particular constituent and its mobility, the chemical character of the

implanted primary ion, and the electric field gradients established in the sample from surface charging. SIMS results for many different samples suggest that this problem is not a major threat to analytical accuracy in most situations; nevertheless, there are situations where anomalous effects are observed and fractionation in the implant zone is a reasonable explanation for the effect.

REFERENCES

1. McHugh, J. A. 10th National Meeting Society for Applied Spectroscopy, St. Louis, Mo., Oct. 18-22, 1971 (unpublished).
2. Honig, R. E. in Advances in Mass Spectrometry, West, A. R. Editor, Vol. 6, 337, Elsevier Applied Sciences Publishers, London (1974).
3. Tarng, M. L. and Wehner, G. K. J. Appl. Phys. 43, 2268 (1972).
4. Dahlgren, S. D. and McClanahan, E. D. J. Appl. Phys. 43, 1514 (1972).
5. Feng, H. C. and Chen, J. M. J. Phys. C: Solid St. Physics 7, L75 (1974).

APPLICATION OF SIMS MICROANALYSIS TECHNIQUES
TO TRACE ELEMENT AND ISOTOPIC STUDIES
IN GEOCHEMISTRY AND COSMOCHEMISTRY

J. F. Lovering

Department of Geology
University of Melbourne
Parkville, Victoria, Australia 3052

I. INTRODUCTION

The development of the electron microprobe during the late 1950's provided a powerful tool for rapid, accurate, nondestructive analysis of micrometer-size areas in a wide variety of samples. These unique capabilities of the electron microprobe were soon realized by the chemical geologist and the last decade has seen this instrument revolutionize the fields of analytical petrology and experimental petrology by providing major element analyses of co-existing micrometer diameter phases in geological materials, meteorites and in experimental charges. Perhaps the best demonstration of the microanalytical power of the electron microprobe has been its major contribution to the unprecedented rapid accumulation of basic chemical data on the mineral, rock and glass samples from the lunar surface returned during the Apollo missions. It is fair to say that our current detailed knowledge of the chemical evolution of the lunar volcanic rocks, breccias and soils would simply not have existed if Castaing had not developed the concept of the electron microprobe when he did in 1951.

However the analytical capabilities of the electron microprobe have certain limitations which restrict its ability to contribute basic analytical data to support what many consider to be the next major advances in geochemical and cosmochemical research. These advances promise to develop from trace element partitioning studies between co-existing phases in rocks, meteorites and experimental products. Clearly, more detailed and rigorous understanding of such fundamental petrological problems as the nature and degree of melting involved in magma production, as well as the subsequent differentiation of magmas as they undergo partial crystallization during their ascent, intrusion and storage in magma chambers and final eruption, will depend on an accurate and precise knowledge of the effects of temperature, pressure and composition on the partitioning of trace elements in the ppm and ppb concentration ranges between minerals and their parental melts. Similarly, an accurate knowledge of trace element partitioning and dif-

fusion gradients in minerals in metamorphic rocks is needed to quantify the role of temperature, pressure, fluid pressure and composition in metamorphic processes. Furthermore, trace element partitioning data between the constituent phases of chondrites are needed to provide more precise models for chondrite origins as a function of condensation processes in the primitive solar nebula and subsequent metamorphic processes within parent meteorite bodies.

The problem with the electron microprobe is that analytical sensitivity is limited to around 10^{-15} - 10^{-16} g by the relatively high X-ray continuum background generated along with characteristic X-ray spectra of the constituent elements in the sample. This places a detection limit of around 50 ppm for relatively heavy elements (*e.g.*, Fe) and about 1000 ppm for the lighter elements (*e.g.*, F) in micrometer diameter analysis volumes with the electron microprobe [1]. It should be emphasized that these are simply detection limits, and realistic limits for meaningful trace element determinations by the electron microprobe may be from 2 to 10 times higher.

The electron microprobe is also severely limited in the depth resolution of analysis by the significant penetration of the electron beam into the sample to depths of several micrometers for silicate matrices. This limitation means that the electron microprobe is unsuitable for providing data for another potentially important field of future geochemical research—the nature and composition of ultrathin (ca. 1000Å) intergranular material in rocks and elemental enrichments on crystal surfaces of phases in rocks. Recent work has shown that the migration of hydrothermal fluids exsolved from magmas and also derived from wall rocks around a cooling intrusive probably plays an important role in the two-way exchange of dissolved elements between wall rocks and intrusive with implications both to chemical fractionations during late-stage igneous alteration and the formation of hydrothermal ore fluids. The most reactive sites for the solution of these dissolved elements would be at intergranular surfaces in rocks, and virtually nothing is known at present of the chemical peculiarities of these sites.

A third limitation of the electron microprobe is its inability to detect H and Li and its low sensitivity to the light elements with atomic number below ten. Consequently little is known of the behavior of the light elements during igneous, metamorphic and other geologically important processes. As a particular example of the importance of light element studies in geology, there is a pressing need for an accurate method for the microanalysis of trace amounts of hydrogen in the lattice of minerals usually considered to be anhydrous, since experiments have shown that the deformational properties of these phases can be drastically altered by trace hydrogen in their lattices [2].

In summary, some of the most important advances in chemical geology to be made in the near future require the development of instruments capable of *in situ* microanalysis of micrometer-size phases at elemental abundance levels in the ppm and ppb range, with adequate sensitivity to

cover the analysis of light elements (including hydrogen), and with a depth resolution during analysis of the order of a few hundred angstroms so that it is possible to study the composition of intercrystalline material and the surface chemistry of phases in rocks. All these capabilities are inherent in the analytical technique known generally as secondary ion mass spectrometry (SIMS) which forms the basis of the family of analytical instruments such as the ion microscope of Castaing and Slodzian [3] and the ion microprobe mass analyzer (IMMA) of Liebl [4]. The SIMS technique has the added capability of *in situ* isotopic analysis of micrometer-size phases, opening up the possibility of Rb/Sr and Pb/Pb dating of individual grains of suitable phases in rocks. Clearly the elegant capabilities of the SIMS microanalytical technique, when fully developed, should provide the chemical geologist with a single instrument which approaches the concept of an "ultimate weapon" as far as *in situ* microanalytical capability is concerned. The purpose of this work is to examine the progress to date of the development of SIMS analytical methods for geological materials to see how near the chemical geologist is to realizing his "ultimate weapon."

II. SIMS INSTRUMENTATION AND TECHNIQUES

A detailed history of the development of SIMS instrumentation and a discussion of the pattern of future development has been given by Liebl [5], and Robinson [6] has also discussed the development of ion microprobe instrumentation. The first SIMS instrument with micro-analytical capability was developed by Castaing and Slodzian [3] as a secondary ion emission microscope. In their original instrument, secondary ions sputtered from a sample surface by bombardment with a 0.5 mm diameter beam of argon ions are mass analyzed, and particular ionic species are selected to form an enlarged image of the sample showing the distribution of the selected ionic species within the irradiated area with a spatial resolution of a few microns. Further developments allowed sputtered ion intensities from selected areas in the sample with dimensions of around 2 micrometers to be measured so that quantitative SIMS microanalysis of these areas can be made. This improved instrument is manufactured commercially by CAMECA (France) as the Ion Analyzer IMS 300.

A different design approach was used by Liebl [4] in his development of the ion microprobe mass analyzer (IMMA) as an analogue of the electron microprobe X-ray analyzer in which the electron microprobe was replaced by an ion microprobe and the X-ray analyzer by a secondary ion mass spectrometer. Essentially IMMA involves the production of a focused (minimum 2 micrometers diameter), high-energy beam of ions of a single species to bombard a sample surface selected for microanalysis by means of an optical microscope. The secondary ions sputtered from the sample are extracted and analyzed according to their mass-to-charge ratio in a secondary ion mass spectrometer. A commercial IMMA (fig. 1) based on Liebl's design is manufactured by Applied Research Laboratories (U.S.A.). A similar IMMA-type design approach has been used by Hitachi (Japan) in their IMA-2 instrument and by A.E.I. (United Kingdom) in

their ion microprobe attachment (IM 20) for the MS 702R mass spectrometer.

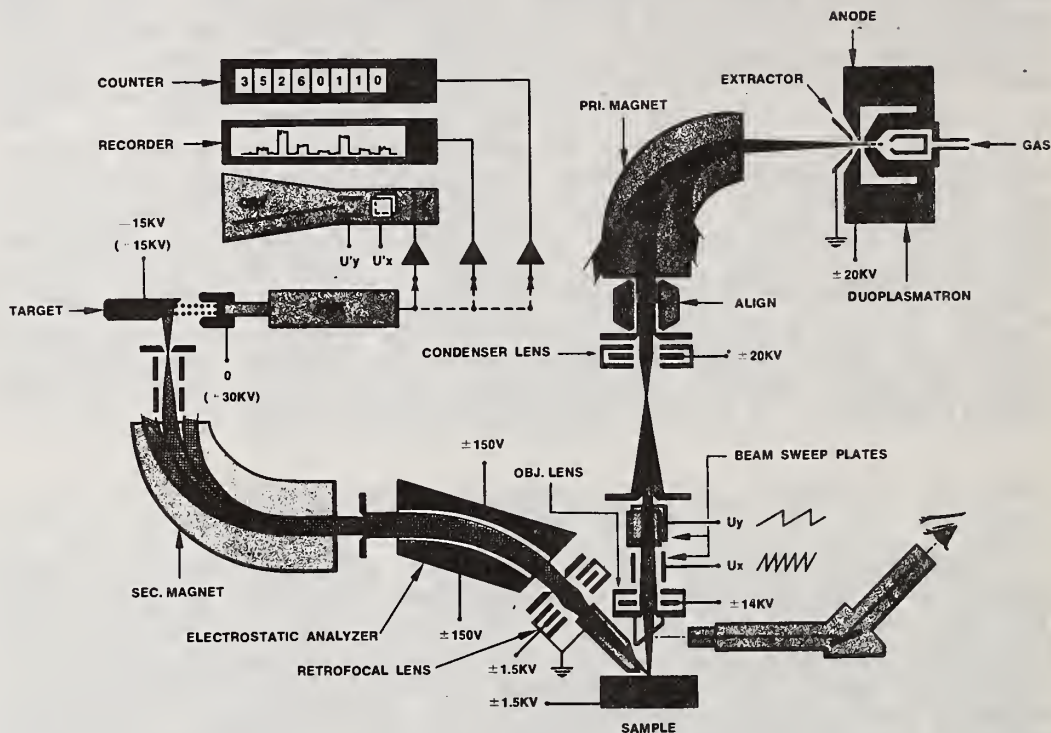


Figure 1. Schematic diagram of the Applied Research Laboratories ion microprobe mass analyzer (IMMA). Reproduced by permission.

The use of a focused primary ion beam provides IMMA with an analytical spatial resolution comparable to that of the electron microprobe. However, the extremely low background noise level in the secondary ion detection system used means that elemental abundances can be measured for trace elements as well as for major elements. Furthermore, the very light elements (including hydrogen) can be analyzed and isotopic ratios determined. In addition the IMMA is capable of isotopically analyzing successive atomic layers of the sample surface as they are eroded away by the impinging ion beam.

Although the secondary ion emission microscope of Castaing and Slodzian (as manufactured by CAMECA) is capable of microanalysis with trace element sensitivity, it is fair to say that most quantitative analytical data published to date on geological samples have been determined on IMMA instruments as manufactured by Applied Research Laboratories (A.R.L.). Furthermore my own ion microprobe analysis experience was gained in the A.R.L.-IMMA laboratory jointly operated by the National Bureau of Standards and the Goddard Space Flight Center

under the direction of K. F. J. Heinrich and situated in the National Bureau of Standards. Consequently much of the following discussion of the methods of SIMS microanalysis of geological samples will be based on the use of A.R.L.-IMMA instruments but the general principles should be applicable to other IMMA-type instruments and to secondary ion emission microscopes.

III. IMMA ANALYSIS OF GEOLOGICAL MATERIALS

1. General

a. Specimen preparation and handling

As with electron microprobe analysis, geological specimens are prepared with highly polished surfaces both as thick samples (for opaque phases) or as thin sections (for transparent phases) with standard techniques [1]. The standard A.R.L.-IMMA instrument has facilities for optical viewing of the sample during analysis (at magnifications up to 300X) in reflected light only, but D. H. Anderson (personal communication) has developed a simple modification to provide viewing in transmitted light for polished thin sections.

b. Surface contamination

Since IMMA analyses are essentially surface analyses and can be restricted to a few tens of angstroms depth, great care must be taken to minimize surface contamination of the sample during its preparation and analysis.

Other possible sources of surface contamination during specimen preparation are the polishing compounds (*e.g.*, alumina, silicon carbide, etc.) and the material in polishing laps (*e.g.*, lead) used in the polishing process. Where phases of very different hardness co-exist in the sample it is possible to find the softer material smearing over the harder one. A good example is the smearing of metal phase over adjacent silicate phases in the preparation of polished surfaces of chondritic meteorites.

Possible sources of surface contamination during analysis arise from condensibles on the sample surface both from impurities in the vacuum environment of the instrument and also from material transferred by sputtering from a previous analysis site on the sample. In the A.R.L.-IMMA, ion and sorption pumps in combination provide a rigorously oil-free vacuum system to minimize silicone and hydrocarbon contamination. A "cold dome" at liquid nitrogen temperatures placed immediately above the sample is essential during quantitative analysis to minimize other environmental condensibles, in particular hydrogen from residual water vapour. The control of material deposited from previously sputtered analysis sites is more difficult although the "cold dome" helps to trap some.

The best way to overcome the problem of possible surface contamination is to "preclean" the analysis surface by rastering the primary ion beam over an area somewhat larger than the analysis spot for sufficient time to sputter away several hundred Angstroms from the surface. Of course, this "preclean" treatment is not possible if surface analysis studies are being undertaken and under those circumstances the only recourse is to recognize possible surface contamination sources and minimize their effects as far as possible.

c. Analysis of nonconducting samples

The IMMA analysis of conducting samples provides no special problems provided the sample is in electrical contact with the sample holder. Conducting paints are completely suitable for making such contacts.

With nonconducting samples, problems arise during analysis because of two separate effects:

- 1) electrical charge build-up on the sample surface resulting from the effects of the charged primary ion beam used for sputtering,
- 2) the electric equipotentials on the sample may be severely distorted by variations in dielectric constant of the sample from point to point.

In the first case, electrical charge buildup can cause the point of impact of the primary ion beam to become unstable so that control of the analysis site is lost. This instability can also lead to drastic changes in the collection efficiency of the selected sputtered ions onto the detector since the bombarded area is stigmatically focused directly onto the resolving slit of the secondary ion mass spectrometer. Charge-up can also lead to significant deceleration of the impinging ion beam. In the Hitachi IMA-2 instrument, surface charge-up of insulators is controlled by flooding the impact site with low energy electrons from a thermal electron emitter [7]. However, Andersen *et al.* [8] have shown that electrical charge-up on insulators is prevented if negatively charged primary ion beams are used instead of positive beams. The mechanism seems to be that a departing secondary electron takes away the negative charge brought in by a negative ion. Consequently IMMA analyses of most geological samples are carried out with negative primary ion beams.

In the second case, residual surface charge arising from triboelectric, piezoelectric or thermoelectric effects may cause the sample surface potential to vary from the sample level by hundreds of volts [6]. In the IMMA design, the sputtered secondary ions are extracted into the secondary mass spectrometer by raising the sample surface potential to a controlled value. If the electrical equipotentials are severely distorted by variations in the dielectric constant of the sample from point to point (as would occur with a

polyphase rock sample) then the efficiency of extraction of the sputtered ions into the secondary mass spectrometer fluctuates drastically as different points on the sample are bombarded. To overcome this problem and fix the surface potential of the sample at a controlled value, insulators (e.g., rock samples) are vacuum coated with a 100 to 200 Å-thick layer of carbon (or conducting metals) before analysis, by the same techniques as for electron microprobe analysis of insulators [1]. However it should be emphasized that the effect of the conducting coating in IMMA analysis of insulators is different from that in the electron microprobe in which it acts to carry away the charge delivered by the electron beam.

In practice, before ion intensity data are measured in IMMA on a coated sample, the conducting coat immediately under the point of beam impact must first be removed by erosion of the primary ion beam so that secondary ion spectra are not contaminated by the coating material. For normal primary ion beam conditions (see below) and with standard thickness carbon coatings, a period of about 10 minutes of erosion by the beam scanning in a raster mode with dimensions which are slightly larger than the analysis area is usually sufficient. For oxygen-free samples, this preliminary bombardment also serves to establish the conditioning of the chemical nature of the sample surface by the implantation of the oxygen from the primary ion beam normally employed in IMMA analysis.

Very thin samples (up to several hundred angstroms) or small particles (a few microns in diameter) on conductive mounts need no special treatment as they cannot support a large enough potential difference from the mount to disturb either the primary or secondary ion beams significantly [6], providing negative primary ion beams are used.

d. Effect of ion bombardment on geological samples

Under normal conditions used for IMMA analysis, the site of impact of the stationary primary beam is normally marked by a conical crater which may be up to a micrometer or more deep after a lengthy trace element analysis has been completed. For most matrices no other visible phenomena are apparent at the point of impact of the primary beam.

It is also important to prevent significant heating of the sample; otherwise volatile elements may be preferentially lost from around the bombarded area and pre-existing elemental diffusion gradients could be modified. However, the use of focussed primary ion beams means that even with specific power density inputs as high as $100\text{w}/\text{cm}^2$, a beam of 2 micrometers diameter delivers only a total of $12.4\ \mu\text{W}$ [6] to the sample. This low total power input would result in a much lower general temperature rise than with the same power density over a larger beam diameter, although the thermal conductivity of the sample is also important in assessing the temperature rise in the sample during sputtering.

Nevertheless some matrices are apparently unstable under ion bombardment and varying sputtered ion intensities may result in these

cases. For example, the U.S. National Bureau of Standards SRM 610-617 series of standard trace element glasses are generally unsatisfactory as ion microprobe standards since they contain 14% Na₂O and such Na-rich glasses are highly unstable with respect to sputtered Na ion intensities even under micrometer-diameter primary ion beams [9]. Similarly instabilities are found in the analysis of Na-rich glasses in the electron microprobe and it is probable that similar hypotheses may explain both phenomena [1].

2. Analytical Conditions

a. Primary ion beam

A fundamental requirement for the development of quantitative IMMA analysis is that there be a constant, high level of intensity of sputtered secondary ions, constant with respect to time, during the primary ion bombardment. Most workers have used inert gas (*e.g.*, argon) primary ion beams for SIMS analysis, but Andersen [10,11] has shown that when an aluminum metal sample is bombarded with $^{40}\text{Ar}^+$ ions, the sputtered $^{27}\text{Al}^+$ ion yield falls exponentially with time as the ability to extract these ions from the sample is progressively destroyed by continued bombardment (fig. 2). Andersen postulated that the diminishing production of Al^+

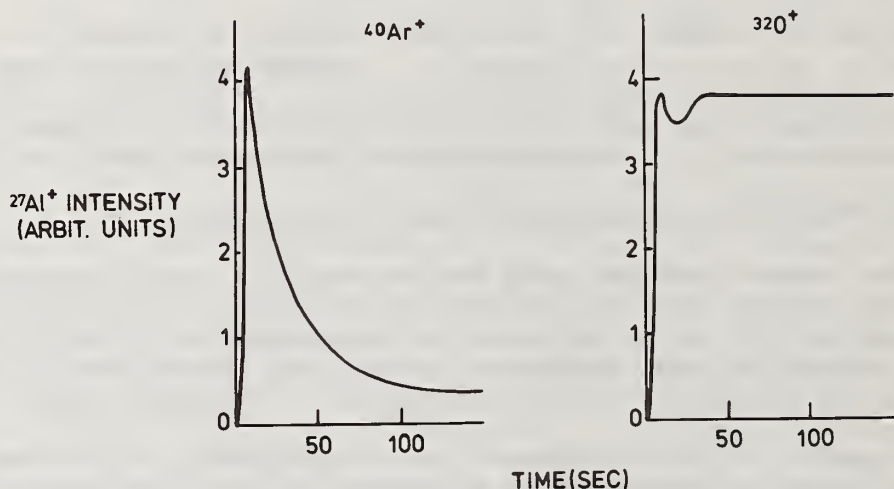


Figure 2. Variation with time of the sputtered $^{27}\text{Al}^+$ ion intensity from aluminum metal using primary ion beams of an inert gas ($^{40}\text{Ar}^+$) and an electro-negative gas ($^{32}\text{O}^+$) [10].

ions was due to the removal of a previously formed thin oxidized film on the sample during the bombardment, and he found that if a primary ion beam of a reactive, electronegative gas (such as oxygen) was used, the yield of Al^+ ions rose rapidly to a maximum stable output (fig. 2).

Presumably the electronegative ion beam implanted into the sample surface forms surface compounds (in this case oxides) which produce stable, high intensity yields of sputtered positive ions. Andersen concluded that the emission of positive ions is enhanced and stabilized by the increased electronic work function of the sample surface created by bombardment with an electronegative gas, such as oxygen. The same situation applies to the production of sputtered negative ions if the work function of the sample surface is decreased by bombarding with ions of an electropositive gas, such as cesium.

Since most elements of general interest to geochemists and cosmochemists have their highest yields in the positive secondary ion spectrum [11], an electronegative gas, normally oxygen, is commonly used in the IMMA analysis of geological specimens. To reduce the possible charge-up of nonconducting samples (see above), negative primary ion beams (*i.e.*, $^{16}O^-$) are used. The acceleration potential for the $^{16}O^-$ ions normally used in IMMA analysis is ≈ 20 keV, and Andersen and Hinthorne [12] have shown that essentially identical analytical results are obtained for a number of accelerating potentials within the range 11 to 18 keV.

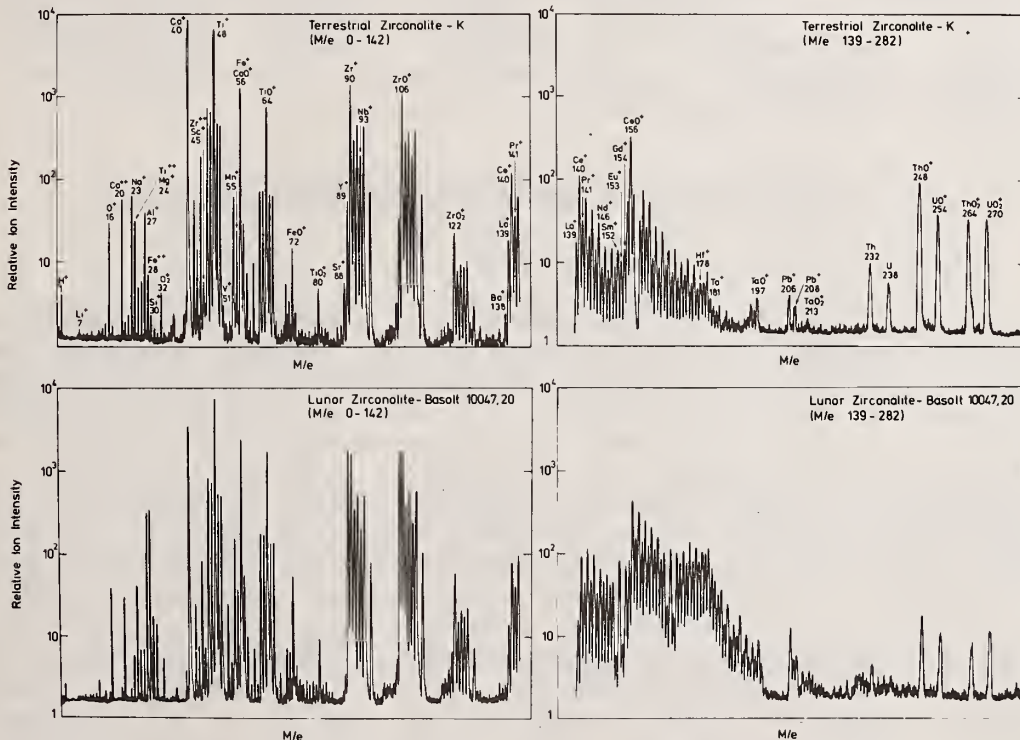


Figure 3. Secondary ion mass spectra from IMMA study of terrestrial zirconolites (K = Kola Peninsula, U.S.S.R.) and lunar zirconolite (Apollo 11 basalt 10047).

Experience to date suggests that an optimum value for primary beam currents for useful elemental analytical sensitivities is around $1-10 \times 10^{-9}$ amperes. Minimum diameter of the primary beam corresponding to a 10×10^{-9} amp beam current is about 20 μm . Any significant drift in the primary beam current should be monitored and the raw secondary ion intensities should be normalized to a standard value of primary beam current. However, experience with at least the A.R.L.-IMMA instrument has shown that, provided the duoplasmatron ion source is clean and has been operating for around two hours (together with the ion optics electronics), the drift in beam current over an analysis is usually less than 2 percent.

b. Ion counting of sputtered secondary ions.

Raw sputtered secondary ion intensities must also be corrected for detector background and detector dead-time. In the A.R.L.-IMMA, the sputtered secondary ion beams are detected by a high gain device of the Daly type that permits single ion counting [13]. Experience has shown that these detectors have detector backgrounds which are essentially constant over the 0-300 mass range at <3 counts/second. Detector and counting electronics dead-times in this instrument are typically around 30 nanoseconds. Significant corrections are required to ion intensities in the $10^5 - 10^7$ counts/second range which are typical for major element secondary ion intensities from geological samples. Consequently an accurate determination of the dead-time for each IMMA ion counting system is extremely important.

IV. QUANTITATIVE IMMA ANALYSIS OF GEOLOGICAL MATERIALS

1. Nature of Secondary Ion Mass Spectra

A detailed model of the mechanisms of secondary ion production is not yet available but a mass spectrum of ionic species sputtered from even the simplest mineral phases shows complexities which highlight the difficulty of quantitative analysis with IMMA [14]. An extreme example is shown in figure 3 in which secondary ion mass spectra of a terrestrial and a lunar example of the complex mineral zirconolite are illustrated. Previous electron microprobe studies of zirconolites have shown that this mineral has an extremely complex composition in which more than 25 elements occur with abundance levels $>0.1\%$ by weight [36]. The secondary ion mass spectra are highly complex with peaks occurring at virtually every mass position in the mass range 0-282. Not all peaks present in the spectra have been identified in figure 3 but sufficient peaks have been labeled to show that the positive secondary ion spectra recorded contain all singly charged ions of the 25 or more elements present, together with XO^+ , XO_2^+ and other multiple atom clusters as well as multiply charged metal ions. All this complexity exists despite the fact that the use of chemically reactive primary ion beams (*e.g.*, $^{16}\text{O}^-$) greatly reduces the number of multiple atom clusters present [6]. Given the complexity of secondary ion mass spectra for minerals, serious problems arise with the possibility of overlap of contaminating ionic

species with the ion peak to be determined. These problems are particularly serious with those instruments (*e.g.*, CAMECA, A.R.L., Hitachi) with secondary ion mass spectrometers of relatively low resolution (~ 500). Part of the problem can be minimized by carefully controlling the abundance of possible contaminants in the sputtering source. Experience with IMMA analysis of geological materials shows that, provided only cryogenic and ion pumping vacuum systems are used, hydrocarbon contamination in the secondary mass spectrum is not a significant problem. Another source of possible contamination is the production of a variety of atomic and molecular ions in the duoplasmatron ion source from impurities in the source gas and from the materials used to construct the ion source. These contaminating species are removed in the A.R.L.-IMMA by means of a primary mass analyzer which allows selection of only one ionic species to form the primary ion beam. A further source of secondary ion contamination is from complex hydride ions produced in the sputtering source from residual water in the vacuum. These hydride ions can be significantly depleted if a "cold dome" at liquid nitrogen temperature is placed just above the sample. However, the presence of the "cold dome" does not prevent the formation of hydride ions in the sputtering source if the phase analyzed contains significant amounts of OH in its lattice. For example, IMMA analyses of OH-bearing terrestrial zirconolites (Table 5) posed a problem with an originally unrecognized $^{57}(\text{CaOH})^+$ contamination of the $^{57}\text{Fe}^+$ peak measured to determine the iron content of this phase.

Undoubtedly many peaks are seriously contaminated by multiply charged, polyatomic and complex molecular ions which are produced in the sputtering source and for which correlation procedures may, or may not, be available. Experience with a wide variety of sample matrices soon builds up an appreciation of significant peak contamination problems but the IMMA analyst must be extremely thorough in searching for all possible peak contaminants. Computer print-outs of selected peak overlaps are available (D. H. Anderson - personal communication) but it is clear that a basic problem with IMMA analysis using currently available instruments is the low resolution of the secondary ion mass spectrometers, which were generally designed for high transmissivities and wide energy bandpass.

However, even with the existing low resolution instruments, it is often possible to correct analytical peaks for significant interfering peaks. For example [15] in an IMMA analysis of a clinopyroxene, peaks with mass/charge (M/e) ratios of 40 and 41 may contain the following species:

<u>M/e</u>	<u>Species</u>	<u>Normalized peak intensities</u>
39	^{39}K	5.15×10^3
40	$^{40}\text{Ca}^+ + ^{24}\text{Mg}^{16}\text{O}^+$	4.49×10^6
41	$^{41}\text{K}^+ + ^{25}\text{Mg}^{16}\text{O}^+$	6.96×10^3

In order to calculate the $^{40}\text{Ca}^+$ intensity for the analysis, we need to subtract the MgO^+ component from the 40 peak.

First of all the $^{41}\text{K}^+$ component in the 41 peak can be calculated from the "clean" $^{39}\text{K}^+$ as follows knowing that in natural potassium:

$$\frac{^{41}\text{K}}{^{39}\text{K}} = \frac{6.88}{93.1}$$

Hence:

$$^{41}\text{K}^+ = ^{39}\text{K}^+ \times \frac{6.88}{93.1} = 5.15 \times 10^3 \times \frac{6.88}{93.1} = 3.81 \times 10^2$$

Then the $^{25}\text{Mg} \ ^{16}\text{O}^+$ component in the 41 peak is given by:

$$\begin{aligned} ^{25}\text{Mg} \ ^{16}\text{O}^+ &= 41 \text{ peak} - ^{41}\text{K}^+ \\ &= 6.96 \times 10^3 - 3.81 \times 10^2 = 6.58 \times 10^3 \end{aligned}$$

knowing $^{24}\text{Mg}^+ / ^{25}\text{Mg}^+ = \frac{79.0}{10.8}$ then

$$\begin{aligned} ^{24}\text{Mg}^+ &= ^{25}\text{Mg} \ ^{16}\text{O}^+ \times \frac{79.0}{10.8} = 6.58 \times 10^3 \times 7.90 = \\ &5.20 \times 10^4 \end{aligned}$$

so that the corrected $^{40}\text{Ca}^+ = 4.47 \times 10^6 - 5.20 \times 10^4 =$
 4.42×10^6

Computer programs have now been developed by Colby [16] and Andersen and Hinthorne [17] to carry out spectrum stripping of contaminated peaks provided the interfering ion species are identifiable. In the general case one extra peak must be measured over the total number of ion species present. A specific example is given below on computer spectrum stripping of interferences on the lead isotopes. Corrections made in this way are not serious provided the species to be corrected for interference is a major contributor to the peak measured; however, if the species sought is a trace element and the interfering species is a major contributor, then serious errors can arise. An example would be trace element determinations of Ca in an Mg-rich olivine where the $^{40}\text{Ca}^+$ peak is interfered with by a significant $^{24}\text{Mg} \ ^{16}\text{O}^+$ and the $^{44}\text{Ca}^+$ peak by $^{28}\text{Si} \ ^{16}\text{O}^+$.

2. Quantitative IMMA Analysis by Comparison with Standard Samples

Some of the earliest attempts at quantitative IMMA analysis [10] followed the familiar "working curve" approach or comparison of absolute secondary ion intensities from unknown samples with a suite of standard samples with known elemental compositions. However, it is now realized that such an approach has severe limitations since absolute sputtered ion intensities depend critically on the work function of the surface from which the ions are produced. For a particular element at a given abundance level, the intensity of the sputtered ions may change by more than an order of magnitude when the work function of the surface changes by a few tenths of a volt [11]. Such local variations are common within a particular sample and between two separate samples, so that in many cases simple comparison of absolute sputtered intensities from standards and samples becomes meaningless.

Bence [18] has also shown that the particular crystallographic orientation of the mineral surface being sputtered can seriously affect the absolute intensities of secondary ions and again lead to problems of absolute intensity comparisons between standards and samples.

A partial solution to the problems of IMMA analysis using sample/standard comparisons follows from observations that, despite local variations in work function values and crystallographic orientations, the ratio of different sputtered ion species from a given mineral matrix is approximately constant for that matrix [6,18]. An example of this approach is the IMMA analysis of F (in humites, amphiboles) and H (in micas, zeolites, epidotes, amphiboles, humites) by Hinthorne and Andersen [19]. They constructed working curves based on H^+/Si^+ and F^+/Si^+ ion intensity ratios (corrected for natural isotopic abundance) from a series of standard silicate samples (normalized for the different silicon abundances) with known fluorine, hydrogen, and silicon abundances. Although it is well known that even ion intensity ratios may change with matrix changes [19], apparently the silicates used in constructing these working curves are sufficiently similar for the ionization efficiency ratios of fluorine, hydrogen, and silicon to remain constant to a first approximation. But Andersen and Hinthorne [19] give a strong warning that it would be unwise to extend the use of these working curves to very different silicate matrices, to oxides or metals without first carrying out a very thorough investigation. Nevertheless, J. R. Hinthorne (personal communication) has recently found that the fluorine working curves can also be used for fluorine analysis of sphenes.

3. Quantitative IMMA Analysis by CARISMA - Local Thermal Equilibrium Approach by C. A. Andersen

The major limitations of the "working curve" approach to IMMA analysis, arising from uncertainty of matrix effects on the relative ionization of different elements and the difficulty of obtaining suitably homogeneous standards for trace elements in a wide variety of matrices, led Andersen [11] and later Andersen and Hinthorne [12,13] to

develop a model of secondary ion generation of theoretically universal applicability for quantitative IMMA analysis. A more detailed discussion of their approach is given elsewhere in this volume by C. A. Andersen but, in general terms, their method has been initially based on the use of $^{16}\text{O}^-$ primary ion beams and assumes that the sputtering source resembles a dense "plasma" of positive and negative ions, neutral atoms and of oxide molecules in local thermodynamic equilibrium. Provided the temperature (T), electron density (N_e) and concentration of free oxygen are known in the "plasma," then, Andersen and Hinthorne conclude, it is possible to calculate the atomic composition of the sputtering source (and of the sputtered sample) from measurement of the singly charged positive ion intensities in the sputtered mass spectrum.

The complex calculations involved are carried out by means of a computer program entitled CARISMA (Corrections to Applied Research Laboratories Ion Sputtering Mass Analysers) which includes several options for establishing the temperature and electron density in the sputtering source. The best tested option (option 3) follows an "internal standard" approach and depends on an independent knowledge of the atomic concentration of two or more elements in the sample. Singly charged positive ion intensities for these internal standard elements are measured, along with related metal—metal oxide ion intensities from one of the combinations O-O₂, Si-SiO, Al-AlO, Ca-CaO to determine the free oxygen concentration in the source. These data are then used as input to CARISMA which searches the T and N_e space to find a set of values for these two parameters consistent with the observed internal standard ion intensities and their known elemental compositions in the sample. The observed ion intensities for all other elements analyzed in the sample are then corrected for these same T and N_e parameters to give the atomic composition of the sample.

In using CARISMA option 3 it is normally advantageous to use as many internal standard elements as possible (up to a maximum of 6 elements) to give the best estimate of the T and N_e parameters for the analysis. Andersen and Hinthorne [12] state that for most geological samples, typical values of T range from 5000° to 15,000°K with the N_e values ranging from $\sim 1.5 \times 10^{14} \text{ cm}^{-3}$ (at lower T) to around $10^{20} - 10^{21} \text{ cm}^{-3}$ (at higher T).

If internal standard information is not available for a sample, CARISMA can be used in option 1 mode when estimated T and N_e values for the particular sample matrix are used in the input. Experience of IMMA analysis of a variety of standard samples with widely different matrices has shown that, if standard operating conditions are used, then reasonably constant T and N_e parameters are found for any matrix type [12]. But clearly IMMA analyses calculated by the option 1 mode will generally be less reliable than those derived using option 3.

In practice, raw secondary ion intensity data arising from an IMMA analysis must first be corrected for detector background, detector dead-

time, primary beam current drift and overlap of analysis peaks in the secondary ion mass spectrum by contaminating species as outlined previously. These corrected ion intensity data are then used as input to CARISMA, under one of the options described here, and Andersen and Hinthorne [12] have shown that this approach can provide "generally acceptable" major and trace element abundances for a large number of elements in a wide variety of geological materials (*e.g.*, silicates, oxides, rock glasses) and man-made products (*e.g.*, metals and alloys) whose compositions are "known" from a number of independent analytical techniques.

However, serious problems arise in attempting a detailed assessment of the accuracy of these CARISMA corrected analyses of geological materials. For example, virtually all of the trace element abundances reported using other analytical techniques are analyses of bulk samples in which the possibility of contamination by other phases is universally a problem. Even without such contamination, inhomogeneities of elemental distributions within the phase are always possible and could drastically effect IMMA analyses carried out with finely focussed primary beams. Even with the major elements, problems arise in comparing IMMA analyses with other methods of analysis since most of the IMMA analyses reported by Andersen and Hinthorne [12] were calculated from CARISMA option 3 in which many of these major elements were themselves used as internal standards. Given these uncertainties, the accuracy of their CARISMA-corrected IMMA analyses can only be assessed in a general way after looking at the comparison trends for the various elements in similar matrices and such an assessment is summarized in Table 1.

4. Independent Assessment of CARISMA-reduced IMMA Analyses of Geological Materials

The apparent general success of the CARISMA-reduction of IMMA analytical data, as reported by Andersen and Hinthorne [20], prompted me to independently investigate the method using the A.R.L.-IMMA instrument in the Analytical Chemistry Division of the U.S. National Bureau of Standards. Silicates (plagioclase, clinopyroxene, tranquillityite), silicate glasses, oxides (chromites, zirconolites), and metals from terrestrial, lunar, meteoritic and man-made materials were analyzed by IMMA and the CARISMA-reduced data compared with independently derived data from electron microprobe and other methods. The results are given in Tables 2 to 8 and standard IMMA analytical conditions described above were used in all cases.

a. Intra-laboratory analytical reproducibility

Little information has been given previously on the reproducibility of repeated IMMA analysis on a single sample within a single laboratory. Duplicate analyses from a number of phases are given in Tables 2 to 8 and, for most cases, reproducibility is satisfactory particularly when the likelihood of inhomogeneities in the trace element distributions on the micrometer scale is considered.

Table 1. General assessment of accuracy of CARISMA-reduced IMMA analyses of "known" samples (after Andersen and Hinthorne [12]).

	Silicates and Oxides	Metals	Unspecified matrix
"Good" correlations	B, Na, Mg, Al, Si, K, Ca, Ti, V, Cr, Mn, Fe, Rb, Sr, Y, Ba	B, C, Si, Cr, Fe, Co, Ni, Cu	
Qualified "satisfactory" correlations	Pb	Al, Ti, Mn, Pb	Be, S, Zn, Ga, Ru, Rh, Ag, In, Sb, Te
Poor correlations (IMMA low)	Li (x 1.25) ^a ; Cs (x 1.5)	V (x?), Sn (x?)	P (x 3.0), As (x 3?), Zr (x 2.5), Nb (x 5.7), Mo (x 6.5), La (x 2.5), Ce (x 2.5), Hf (x ?), W (x ?), Th (x ?), U (x ?)
Poor correlations (unspecified error)			Pd, Cd, Os, Ir, Hg

^a indicated error factor.

Table 2. IMMA analyses of plagioclase and clinopyroxene from the Moama eucrite

	Plagioclase (grain 4)		Clinopyroxene (grain 4)	
	Electron microprobe	IMMA	Electron microprobe	IMMA
<u>atomic per cent</u>		1	2	
Mg	0.04 a	0.016	0.018	10.7 ^a
Al	14.9 a	15.0	14.8	0.09
Si	15.9 a	16.3	16.4	19.8 a
Ca	7.3 a	7.2	7.2	1.53
Fe	0.03	0.15	0.14	7.70 a
<u>ppm atomic</u>				
Li	-	4.6	4.9	-
Na	4300	3710	4540	600
K	~100	95	116	~100
Ti	-	13	20	~800
V	-	2.3	2.3	-
Cr	-	3.2	5.6	~800
Mn	-	44	39	-
Rb	-	1.5	1.8	-
Sr	-	38	40	-
Ba	-	1.9	2.3	-
<u>CARISMA parameters</u>				
Option:		3	3	3
T (°K)		13,520	13,300	12,180
Ne (cm ⁻³)		1.154x10 ²¹	1.452x10 ²¹	0.551x10 ²⁰

a internal standards used in CARISMA option 3 calculations.

Table 3. IMMA analyses of chromite from the Moama eucrite

	Chromite		
	Electron microprobe	IMMA	
		Grain 4	Grain 5
<u>atomic per cent</u>			
Mg	1.79 ^a	2.18	2.46
Al	4.59 ^a	6.59	6.99
Ti	2.04 ^a	2.10	2.04
Cr	20.0 ^a	17.3	16.9
Fe	13.8 ^a	13.9	13.8
<u>ppm atomic</u>			
Li	-	5.3	6.0
Na	-	4.8	29
Si	~50	1830	562
K	-	4.2	3.3
V	2700	1840	1870
Mn	3500	1940	2110
Ni	-	124	124
Rb	-	<1	<1
Sr	-	<1	<1
Zr	-	7.0	5.2
Nb	-	30	15
Cs	-	0.6	<0.5
Ba	-	2.2	<2
<u>CARISMA parameters</u>			
Option		3	3
T (°K)		2,800 ^b	3,400 ^b
Ne (cm ⁻³)		0.123 x 10 ^{8b}	0.690 x 10 ^{10b}

a internal standards used in CARISMA option 3 calculations

b values seem unusually low (see text)

Geochemical Applications

Table 4. IMMA analyses of fission track
c
 standard glasses.

Element	Glass TT42		Grant glass		Saratoga glass	
	Electron ^b Microprobe	IMMA	Electron ^b Microprobe	IMMA	Electron ^b Microprobe	IMMA
<u>atomic per cent</u>						
Mg ^a	1.85	1.64	1.43	1.22	0.127	0.108
Si ^a	23.91	23.60	25.71	25.90	27.16	27.60
K	0.22	0.224	0.022	0.027	6.90	6.43
Ca ^a	1.79	1.75	1.38	1.38	2.68	2.72
<u>atomic ppm</u>						
Li		119		5.4		8.8
Be		< 0.1		<0.1		<0.1
B		5310		108		61.2
Cd		<0.3		<0.3		<0.2
<u>CARISMA parameters</u>						
Option		3		3		3
T (°K)		13,860		14,460		13,800
Ne (cm ⁻³)		1.157x10 ²⁰		1.099 x 10 ²⁰		1.044 x 10 ²⁰
¹⁶ O + ³² O ₂ ⁺		22.27		24.22		23.61

a. internal standards used in CARISMA option 3 calculations.

b. analyst : J. Nelen, Mineral Sciences, Smithsonian Institution.

c. samples from B.S. Carpenter (National Bureau of Standards).

Table 5. IMMA analyses of zirconolites.

atomic per cent	Zirconolite A (Aldan, U.S.S.R.) ^c				Zirconolite K (Kola Peninsula, U.S.S.R.) ^c				Niobozirconolite S (Kola Peninsula, U.S.S.R.) ^c			
	Electron Microprobe		IMMA Lab. 1 ^c		Electron Microprobe		IMMA Lab. 1		Electron Microprobe		IMMA Lab. 1	
			1	2			1	2			1	2
Ce ^a	7.90	7.86	7.86	7.91	6.80	6.81	6.81	6.81	7.42	7.42	7.42	7.58
Ti ^a	13.8	13.8	13.8	13.8	12.35	12.35	12.35	12.35	9.73	9.73	9.73	9.69
Fe ^a	2.31	2.34	2.34	2.31	3.12	3.12	3.12	3.12	3.36	3.36	3.36	3.31
Zr	9.51	4.30	4.26	5.46	9.54	3.58	3.95	3.95	4.37	4.17	4.17	7.39
Na	0.055	0.082	0.066	0.048	0.12	0.09	0.06	0.06	0.49	0.079	0.061	0.047
Mg	0.077	0.16	0.21	0.076	0.19	0.14	0.11	0.11	0.47	0.081	0.081	0.39
Al	0.067	0.17	0.19	0.14	0.071	0.12	0.13	0.13	0.17	0.31	0.43	0.22
Si	0.017	0.18	0.72	0.078	-	0.056	0.12	0.12	-	0.040	0.091	0.053
Y	0.091	0.12	0.11	0.11	0.035	0.11	0.12	0.12	0.048	0.112	0.135	0.157
Nb	1.15	0.46	0.41	0.48	1.42	0.32	0.30	0.30	3.59	1.48	1.41	2.21
ppm atomic												
Li	-	0.19	2.7	2.1	-	0.03	0.03	0.03	-	9.1	11	2.1
K	-	30	36	3.8	-	10	36	36	-	50	15	31
Sc	-	35	46	30	-	5.5	3.7	3.7	-	6.0	8.1	-
V	-	57	60	54	-	24	28	28	-	57	53	49
Cr	140	115	1050	3.4	-	-	-	-	-	-	-	232
Mn	680	710	1050	347	1780	900	800	800	2350	1700	3700	1600
Sr	-	-	-	41	-	-	-	-	-	-	-	49
La	360	68	58	86	530	100	80	80	-	137	128	313
Ce	3040	816	780	851	6060	1500	1500	1500	4810	1450	1470	2310
Pr	350	153	131	154	660	200	150	150	216	216	165	363
Nd	2570	1250	1170	1070	4330	1500	1400	1400	1800	1490	1330	1970
Sm	890	327	279	277	1340	310	220	220	341	250	225	392
Eu	310	116	106	87	490	110	80	80	-	100	73	121
Hf	770	124	108	-	240	70	70	70	421	28	73	-
Ta	1140	138	145	-	470	170	120	120	2210	150	250	-
Pb ^b	290	256	245	59	470	70	180	180	-	240	267	33
Th	2380	67	59	74	9660	72	75	75	5970	278	146	298
U	1150	19	14	30	2070	15	12	12	1700	49	20	74
CARISMA parameters												
Option	-	3	3	3	-	3	3	3	-	3	3	3
T(°K)	-	10380	10160	13720	-	11020	9740	9740	11960	-	11660	14200
Ne (cm ⁻³)	-	5.06 x 10 ²⁰	3.92 x 10 ²⁰	1.05 x 10 ²⁰	-	1.13 x 10 ²⁰	3.93 x 10 ¹⁹	3.93 x 10 ¹⁹	4.70 x 10 ¹⁹	-	2.26 x 10 ¹⁹	2.01 x 10 ²⁰
												1.22 x 10 ²⁰
												10

a internal standards used in CARISMA option 3 calculations.

b calculated assuming $^{206}\text{Pb} : ^{207}\text{Pb} = 208\text{pb} : 1 : 0 : 1$

c IMMA Lab. 1 Analytical Chemistry Division, U.S. National Bureau of Standards, Washington, D.C. (Analyst: J. F. Levering).

d IMMA Lab. 2 Hasler Research Center, Applied Research Laboratories, Santa Barbara, California (Analyst: J. R. Hinthorne).

Geochemical Applications

Table 6. IMMA analysis of tranquillityite (grain 20A-27)
in Apollo 11 basalt 10047

	Tranquillityite	
	Electron Microprobe	IMMA ^b
<u>atomic per cent</u>		
Si	7.14 ^a	7.16
Ti	7.76 ^a	7.75
Fe	18.8 ^a	18.8
Zr	4.32	2.15
Al	0.54	0.77
Ca	0.58	0.64
Mn	0.16	0.11
Y	0.70	0.49
Nb	-	0.046
<u>ppm atomic</u>		
Li	-	3.3
B	-	25
Na	-	23
Mg	-	148
P	-	105
K	~200	709
Ba	-	11
Ce	~300	34
<u>CARISMA parameters</u>		
Option		3
T (°K)		8,960
Ne (cm ⁻³)		0.985x10 ¹⁷

^a internal standards used in CARISMA option 3 calculations

^b Hf, Pb, Th, U all <10 ppma

b. Inter-laboratory analytical reproducibility

No data have been published previously on the reproducibility of CARISMA-reduced analyses on the same samples determined in separate IMMA laboratories. Table 5 includes IMMA analyses of identical samples of zirconolite from two separate laboratories and, for most elements, the reproducibility is satisfactory, particularly when known sample inhomogeneities are considered. However, in a few cases, there does seem to be certain systematic differences between the laboratories. For example, zirconium and uranium are consistently higher in the IMMA Lab 2 analyses while Pb is consistently higher in the IMMA Lab. 1 analyses. The explanation of these differences is not clear at present.

c. Assessment of analytical accuracy

Following the discussion above concerning the problem of comparing IMMA analyses with independently determined analyses, it is unprofitable to attempt to discuss in detail the relative accuracy of the IMMA analytical data in Tables 2 to 8. A more realistic approach would be for each individual to make his own assessment of these data on the basis of his own experience of the relevance of the independently derived abundance data available for comparison in the Tables. For example, in assessing the IMMA analyses of the NBS standard steel sample (Table 7) it must be remembered that samples SRM661, 662, 663, 664 and, to a lesser extent 665, contain significant numbers of inclusions of various types into which a variety of elements (*e.g.*, B, C, Ti, Nb, Zr, Tb, Si, Mn, S, Se, Ce, Mg, Al, Mo, Fe, Ag, V, etc.) have been segregated (R. L. Myklebust, personal communication). Consequently the standard NBS average analyses for these elements as reported in Table 7 can only be compared in a general way with IMMA data measured on highly localized areas.

The IMMA analyses of the ultrahigh purity iron (FER BNMZ F 1) sample (Table 8) illustrates other problems which may arise. Independent studies (I. L. Barnes - personal communication) have indicated that C, Mn and Cu all occur in this sample at abundance levels ≤ 1 weight ppm so that the higher levels in the IMMA analyses must reflect analytical problems. It seems that the C may result from hydrocarbon contamination and the Cu could have been smeared on the sample from the brass sample holder in which it had been polished. The relatively high Mn abundance reported could have resulted from FeH^+ contamination on the $^{55}\text{Mn}^+$ peak measured. However, the IMMA abundance levels for the other elements analyzed are in general agreement with the ultrahigh purity of this material.

On the overall assessment of the data in Tables 2 to 8, it may be concluded that the results of these new IMMA analyses of geological materials confirms the previous conclusions of Andersen and Hinthorne [20] as summarized in Table 1. Where suitably homogeneous and well characterized samples have been analyzed by IMMA using CARISMA data reduction, the results show that relatively accurate determinations of

Table 7. IMMA analyses of NBS standard steels.

atomic per cent	SRM 661				SRM 662				SRM 663				SRM 664				SRM 665			
	AISI 4340 steel				AISI 94317 steel				Cr-V steel				High-carbon steel				Electrolytic iron			
	NBS		IMMA		NBS		IMMA		NBS		IMMA		NBS		IMMA		NBS		IMMA	
Fe	94.1 ^a	93.4	94.8 ^a	95.2	91.4 ^a	88.0	86.6	94.1 ^a	94.0	91.3	99.8	99.1	98.5	99.1	98.5	99.8	99.1	98.5	99.1	98.5
C	1.75 ^a	1.75	0.74 ^a	0.74	2.79 ^a	2.73	2.69	3.93 ^a	3.93	3.82	0.03	0.77	1.38	0.77	1.38	0.03	0.77	1.38	0.77	1.38
Si	0.44 ^a	0.43	0.77 ^a	0.40	1.43 ^a	1.28	1.36	0.13 ^a	0.28	0.17	0.016	0.047	0.059	0.047	0.059	0.016	0.047	0.059	0.047	0.059
Cr	0.73 ^a	1.50	0.32 ^a	0.53	1.36 ^a	2.69	3.10	0.068 ^a	0.11	0.16	0.0078	0.014	0.015	0.0078	0.014	0.0078	0.014	0.015	0.014	0.015
Mn	0.67	1.28	1.05	1.38	1.47	2.87	3.27	0.25	0.47	0.53	0.054	0.015	0.015	0.054	0.015	0.054	0.015	0.015	0.015	0.015
Co	0.028	-	0.28	0.18	0.044	0.031	0.036	0.14	0.11	0.09	0.0067	0.0043	0.0045	0.0067	0.0043	0.0067	0.0043	0.0045	0.0043	0.0045
Ni	1.86 ^a	1.08	0.56 ^a	0.24	0.30 ^a	0.20	0.22	0.13 ^a	0.12	0.08	0.039	0.022	0.020	0.039	0.022	0.039	0.022	0.020	0.022	0.020
Cu	0.036	0.066	0.44	0.20	0.083	0.096	0.107	0.21 ^a	0.21	0.18	0.0051	0.0017	0.0021	0.0051	0.0017	0.0051	0.0017	0.0021	0.0021	0.0021
ppm atomic																				
B	25	50	128	468	45	396	371	554	3810	2.9%	8	24	85	8	24	8	24	85	24	85
Na	-	2.4	-	11	-	5.1	6.0	-	35	13	-	15	15	-	15	-	15	15	15	15
Mg	-	316	14	16	11	8.8	9.0	(2)	34	74	-	-	-	-	-	-	-	-	-	-
Al	433	2700	1960	6200	0.48%	1.47%	1.94%	16	695	880	-	-	-	-	-	-	-	-	-	-
K	-	2.1	-	6.5	-	4.8	12	-	48	14	-	-	8.6	-	-	-	-	8.6	-	-
Ca	-	27	3	19	-	7.3	9.9	-	140	20	-	19	25	-	-	-	-	19	25	25
Ti	230	934	970	2200	563	580	740	2720	1490	1850	7.0	1.1	1.0	7.0	1.1	7.0	1.1	1.0	1.0	1.0
V	120	188	447	447	169	58	72	1120	1050	2220	617	8.3	9.0	617	8.3	617	8.3	9.0	8.3	9.0
Zr	54	72	1160	979	290	9.1	26	405	-	48	-	0.2	0.1	-	0.2	-	0.2	0.1	0.2	0.1
Nb	130	181	1730	1240	285	85	120	2780	-	135	-	<0.1	<0.1	-	<0.1	-	<0.1	<0.1	<0.1	<0.1
Mo	1090	517	390	113	169	58	72	2780	-	1910	29	8.1	9.8	29	8.1	29	8.1	9.8	8.1	9.8
Ta	61	162	620	205	16	25	18	330	-	6	-	0.4	0.5	-	0.4	-	0.4	0.5	0.4	0.5
Pb	-	-	1.1	2.3	6	17	3.8	63	-	62	-	1.5	2.0	-	1.5	-	1.5	2.0	1.5	2.0
CARISMA Parameters																				
Option	3	3	3	3	3	3	3	3	3	3	3	3	3	3	3	3	3	3	3	3
T (°K)	8,860	8,740	9,580	10,040	7,980	7,980	8,620	8,680	8,160	8,160	8,740	8,740	8,740	8,740	8,740	8,740	8,740	8,740	8,740	8,740
Ne (cm ⁻³)	0.190 x 10 ¹⁹	0.120 x 10 ¹⁹	0.346 x 10 ¹⁹	0.374 x 10 ¹⁹	0.551 x 10 ¹⁸	0.551 x 10 ¹⁸	0.200 x 10 ¹⁹	0.579 x 10 ¹⁸	0.309 x 10 ¹⁸	0.309 x 10 ¹⁸	0.120 x 10 ¹⁹									

a internal standards used in CARISMA option 3 calculations.

Table 8. IMMA analyses^a of ultra high purity iron and metal phase from the Moama eucrite

	Ultra high purity iron ^b		Metal phase from Moama eucrite						
	IMMA		IMMA						
	1	2	Electron microprobe	Grain 10			Grain 12		Grain 32(A)
				1	2	3	1	2	
<u>atomic per cent</u>									
Fe	99.4	99.9	99.7	99.4	96.2	97.5 ^c	99.0	99.4	96.9 ^c
C	0.52	0.025	-	0.35	3.5 ^c	2.1	0.75	0.11	2.80 ^c
Co	0.0003	0.0003	0.22	0.16	0.15	0.15	-	0.17	0.16
Ni	0.0006	0.0005	0.11	0.030	0.025	0.030	0.054	0.053	0.030
<u>ppm atomic</u>									
B	30	2.0	-	22	4.7	7.0	19	26	<3
Na	1.7	3.3	-	2.7	8.7	10.2	38	44	94
Mg	25	3.2	-	6.8	6.1	4.0	34	57	23
Al	31	51	-	111	80	76	160	92	101
Si	310	206	-	-	874	1030	1215	1600	618
K	5	0.7	-	17	14	13	30	30	19
Ca	0.8	0.5	-	3.6	2.5	2.2	28	36	3.2
Ti	1.2	1.2	-	1.3	1.3	0.8	2.2	2.7	38
V	0.5	0.6	-	3.7	4.2	3.2	4.6	3.7	4.1
Cr	1.1	1.0	-	12	15	14	14	14	15
Mn	52	59	-	57	44	37	72	53	55
Cu	141	153	-	234	242	204	191	213	250
Zr	0.1	0.7	-	0.4	0.3	0.3	0.5	0.7	0.5
Nb	0.1	0.3	-	0.4	0.6	0.4	1.3	0.9	0.8
Mo	0.4	<0.1	-	4.7	6.6	4.6	17	9.1	12
Ta	0.3	0.3	-	0.5	0.2	0.7	0.3	1.2	1.0
Pb	1.1	14	-	0.8	0.8	0.4	1.0	1.3	0.7

a all IMMA analyses calculated using CARISMA option 1 with
 $T = 8,740 \text{ }^\circ\text{K}$ and $\text{Ne} = 0.120 \times 10^{19} \text{ cm}^{-3}$.

b sample from K.F.J. Heinrich .

c possibly contaminated by carbon vacuum coating.

Geochemical Applications

elemental abundances in geological materials are possible for those elements in Table 1 (other than those described in "poor correlations") if option 3 CARISMA reduction of ion intensity data is used. The greatest source of error lies in the possibility that incorrect ion intensities are used as input to CARISMA for one or more internal standards in option 3. Such errors arise if an unsuspected contamination exists in the internal standard ion peak measured and these incorrect data will seriously perturb the "best fit" in $T - N_e$ space from which the sample composition is calculated.

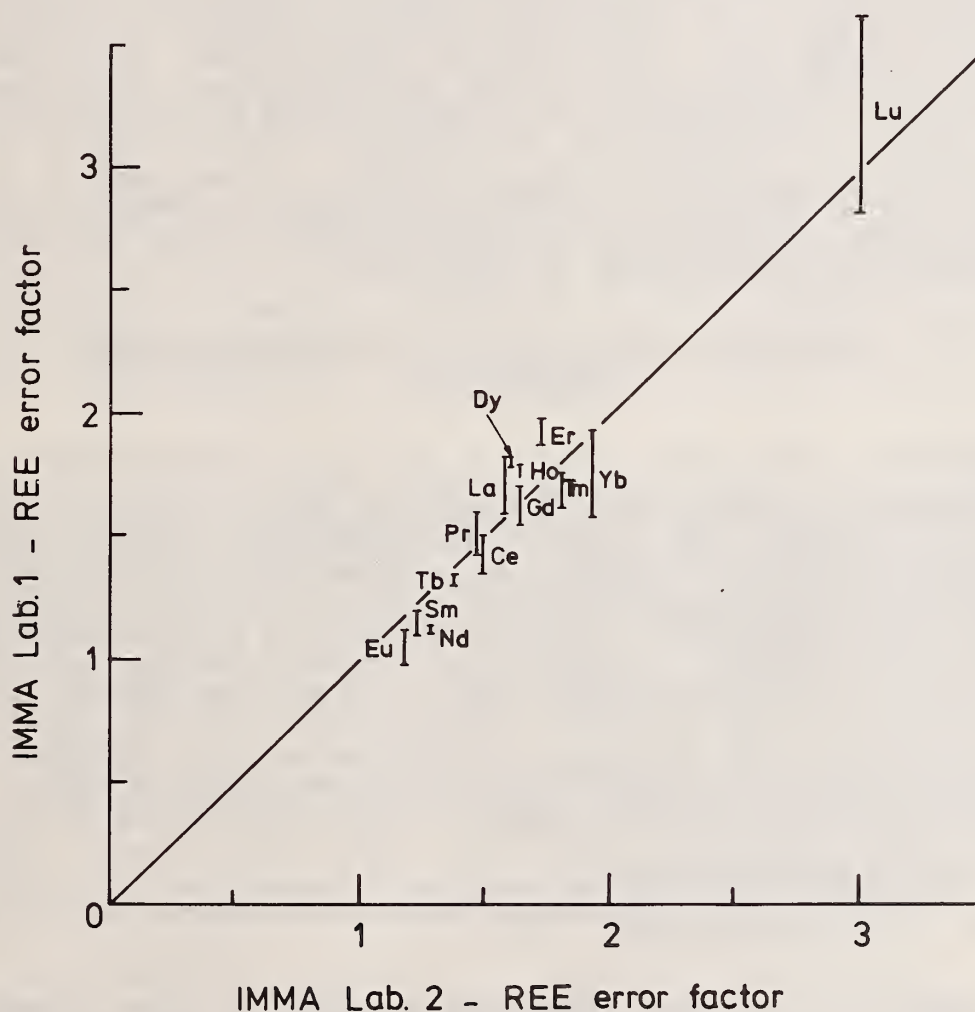


Figure 4. Error factors for REE analyses using CARISMA-reduced data from two IMMA laboratories (see Table 5).

d. Failure of CARISMA analyses

The IMMA analyses of Andersen and Hinthorne [12], and those reported in the present work, found that CARISMA consistently predicted values for zirconium, niobium, molybdenum, lanthanum, rare earth elements (REE), hafnium, tungsten, thorium, and uranium abundances which were much less than the known abundances in the samples analyzed. All these elements are characterized by large molecular oxide ion components in the secondary ion spectrum and, in many cases, the metal monoxide ion peak is actually greater than the atomic ion peak (*e.g.*, see fig. 3). Preliminary work (Lovering, Andersen and Hinthorne, unpublished report) on IMMA analyses of REE and lanthanum standard glasses in two separate A.R.L.-IMMA laboratories has indicated variable error factors for these elements which are relatively reproducible between the two laboratories (fig. 4). These data suggest that the error factors are not dependent on instrumental effects but are more likely to be due to inadequacies in the procedure in CARISMA used to calculate the contribution of REE molecular oxide species in the sputtering source. Further work is at present underway to establish the error factors for the elements Zr, Nb, Mo, Hf, W, Th, U so that the accuracy of IMMA analyses of these geochemically important elements can be improved.

V. APPLICATIONS OF SIMS MICROANALYSIS IN GEOCHEMISTRY AND COSMOCHEMISTRY

1. General

Commercially manufactured SIMS instruments have only been generally available since about 1970, and quantitative IMMA analysis methods using the CARISMA approach have only been generally available since 1972 [13]. Consequently the applications of SIMS microanalysis to the study of geochemical and cosmochemical problems as published up to the present are rather limited in number. It must also be remembered that the bulk of the quantitative IMMA analyses published to date have been produced in a single IMMA laboratory (at Hasler Research Center, Applied Research Laboratories) by two analysts (C. A. Andersen and J. R. Hinthorne). Nevertheless the limited applications that have been published serve to clearly illustrate the potential power of SIMS microanalysis to geology.

2. Trace Element Geochemistry

a. Terrestrial materials

Relatively few data have been published on trace element distributions in terrestrial rocks and minerals using IMMA analysis. Andersen and Hinthorne [9] have reported IMMA-derived abundances for a wide range of trace elements in pyroxenes, amphiboles, olivines, garnets, scapolites, K-feldspars and plagioclase feldspars. They have also reported determinations of trace elements in glasses produced from the USGS series of standard rocks (*i.e.*, G-2, AGV-2, GSP-1) and have

thus shown how IMMA can be used to measure trace element abundances in rocks.

Andersen [20], and Stout and Hinthorne [21] have reported the first *in situ* determinations, using IMMA, of trace element distribution coefficients between co-existing hornblende and cummingtonite in cummingtonite-gedrite hornblende and cummingtonite-garnet-hornblende assemblages in sillimanite grade metamorphic rocks from the Keen Dome, New Hampshire. Average distribution coefficients, K_D (hornblende/cummingtonite) were determined as follows: Li = 3.0, P = 3.0, V = 6.6, Cr = 0.44, Co = 5.0, Sr = 2.5, Y = 10.0. High concentrations of Li in gedrite and of B, Cs and Ce in hornblende were also observed together with marked fractionation of Cr, Zr, Pb into cummingtonite relative to coexisting Fe-Mg (*i.e.*, garnet) phase. Similar partitionings have also been observed (J. R. Hinthorne personal communication) between the identical co-existing phases in sillimanite grade rocks of the same bulk composition from Norway.

Trace-element partitioning between co-existing phases in igneous rocks has yet to be studied in detail using *in situ* IMMA analysis, but Andersen and Hinthorne [22] have reported IMMA analyses for a variety of co-existing silicate and oxide phases in an oceanite, trachyte, and nephelinite from Hawaii, a tholeiitic basalt and basanite from the Mojave Desert, a high-alumina basalt from the Mid-Atlantic Ridge, a metallic iron-bearing basalt from Disko Island, and a spinel peridotite from St. Paul's Rocks.

Havette-Ledebt [23] has used ion microscope pictures and semiquantitative analyses to study the behavior of Ni, Ca and other elements during the serpentinisation of peridotites from Bagilet Auliac (France) and the relationships and origin of glass components of palaeozoic ignimbrites from Jersey, Alegon, Cœvrons, Bas Bocage Vendéen, Genis and Montagne Noire (France). She also presented ion microscope studies of the distribution of fission product elements within the natural atomic pile which had formed spontaneously in 20-30% U lenses within the uranium ore deposit at Oklo, Gabon.

Hinthorne and Ribbe [24] reported analyses of trace elements (*i.e.*, Al, P, Be, Li, Na, K, Ti, V, Mn, Sr, Y, Zr, Cr, Ce) in a number of samples of chondrodites as part of a study of the B geochemistry of this phase. Lovering (this work) has carried out IMMA analyses of zirconolites from several localities in the U.S.S.R. (Table 5) which confirm the extraordinary chemical complexity of this phase.

b. Meteorites

Jerome and Slodzian [25] have described a semiquantitative ion microscope study of trace element distributions in the Juvinas eucrite (basaltic achondrite). They found that two pyroxenes co-exist in Juvinas with one pyroxene (Ca and Ti-rich but relatively poor in Mg, Si, Fe, Mn) existing as lamellae in another pyroxene (Ca- and Ti-poor and relatively enriched in Mg, Si, Fe, Mn). Both pyroxenes were Al-poor and

inclusion of a Ti-rich phase (rutile?) occur in the host Ca-poor pyroxene.

IMMA analyses have been reported to illustrate trace element fractionations between co-existing silicate-oxide phases in the Bereba [26], Cachari [22] and Juvinas [22] eucrites (basaltic achondrites) and between silicate-oxidemetal phases in the new Moama eucrite (Lovering—See Tables 2, 3, 8 in this work). Similar studies have been made of trace element distributions between co-existing plagioclase-clinopyroxene-olivine-chromite in the unique Chassigny olivine-rich achondrite, co-existing clinopyroxene-olivine in the Nakhla diopside-olivine achondrite and in olivine fragments and plagioclase-rich inclusion in the Allende carbonaceous chondrite [27].

Andersen and Hinthorne* have also listed IMMA analyses of augites [22] and a REE-rich phosphate [27] in the Angra dos Reis augite achondrite. The phosphate REE fractionation pattern is essentially horizontal for the light REE's from Ce to Eu, and no Eu anomaly of any kind is observed. In the lunar rocks, phosphate phases usually show similarly horizontal patterns, Ce to Sm, but all show prominent negative Eu anomalies which are characteristically larger than those in the host rocks [26]. On this basis it can be concluded that the Angra dos Reis achondrite itself does not have a strong negative Eu anomaly, although Schnetzler and Philpotts [28] have reported a small negative Eu anomaly in a total sample. On the other hand, $^{18}\text{O}/^{16}\text{O}$ ratios indicate a close relationship between lunar rocks and chondrites, enstatite achondrites and the Angra dos Reis achondrite (Group II materials), while basaltic achondrites, hypersthene achondrites and mesosiderites form the distinct and separate Group I materials [29]. The REE data discussed here would imply that, within Group II extra-terrestrial materials, the Angra dos Reis is more closely allied to the chondrites (and enstatite achondrites) than to the lunar rocks.

c. Lunar rocks and minerals

Since the advent of SIMS instrumentation and the development of analytical methods for these instruments coincided with the return of lunar samples during the Apollo lunar landings from 1969 to 1972, it is not surprising that much of the IMMA analytical data published to date has been concerned with the analysis of these unique materials. Andersen *et al.* [30] reported IMMA analyses of trace elements (*e.g.*, B, Be, P, Si, Al, Li, V, Mg, Ti, Cr, Fe, Mn, Hf, Zr, Y, Na, Ca, Sr, K, Ba, Pb) in glass, clinopyroxenes, pyroxenoids (=pyroxferroite), plagioclases and ilmenites in Apollo 11 samples. Fredriksson *et al.* [31] carried out IMMA analyses of trace elements (*e.g.*, Li, B, Na, P, K, Rb, Sr, Y, Zr, Ba, La, Ce) in low-alkali "normal" glasses, KREEP glasses and groundmass-welded glass in breccias from the Apollo 12 site. Prinz *et al.* [32] used IMMA analysis to characterize various basaltic glass fragments in an Apollo 15 microbreccia on the basis of Li, B, V, Sr, Y, Zr, Ba, Rb, Na, K, P, Ti, Cr, Mn, La, Ce, Pr, Nd abundances. Similar trace element suites have been measured by Andersen and Hinthorne in glasses

from Apollo 14 [22], Apollo 15 [26], Luna 16 [22], and Luna 20 [27] sites.

Trace element fractionations have been measured between co-existing silicate (olivine, clinopyroxene, orthopyroxene, pyroxmangite, plagioclase, cristobalite) and oxide (spinel, ilmenite) phases, as well as in single mineral grains, in a wide range of lunar basalts, norites, anorthosites and breccias from Apollo 11, 12, 14 [22], Apollo 15 [26,27], Apollo 16 [27], Luna 16 [22] and Luna 20 [27] sites. These studies have produced an immense quantity of basic trace element abundance data which have not yet been adequately considered in the light of current models for the evolution of the lunar rocks.

Meyer *et al.* [14] have discussed in some detail the problems of interference (*e.g.*, Fe^+ with Al_2^+ , CaO^+ , CaOH^+ and Rb^+ with CaSiO^+ and CaAlO^+) on IMMA analyses of trace elements in lunar plagioclases. Data are presented for Li, Mg, Ti, Sr and Ba abundances determined after making corrections for specific interferences and further empirical corrections to CARISMA-reduced values on the basis of comparisons with isotope dilution analyses determined on a bulk sample of a single terrestrial plagioclase. On the basis of their trace element data, they conclude that considerable variation in plagioclase compositions observed indicates a wide variety of rock types in the lunar crust before it was brecciated and sintered to its present state.

Bence and Autier [33] used a CAMECA ion microscope to compare ion intensities for Li, Na, Mg, Al, K, Ca, Ti, Mn, and Ba along traverses across a pigeonite-augite junction in Apollo 15 basalt 15499 and between pigeonite, augite, Fe-augite and plagioclase in Apollo 12 basalt 12033. Andersen and Hinthorne [22] have reported IMMA analyses of a zoned clinopyroxene grain from the Apollo 12 fines sample 12032 which has a core of pigeonite surrounded by subcalcic augite and finally rimmed by a pyroxene of intermediate composition. Virtually all the trace elements analyzed (*i.e.*, Li, B, P, K, Na, V, Ti, Cr, Ba, Y, Zr, Al, Ca) are highly fractionated into the augite phase and only Sr shows relative enrichment in the pigeonite.

Scanning ion micrographs of an Apollo 11 lunar basalt 10085 were used by Andersen and Hinthorne [34,35] to illustrate the fractionation of U, Th, Pb and REE into the accessory minerals apatite, whitlockite, zircon, baddeleyite, zirkelite (= zirconolite [36]) and tranquillityite. K, Ba, Rb and Sr are localized in K-rich, U- and Th-poor glasses commonly associated with these accessory phases. Although absolute determination of REE abundances by CARISMA-reduced IMMA analyses awaits final quantification, they have calculated REE fractionation patterns for these phases in arbitrary units with respect to the known abundances in chondritic meteorites [17, 21, 26, 27, 34, 35]. The various REE's within a single phase are in the correct relationship to each other and the final calibration will only change the absolute position of the fractionation curves for each mineral with respect to each other [27]. A selection of their REE fractionation curves for a number of lunar phases is shown in figure 5. In general,

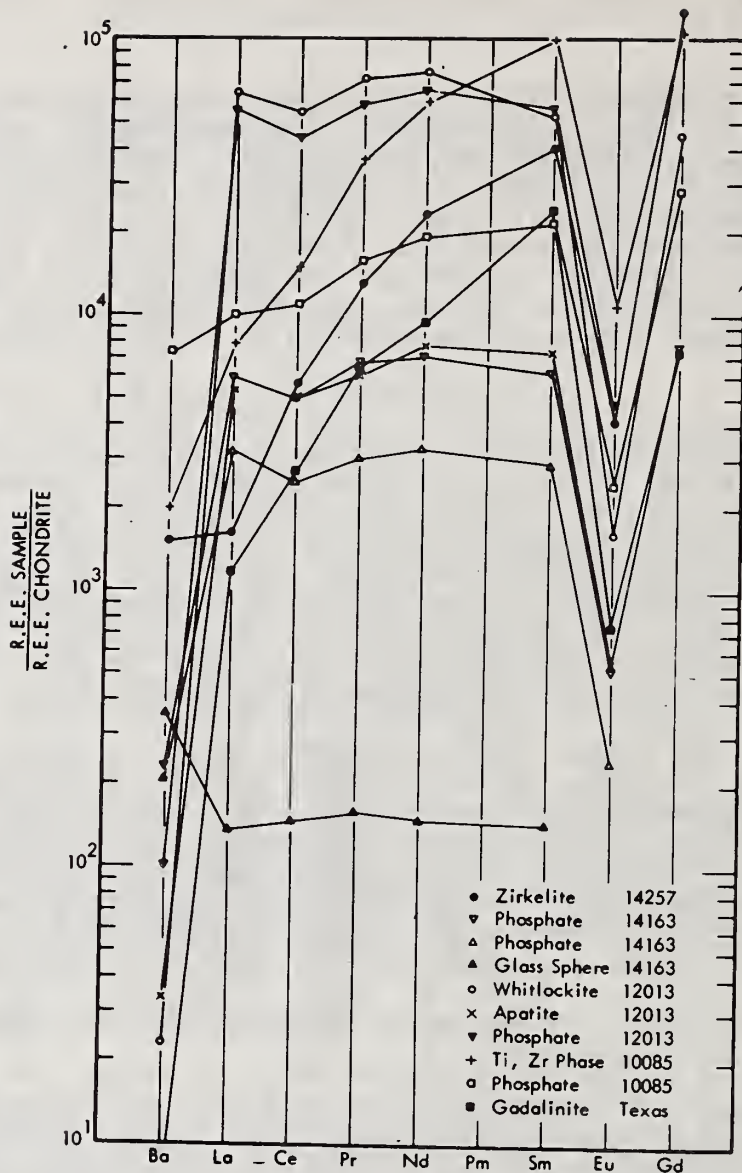


Figure 5. Relative REE fractionation patterns (chondrite normalized) of individual accessory phases in lunar rocks determined by IMMA analysis [35].

apatites and whitlockites show rather flat fractionation patterns for the light REE's (La to Gd) with a strong negative Eu anomaly, while Zr-rich phases (*i.e.*, baddeleyite, zirkelite = zirconolite, tranquillityite) tend to show patterns with the light REE's which rise

with increasing atomic number except for a strong negative Eu anomaly. One exception to this rule is in the Apollo 11 mare basalt 10047 where the apatites show rising patterns similar to the patterns normally seen for Zr-rich phases [26]. Lovering and Wark [37] have shown independently with electron microprobe analyses that the apatites in 10047 do exhibit this unusual rising REE fractionation pattern. Andersen and Hinthorne have also reported that Y-bearing armalcolites in Apollo 16 spinel troctolite 65785 show falling patterns from La to Sm, a negative Eu anomaly and rise to Gd [26] while plagioclase from Apollo 16 anorthosite 60025 shows a positive Eu anomaly in agreement with independently published bulk analyses [26]. They have commented that all accessory phases analyzed by them generally show larger Eu anomalies than do the bulk rock samples [26].

Lovering (this work—Table 6) has reported an IMMA analysis of trace element abundances in the same tranquillityite grain (20A-27) in Apollo 11 basalt 10047 which had also been analyzed for REE's [26] and lead isotopic composition (Table 9).

3. Light Element Geochemistry

Hinthorne and Ribbe [24] have reported IMMA analyses of B in a number of chondrodites and were able to show that B can substitute for as much as 6% of the Si atoms in this phase. However, in other humite minerals, the B substitution does not exceed 0.7% of the Si atoms in the structure.

The geochemical importance of trace determinations of H and F in minerals have been discussed by Hinthorne and Andersen [19]. They have developed a technique for H (detection limit ~100 weight ppm) and F (detection limit ~20 weight ppm) analysis by IMMA which depends on the comparison of H^+/Si^+ and F^+/Si^+ intensity ratios with working curves which have been constructed using similar data from standard materials of known compositions. This particular approach to the analytical problem was required because experience has shown that CARISMA, as it is presently constituted, is not complete enough to use reliably on elements with high ionization potentials such as F (17.42 eV) and H (13.60 eV).

Lovering (this work) has reported quantitative Li and B analyses of three glasses used as fission track geochronological standards (Table 4).

4. Isotope Ratio Analysis

a. General

Isotope ratio measurements by SIMS can be carried out either by an automatic, rapid peak-switching system [13] or by high speed mass scanning into a synchronized multichannel scaler [38].

Andersen and Hinthorne [38] have used the multichannel scaler approach to measure the $^{207}Pb/^{206}Pb$ composition of the C.I.T. reference

SIMS/IMMA

Table 9. IMMA analyses of lead isotopic composition and $^{207}\text{Pb}/^{206}\text{Pb}$ ages of uranium-rich phases in lunar rocks and fines.

Lunar locality	Rock type (NASA catalogue number)		Phase	Th/U (atomic)	$^{208}\text{Pb}/^{206}\text{Pb}$	$^{207}\text{Pb}/^{206}\text{Pb}$ ^a	Age ^b ($\times 10^9$ years)	Reference
Apollo 11	Anorthositic fragment in fines (10085)		Ti, Zr silicate (tranquillityite?)	2.16	0.59	0.40	3.90	[34]
			Baddeleyite (2rO_2)	0.49	0.133	0.455	4.11	
			REE phosphate	5.54	1.78	0.75	4.79	
	Mare Basalt (10047)		Zirconolite (20A-1)	1.92	0.502	0.3617 \pm 0.0090	3.75 \pm 0.05	[26]
			Tranquillityite (20A-27)	0.60	0.139	0.3659 \pm 0.0228	3.76 \pm 0.10	
Apollo 12	Dark/Light K-rich rock (12013)	Dark Region	Zircon	0.48	0.144	0.483	4.18	[34]
		Light Region	Whitlockite	20.4	3.64	0.49	4.19	
	Fines (12032)	2r-phase in K-rich vein	1.22	0.381	0.414	3.96		
		Zircon	0.79	0.294	0.408	3.94		
Apollo 14	2-4 mm Fines (14257)		Zirconolite	1.55	0.383	0.412	3.96	[34]
			Zirconolite	1.73	0.374	0.425	4.00	
	<1 mm Fines (14163)		Baddeleyite	--	0.34	0.406	3.93	
	Basalt (14310)		Y-REE oxide(?)	1.76	0.5003	0.3968 \pm 0.0081	3.96 \pm 0.03	[40]
Apollo 15	Basalt (15555)		Y-Zr oxide(?)	7.7	1.506	0.2732 \pm 0.0105	3.36 \pm 0.06	
			Y-Zr oxide(?)	--	0.8295	0.2888 \pm 0.0153	3.46 \pm 0.09	
	Basalt (15016)	Phosphate	--	1.302	0.3507 \pm 0.0576	3.75 \pm 0.27		
Apollo 16	Anorthositic gabbro (68415)		REE phosphate	1.72	0.3778	0.4006 \pm 0.0465	3.96 \pm 0.18	[26]
			Y-Zr phase	1.45	0.3982	0.4007 \pm 0.0740	3.96 \pm 0.28	
	Troctolitic anorthosite (65785)		Armalcolite (16)	1.67	0.388	0.4229 \pm 0.0526	3.99 \pm 0.19	
			Armalcolite (13)	1.20	0.316	0.4484 \pm 0.0383	4.07 \pm 0.13	
			Armalcolite (15)	1.08	0.308	0.409 \pm 0.1584	3.94 ^{+0.49} _{-0.79}	
Luna 20	Micro-breccia fragments in (22003)		REE phosphate	1.71	0.5046	0.4397 \pm 0.0122	4.12 \pm 0.04	[40]
			Y-Zr phase	1.34	0.3728	0.5418 \pm 0.0433	4.42 \pm 0.11	

^a ± 2 standard deviations.^b $^{207}\text{Pb}/^{206}\text{Pb}$ ages calculated using constants given in text (± 2 standard deviations).

lead sample and have concluded that IMMA instrumental factors will not lead to errors of precision or accuracy in Pb isotopic ratios much in excess of 1 to 2 percent (one standard deviation). It should be remembered that these conclusions refer to measurements on a pure lead nitrate sample and IMMA measurements of the isotopic composition of lead in geological materials may be complicated by interferences with other ionic species on the lead peaks in the secondary ion spectrum (see below).

b. Molecular ion interference corrections in lead isotope studies

Andersen and Hinthorne [17] have developed a correction program for molecular ions in the mass range of 202-210 for zircon which calculates corrected ^{204}Pb , ^{206}Pb , ^{207}Pb and ^{208}Pb relative ion intensities on the basis of the following interferences:

202	Zr ₂ O, Zr ₂ OH, HfSi
203	Zr ₂ O, Zr ₂ OH, HfSi
204	Zr ₂ O, Zr ₂ OH, HfSi, Pb
205	Zr ₂ OH, HfSi
206	Zr ₂ O, HfSi, HfO ₂ , Pb
207	Zr ₂ OH, HfSi, HfO ₂ H, Pb
208	Zr ₂ O, HfSi, HfO ₂ , Pb
209	HfSi, HfO ₂ , HfO ₂ H, Zr ₂ OH
210	HfSi, HfO ₂ , HfO ₂ H

In their method [17] the ion intensities at each mass unit peak in range 202-210 are measured and, since there are nine components and nine peaks, the interferences on each of the lead peaks may be calculated by properly ordering the corrections in a computer program. The largest corrections on the Pb isotopes is for Zr₂O and HfO₂ while the HfSi is small and Zr₂OH, HfO₂H are either minor or negligible.

Corrections for nonradiogenic Pb in minerals are normally based on ^{204}Pb abundances but this is usually small in Zr-rich phases and the observed $^{204}\text{Pb}^+$ ion intensity is usually less than the statistical variation on the total 204 peak measured. Andersen and Hinthorne [17] have also included in their lead isotope correction computer program a common lead correction based on the radiogenic $^{208}\text{Pb}/^{206}\text{Pb}$ predicted from the measured Th/U ratio in the mineral. This assumes no subsequent movement of Th relative to U, or of ^{208}Pb relative to ^{206}Pb .

The following decay constants and $^{238}\text{U}/^{235}\text{U}$ ratios, recently recommended by Tatsumoto *et al.* [39], have been used in all data reported here:

$$\lambda^{235} = 9.8485 \times 10^{-10} \text{ yr}^{-1} \quad \lambda^{238} = 1.5525 \times 10^{-10} \text{ yr}^{-1},$$

$$\lambda^{232} = 0.49475 \times 10^{-10} \text{ yr}^{-1} \quad ^{238}\text{U}/^{235}\text{U} = 137.88.$$

c. $^{207}\text{Pb}/^{206}\text{Pb}$ Geochronology

Andersen and Hinthorne [17] have reported IMMA-derived $^{207}\text{Pb}/^{206}\text{Pb}$ ages on zircons from two localities (Cardiff Mine, Ontario and Stillwater Complex) that have been previously analyzed and documented by conventional techniques. Their data, indicating ages of 1059 ± 39 m.y. for the Cardiff Mine zircons and 2838 ± 134 m.y. for the Stillwater Complex samples, are in excellent agreement with independently derived data published previously. This result is strong evidence in support of their conclusion that IMMA-derived lead isotopic compositions, when corrected by the procedure described above, are capable of producing accurate $^{207}\text{Pb}/^{206}\text{Pb}$ ages of U-enriched minerals within polished sections of rocks.

They have also examined a number of U-rich minerals in a variety of lunar rocks and soils ("fines") [34, 35, 38, 40] and a summary of their $^{207}\text{Pb}/^{206}\text{Pb}$, $^{208}\text{Pb}/^{206}\text{Pb}$, Th/U ratios and calculated $^{207}\text{Pb}/^{206}\text{Pb}$ ages for these phases is given in Table 9. All Pb isotopic ratios have been corrected for Zr_2O^+ , HfO_2^+ , YbO_2^+ , LuO_2^+ and CaO.BaO^+ interferences wherever applicable to the particular phase analyzed. However, for most phases, these corrections are usually $<0.1\%$. No common Pb corrections were applied because $^{204}\text{Pb}^+$ could not be detected. The Th/U atomic ratios were determined from observed ThO^+/UO^+ intensity ratios and are said by them to have an accuracy of about 10% [38] and are generally compatible with $^{208}\text{Pb}/^{206}\text{Pb}$ ratios.

They have concluded that model $^{207}\text{Pb}/^{206}\text{Pb}$ ages calculated from their IMMA analyses are generally consistent with ages determined by other workers using conventional Rb/Sr, K/Ar and Ar/Ar dating techniques (fig. 6). Their data also indicate a younger age for the "intrusive," light (K-rich) material relative to the dark matrix breccia of Apollo 12 rock 12013 which is generally consistent with a two-stage evolution of Pb in this rock proposed by Tatsumoto [41] on the basis of U-Th-Pb systematics.

d. U/Pb dating of zircons

Studies of the U/Pb systematics in zircon have shown that this mineral has the ability to retain some age evidence of an event which preceded the last significant metamorphic event in an area (see summary by Catanzaro [42]). Up to the present U/Pb dating has been confined to bulk samples of zircons separated from rocks, but IMMA has the capability of providing data on the $^{206}\text{Pb}/^{238}\text{U}$ and $^{207}\text{Pb}/^{235}\text{U}$ ratios (from which U-Pb dates are calculated) on micrometer areas of individual grains of zircons within polished thin sections of rocks.

Andersen and Hinthorne [17] have proposed a method for converting observed U (and Th) and Pb ion intensities measured by IMMA to absolute U and Pb atomic abundances on the basis of sputtering source temperatures estimated from observed UO^+/U^+ (and ThO^+/Th^+) ratios. Correction factors calculated from the measured UO^+/U^+ ratio for each

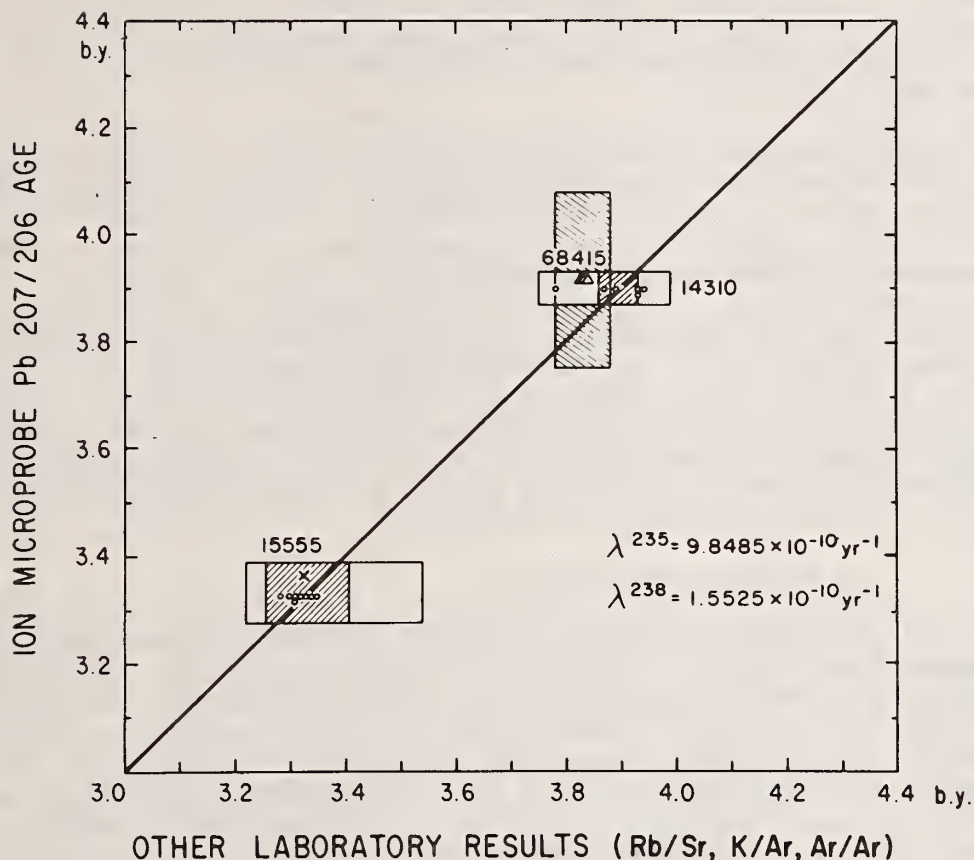


Figure 6. $^{207}\text{Pb}/^{206}\text{Pb}$ crystallization ages of individual U-rich accessory phases in lunar rocks from the Apollo 14 (14310), 15 (15555) and 16 (68415 sites calculated from IMMA analyses and compared (1:1 correlation line) with independent rock ages determined by $^{87}\text{Rb}/^{87}\text{Sr}$, $^{40}\text{K}/^{40}\text{Ar}$ and/or $^{40}\text{Ar}/^{39}\text{Ar}$ techniques [17]. IMMA errors shown are ± 1 standard deviation and other method errors include total range of ages published including standard deviations quoted.

analysis are applied to the 232, 238 and 206 sputtered ion intensities (after correcting the 206 peak for interferences and common Pb contribution as described above) to derive the $^{206}\text{Pb}/^{238}\text{U}$ atomic ratios. The $^{207}\text{Pb}/^{235}\text{U}$ ratio is calculated directly from the measured radiogenic $^{207}\text{Pb}/^{206}\text{Pb}$ ratio and the known $^{238}\text{U}/^{235}\text{U}$ ratio. The $^{206}\text{Pb}/^{238}\text{U}$ and $^{207}\text{Pb}/^{235}\text{U}$ ratios are then plotted on the "concordia" diagram and ages interpreted on the basis of presently accepted hypotheses for radiogenic lead evolution in zircons (see summary in [42]).

Using this approach, Andersen and Hinthorne [17] have plotted IMMA data for $^{206}\text{Pb}/^{238}\text{U}$ and $^{207}\text{Pb}/^{235}\text{U}$ measured on a number of individual

grains of a zircon sample from the Cardiff Mine, Ontario onto the "concordia" diagram and have shown that they fall on a 1040 m.y. isochron, in good agreement with independent ages measured by U/Pb, K/Ar and Rb/Sr techniques.

They have also reported U/Pb studies of U-enriched phases in the K-rich light areas which apparently penetrate the dark colored breccia matrix of unique Apollo 12 rock 12013 [17]. A single grain of Zr-Nb-Y-(Ti?) oxide, probably zirconolite, occurring in the light area was analyzed by IMMA and a discordant age of 3865 m.y. calculated from the "concordia" diagram. Similarly a zircon from the dark breccia matrix was studied by them and discordant age of about 4470 m.y. calculated. Subsequent work (J. R. Hinthorne—personal communication) on other U-rich phases in both light and dark regions have confirmed these ages. The apparent older age of the dark matrix relative to the "intrusive" light material is consistent both with $^{207}\text{Pb}/^{206}\text{Pb}$ ages discussed above (see Table 9) and also generally with a two-stage model for Pb evolution on bulk samples proposed by Tatsumoto [41].

e. Pb isotope Cosmochemistry

On the basis of IMMA studies, Hinthorne and Andersen [43] have reported that Pb (2-35 weight ppm ^{206}Pb), associated with goethite alteration rims around troilite in the Apollo 16 "rusty rock" 66095, has $^{207}\text{Pb}/^{206}\text{Pb}$ and $^{208}\text{Pb}/^{206}\text{Pb}$ ratios which are unsupported by either Th and/or U. Similarly Meyer and McKay [44] have studied the isotopic composition of Pb occurring as a thin coating (100-1000 Å) on the orange glass spheles occurring in the Apollo 17 "orange soil" (74220). Their data indicate a primitive isotopic composition for this volatile Pb indicating a source from a U-poor, volatile element rich environment inside the moon and not from meteoritic contamination.

f. $^{87}\text{Rb}/^{87}\text{Sr}$ Geochronology

The use of relatively low resolution secondary ion mass spectrometers in most SIMS instruments poses problems in the $^{87}\text{Rb}/^{87}\text{Sr}$ dating of many silicate minerals (*e.g.*, plagioclase feldspars) due to the following selected spectral overlaps:

- 84 CaSiO, Si₃, Sr
- 85 CaSiO, Si₃, Rb
- 86 Al₂O₂, CaAlO, Si₃, Sr
- 87 CaAlO, SiAlO₂, Si₃, Rb, Sr
- 88 SiAlO₂, Si₂O₂, Si₃, Sr

Meyer *et al.* [14] have concluded that, although not all these interferences are significant (*e.g.*, $^{28}\text{Si}_2^{16}\text{O}_2^+$ interference on $^{88}\text{Sr}^+$ is <3% at 200 weight ppm Sr in plagioclase), the overall uncertainties of all possible molecular ion interferences means that present instruments are unsuitable for Rb/Sr dating. On the other hand it is highly probable that correction procedures can be developed for specific mineral matrices using the approach used by Andersen and Hinthorne [17]

and described above in correcting molecular ion interferences on lead peaks. In some cases molecular ion interferences will be negligible and Andersen and Hinthorne [13] have reported good agreement between the Rb/Sr isochron defined by a suite of K-feldspars on the basis of previous isotope dilution studies, and IMMA data for $^{87}\text{Rb}/^{86}\text{Sr}$ and $^{87}\text{Sr}/^{86}\text{Sr}$ isotope ratios on the same samples. Their results suggest that, in these old Rb-enriched phases, KSiO^+ interferences on the ion peaks measured at mass 85, 86 and 87 are negligible.

g. $^7\text{Li}/^6\text{Li}$ and $^{11}\text{B}/^{10}\text{B}$ Ratio Measurements in Cosmochemistry

Balsiger *et al.* [45] have briefly discussed current nucleosynthesis models for the origin of the light nuclei D, Li, Be and B which either assume their formation in the solar system or else in earlier galactic processes. The solar system model alone should lead to local variations in the $^7\text{Li}/^6\text{Li}$ and $^{11}\text{B}/^{10}\text{B}$ ratios if the primitive solar system material was not subsequently thoroughly mixed. Consequently considerable effort has gone into attempting to document variations in these ratios within chondritic meteorites.

An early SIMS study by Poschenrieder *et al.* [46] suggested local variations of $^7\text{Li}/^6\text{Li}$ ratios in the Holbrook chondrite from 9.5 to 27.9. However later $^7\text{Li}/^6\text{Li}$ ratio measurements by SIMS in a number of chondrites [47, 48, 49, 50] showed values varying by less than $\pm 10\%$. Preliminary $^7\text{Li}/^6\text{Li}$ ratios have been measured by J. R. Hinthorne (personal communication) in W-1 rock glass, a South African zircon, glass in Apollo 15 sample 15017 and in various silicate components of the Allende carbonaceous chondrite using the A.R.L.-IMMA. His data indicate all $^7\text{Li}/^6\text{Li}$ ratios measured lie in the range 11.9 to 12.3 and are indistinguishable from each other and consistent with the results of bulk $^7\text{Li}/^6\text{Li}$ ratios measured in a number of separated components from a variety of meteorites by Balsiger *et al.* [46].

5. Surface Analysis

Hofmann *et al.* [51] have used the ability of IMMA to measure the isotopic composition of a solid as a function of depth in the solid with a depth resolution of tens of angstroms to study the self-diffusion of potassium in biotite. They heated a biotite sample in an alkali chloride solution enriched with ^{41}K for 41 days at 650°C and 2000 bars and, on IMMA analysis for $^{39}\text{K}/^{41}\text{K}$ ratios, found a decrease with depth indicating potassium diffusivity in the a- and b- directions to be greater than the c- direction by 2 to 4 orders of magnitude. In the c- direction, $D = 1 \times 10^{-17} \text{ cm}^2 \text{ sec}^{-1}$ with an estimated error of a factor of 10 which was completely consistent with values calculated from independent methods previously.

Clearly the surface analysis capability of IMMA provides an important tool for diffusion and surface composition studies in mineral grains and intergranular thin film analysis in rocks.

VI. FUTURE DEVELOPMENTS

1. SIMS Instrumentation

The major need is for the development of SIMS instruments with secondary ion mass spectrometers which have greatly improved resolution (at least to 3000 [18] and preferably higher) coupled with high transmissivities so that present analytical sensitivities can be retained or even improved further without surrendering the micrometer-diameter spatial resolution of the analysis area. These requirements pose severe design criteria and it may yet prove impossible to meet them all using current concepts of mass spectrometer design. An alternative, though possibly less satisfying, approach is to correct for molecular ion interference by spectrum stripping using computers. Colby [16] and Andersen and Hinthorne [17] have shown that this approach can successfully overcome the limited resolution of most present day SIMS instruments in many analytical situations.

There is also a need to improve spatial resolution of the SIMS analysis region by decreasing primary beam diameters without seriously sacrificing analytical sensitivity. Current estimates suggest that 1000 Å will be the useful limit to ion beam diameters from duoplasmatron ion sources [5].

The need for independently measured abundances of internal standard elements, for use in CARISMA reduction of IMMA analytical data with the option 3 mode, has enhanced the relevance of combined electron microprobe/IMMA instrument designed by Liebl [52]. This instrument

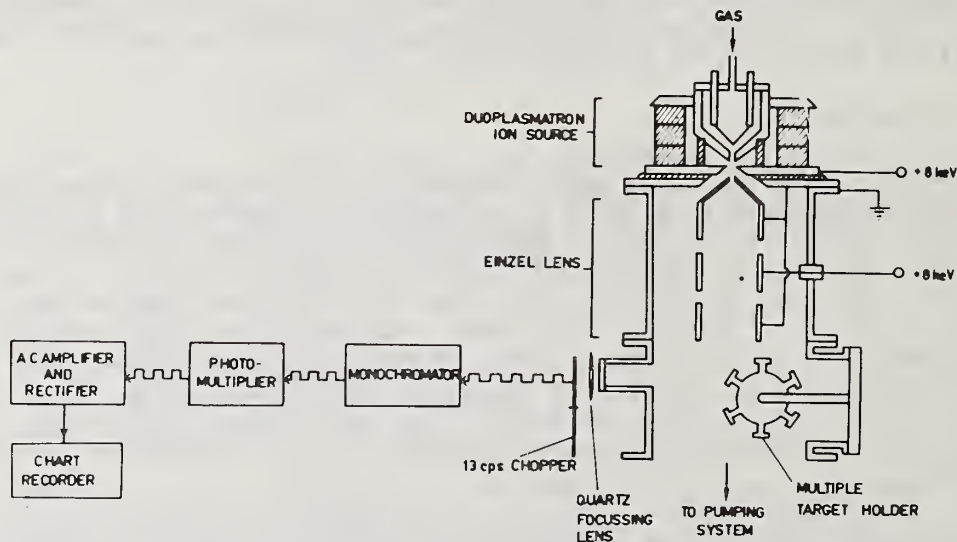


Figure 7. Schematic diagram of ion beam spectrochemical analyzer (IBSCA) developed for quantitative analysis of geological materials [54].

would allow elemental abundance determinations to be made at an identical sample site first by electron microprobe and then by IMMA.

2. Quantitative IMMA Analysis

Considerable modification of the CARISMA approach to quantitative IMMA analysis is required in the use of those elements with high ionization potential (*e.g.*, F, H) and those which have high oxide ion intensities in the secondary mass spectrum (*e.g.*, Zr, Hf, Ta, REE, etc.). But there is still a major need to unequivocally demonstrate (and further improve where necessary) the accuracy of the CARISMA-reduction of IMMA data by the preparation of critically homogeneous trace element standard samples with geologically relevant matrices. The need for such standards is critical if the geochemical community is to generally accept the accuracy of CARISMA-reduced IMMA analysis for trace element abundances in geological materials.

3. IBSCA Analysis

Tsong and McLaren [53] have shown that the bombardment of a solid sample with an energetic ion beam causes the spontaneous emission of ultraviolet and visible radiation as well as the emission of sputtered secondary ions. This emitted radiation has been shown by them to contain the characteristic lines of the constituent elements in the sample and an instrument known as the ion beam spectrochemical analyzer (IBSCA) has been constructed to analyze the radiation (fig. 7). The potential of the IBSCA technique as a quantitative analytical tool has been empirically demonstrated by comparison of IBSCA analyses of a suite of plagioclase samples with analyses independently determined by electron microprobe. Further developments suggest trace element sensitivities for the IBSCA technique are possible [54].

The general theory of quantitative IBSCA analysis has been discussed by Tsong and McLaren [54] who have shown that the intensity of a spectral line corresponding to a particular element in the sample is proportional to the product of the rate of mass loss in sputtering and the weight concentration of that element in the sample. Consequently, if the mass loss during sputtering can be measured, it is possible to calculate the concentration of the element in the sample by direct comparison of intensities with a standard sample.

Clearly the limitation of the method at present is the difficulty in accurately measuring the mass loss of the sample during sputtering. However the relative simplicity and cheapness [53] of the apparatus required for IBSCA analysis will encourage the further development of the technique in the near future.

VII. ACKNOWLEDGMENTS

The IMMA analyses were carried out during the tenure of a N.A.S.A. Senior Research Associateship at Goddard Space Flight Center. The

electron microprobe data were largely determined by D. A. Wark under a grant to me from the Australian Research Grants Committee. My own experience with IMMA quantitative analysis has drawn heavily on the pioneering work of C. A. Andersen, and J. R. Hinthorne of the Hasler Research Center (Applied Research Laboratories) and I gratefully acknowledge their ever-ready assistance, and the co-operation in data reduction and in providing independent IMMA analyses of some phases in Tables 2 to 8. I must also acknowledge the considerable support given to me by my colleagues K. F. J. Heinrich and R. J. Myklebust (National Bureau of Standards) and L. S. Walter and H. Thomas (N.A.S.A. Goddard Space Flight Center).

VIII. REFERENCES

1. Smith, D. G. W. and Rucklidge, J. C., Electron Microprobe Analysis in the Earth Sciences, Advances in Geophysics 16, 57-154 (1973).
2. Griggs, D. T., Hydrolytic Weakening of Quartz and Other Silicates, Geophys. J. Roy. Astron. Soc. 14, 19-31 (1967).
3. Castaing, R. and Slodzian, G., Microanalyse par Émission Ionique Secondaire, J. Microscopie (Paris) 1, 395-410 (1962).
4. Liebl, H., Ion Microprobe Mass Analyzer, J. Appl. Phys. 38, 5277-5283 (1967).
5. Liebl, H., Ion Microprobe Analysers: History and Outlook, Anal. Chem. 46, 22A-30A (1974).
6. Robinson, C. F., Ion Microprobe Instrumentation in Microprobe Analysis, Andersen, C. A., ed., pp. 507-530, Wiley-Interscience, New York (1973).
7. Nakamura, K., Aoki, S., Tamura, H. and Doi, H., A New Technique for Analyzing Insulating Materials by means of the Ion Microanalyzer in Proceedings of the Sixth International Conference on X-Ray Optics and Microanalysis, Shinoda, G., Kohra, K. and Ichinokawa, T., eds., pp. 447-454, Univ. of Tokyo Press, Japan (1972).
8. Andersen, C. A., Roden, H. J. and Robinson, C. F., Negative Ion Bombardment of Insulators to Alleviate Surface Charge-Up, J. Appl. Phys. 40, 3419-3420 (1969).
9. Lovering, J. F., Ion Microprobe Mass Analyser (IMMA): Ultimate Weapon for the Geochemist (?), Comments on Earth Science: Geophysics 3, 153-163 (1973).
10. Andersen, C. A., Progress in Analytic Methods for the Ion Microprobe Mass Analyzer, Int. J. Mass Spectrom. Ion Phys. 2, 61-74 (1969).

Geochemical Applications

11. Andersen C. A., Analytic Methods for the Ion Microprobe Mass Analyzer. Part II. Int. J. Mass Spectrom. Ion Phys. 3, 413-428 (1970).
12. Andersen, C. A. and Hinthorne, J. R., Thermodynamic Approach to the Quantitative Interpretation of Sputtered Ion Mass Spectra, Anal. Chem. 45, 1421-1438 (1973).
13. Andersen, C. A. and Hinthorne, J. R., Ion Microprobe Mass Analyzer, Science 175, 853-860 (1972).
14. Meyer, C., Jr., Anderson, D. H. and Bradley, J. G., Ion Microprobe Mass Analysis of Plagioclase from "Non-Mare" Lunar Samples in Proc. Fifth Lunar Sci. Conf., Geochim. Cosmochim. Acta, Suppl. 5 1, 685-706 Pergamon.
15. Hinthorne, J. R. and Andersen, C. A., Ion Microprobe Mass Analyzer Operation Manual, Sec. 3, pp. 47-48, Applied Research Laboratories, Sunland, California (1972).
16. Colby, J. W., Ion Microprobe Mass Analysis in Scanning Electron Microscopy and Electron Probe Microanalysis, Goldstein, J. I. and Colby, J. W., eds., Plenum Press, New York (1975).
17. Andersen, C. A. and Hinthorne, J. R., Ion Microprobe Determinations of Ages of Individual Minerals and the Distribution of U, Th, Pb and the KREEP Elements in Returned Lunar Material, Progress Report Lunar Sample Research Program NASA Contract No. NAS 9-13299 (1974).
18. Bence, A. E., Electron and Ion Probes in Mineralogy (abstract), Geol. Soc. Amer. Abstr. Programs 5, 546-547 (1973).
19. Hinthorne, J. R. and Andersen, C. A., Microanalysis of Fluorine and Hydrogen in Silicates with the Ion Microprobe Mass Analyser, Amer. Mineral. 60, 143-147, (1975).
20. Andersen, C. A., Analytic Methods and Applications of the Ion Microprobe Mass Analyzer in Microprobe Analysis, Andersen, C. A., ed., pp. 531-553, Wiley-Interscience, New York (1973).
21. Stout, J. H. and Hinthorne, J. R., Comparative Ion Microprobe and Electron Microprobe Analyses of Coexisting Amphiboles and Garnet (abstract), Geological Soc. Amer., Annual Meeting (Washington, D. C.), Abstracts Program pp. 723-724 (1971).
22. Andersen, C. A. and Hinthorne, J. R., Ion Microprobe Mass Analysis of Lunar Samples, Progress Report Lunar Sample Research Program NASA Contract No. 9-11566 (1971).
23. Havette-Ledebt, A., Examen de Certains Problèmes Méthodologiques Posés par l' utilisation de l'Analyseur Ionique en Géologie.

- Application à l'Étude de Quelques Sujets Pétrologiques, Thesis, Université de Paris-Sud, Centre d'Orsay, p. 1-149 (1974).
24. Hinthorne, J. R. and Ribbe, P. H., Determination of Boron in Chondrodite by Ion Microprobe Mass Analysis, Amer. Mineral. 59 1123-1126 (1974).
 25. Jérôme, D. Y. and Slodzian, G., Utilisation du Microanalyseur Ionique en Géochimie Application à la météorite de Juvinas, Bull. Soc. Française Miner. Cristallog. 94, 538-548 (1971).
 26. Andersen, C. A. and Hinthorne, J. R., Ion Microprobe Mass Analysis of Lunar Samples, Progress Report Lunar Sample Research Program NASA Contract No. NAS 9-13299 (1973).
 27. Andersen, C. A. and Hinthorne, J. R., Ion Microprobe Mass Analysis of Lunar Samples, Progress Report Lunar Sample Research Program NASA Contract No. NAS 9-11566 (1972).
 28. Schnetzler, C. C. and Philpotts, J. A., Genesis of the Calcium-Rich Achondrites in the Light of Rare Earth and Barium Concentrations in Meteorite Research, Millman, P. M., ed., Reidel, Dordrecht (Holland), pp. 206-216 (1969).
 29. Taylor, H. P., Duke, M. B., Silver, L. T. and Epstein, S., Oxygen Isotope Studies of Minerals in Stony Meteorites, Geochim. Cosmochim. Acta 29, 489-512 (1965).
 30. Andersen, C. A., Hinthorne, J. R. and Fredriksson, K., Ion Microprobe Analysis of Lunar Material from Apollo 11, Proc. Apollo 11 Lunar Sci. Conf., Geochim. Cosmochim. Acta. Suppl. 1, Vol. 1, 159-167 (1970).
 31. Fredriksson, K., Nelen J., Noonan A., Andersen, C. A. and Hinthorne, J. R., Glasses and Sialic Components in Mare Procellarum Soil, Proc. Second Lunar Sci. Conf., Geochim. Cosmochim. Acta Suppl. 2, Vol. 1, 727-735 (1971).
 32. Prinz, M., Dowty, E., Keil, K., Andersen, C. A. and Hinthorne, J. R., Ion Microprobe Study of High-Alumina Basaltic Glasses in Lunar Science IV, Chamberlain, J. W. and Watkins, C., eds., pp. 603-605, Lunar Science Institute, Houston, Texas (1973).
 33. Bence, A. E. and Autier, B., Secondary Ion Analysis of Pyroxenes from Two Porphyritic Lunar Basalts in The Apollo 15 Lunar Samples, Chamberlain, J. W. and Watkins, C., eds., pp. 191-194, Lunar Science Institute, Houston, Texas (1972).
 34. Andersen, C. A. and Hinthorne, J. R., U, Th, Pb and REE Abundances and $^{207}\text{Pb}/^{206}\text{Pb}$ Ages of Individual Minerals in Returned Lunar Material by Ion Microprobe Mass Analysis, Earth Planet. Sci. Letters 14, 195-200 (1972).

Geochemical Applications

35. Andersen, C. A. and Hinthorne, J. R., U, Th, Pb and REE Abundances and Pb 207/206 Ages of Individual Minerals in Returned Lunar Material by Ion Microprobe Mass Analysis in Lunar Science III, Watkins, C., ed., pp. 21-23, Lunar Science Institute, Houston, Texas (1972).
36. Wark, D. A., Reid, A. F., Lovering, J. F. and El Goresy, A., Zirconolite (versus Zirkelite) in Lunar Rocks in Lunar Science IV, Chamberlain, J. W. and Watkins, C., eds. pp. 764-766 (1973).
37. Lovering, J. F. and Wark, D. A., Rare Earth Element Fractionation in Phases Crystallizing from Lunar Late-Stage Magnetic Liquids, in Lunar Science V, pp. 463-465, Lunar Science Institute, Houston, Texas (1974).
38. Andersen, C. A. and Hinthorne, J. R., $^{207}\text{Pb}/^{206}\text{Pb}$ Ages of Individual Mineral Phases in Lunar 20 Material by Ion Microprobe Mass Analysis, Geochim. Cosmochim. Acta. 37, 745-754 (1973).
39. Tatsumoto, M., Knight, R. J. and Allegre, C. J., Time Differences in the Formation of Meteorites as Determined from the Ratio of Lead-207 to Lead-206, Science 180, 1279-1283 (1973).
40. Andersen, C. A. and Hinthorne, J. R., $^{207}\text{Pb}/^{206}\text{Pb}$ Ages and REE Abundances in Returned Lunar Material by Ion Microprobe Mass Analysis in Lunar Sciences IV, Chamberlain, J. W. and Watkins, C., eds., pp. 37-39, Lunar Science Institute, Houston, Texas (1973).
41. Tatsumoto, M., U-Th-Pb Age of Apollo 12 Rock 12013, Earth Planet. Sci. Letters 9, 193-200 (1970).
42. Catanzaro, E. J., The Interpretation of Zircon Ages in Radiometric Dating for Geologists, eds. Hamilton, E. J. and Farguhar, R. M., Interscience, New York, pp. 225-258 (1968).
43. Hinthorne, J. R. and Andersen, C. A., Uranium-Lead and Lead-Lead Ratios in Lunar Samples 66095 and 12013 by Ion Microprobe Mass Analysis in Lunar Science V, pp. 337-339, Lunar Science Institute, Houston, Texas (1974).
44. Meyer, C., Jr. and McKay, D. S., Ion Microprobe Analyses of Lead and Other Volatiles in Lunar Sample 74220 (Abstract), Los Angeles (California) Meeting of the Meteoritical Society (1974).
45. Balsiger, H., Geiss, J., Groegler, N. and Wyttenbach, A., Distribution and Isotopic Abundance of Lithium in Stone Meteorites, Earth Planet. Sci. Letters 5, 17-22 (1968).
46. Poschenrieder, W. P., Herzog, R. F., and Barrington, A. E., The Relative Abundance of the Lithium Isotopes in the Holbrook Meteorite, Geochim. Cosmochim. Acta 29, 1193-1195 (1965).

47. Gradsztajn, E., Salome, M., Yaniv, A. and Bernas, R., Isotopic Analysis of Lithium in the Holbrook Meteorite and in Terrestrial Samples with a Sputtering Ion Source Mass Spectrometer, Earth Planet. Sci. Lett. 3, 387-393 (1967).
48. Bernas, R., Gradsztajn, E. and Yaniv, A., Isotopic Composition of Lithium in Some Meteorites and the Role of Neutrons in the Nucleosynthesis of the Light Elements in the Solar System in Meteorite Research, Millman, P. M., ed., Reidel, Dordrecht (Holland), pp. 123-131 (1969).
49. Nishimura, H. and Okano, J., Preliminary Analysis of Meteorites with an Ion Probe Mass Analyzer (in Japanese), Mass Spectros. Japan 18, 894-904 (1970).
50. Nishimura, H., Fujiwara, T. and Okano, J. Elements and Isotope Analysis with the Ion Probe Mass Spectrometer in Proceedings of the Sixth International Conference on X-Ray Optics and Microanalysis, Shinoda, G., Kohra, K. and Ichinokawa, T., eds., pp. 431-437, Univ. of Tokyo Press, Japan (1972).
51. Hofman, A. W., Giletti, B. J., Hinthorne, J. R., Andersen, C. A. and Comaford, D., Ion Microprobe Analysis of a Potassium Self-Diffusion Experiment in Biotite, Earth Planet. Sci. Letters 24, 48-52 (1974).
52. Liebl, H., Design of a Combined Ion and Electron Microprobe Apparatus, Int. J. Mass Spectrom. Ion Phys. 6, 401-412 (1971).
53. Tsong, I. S. T. and McLaren, A. C., Quantitative Spectrochemical Analyses of Feldspars by Ion Bombardment, Nature 248, 43-45 (1974).
54. Tsong, I. S. T. and McLaren, A. C., An Ion Beam Spectrochemical Analyzer - With Application to the Analysis of Rock Forming Silicates, Spectrochim. Acta (In press, 1975).

FACTORS THAT INFLUENCE AN ELEMENTAL DEPTH CONCENTRATION PROFILE

J. A. McHugh

General Electric Company
Knolls Atomic Power Laboratory
Schenectady, New York 12301

One of the attractive capabilities of secondary ion mass spectrometry (SIMS) is concentration profiling with high depth resolution for both major and minor constituents. The general procedure for producing a SIMS depth profile is to monitor the secondary ion signal of an element of interest as a function of sputter time. In a uniform matrix, time can be translated to depth through suitable calibration experiments (known film thickness, crater depth measurements, sputter yield, *etc.*).

Figures 1 and 2 demonstrate the depth profiling capability of SIMS. Figure 1 is a phosphorus profile from a Ta_2O_5 film having a ^{31}P -rich layer located 230 Å below the surface. The true width (full width at half maximum) of the layer lies somewhere in the range of 50-70 Å. The anodically produced amorphous Ta_2O_5 film sputters uniformly and thus forms a good test matrix. The profile was obtained by monitoring the $^{31}P^+$ secondary ion current as a function of sputtering time (which is proportional to the amount of film removed). The time scale was converted to Angstrom units (Å) by measuring the time to sputter through a known thickness of Ta_2O_5 . The sputter ion beam was O_2^+ at 3.5 keV. A number of effects must be considered and kept under control to produce a profile that approaches the true concentration gradient (for example fig. 1). These factors will be discussed shortly.

Figure 2 is also a profile produced from a Ta_2O_5 film; however, this time the interest is directed at a particular isotope of an element rather than the element itself. It demonstrates the value of the isotopic analysis capability of SIMS which is especially valuable in diffusion and ion implantation studies.

The film was anodically produced in three steps. The second anodization was carried out in an electrolyte enriched in $H_2^{18}O$. Each layer is about 1000 Å thick. This particular profile was produced from a 50 x 50 μm area on the sample. $Ta^{18}O^+$ was monitored as the measure of the ^{18}O level. The $Ta^{18}O^+$ signal from layer 1 and 3 represent the ^{18}O contribution from normal oxygen (~ 0.2 percent). Approximately 2 percent of the oxygen atoms were ^{18}O in the enriched layer. The leading and

trailing edges of the profile can give information on the resolution of the profiling method and information on the transport of film constituents during film formation.

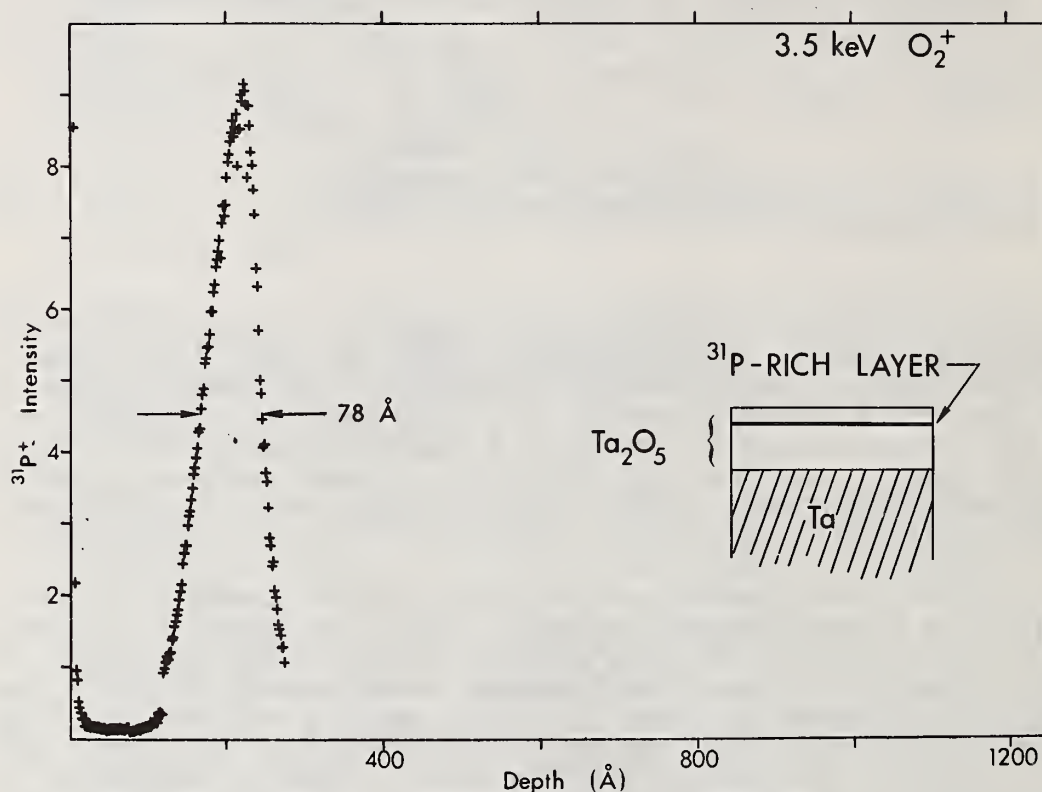


Figure 1. Phosphorus depth profile generated by 1.75 keV ^{16}O bombardment (O_2^+ at 3.5 keV). The FWHM of the distribution is 78 \AA . A 1050 \AA Ta₂O₅ film with a ^{31}P -rich layer located 230 \AA below the surface was profiled with an ARL ion microprobe.

The factors that influence an elemental concentration profile (those factors which produce a distorted representation of the true concentration gradient) can be divided into two classes: Instrumental Effects and Ion-Matrix Effects. For the instrumental effects, one has some control over reducing or eliminating them. One has very little or no control over ion-matrix effects.

Depth Profiles

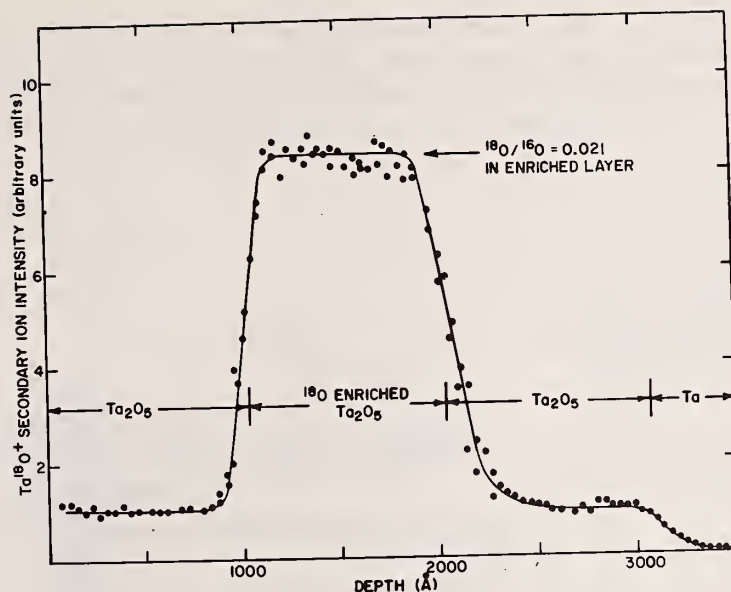


Figure 2. The depth concentration profile of ^{18}O in a Ta_2O_5 sample containing a layer enriched in ^{18}O . The profile was performed with 8.5 keV N_2^+ on an ARL ion microprobe and the monitor of the ^{18}O concentration was $\text{Ta } ^{18}\text{O}^+$. The ^{18}O is ~ 2 percent of the oxygen in the enriched layer. The $\text{Ta } ^{18}\text{O}^+$ signal preceding and following the enriched layer peak is due to the ^{18}O level in normal oxygen.

I. INSTRUMENTAL EFFECTS

The instrumental factors that must be considered are: 1) uniformity of the primary ion current density, 2) constancy of the primary ion current, 3) redeposition, 4) memory, 5) primary ion beam tailing and the nonfocused component, 6) chemical purity of the primary ion beam and 7) residual gas impurities.

It is virtually impossible to extract meaningful depth profile information from SIMS data unless one maintains constant primary ion intensity and uniform primary ion current density over the secondary ion extraction area of the sample. Uniform primary ion current density is produced usually by defocusing a static or stationary beam, or by sweeping a beam in raster fashion over the sample surface to produce a region of uniform current density. Constant primary ion current is desired so that the penetration rate remains constant; therefore, time is directly proportional to depth in a uniform matrix. Redeposition [1,2] and memory will also distort a profile. The influence that these first four points have on a profile is illustrated in figure 3.

The secondary ion intensity of the layer species is measured as a function of time. The ideal profile is indicated in the tail region by

the dashed curve. For a stationary primary ion beam with nonuniform current density and a secondary ion analyzer whose information zone extends over the complete beam diameter, a distorted profile (as indicated in fig. 3) is produced because of contributions from the crater edge.

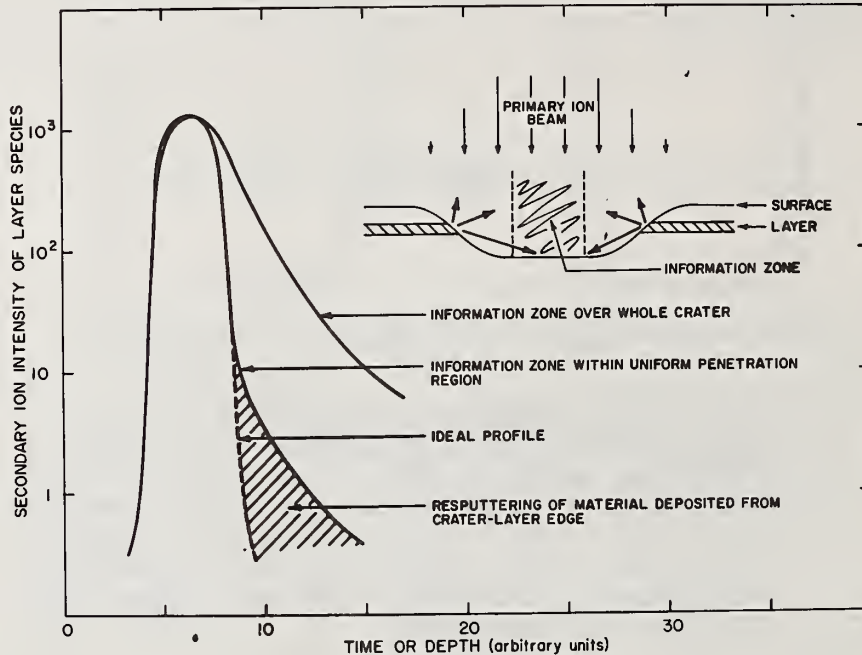


Figure 3. Illustration of a concentration profile of a sub-surface layer and various instrumental factors that produce a distorted profile of the true distribution.

We can restrict the information zone to the area of uniform penetration and remove most of the tail. This can be accomplished by 1) having the uniform region much larger than the acceptance area of the secondary ion analyzer, 2) in the direct-imaging analyzer by selective aperturing, and 3) in the scanning ion probe by gating the ion detector on when the rastered primary ion beam is in the region of uniform penetration. Even with the information zone restricted to the uniform penetration region, a distortion of the ideal profile can result from resputtering of redeposited material or from contamination of the surface by layer species that have a source elsewhere in the instrument — "memory."

The tail and the nonfocused component of the primary ion beam are important factors to be considered in scanning ion probe type instruments—both for depth profiling of trace constituents and trace element analysis in general. Figure 4 schematically depicts this situation. The nonfocused component can be as high as 0.1 to 1 percent

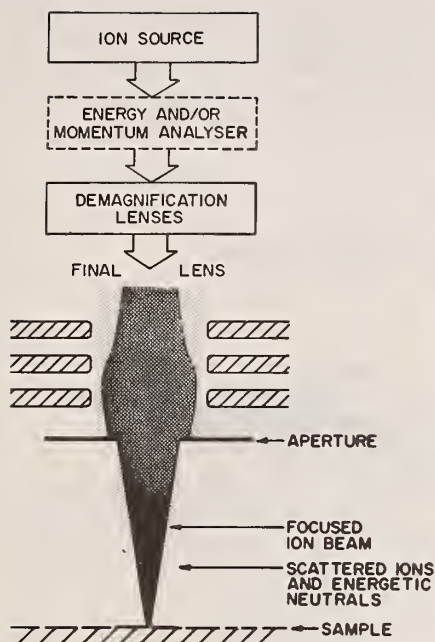


Figure 4. Schematic representation of the scattered ion and neutral component of a focused ion beam.

of the total number of beam particles, and it depends on lens design, residual gas pressure in the primary ion column, location and size of apertures and the geometrical arrangement of the column elements. A significant energetic particle component falling outside the area of interest, and over a large area of the sample, can create serious problems in trace analysis and depth profiling. The problem is most severe when the elements of the primary column are on a common axis, and this axis intersects the ion optic axis of the secondary ion analyzer. Reducing the size of the secondary analyzer acceptance area (at the sample surface) and deflecting the primary ion beam so that the neutral and scattered-ion impact region is removed from the focused beam impact point is one solution to this problem.

A partial solution to the above problem is illustrated in figure 5. The secondary ion emission induced by the nonfocused component illuminating the contaminant layer can be suppressed by overcoating the sample with a substance that is of no consequence in an analysis or depth profile. Carbon is a very good choice for a number of reasons: 1) it gives a very pure film, 2) it is conducting, and 3) the secondary ion yields are low from carbon surfaces. This technique is very beneficial for depth profiles of elements that are major surface contaminants and for the general trace analysis of solids for constituents which are also major surface contaminants. It is also useful in micro-area analyses of O_2 , N_2 and H_2 in reactive metals.

The chemical purity of the primary beam is important to prevent implantation of the sample with elements of interest in an analysis. For example, a 1 ppm impurity in the primary ion beam would appear as 0.1 ppm atomic concentration in the solid (assuming that sputtering has proceeded to the point of exposing the primary ion implant region). Especially important are solids analyses for the elements O_2 , N_2 and H_2 . Mass analysis of the primary ion beam eliminates this problem.

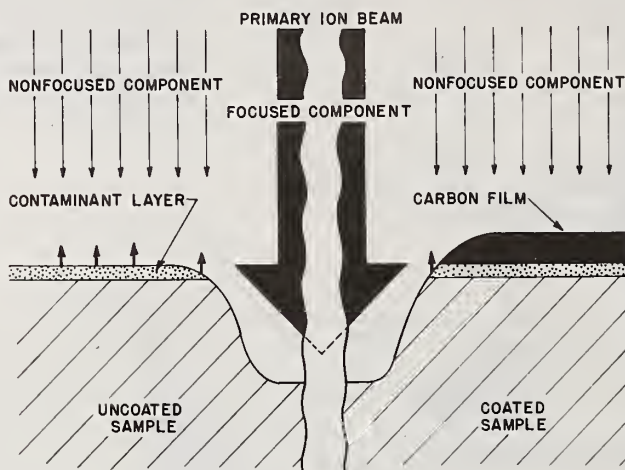


Figure 5. An illustration of the effect that a carbon overcoating has on suppressing the secondary ion emission from points other than the analysis point. It reduces the problems introduced by the tail of the focused primary ion beam and the nonfocused component of the beam.

Recontamination of the surface by residual gases complicates solids analyses directed at determining the bulk concentration of these elements. This problem is brought out in the microarea analysis of N_2 in Nb. A calibration curve is shown in figure 6. The measure of the nitrogen level is the NbN^+/Nb^+ ratio. Four standards were analyzed: 83, 521, 618 and 1055 ppm N_2 by weight. The uncorrected experimental data and the background corrected calibration curves are given. At the recontamination levels present in the instrument, the analysis of N_2 at levels below a few hundred ppm is virtually impossible (background in this specific instance is ~ 600 ppm). The cross hatched region shows the typical variation of the uncorrected experimental curve for different instrument and sample conditions. Higher current density and improved primary ion beam focusing reduces this effect. However, one cannot escape this problem without some means to limit the information zone to the high current density region of the primary ion beam. It is clear from figure 6 that depth profiles covering a wide concentration range can encounter problems. Similar effects result from memory and redeposition phenomena.

Depth Profiles

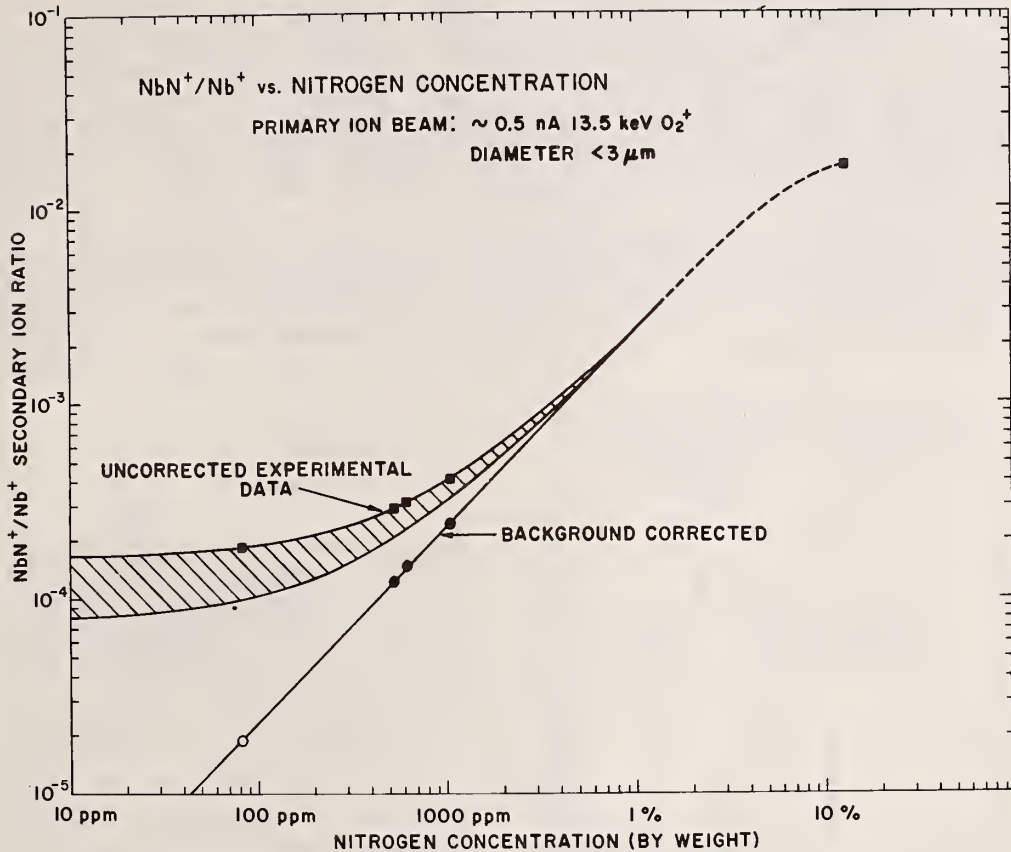


Figure 6. Quantitative working curve for the determination of nitrogen in Nb using an ARL ion microprobe. The NbN⁺/Nb⁺ secondary ion ratio is used as the measure of nitrogen in the Nb standards. The departure of the experimental curve from the corrected curve is due to a background NbN⁺ signal from N₂ recontamination of the surface. Higher current density and optimized current density distribution in the focused primary ion beam can improve the above results; however, it can not completely eliminate the effect.

II. ION MATRIX EFFECTS

The major factors that affect a depth concentration profile which can be classified as ion matrix effects are: 1) the mean escape depth of secondary ions, 2) recoil implantation, 3) molecular ion interferences, 4) primary ion beam induced diffusion of matrix species, 5) nonuniform sputter removal of matrix layers, and 6) implanted primary ion chemical and lattice damage effects.

The escape depths for sputtered particles cover a range from the outer surface layer to depths >20 Å. The median escape depths are generally <10 Å. Decreasing the primary ion energy shifts the depth-of-origin distribution for sputtered particles (secondary ions) nearer the surface and thus reduces contributions from deep layers. The escape depth does not play a significant role in depth resolution or profile distortion because other factors have a much greater effect.

The effect of primary ion energy on recoil implantation of layer species or mixing in subsurface layers [3] is demonstrated in figure 7. This is the same ^{31}P - Ta_2O_5 film sample discussed previously. It shows the profiles for 1.75, 7.75 and 18.5 keV ^{16}O bombardment. A dramatic effect with significant distortion of the true shape is evident.

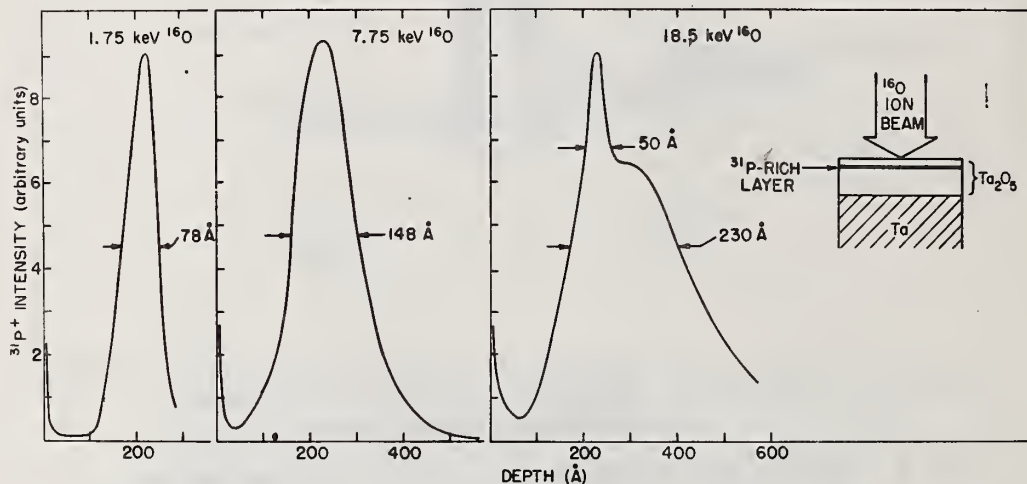


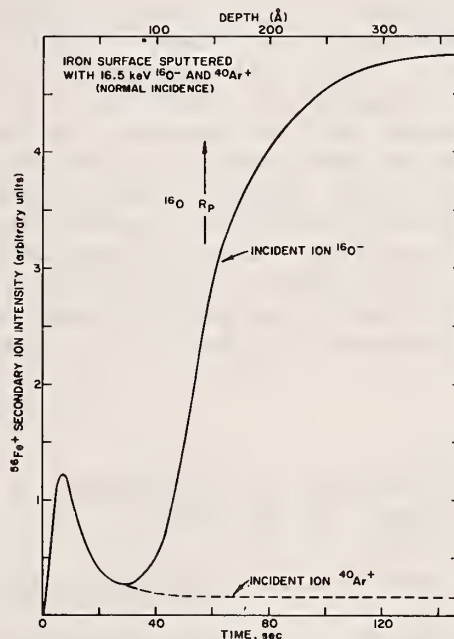
Figure 7. Phosphorus depth profiles of a Ta_2O_5 film containing a ^{31}P -rich subsurface layer. The profiles were obtained using normal incident ^{16}O sputtering beams of 1.75, 7.75 and 18.6 keV. These results illustrate the effect of incident ion energy on a measured profile. (From McHugh [3]).

However, at 18.5 keV some characteristics of the true profile remain. This is because the mean penetration depth of ^{16}O is initially beyond the layer, and it indicates for certain situations that high energy beams can provide useful information [3]. In addition, profiling thin surface films (<100 Å) or regions near the surface with a high energy, mass analyzed, low- Z ion beam is useful because an approximate depth calibration or sputter rate can be established from the implanted primary ion profile, and the calculated location and shape of the primary ion implant profile.

The remaining factors affect a profile in the following way. A given sample matrix produces a characteristic group of molecular ion interferences which can interfere with certain element analyses—especially at trace levels in low mass resolution instruments [4-7]. Surface charges can build up on thin insulating films causing migration of ionic species in the film (e.g., alkali and halogen constituents) [8,9]. A uniform primary ion current density does not in itself imply uniform etching of the surface. This characteristic is controlled by surface topography, cleanliness, and sample uniformity which depends on composition, physical state and crystallographic orientation.

Figure 8.

The time or depth dependence of the $^{56}\text{Fe}^+$ secondary ion intensity from an iron surface for normal incidence $^{16}\text{O}^-$ and $^{40}\text{Ar}^+$ ion bombardment. The $^{56}\text{Fe}^+$ peak heights and positions corresponding to the surface oxide film were normalized in the $^{40}\text{Ar}^+$ and $^{16}\text{O}^-$ cases for ease of comparison. $R_p \approx 140 \text{ \AA}$ for 16.5 keV $^{16}\text{O}^-$ ions incident on an Fe target. R_p is the projected range.



Since depth profiles usually extend to depths greater than a few hundred angstroms, the chemical effects of the implanted primary ion are usually evident in a profile. The chemical effect is demonstrated in figure 8 where the surface of an iron sample is sputtered with oxygen and argon ions, and the $^{56}\text{Fe}^+$ is measured as a function of time. The initial peak is due to enhanced emission from a surface oxide film. Then the growth in intensity is due to reaching the implant zone. The plateau is generally reached at depth equal to 2 to 3 times the mean projected range of the primary ion in the solid. The profile with Ar^+ shows just the surface film enhancement. The implantation of the inert species Ar produces no enhancement. If the sputter etching is accomplished with a primary particle energy of $\sim 100 \text{ eV/amu}$, the changing matrix condition caused by ion implantation is confined to within 100 \AA of the surface; beyond 100 \AA the implant ion concentration remains constant and a stable matrix condition is attained. In many cases, the

effects resulting from this type of chemical enhancement can be controlled by introducing oxygen gas in the vicinity of the sample. Adsorption of O_2 on surfaces generally enhances and stabilizes the secondary ion yield [10,11]. The result is that element sensitivity is improved and certain matrix effects are reduced or eliminated which gives more meaning to the secondary ion signal as a direct measure of element concentration. Also, the variation of secondary ion yield with crystal orientation is eliminated in a number of cases by O_2 adsorption on a surface [12,13]. The usefulness of this method in an analytical application has been demonstrated [1,14].

From the above example it is evident that the variation of secondary ion intensity is not always a measure of a relative difference in element concentration; therefore, care must be exercised in the interpretation of depth profiles — especially profiles near the surface or of films composed of dissimilar layered phases, or matrices with nonhomogenous distribution of trace elements that have a major influence on the secondary ion emission characteristics of the matrix. To reduce these effects so that meaningful results are obtained, one of the following methods should be used 1) apply quantitation procedures to the data, 2) reference the profiled element intensity to the secondary ion intensity of one or more uniformly distributed constituents of the film, or 3) change the character of the secondary ion emitting surface by performing the profile under conditions of high reactivity gas (*e.g.* O_2) pressure in vicinity of the sample surface.

III. REFERENCES

- [1] Blanchard, B., Hilleret, N., and Quoirin, J. B., J. Radioanal. Chem. 12, 85 (1972).
- [2] Croset, M., J. Radioanal. Chem., 12, 69 (1972).
- [3] McHugh, J. A., Rad. Effects 21, 209 (1974).
- [4] Hernandez, R., Lanusse, P., and Slodzian, G., C. R. Acad. Sci., Ser. B, 271, 1033 (1970).
- [5] Hernandez, R., Lanusse, P., Slodzian, G., and Vidal, G., Method. Phys. Anal. 6, 411 (1970).
- [6] Colby, B. N. and Evans, C. A., Jr., Appl. Spect. 27, 274 (1973).
- [7] Bakale, D. K., Colby, B. N., Evans, C. A., Jr., and Woodhouse, J. B., in Proceedings of the Eighth National Conf. of the Electron Probe Analysis Soc. of America, p. 7A, New Orleans, La., August (1973).
- [8] Brown, F. and Mackintosh, W. D., J. Electrochem. Soc. 120, 1096 (1973).

Depth Profiles

- [9] Hughes, H. L., Baxter, R. D., Phillips, B., IEEE Trans. Nucl. Sci. NS-19, 256 (1972).
- [10] Slodzian, G., Ann. Phys. 9, 591 (1964).
- [11] Slodzian, G. and Hennequin, J. F., C. R. Acad. Sci., Ser. B, 263, 1246 (1966).
- [12] Bernheim, M., Rad. Effects, 18, 231 (1973).
- [13] Bernheim, M. and Slodzian, G., Int. J. Mass Spectrom. Ion Phys., 12, 93 (1973).
- [14] Blanchard, B., Hilleret, N. and Monnier, J., Mat. Res. Bull., 6, 1283 (1971).

A COMPARISON OF AUGER ELECTRON SPECTROSCOPY (AES) AND SECONDARY ION MASS SPECTROMETRY (SIMS)

J. M. Morabito
Bell Telephone Laboratories, Inc.
Allentown, Pennsylvania

ABSTRACT

This paper compares the analytical capabilities and limitations of Secondary Ion Mass Spectrometry (SIMS) and Auger Electron Spectroscopy (AES) beginning with the modes of operation available: 1) SIMS and AES spectra, 2) ion and Auger imaging, 3) AES and SIMS depth profiling. Vacuum requirements, the volume of sample consumed, and the status of quantitative analyses by SIMS and AES are also discussed; followed by a comparison of SIMS and AES bulk, in depth, and surface detectability limits. It becomes clear from the data presented that the limitations and capabilities of both SIMS and AES dictate the use of both, when possible, in materials analysis. SIMS does have, for many elements, a sensitivity advantage over AES but AES is preferred for the surface analyses of small areas ($<50 \mu\text{m}^2$) at concentrations >1 at. %, particularly when sample removal by sputtering is undesirable.

I. INTRODUCTION

Fundamentals of the sputtering process as related to Secondary Ion Emission Mass Spectrometry (SIMS), possible ionization mechanisms, instrumentation, modes of operation, and methods of SIMS quantitative analysis have been discussed in previous papers of this monograph. This paper will discuss the analytical capabilities and limitations of SIMS in comparison to those of Auger Electron Spectroscopy (AES). Both SIMS and AES are capable of localized, *i.e.*, small selected volume, analysis from the surface into the bulk and can provide three-dimensional (x, y, z) microchemical analysis by means of depth profiling (z) and "ion" or "Auger" imaging (x, y). The limitations of both techniques are inherent in the instrumentation used, the extent to which the physics of AES and SIMS is understood, and the availability of accurate data on parameters such as Auger yields and escape depths, sputtering and secondary ion yields, atomic and molecular partition functions, etc. The limitations and capabilities of both SIMS and AES dictate the use of both, when possible, in materials analysis.

II. MODES OF OPERATION AVAILABLE

The modes of operation available in SIMS and AES are illustrated in figure 1.

1. Spectra

A. SIMS Spectra

Secondary ion mass spectra can be used to identify all elements (with the possible exception of neon and helium) and isotopes. Both positive and negative secondary ion mass spectra can be obtained. However, the yield (number of secondary ions)/(number of sputtered atoms) of positive and negative secondary ions can vary [1] by several orders of magnitude over the periodic table and is a function of parameters such as primary ion energy [2], nature of the primary ion [3] (e.g., argon or oxygen ($^{16}\text{O}_2^+$, $^{16}\text{O}^-$)), chemistry [4] orientation [5], and other parameters discussed in the literature. The use of mass spectrometric detection results in very low instrumental background, and hence signal-to-background ratios of 10^5 - 10^6 are achievable in the absence of mass interferences.

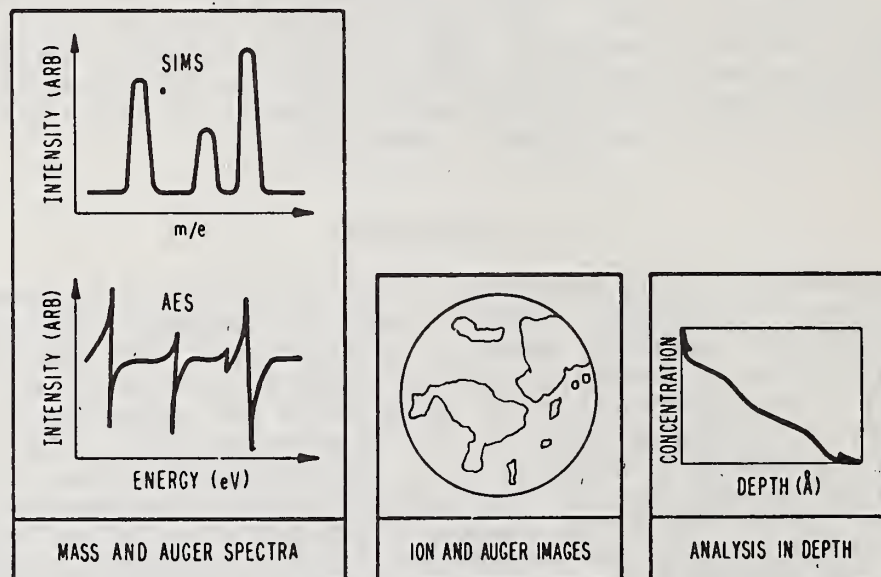


Figure 1 - Modes of operation available in AES and SIMS.

The possibility of mass interference makes good mass resolution, ($M/\Delta m$), a necessity in SIMS, since mass interferences can limit detection sensitivity and complicate depth profiles, surface analysis, and isotope abundance measurements. The mass resolution needed to resolve elements in the mass range of 27 to 238 from hydrocarbon interferences is shown in table 1 along with the resolution required to separate multiply charged and polyatomic species in the mass range of 14 to 58. Mass resolution of 1,000 to 3,000 is not possible with state-of-the-art quadrupole mass spectrometers or with double focussing spectrometers of the type described by Liebl [6] without the use of some type of secondary ion energy discrimination. The technique of low-energy discrimination (LED) has been described in detail [7,8] and has been demonstrated to reduce the intensity of polyatomic ion species without significantly reducing the intensity of the singly charged species. This type of discrimination is possible since the kinetic energy distribution of polyatomic and multiply charged ions is lower than that of monoatomic ions [9]. High-energy filtering is also desirable since a high energy limit minimizes chromatic aberration [11]. The resolution obtainable with the Castaing-Slodzian [10] mass spectrometer design in combination with a 90° spherical electrostatic

Table 1. Resolution (10% valley) of elements from hydrocarbon and polyatomic species.

Hydrocarbons

Mass	Doublet	$M/\Delta m$
27	$C_2H_3 - {}^{27}Al$	642
63	$C_5H_3 - {}^{63}Cu$	670
138	$C_{10}H_{18} - {}^{138}Ba$	570
208	$C_{15}H_{28} - {}^{208}Pb$	866
238	$C_{17}H_{34} - {}^{238}U$	1100

600 - 1000 is required

Polyatomic

Mass	Doublet	$M/\Delta m$
14	$Si^{++} - N^+$	960
28	$Si^+ - Fe^{++}$	2,980
56	$Si_2^+ - Fe^+$	2,895
58	${}^{28}Si {}^{30}Si^+ - Ni^+$	3,800

analyzer is shown in figure 2 [11]. The separation of $^{56}\text{Fe}^+$ from $^{27}\text{Al}_2^+$, shown in figure 2, implies a mass resolution ($M/\Delta m$) of 3,500. Higher mass resolution in SIMS requires the use of a Mattauch-Herzog type spectrometer as described by Hernandez *et al.* [12].

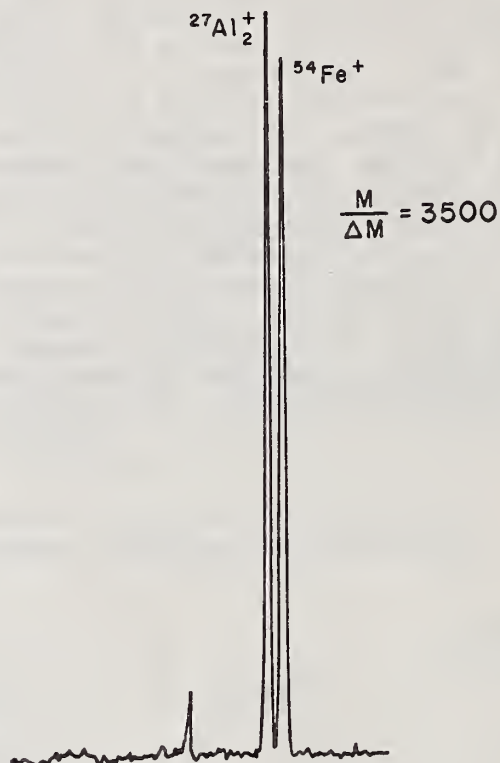


Figure 2 - Mass resolving power of IMS 300 with electrostatic analyzer (Reference 11).

The SIMS spectrum also contains information on the chemistry of the sample (*e.g.*, the presence of oxides, carbides, intermetallic compound formation, etc.). Methods have been developed to unravel the chemical information contained in SIMS spectra by means of standard "fingerprint" spectra [13] (*e.g.*, from a series of metal oxides such as CrO_3 , CrO_2 , Cr_2O_3 , etc.). However, the limitations of "fingerprint" mass spectrometry for information on sample chemistry have not yet been systematically investigated.

B. Auger Spectra

Auger spectra can be used to detect and identify all elements with the exception of hydrogen and helium, but AES spectra provide no information on the isotopes of elements. The variation in Auger yield

is less than a factor ten over most of the periodic table for a fixed primary electron energy. The Auger yield depends primarily on the cross section for ionization ϕ , the backscattering factor r , and the escape depth, d . All of these factors are a function of primary energy. The backscattering factor r is due to primary electrons backscattered with sufficient energy to produce additional Auger electrons. The signal-to-background of differentiated Auger spectra is on the order of 100:1.

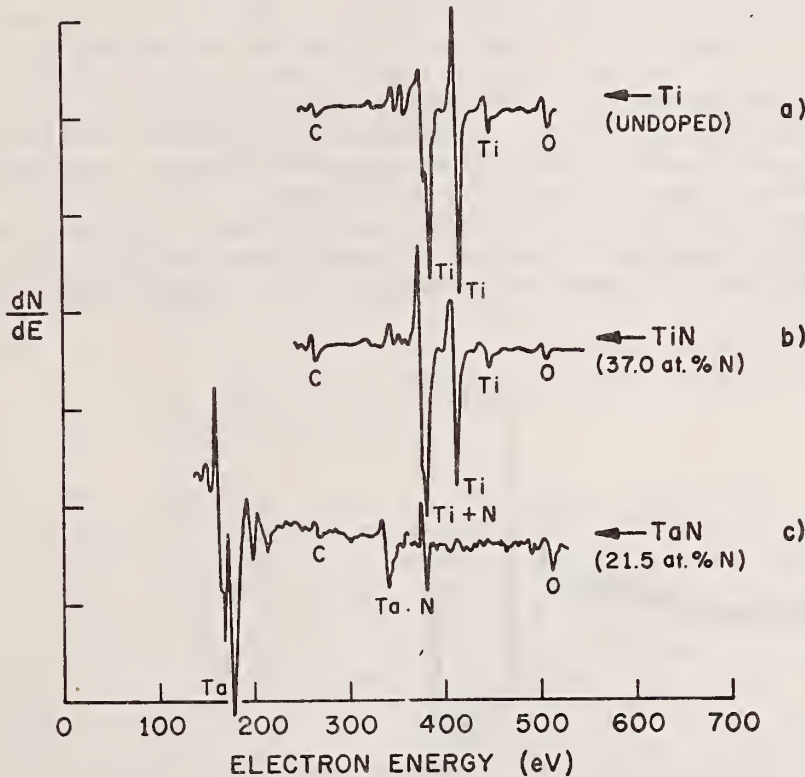


Figure 3 - Spectral interferences of nitrogen and titanium in AES.

Spectral interferences in AES are less severe than mass interferences since most elements have several (3-5) Auger transitions over a wide energy range, but there are several combinations of elements which result in serious interference effects (*e.g.*, nitrogen and titanium, argon and boron). The inherent energy spread of Auger electrons which determines the width of the Auger peak, and hence spectral interferences, is several electron volts. Therefore, Auger transitions with energies within several eV of each other are difficult to resolve with electrostatic spectrometers including the higher resolution double-pass type recently described by Palmberg [14].

However, the double pass spectrometer is also suitable for photoelectron spectroscopy—more commonly known as ESCA—and many Auger instruments are being modified to include the ESCA capability. The combination of ESCA and AES in the same instrument should reduce spectral interference difficulties considerably. However, it should be noted that the spatial resolution of ESCA is two to three orders of magnitude poorer than that of AES.

Figure 3 shows the Auger spectra of Ti(a) and TiN(b). The 418 eV titanium transition is more intense than the 387 eV transition in the case of pure titanium, but there is an interference between the titanium 387 eV and the nitrogen 380 eV transitions (shown for TaN(c)). This interference makes the 387 eV Ti peak more intense than the 418 eV peak for nitrogen doped Ti films. Unfortunately, oxidation of titanium also results in an increase in the 387 eV peak which further complicates the identification of nitrogen in titanium. Figure 4 shows the photoelectron spectra of TiN and demonstrates the clear separation between the nitrogen and titanium photoelectron transitions. For a brief comparison of Auger and photoelectron spectroscopy—ESCA—see reference 15.

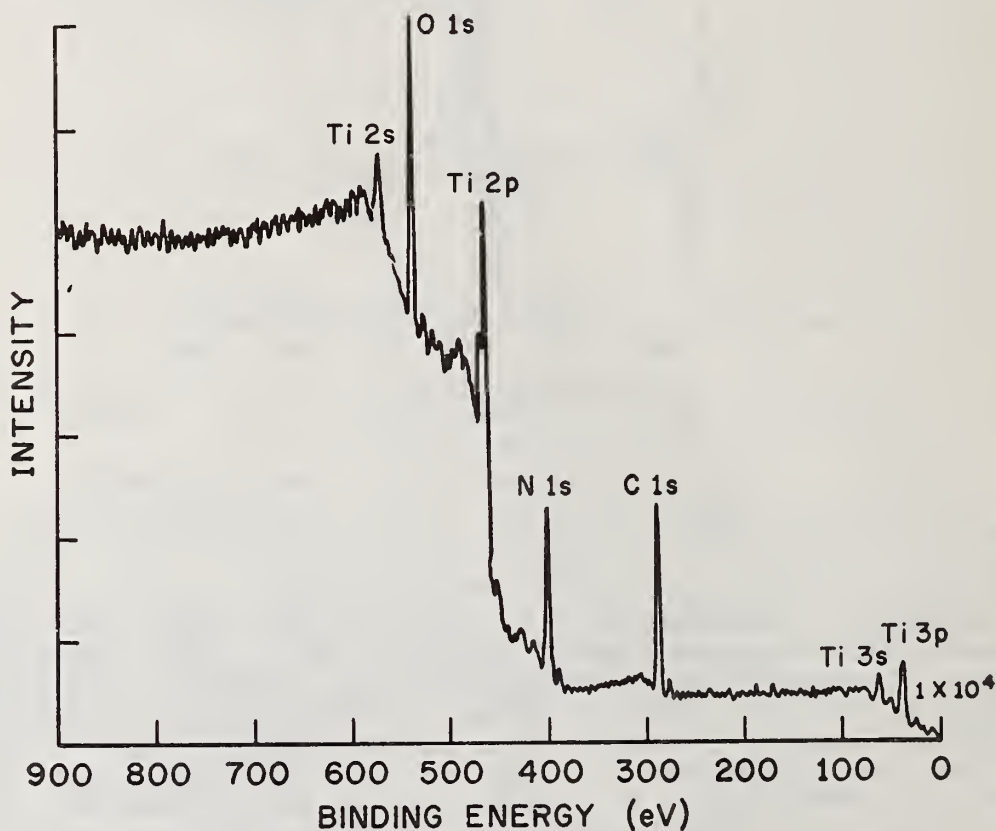


Figure 4 - ESCA Spectrum of TiN.

Auger spectra also contain information on the chemistry of the sample, but interpretation is difficult since the Auger process can involve as many as three atomic energy levels. The Auger spectra therefore, like the SIMS spectra, can only provide a fingerprint of the chemical environment. Changes in the Auger spectra which are used to provide information on chemical environment include: 1) energy shifts in the Auger peaks, 2) changes in the peak shape of valence Auger electrons, 3) additional "fine structure" on the low energy side of the Auger peak.

2. Ion and Auger Images

Both ion and Auger images can provide a two-dimensional map of the distribution of surface impurities. Ion imaging requires the volatilization of material by sputtering; Auger imaging does not. The lateral resolution of ion images depends on the method used to obtain the image. The two methods available are by scanning a focussed ion beam [6] and intensity-modulating the z-axis of a cathode ray tube (CRT) or by focussing the ions by means of an ion-optical system [10]. Image resolution by the scanning method is limited by the ion beam diameter $\sim 2 \mu\text{m}$. The resolution possible by the ion-focussing approach is limited only by the chromatic aberration present in the ion optics and is independent of ion beam size. Ion image resolution by this method on the order of $.5 \mu\text{m}$ has been obtained [16].

The Auger image can only be obtained by the scanning intensity modulation method and is therefore theoretically limited by the electron beam size consistent with practical recording times ($\sim 200 - 400 \text{ s}$). Brandis [17] has obtained an Auger image resolution of $.5 \mu\text{m}$ for a 1,500 mesh silver grid with a beam current of $4 \times 10^{-7} \text{ A}$ and a recording time of 200 sec. Auger imaging is limited to concentrations in the range of 1 at. %, but ion images at concentrations below 1 at. % can be obtained for elements with high secondary ion yield such as Na, Al, Mg. Ion and Auger images from small ($5 - .10 \mu\text{m}^2$) areas are usually not taken due to poor image resolution, but ion images from precipitates as small as 50 \AA have been recorded [18]. Table 2 summarizes the salient differences between Ion and Auger imaging.

3. AES and SIMS Depth Profiling

In-depth profile analysis by AES and SIMS is accomplished by monitoring a particular or series of Auger and/or secondary ion peaks while sputtering through the sample. The depth scale (\AA) is obtained by calibrating for the sputtering rate ($\text{\AA}/\text{s}$ or $\text{\AA}/\text{min}$) by measuring the sputtering time and the crater depth formed by the sputtering. Crater depth measurements are typically obtained with interferometers [19] or by a Talystep [20] which are only accurate for flat bottom craters.

Sputtering rates calculated from crater depth measurements assume a constant sputtering rate during the measurement. Unfortunately, the sputtering rate (z) can change during the analysis of multicomponent

Table 2. A comparison of Auger and ion imaging.

1. Lateral resolution of $\sim 5\mu\text{m}$ has been demonstrated for both.
2. Auger imaging does not require sample consumption, but is limited to ≥ 1 at % concentration.
3. Ion imaging requires sample consumption, but is not limited to concentrations as high as 1 at % for elements with high secondary yields.
4. Auger or ion imaging of small areas ($1 - 10\mu\text{m}^2$) is not practical.

films, especially when interdiffusion has occurred. However, Dahlgren and MacClanahan [21] have shown that the sputtering rate for a two-component system under equilibrium conditions is often limited by and equal to that of the element with the lower sputtering yield. Figure 5a and figure 5b show the Auger depth profiles of Ti-Pd-Au films (Sample 1 and 2) after interdiffusion has occurred. A thickness monitor was used to deposit films of different Ti and Pd thickness. The Ti thickness ratio was 1.73 and the palladium thickness ratio was 2. The gold thickness was 3,600 Å for both films. Therefore, by measuring the sputtering rate of gold (\dot{z}_1) and defining the Pd thickness to be from the point where the gold profile intersects the palladium profile (A) to the point where the Ti profile begins (B) (as shown in figures 5a and 5b), and using the ratio of the sputtering efficiency of palladium to gold (.87) to calculate the sputtering rate of palladium (\dot{z}_2), the thickness of the Pd region of Sample 1 calculates to be 964 Å and that of Sample 2 calculates to be 482 Å, a ratio of 2. From Point B (figs. 5a and 5b) a titanium rich ternary alloy is present and it is reasonable to assume that the sputtering rate (\dot{z}_3) of this alloy is limited by and equal to the sputtering rate of titanium which has a lower sputtering yield than the gold or palladium constituents of the alloy. The thickness of the titanium rich region of Sample 1 is calculated under this assumption to be 504 Å and that of Sample 2 to be 892 Å, a ratio of 1.77. This example is cited to demonstrate that accurate depth scales can be obtained for the case of a varying sputtering rate. The same method could be used for the SIMS profiles provided chemical effects do not distort the SIMS profiles significantly.

Other practical problems inherent in the sputtering process used in SIMS and AES profiling include the possibility of differential

sputtering in the case of alloys which can change sample composition at the surface, recoil or "knock on" whereby lattice atoms are pushed deeper into the solid [22], primary ion implantation effects [23,24], redeposition [25] and crater wall effects [26]. Numerous instrumental techniques have been developed in both AES and SIMS to avoid crater wall effects. Both sputtering and instrumental artifacts decrease the depth resolution possible by AES or SIMS profiling. The magnitude of the degradation depends on sputtering conditions used and the nature of the sample.

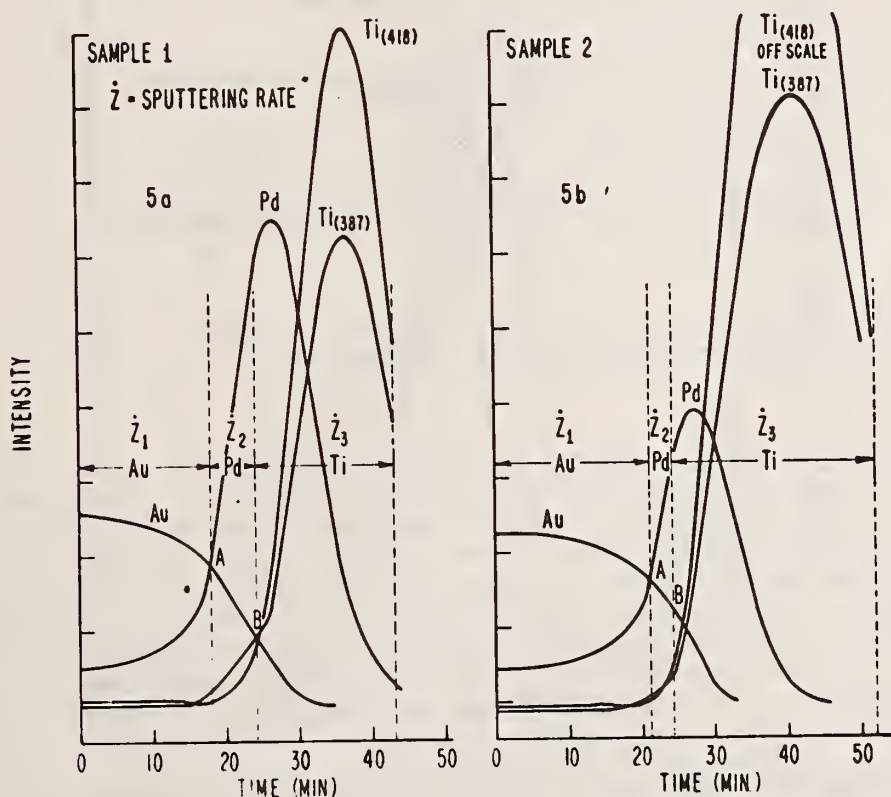


Figure 5 - AES profiles of Ti-Pd-Au films with different Ti and Pd thicknesses.

As discussed by Evans [27], "depth resolution" can be defined in several ways, the most common being the ability to distinguish between two subsurface features. With this definition and in the absence of sputtering artifacts, the depth resolution possible in AES and SIMS profiling has been shown [27,28] to be 5 - 10 percent of the thickness removed by sputtering, *e.g.*, 100 Å for a 1,000 Å film. Depth resolution can also be evaluated by the distortion imposed on a step function change in concentration. Figure 6 shows the AES profile obtained on a Pt-Al multilayer film [29] on a silicon substrate. The profile clearly shows an aluminum-rich zone of ~ 47 Å in width (δ). The measured aluminum profile has a Gaussian distribution, but the actual aluminum

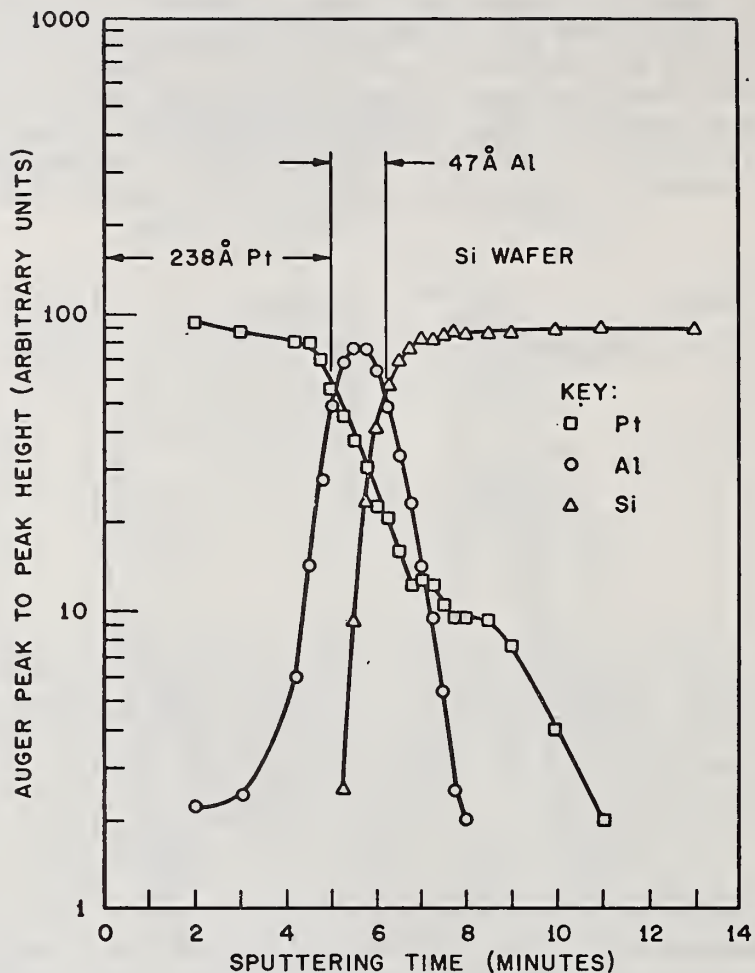


Figure 6 - AES depth profiles for platinum, aluminum, and silicon in thin films sputtered onto silicon.

profile was most probably a step function (*i.e.*, $c(x) = c$ for $0 < x < \delta$; $c(x) = 0$ elsewhere). This distortion is due in part to the sputtering process, but also to the response of the AES or SIMS techniques to this change in concentration. The response of AES and SIMS is determined by the escape depth of the Auger and secondary ions which are in the range of 5 - 20 Å in AES and believed to be in the range of 25 - 50 Å in SIMS. Impurity regions of thickness less than or comparable to the escape depth of Auger or secondary ions will exhibit an AES or SIMS profile different in shape than the actual impurity profile even in the absence of sputtering effects such as "knock on" as recently discussed by Chou *et al.* [30]. The lower escape depths of Auger electrons and the lower primary ion energies (≤ 2 keV compared to ≥ 2 keV in SIMS) used in AES profiling makes the distortion of sharp or step-function like concentration gradients less of a problem in AES than SIMS.

SIMS/AES Comparison

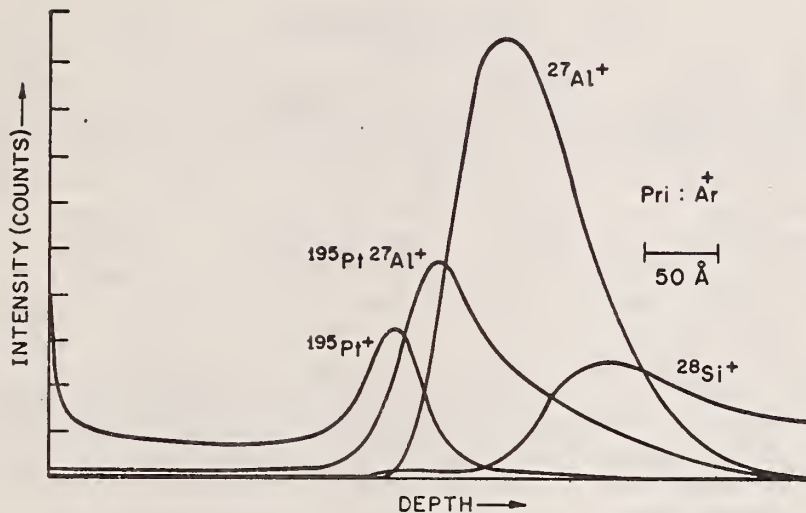


Figure 7 - SIMS depth profiles for platinum, aluminum, and silicon in thin films deposited onto silicon.

Figures 7 and 8 are the SIMS profiles obtained on the same Pt-Al film analyzed by AES (fig. 6). The data shown in figure 7 were obtained using positive primary argon ions at 5 keV. The secondary ion yield of $^{195}\text{Pt}^+$ is enhanced on the surface and at the Pt-Al interface due to the presence of impurities such as oxygen, aluminum, and magnesium. This enhancement is evidence for alloying between Pt and these elements which could have taken place during deposition of the films or promoted by the collision cascades produced by the high energy primary argon ions. The latter possibility has not yet been thoroughly investigated. It is possible, however, by SIMS to monitor cluster ions such as $^{195}\text{Pt}^{27}\text{Al}^+$, $^{27}\text{Al}^{28}\text{Si}^+$. The presence of these species in the SIMS spectra suggest that alloying has occurred either during film deposition or by the primary ion impact-collision cascade process. The width of the aluminum-rich region in the SIMS profile of figures 7 and 8 is similar to that found during AES profiling (fig. 6). The profiles in figure 8 were obtained using primary O_2^+ ions at 2.5 keV. The same enhancement effects are observed for Pt and Si using primary oxygen ions (see fig. 7). Note that the $^{28}\text{Si}^+$ profile is similar in shape to that of $^{27}\text{Al}^{28}\text{Si}^+$, suggesting that alloying also occurs between Al and Si.

There was nothing in the AES spectra or in the AES profile which indicated alloying between Pt, Al, and Si. The indication of alloying from the SIMS data could be an artifact of the sputtering process, but could also be real and, therefore, an important capability of the SIMS technique. If it was not an artifact, SIMS could be very useful in the study of the stability of interfacial phases in thin films [31] which are not in thermal equilibrium.

III. VACUUM REQUIREMENTS

The mechanism of secondary ion emission is such that vacuum conditions are perhaps of more concern in SIMS than in AES since the presence of contaminants such as H_2O , CO , CO_2 , and hydrocarbons not only complicate analysis for these species, but also reduce the sputtering rate, contribute to molecular ion formation, and complicate the ionization mechanism. In addition, the presence of numerous molecular ions such as M_xO_y in the SIMS spectra increases the probability of mass interference effects particularly at the high mass end of the spectra. Ultrahigh vacuum conditions (10^{-10} torr) are particularly important for surface analysis with SIMS since the extremely low primary ion currents (10^{-9} A/cm²) used for surface analysis are considerably below those required to maintain a contamination-free surface at 10^{-7} or 10^{-8} torr. It is for this reason that the SIMS instrumentation used for surface studies are designed with ultrahigh vacuum capabilities similar to those of AES instrumentation, *i.e.*, 10^{-10} torr or better. The possible presence of contaminants in the sample chamber during AES or SIMS profiling also means that a minimum sputtering rate must be maintained during AES or SIMS profiling of chemically active samples such as

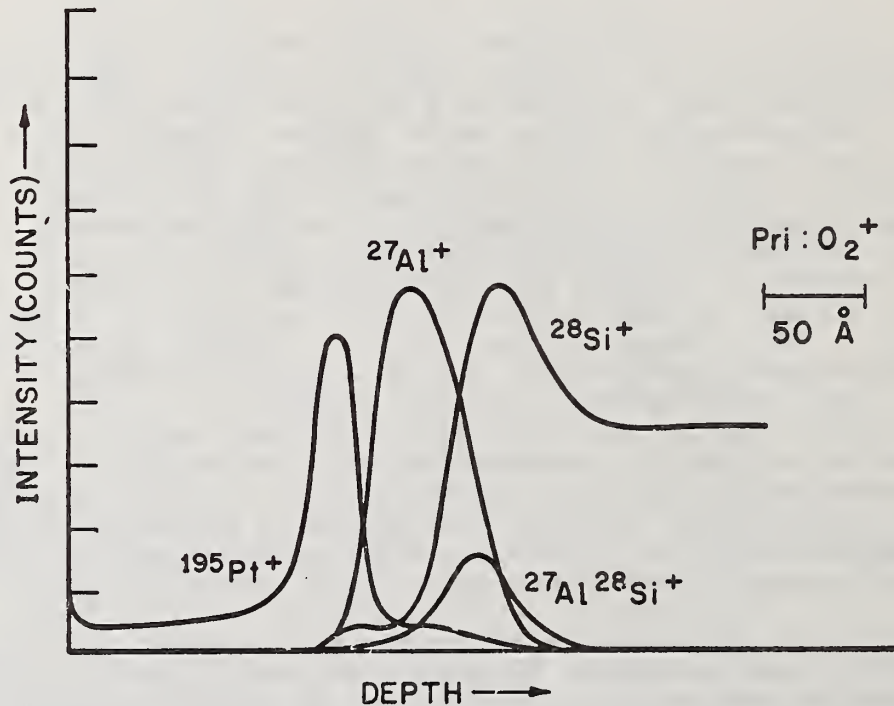


Figure 8 - SIMS depth profiles for platinum, aluminum, and silicon in thin films sputtered onto silicon.

SIMS/AES Comparison

metals. The portions of the sample sputtered below this minimum rate should not be allowed to contribute to the Auger or secondary ion spectra since these portions are often contaminated by residuals in the sample chamber. Sputtering rates in the range of 10 Å/min. are usually sufficient to prevent contamination of active surfaces surrounded by residuals (H₂O, X₀, CO₂) that have a partial pressure in the range of 10⁻⁸ torr.

IV. VOLUME CONSUMED IN SIMS AND AES ANALYSIS

A. SIMS

Since only a small fraction of the sputtered particles are ionized, a finite volume (δ^3) of the sample must be volatilized to detect a specified concentration (C) with a precision (p) on the measurement [32]. This minimum volume can be estimated, by the following equation [33]

$$\delta^3 = \frac{(\text{CNK})^{-1} \frac{10^4}{p^2} \frac{100}{a}}{\rho N_{AV}/M} \quad (1)$$

where

- δ^3 - Volume (cm³)
- C - Concentration (atom fraction)
- N - Collection efficiency x transmission of the mass spectrometer
- K - Secondary ion yield (ions/sputtered neutral)
- p - Precision (%)
- a - Isotopic abundance
- ρ - density
- M - atomic weight
- N_{AV} - Arogadro's number

This minimum volume can be expressed in terms of the area analyzed (A) and the depth (d) removed to obtain this required volume. Table 3 shows the results obtained for the common dopants (B, P, and As) in silicon. The secondary ion yields used for these calculations were K (boron) = 5.2 x 10⁻⁶, K (phosphorus) = 3.5 x 10⁻⁶ and K (arsenic) = 5.2 x 10⁻⁷. These yields were estimated from measurements of the number of counts obtained from a known volume of ion implanted silicon samples and assuming the transmission collection efficiency factor to be 10 percent. The precision used was 3 percent. The yields used are conservative, but it is doubtful that the secondary ion yields of these elements are more than two orders of magnitude better, *i.e.*, K (boron) is 5.2 x 10⁻⁴ > K > 5.6 x 10⁻⁶ under typical instrument operation. The analyzed area was varied from 20 μm^2 to 9 x 10⁴ μm^2 and the minimum depth required to detect concentrations of 10⁻², 10⁻⁴ and 10⁻⁶ (atom fraction) of boron, phosphorus, and arsenic are listed in table 3. These minimum depths

will increase for elements with lower secondary ion yields (*e.g.*, Pd, Ag, Zn) and will decrease for elements of higher secondary ion yield (*e.g.*, Li, Al, Si, Na).

Table 3. The minimum sputtered depth versus concentration for boron, phosphorus, and arsenic in silicon.

Element	Concentration	Area		
		20 μm^2 Depth	10 ⁴ μm^2 Depth	9 x 10 ⁴ μm^2 Depth
¹¹ B+	10 ⁻²	250 \AA	5 \AA	.55 \AA
¹¹ B+	10 ⁻⁴	2.5 μm	500 \AA	55.5 \AA
¹¹ B+	10 ⁻⁶	250 μm	5 x 10 ⁴ \AA	5.5 x 10 ³ \AA
³¹ P+	10 ⁻²	370 \AA	7.4 \AA	.82 \AA
³¹ P+	10 ⁻⁴	3.7 μm	740 \AA	82 \AA
³¹ P+	10 ⁻⁶	370 μm	7.4 x 10 ⁴ \AA	8.2 x 10 ³ \AA
⁷⁵ As+	10 ⁻²	2500 \AA	50 \AA	5.5 \AA
⁷⁵ As+	10 ⁻⁴	25 μm	5000 \AA	555 \AA
⁷⁵ As+	10 ⁻⁶	2500 μm	5 x 10 ⁵ \AA	5.5 x 10 ⁴ \AA

The results clearly show that; 1) the depth resolution possible for a given concentration can be dependent on the area analyzed depending on the secondary ion yield, 2) depth profiles of elements with low secondary ion yields at concentrations below .1 at. % with good depth resolution—5 to 10 percent of the thickness removed by sputtering—are difficult to obtain with good precision (*p*) when the analyzed area is less than 10⁴ μm^2 , 3) surface analysis (< 20 \AA depth) with SIMS for concentrations below 1 at. % of low secondary ion yield elements requires a large area of analysis. The results shown in table 3 can only serve as an estimate of the required depth, since Equation (1) does not correct for background and mass interference effects which can only serve to increase the minimum volume requirement consistent with a specified precision. Calculations with Equation (1) are, therefore, not often realistic, but are helpful to establish a "modus operandi" for the objectives of the experiment.

The requirement of a minimum volatilized volume has important consequences when the objective is the analysis of small areas (< 20 μm^2) with small diffusion depths (< 1 μm), *e.g.*, a transistor on a

SIMS/AES Comparison

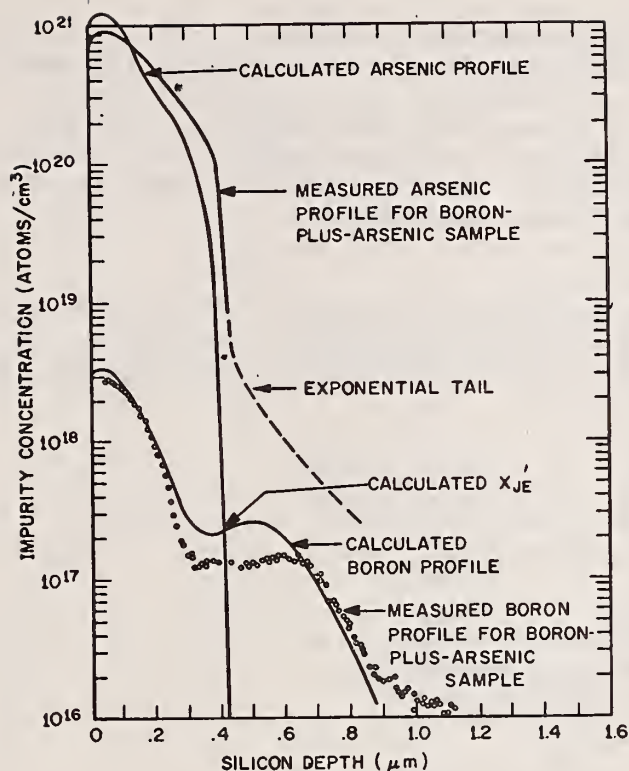


Figure 9 - SIMS profiles (measured and calculated) of arsenic and boron in silicon ion implanted with both boron and arsenic.

typical silicon integrated circuit. Figure 9 shows SIMS profiles of arsenic and boron in silicon ion-implanted with both boron and arsenic. The area of analysis was $9 \times 10^7 \mu\text{m}^2$, but the depth of analysis was limited to $\sim 1 \mu\text{m}$. Within this volume ($\sim 10^5 \mu\text{m}^3$), the entire boron profile down to 10^{16} atoms/cm³ could be detected. The redistribution in the boron profile compared to the calculated [34] profile (also shown in fig. 9) has also been observed by Bonis *et al.* [36] using a nuclear activation technique. The redistribution of boron is believed to be due to the arsenic implantation and subsequent anneal. A possible mechanism has been discussed by Ziegler [36].

It was not possible, within this volume, to detect the entire arsenic profile. The tail in the arsenic profile is an artifact in the SIMS technique due, perhaps, to mass interference [37] or redeposition effects [25]. If real, the arsenic concentration for all depths would be greater than the boron concentration. This is not possible since there is an emitter-base junction (X_{jE}) at $0.41 \mu\text{m}$. The tail in the arsenic profile begins at $\sim 5 \times 10^{18}$ atoms/cm³ and occurs at a depth of $\sim 5,000 \text{ \AA}$. Very little of the boron and arsenic profile could be measured with a precision of 3 percent if the area of analysis was

decreased to $20 \mu\text{m}^2$, which would be the area of an actual transistor fabricated by arsenic (emitter) and boron (base) doping in the range of $10^{16} - 10^{19}$ atoms/cm³ by chemical or ion implantation methods. However, the profiling of elements with high ion yields down to 10^{16} atoms/cm³ within a volume of $20 \mu\text{m}^3$ would be possible. Methods to increase the ion yield of the common dopants in silicon to the range of 10^{-1} to 10^{-3} would be of considerable practical importance in the silicon integrated circuit technology.

Table 4. The minimum time constant, τ_{min} required for Auger surface analysis as a function of beam size (μm^2) for a constant current density (j).

		$j = 10^{-7} \text{ A}/\mu\text{m}^2$			
		A	A	A	A
		$10^3 \mu\text{m}^2$	$10^2 \mu\text{m}^2$	$10 \mu\text{m}^2$	$1 \mu\text{m}^2$
S/N	C(at%)	τ_{min}	τ_{min}	τ_{min}	τ_{min}
10/1	10	$1 \times 10^{-2} \text{ s}$.1 s	.1 s	10 s
100/1	1	.1 s	1 s	10 s	100 s

		$j = 10^{-6} \text{ A}/\mu\text{m}^2$			
		A	A	A	A
		$10^3 \mu\text{m}^2$	$10^2 \mu\text{m}^2$	$10 \mu\text{m}^2$	$1 \mu\text{m}^2$
S/N	C(at%)	τ_{min}	τ_{min}	τ_{min}	τ_{min}
10/1	10	$1 \times 10^{-3} \text{ s}$.01 s	.1 s	1 s
100/1	1	.01 s	.1 s	1 s	10 s

$$\tau_{\text{min.}} \propto \frac{1}{jA} \text{ OR } \frac{1}{i_B}$$

B. AES

Chemical analysis by Auger electron detection does not require material consumption. Removal of material is only used to bring regions of interest to the surface where they can be analyzed. Reducing the electron beam size, hence area of analysis, for a constant primary current density (j) does not increase the depth of sample analyzed but does increase the time constant necessary to achieve a required signal-to-noise ratio on the lock-in amplifier used in the AES detection scheme. The depth of sample analyzed in AES is determined only by the escape depth of the Auger electrons (d_e). Table 4 shows the minimum time constant, τ_{min} , required to detect concentrations of 10 and 1 at. % (corresponding to S/N ratios of 10/1 and 100/1) as a function of

electron beam size (μm^2) for current densities of 10^{-7} A and 10^{-6} A. A practical limit on the time constant is 10 seconds which is reached at an area of $1 \mu\text{m}^2$ and concentration of 10 at. % when j is 10^{-7} A and at an area of $1 \mu\text{m}^2$ and concentration of 1 at. % when $j = 10^{-6}$ A. It would be difficult for SIMS (see table 3) to detect elements of low secondary ion yield down to concentrations of 1 at. % when the area of analysis is limited to $1 \mu\text{m}^2$ and the depth to $\sim 10 \text{ \AA}$, but the surface analysis of these elements down to 1 at. % from small areas ($\sim 1 \mu\text{m}^2$), and depths ($\sim 10 \text{ \AA}$) is possible with AES as shown in table 4. From the data of Table IV we also see that λ_{min} is proportional to $1/jA$.

AES with a small focused electron beam is therefore well suited to the analysis of actual integrated circuit devices provided current densities in the range of 10^{-7} A to 10^{-6} A can be obtained. Current densities in this range are achievable, as shown in figure 10, for tungsten and lanthanum hexaboride (LaB_6) sources [17]. There is, however, the possibility of beam damage, electron induced desorption [38], surface heating, *etc.* at these current densities—especially for oxides.

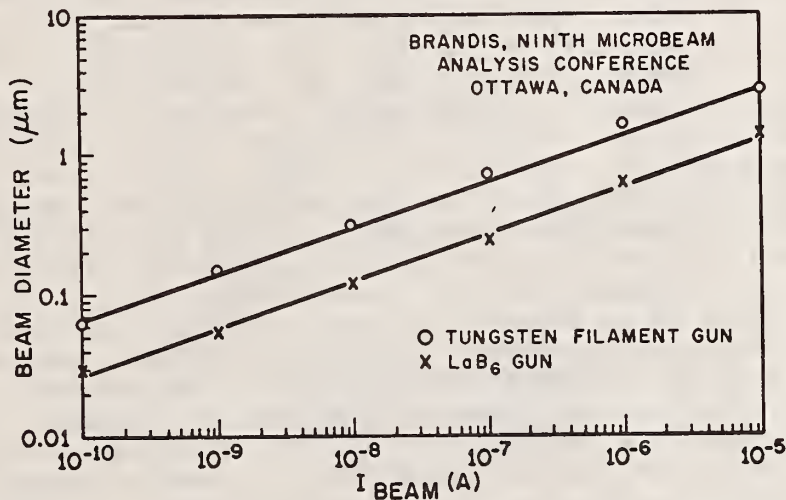


Figure 10 - Primary electron beam diameter versus beam current.

V. STATUS OF QUANTITATIVE AES AND SIMS ANALYSIS

1. SIMS

A. Models

Quantitative SIMS analysis by the use of standards, and by the use of a local thermal equilibrium (LTE) model and a quantum mechanical model have been described in this monograph and the literature [33, 39, 40, 41].

Despite the apparent success of the LTE model [40], the assumptions upon which it is based have been questioned [42,43]. In addition, the often unpredictable effects of active elements on secondary ion yields-chemical effects, matrix and orientational effects on ion yields, and mass interference effects caution against the routine use of any model [44]. The LTE model, like the BET model [45] used to calculate surface areas, might only provide a working formalism with the "temperature" and electron density of the plasma serving as adjustable parameters. Experiments to prove or disprove the validity of the LTE model are in progress in several laboratories [46]. These experiments, together with a more detailed analysis of the energy absorbed and subsequently dissipated by the lattice atom-primary ion collision process, should provide some insight into the conditions necessary for the formalism to apply to ion emission.

B. Standards

The formalism used for quantitative SIMS analysis by the use of standards has also been described in several publications [33,39]. It has become common practice to reference or normalize the secondary ion current from the impurity dopant (i) to the secondary ion signal from the matrix (M). This normalization procedure corrects for any changes in the sputtering rate (\dot{z}) or surface atom density (σ) during the measurement. In-depth profiling and ion imaging can be used to establish that the dopant is homogeneously distributed throughout the sample(s) to be used as a standard. The methods which have been used to prepare standards for quantitative SIMS analysis include ion implantation [37,47,48], reactive sputtering [49], bulk doped samples [50,51], thin film deposition techniques, *etc.* The work with standards has confirmed that SIMS measurements are quantitative particularly when the dopants are homogeneous at low concentrations, *e.g.*, < 10 at.% total, and there are no chemical and matrix effects. Quantitative SIMS analysis by the use of standards is preferred over the various model formalisms provided standards are available and the unknown is similar in chemistry, density, and crystallinity to the standard. A SIMS calibration curve for nitrogen in gallium phosphide, using the ion implantation method of standard preparation, is shown in figure 11 [48].

2. AES

A. Standards

Quantitative analysis by AES depends, at the present time, on the use of standards and on an equation of the form [52]

$$C_i = \frac{(A_{rel}^i)^{-1} I_i}{\sum_j A_{rel}^j I_j} \times 100 \quad (2)$$

where C_i is the concentration in at.%, A_{rel} is the relative Auger yield of the impurity (i) referenced to the matrix, I_i is the measured peak height(s) of the dopant(s), and j is a running index over all the elements present in the sample. Equation (2) assumes a homogeneous distribution of dopant and the complete absence of matrix effects since A_{rel} must often be measured by the use of "pure" elements; e.g., the relative Auger yields of iron and copper for a Fe-Cu-Au alloy would

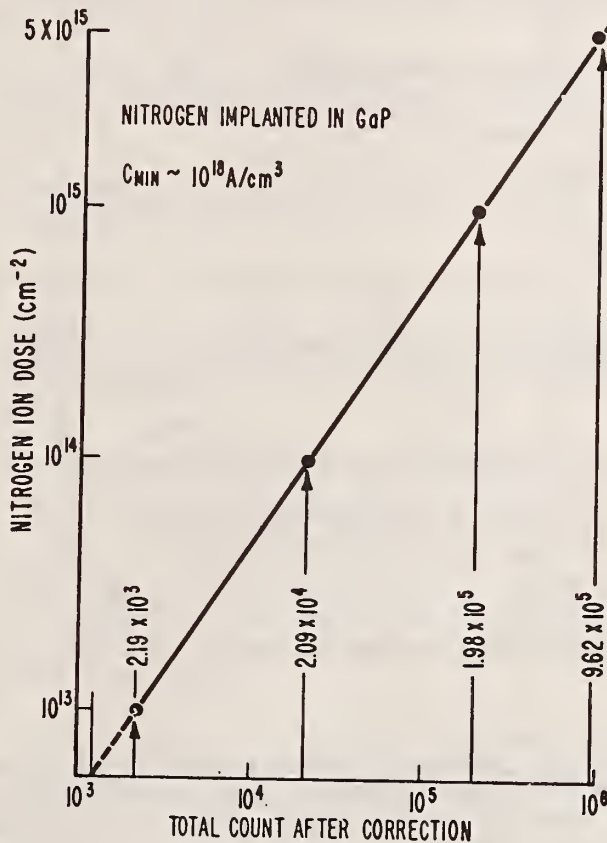


Figure 11 - SIMS calibration curve for nitrogen in GaP.

be measured by measuring Auger peak heights from "pure" iron, copper, and gold samples and referencing these peak heights to gold whose A_{rel} is defined as 1. The A_{rel} 's measured in this way are not always in agreement with those measured from a series of Fe-Cu-Au alloys of known and varying Fe, Cu, and Au composition. The use of Equation (2) also assumes that A_{rel} is independent of concentration. In addition, quantitative analysis by AES requires the use of sputtering to remove oxide and carbon layers which can attenuate the Auger peak of interest. There is a surface compositional change due to sputtering and, therefore, the Auger measurements can only provide a relative measure [53] of the actual concentration in the bulk. It is possible, however, to calculate the concentration in the bulk from the surface concentration

measured by AES and the sputtering yields [53]. Unfortunately, the sputtering yields are not often accurately known. In contrast, SIMS measures not what remains on the surface but that which leaves and can therefore provide, in principle, the actual concentration in the bulk of the sample.

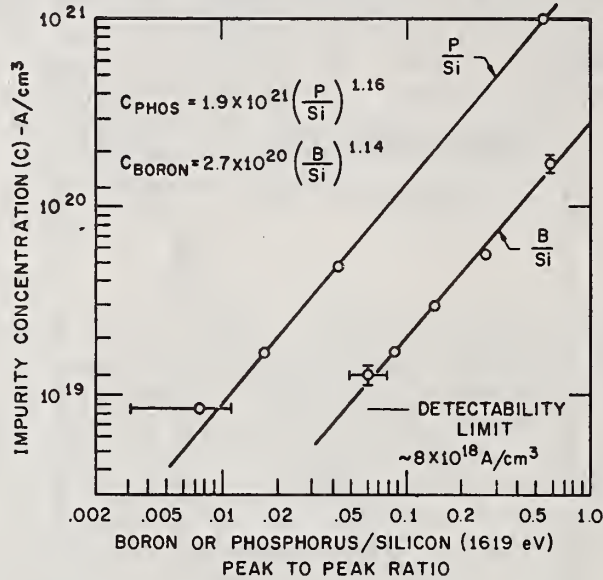


Figure 12 - Auger calibration curves for B and P in silicon.

Figure 12 shows the calibration curves obtained for the Si-B and Si-P systems using bulk grown doped silicon standards [54]. Calibration curves of this type can be routinely used to provide quantitative AES analysis and establish AES detectability limits. For a two-component system, Equation (2) reduces [53] to

$$C_i = \frac{I_i}{I_m} \frac{C_m}{A_{rel}} \quad (3)$$

where C_m is the concentration of the matrix. A plot of C_i/C_m vs. I_i/I_m can then be used to calculate A_{rel} of the dopant which can then be compared to the A_{rel} calculated by the use of pure elements, *e.g.*, pure silicon and pure boron.

B. First Order Approximation to Quantitative Auger Analysis with the CMA Analysis

Quantitative AES analysis by models analogous to those used by the electron microprobe [55] are not yet available. The reasons for the present lack of a model include:

- 1) The detection scheme used does not measure the absolute Auger current (i_A) directly.
- 2) Auger escape depths (d_e) for many elements have not yet been accurately measured or tabulated for routine quantitative analysis.
- 3) Backscattering correction factors (r) are not available for most elements or easily measured.
- 4) A tabulation of ionization cross sections (ϕ) is not available.
- 5) The effect of surface roughness on the Auger signal intensity has not been sufficiently studied with regard to quantitative analysis.

The information available on 1) to 4) has shown that:

- 1) The Auger peak-to-peak height from the differentiated energy distribution is proportional [56] to the Auger current (i_A) provided the peak shape in the $N(E)$ function does not change, and the integral of the $N(E)$ peak is a more accurate relative measure of the Auger current (E is the kinetic energy of the Auger electrons) [57].
- 2) The escape depth of Auger electrons is determined by the valence band of the element, and in the energy range of 100 eV to $\sim 1,500$ eV is proportional [58] to \sqrt{E} .
- 3) Backscattered primary electrons contribute no more than 20-30 percent to the Auger yield [59].
- 4) The ionization cross sections are approximately proportional to $1/E^2$ [60] for K and perhaps L shell ionizations provided the primary energy (E_0) is a factor 2 or 3 greater than the binding energy (E_B) of the ionized level.

Therefore, for a given matrix (*e.g.*, Si), primary electron current and energy (where $E_0 \gg E_B$), concentration C , and angle of incidence (α) the Auger yield from a smooth surface can be defined as the product, $\psi\phi d_e \eta(E)r$. The product of these parameters should be proportional to $1/\sqrt{E}$ since $\eta(E)$, the transmission of the CMA spectrometer, is approximately proportional to E up to $\sim 1,000$ eV. However, this linear dependence of the CMA transmission with energy is only valid when the acceptance window of the spectrometer is small compared to the natural

line width of the Auger peak. The acceptance window of the spectrometer is the product of spectrometer energy resolution ($\sim .5$ percent) and the kinetic energy of the Auger transition of interest, *e.g.*, it is 5 eV at a kinetic energy of 1000 eV. The transmission of the retarding field type analyzer is constant with energy and therefore the suggested $1/\sqrt{E}$ dependence would not apply to data obtained with this type of analyzer.

The Auger transition probability, ψ , is assumed to be close to unity for the major, more intense, Auger transitions. There are, of course, several transitions (peak splitting) possible from a single ionization (KL_1L_1 , KL_1L_2 , etc.) and each has its own transition probability. For most elements, however, one of the possible transitions associated with a K, L, M, etc. ionization will predominate and it is these transitions which are most often used in qualitative Auger analysis.

The ratio of the differentiated or integrated Auger signal (I) of element A normalized to the matrix (I^M) signal to that of element B normalized to the same matrix at a constant concentration C can be expressed by

$$\left(\frac{I^A/I^M}{I^B/I^M} \right)_C = \frac{\sqrt{E^M}}{\sqrt{E^A}} \times \frac{S_B}{S_A} \times \frac{r_A^M}{r_B^M} \times \frac{\psi_A}{\psi_B} \quad (4)$$

The Auger signals (I^A , I^B , I^M) should be corrected for any variation in the electron multiplier gain (G) of the CMA with E . The gain of the electron multiplier in the Physical Electronics CMA has been found to be essentially constant above ~ 150 eV [61]. The sputtering yield ratio of elements A and B, S_B/S_A , should approach 1 at low concentrations (< 19 at. %). This sputtering yield ratio is a necessary correction since most Auger data for quantitative analysis are taken during sputtering [49,53]. The backscattering ratio, r_A^M/r_B^M , should also be close to 1 at low concentrations since it is primarily determined by the matrix. For the same matrix and for major transitions of the same type (KLL, LMN, etc.) and shape, $\psi_A/\psi_B \sim 1$ and Equation (4) then reduces to:

$$\left(\frac{I^A/I^M}{I^B/I^M} \right)_C = \frac{\sqrt{E^B}}{\sqrt{E^A}} \times \frac{S_B}{S_A} \times \frac{r_A^M}{r_B^M} \quad (5)$$

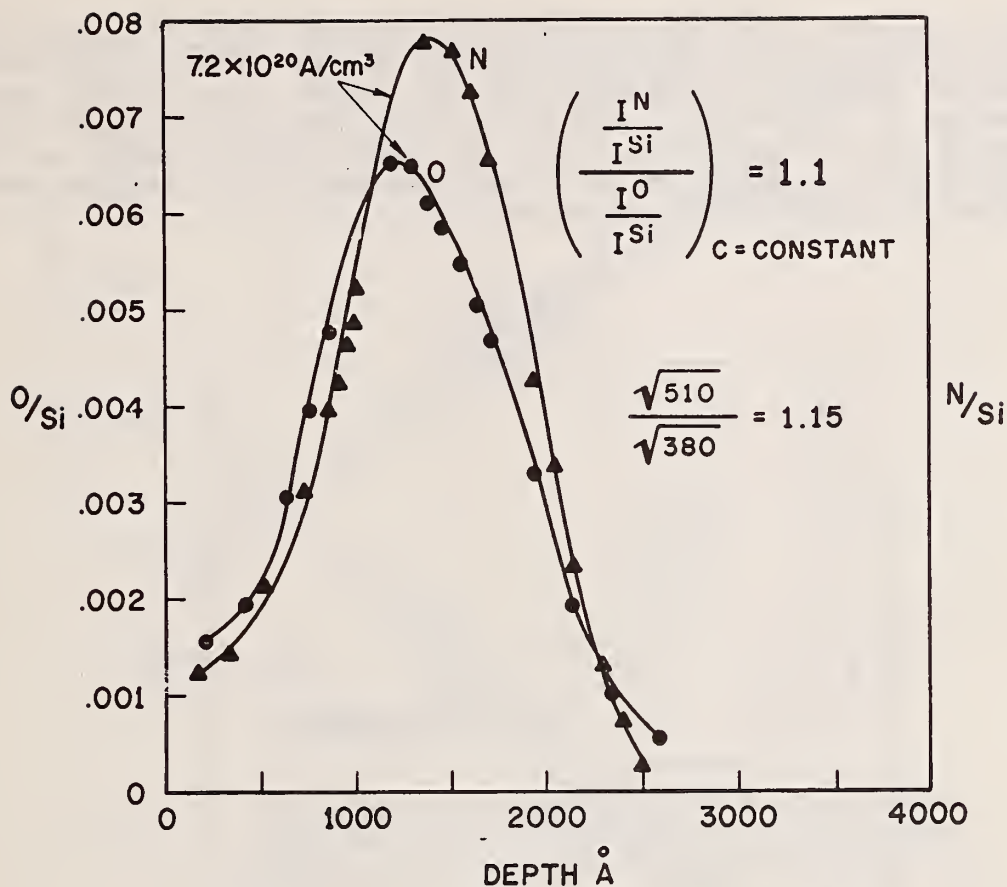


Figure 13 - Auger profile of oxygen and nitrogen ion implanted into silicon.

The validity of Equation (4) has been tested by the author at low concentrations (< 10 at. %) by ion-implanting nitrogen and oxygen into silicon and at higher concentrations (>10 at. %) by preparing nitrogen, oxygen, and carbon doped tantalum thin films using reactive sputtering. The concentration of the ion implanted samples was calculated from the dose (at./cm²) implanted into the sample and the LSS theory [34]. The measured nitrogen and oxygen profiles, obtained by combining Auger analysis with argon ion sputtering, have a Gaussian distribution in good agreement with LSS theory [34]. The measured profiles are shown in figure 13. The implanted concentration (at./cm³) versus the normalized Auger peak heights over the concentration range where the nitrogen and oxygen data overlap is shown in figure 14. The use of ion implantation to calibrate Auger and SIMS data for quantitative analysis has been discussed in several publications [37,47,48]. The ratio of the nitrogen and oxygen normalized peak heights, $\frac{I^N}{I^{Si}} / \frac{I^O}{I^{Si}}$ at the same concentration,

e.g., 2, 3, etc. $\times 10^{20}$ at./cm³ (fig. 14) measures to be ~ 1.1 with an estimated error of $<20\%$ at these low concentrations. This ratio compares very well with the ratio of the square root of the Auger energies of oxygen (510 eV) and nitrogen (380 eV) which is 1.15 and suggests that the sputtering yield and backscattering ratio can be approximated by unity in this low concentration range and the Auger yields of nitrogen and oxygen are about the same.

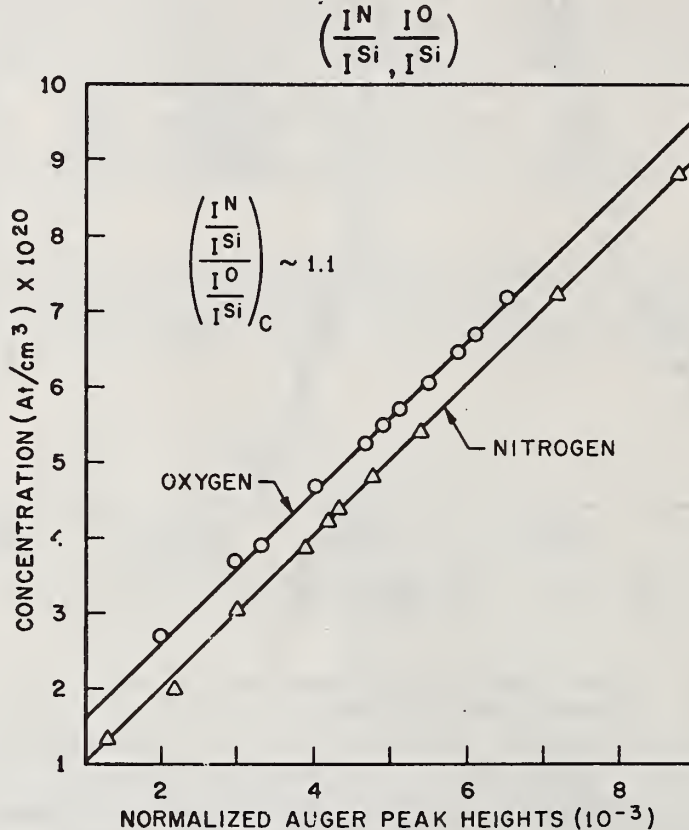


Figure 14 - Concentration (At./cm³) of ion implanted nitrogen and oxygen vs. normalized Auger peak heights

The validity of Equation (4) at higher concentrations (>10 at. %) was also studied. Figure 15 is a plot of the concentration of nitrogen, oxygen, and carbon in reactively sputtered tantalum films. The concentration of these elements was determined by the electron microprobe [53]. Nitrogen and oxygen which have similar Auger peak shapes were found to have, within experimental error, the same calibration curve but carbon, with a different Auger peak shape, falls slightly below both oxygen and nitrogen. The calibration curves for (104 eV) and (179 eV) should then be more similar to the carbon calibration curve.

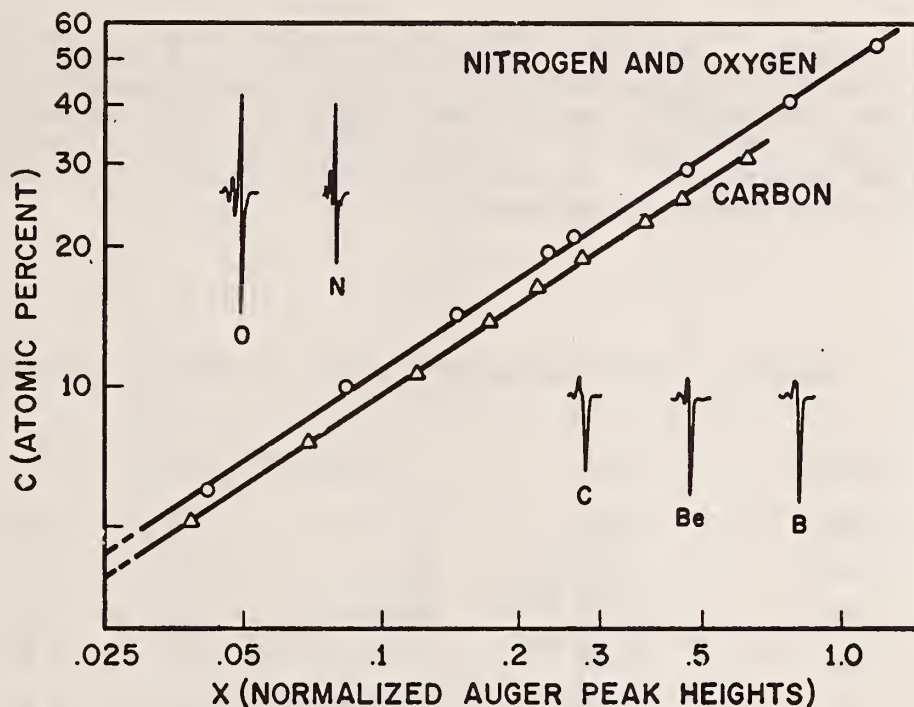


Figure 15 - Log C (at. %) determined by the electron microprobe vs. log of normalized N. O. C auger peak height (X) in reactively sputtered tantalum thin films.

The peak shapes for nitrogen, oxygen, carbon, beryllium and boron are inserted in figure 15. Similarity in peak shape would not be required if the integral rather than the differentiated peak-to-peak height was used.

The application of Equation (4) to data obtained on vacuum-cleaved MgO [52], Cu₂O [62], CdS [61], GaP [61], and KCl [61] is summarized in table 5. The A_{rel}^0 's listed in Table V were calculated assuming that the sputtering yield and backscattering ratios are approximately one, *e.g.*, for MgO,

$$A_{rel}^0 = \frac{\sqrt{E^{Mg}}}{\sqrt{E^0}} = 1.5 \quad (6)$$

$A_{rel}^{Mg} = 1$ since Mg is the matrix. These calculated A_{rel} 's (table 5) were then used together with Equation (2) to calculate the composition from the measured differentiated peak-to-peak heights (I) which are shown for MgO, Cu₂O and CdS in figure 16. The peak heights for GaP and KCl were taken from Reference 61. The running index j of Equation (2) includes all the elements present in the sample.

Table 5. Calculated compositions of compound standards.

Sample	A_{rel}	Calculated Composition ^a			
MgO	1.50	56	at. % O	44	at. % Mg
Cu ₂ O	1.34	35	at. % O	65	at. % Cu
CdS	1.57	48.5	at. % S	51.5	at. % Cd
GaP	2.99	47	at. % P	53	at. % Ga
KCl	1.18	47.4	at. % Cl	52.6	at. % K

^aAll data (except MgO) were taken while sputtering.

The results suggest that a sensitivity—relative Auger yield (A_{rel})—factor can be estimated without standards by Equation (4) provided the transitions have similar Auger peak shapes and transition probabilities in the energy range ~ 100 eV to $\sim 1,000$ eV. The use of Equation (4) is restricted to data obtained with the CMA spectrometer and is presented as a semi-empirical attempt to convert measured peak-to-peak heights into quantitative atomic concentrations. The limitations of the suggested $1/\sqrt{E}$ dependence are increased by our present lack of information on transition probabilities for specific transitions, backscattering correction factors and the corrections necessary due to sputtering during Auger analysis. In the absence of sputtering artifacts, the largest error should occur when the transitions chosen are of different type (K, L), shape and natural line width. Errors due to the above are minimized by integrating the differentiated Auger peaks. It is highly improbable that the sputtering yield (S) and backscattering corrections (r) are independent of concentration. Measurements on alloys indicate that S does change with concentration [21]. The effect of dopant concentration on the backscattering correction remains to be established.

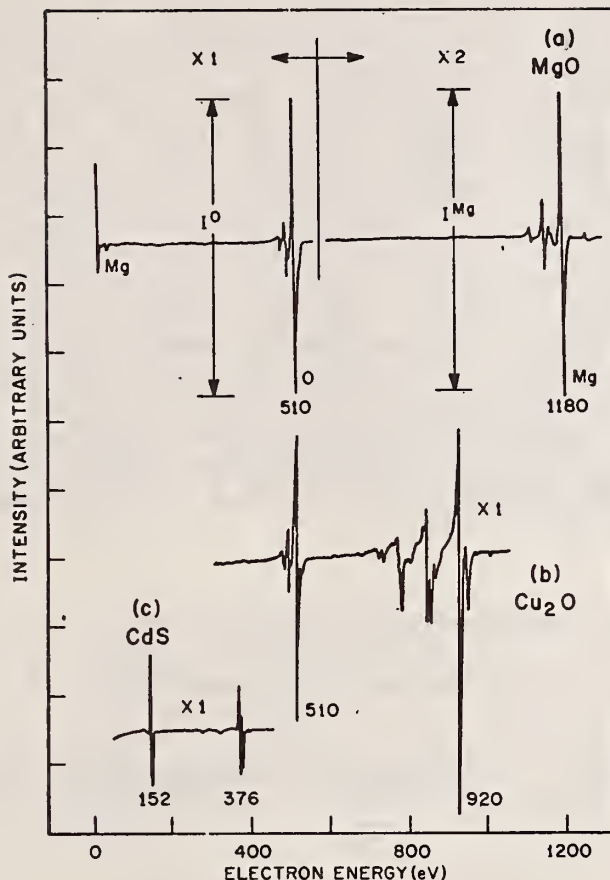


Figure 16 - Auger spectra of vacuum cleaved MgO, single crystal Cu₂O, and CdS.

VI. COMPARISON OF SIMS AND AES BULK, IN-DEPTH, AND SURFACE DETECTABILITY LIMITS

Bulk detectability limits for SIMS refer to operation without restrictions on the area and depth of analysis. In AES, this implies an electron beam diameter of $\sim 100 \mu\text{m}$, high primary currents (*e.g.*, 20 to 50 μA) and a long time constant on the lock-in amplifier—on the order of several seconds. Table 6 lists the AES and SIMS bulk detectability limits [8] for the common dopants (B, P, As) in silicon and for light elements in tantalum. The bulk detectability of AES is limited to $\sim 10^{19}$ atoms/cm³ or .1 at. %. SIMS is clearly a far more sensitive technique than AES for bulk analysis (see table 6), and thus particularly useful for the precharacterization of samples prior to electron microprobe or Auger analysis. Precharacterization with SIMS can reduce the time necessary for comprehensive AES or electron microprobe analysis.

The detectability limits of SIMS for in-depth analysis depend to a great extent on the depth over which the impurity is diffused, on the magnitude of the secondary ion yield, on the required precision (p), and depth resolution needed in the profile. Over a depth of 1,000 Å, a precision of 3%, and a depth resolution of 50 to 100 Å, the in-depth detectability of SIMS for elements with ion yields in the 10^{-2} range could be as low as 10^{15} atoms/cm³, assuming no limitation on the area of analysis and the absence of mass interference effects. For most elements, the above conditions would result in an in-depth detectability limit of from 10^{17} atoms/cm³ to $\sim 5 \times 10^{18}$ atoms/cm³. The in-depth detectability limits of AES under the same conditions has been measured [47] to be $\sim 10^{20}$ atoms/cm³ or from two to three orders of magnitude less sensitive than SIMS. The in-depth detectability limits of AES under the same conditions has been measured [47] to be $\sim 10^{20}$ atoms/cm³ or from two to three orders of magnitude less sensitive than SIMS. The in-depth sensitivities of AES and SIMS become more similar as the depth of the diffused region decreases below ~ 100 Å and the area of analysis is restricted to $10 \mu\text{m}^2$ or less.

Table 6. Comparison of bulk sensitivity limits for P, B, and As in silicon and for N, O, C in tantalum using AES and SIMS.

<u>Element</u>	<u>Technique</u>	<u>Detectability Limit</u>
N, O, C	AES	10

Table 6. Comparison of bulk sensitivity limits for P, B, and As in silicon and for N, O, C in tantalum using AES and SIMS.

<u>Element</u>	<u>Technique</u>	<u>Detectability Limit</u>
N, O, C	AES	10^{19} atoms/cm ³
N	SIMS	10^{19} atoms/cm ³
C, O	SIMS	10^{17} atoms/cm ³
P, B	AES	10^{19} atoms/cm ³
As	AES	10^{20} atoms/cm ³
B	SIMS	10^{14} atoms/cm ³
P	SIMS	10^{17} atoms/cm ³
As	SIMS	10^{18} atoms/cm ³

The surface detectability limit of AES is the same as its bulk detectability limit, $\sim .1$ at. %, since the Auger electrons are coming from the same depth whether the surface or bulk (after material removed by ion sputtering) analysis is performed. Surface analysis by SIMS requires the use of small current densities (10^{-9} A/cm²) to limit material removal to fractions of a monolayer, and large areas of analysis ($\sim .1$ cm²) to remove a sufficient volume (δ^3) of sample. Surface analysis by SIMS can be complicated by hydrocarbon mass interference effects [12,33], secondary ion enhancement due to the presence of chemically active elements on the surface [33], and primary ion implantation effects [23]. High mass resolution and the simultaneous detection of a wide mass range by means of a photoplate [12] are particularly useful when performing surface analysis with SIMS. Although the interpretation of SIMS surface analysis can be difficult, the surface detectability limit of SIMS is several orders of magnitude more sensitive than AES. However, surface analysis is more routinely performed by AES which is the preferred technique when surface analysis from selected areas < 50 μm^2 is required, especially when material removal is undesirable.

VII. SUMMARY AND CONCLUSIONS

Both SIMS and AES have unique analytical capabilities for materials characterization from the surface into the bulk. They are the only analytical techniques capable of three-dimensional microchemical analysis with good lateral and depth resolution. Lateral resolution < 1 μm and depth resolution from 5 to 10% of the thickness removed by sputtering can be obtained.

AES surface and bulk analysis is limited to $\sim .1$ at. %. In-depth profiling by AES and Auger imaging are limited to ~ 1 at. % (depending on the material, current density, analysis time, etc.). Quantitative bulk and in-depth analysis based on standards or by a first order approximation method are accurate to within 20-30 percent, but a generalized model for quantitative analysis without standards is not yet available. For a model to be acceptable, it would also have to include sputtering parameters such as sputtering yields (S) since ion sputtering is routinely used in AES bulk and in-depth profile analysis.

Sputtering is not often used in AES surface analysis, since it would remove elements of interest from the surface. It is, however, often necessary to remove contaminants such as carbon, sulfides, etc. from the surface since they can attenuate or completely mask other surface impurities. Attenuation effects and the often nonhomogeneous distribution of impurities within the plane of the surface and within the escape depth region makes quantitative AES surface analysis of real surfaces very difficult. Quantitative AES surface analysis is possible, however, from surfaces prepared under ultrahigh vacuum conditions with varying amounts of contaminants or cleaved in ultrahigh vacuum. The analysis of surfaces prepared under such ideal conditions should eventually provide the information on escape depths, backscattering

corrections, ionization cross sections, *etc.* necessary for routine AES quantitative analysis without standards.

For optimum detection limits, SIMS surface, in-depth profile, and bulk analysis should be performed using a large bombarded area (10^{-3} - 10^{-1} cm^2) with low current densities (10^{-9} A/cm^2) for surface analysis and higher current densities (10^{-7} - 10^{-6} A/cm^2) for in-depth profile and bulk analysis. Bulk detection limits for many (but not all) elements, in the absence of mass interferences, can be in the PPM range for elements with ion yields of 10^{-3} or better. Surface and in-depth profile detection limits depend on the requirements of the measurement, but should be from one to two orders of magnitude less than bulk detection limits since a reduced sample volume is available for volatilization. Mass interferences should be reduced in SIMS analysis which is possible by using high resolution mass spectrometry [12] or some type of energy filtering [7,8,11]. The technique of introducing a controlled oxygen jet [63] on the sample during primary ion bombardment can be useful in minimizing chemical, matrix and orientation effects during SIMS in-depth profiling provided the oxide formed is amorphous. As understanding and experience with SIMS progresses, chemical, matrix, and orientation effects on secondary ion yields will also be used to advantage in materials characterization. The ion image is, in fact, a two-dimensional representation of the chemical, matrix, and orientation effects in SIMS.

Ion images are often required to interpret anomalous structure in SIMS depth profiles which can be due to the presence of precipitates in grain boundaries, porosity between thin film layers, changes in ion yield due to orientation effects, *etc.* The ion image mode is of particular value in identifying different phase regions in alloys as a function of heat treatment. Detection limits with the ion imaging mode are, however, limited since it is often necessary to have an image within 200 to 500 Å of a specified depth in the sample. The concentration or secondary ion yield of the element must therefore be high to obtain a sufficient signal from a volume element whose depth is limited to 200-500 Å .

The sensitivity of secondary ion yields to subtle changes in sample chemistry, crystallography, *etc.* serves only to complicate quantitative analysis, but quantitative analysis has been demonstrated in several laboratories by the use of well-characterized standards. The quantitative models available in SIMS suggest that standardless analysis is possible in the absence of chemical and other effects on ion yield, but there are difficulties with the available models. The major objection to the LTE model proposed by Andersen [40] is that thermal equilibrium cannot exist in the target as discussed by Carter [43] and Werner [42]. It is also not clear if the LTE model is useful for low primary ion current densities which are most often used in the analysis of surfaces and thin films.

From results obtained with both AES and SIMS on the same samples [8], it is quite clear that the techniques are very complementary. AES (which is less sensitive to the chemical state of the element) is

preferred for routine surface analysis of small ($<50 \mu\text{m}^2$) selected areas, and for the detection of impurities whose concentration is greater than 1 at. %. SIMS can provide elemental detection and identification of most elements below 1 at. %, information on isotopic abundance, and the chemical state of the impurities (*i.e.*, oxides, precipitates, etc.). The sensitivity of SIMS makes it ideal for trace analysis and for the profiling of common dopants used in the silicon integrated circuit technology. Both techniques are being used in a wide variety of areas previously inaccessible to comprehensive analytical investigation.

ACKNOWLEDGMENTS

P. W. Palmberg of Physical Electronics Industries obtained the ESCA data shown in figure 4. R. K. Lewis of Cameca Instruments performed the SIMS measurements shown in figures 7 and 8.

REFERENCES

1. Beske, H. E., Z. Naturforsch., D 19a, 1627 (1964).
2. Bradley, R. C., J. Appl. Phys. 30, 1 (1959).
3. Benninghoven, A., Z. Naturforsch. 22a, 841 (1967).
4. Castaing, R., and Hennequin, J. F., Advances in Mass Spectrometry, ed. A. Quayle (Institute of Petroleum, London), 5, 419 (1972).
5. Bernheim, M., and Slodzian, G., Sur. Sci. 40, 169 (1973).
6. Liebl, H., J. of Appl. Physics 38, 5277 (1967).
7. Herzog, R. F., Poschenrieder, W. P., and Satkewicz, F. G., NASA Report CR-(1967), 683.
8. Morabito, J. M., and Lewis, R. K., Methods of Surface Analysis, S. P. Wolsky and A. W. Czanderna, ed. Elsevier Publishing Co., Amsterdam—in press (1975).
9. Blaise, G., and Slodzian, G., Rev. Phys. Appl. Paris 8, 105 (1973).
10. Castaing, R., and Slodzian, G., J. de Microscopie 1, 395 (1961).
11. Lewis, R. K., Vastel, J., Proc. of Ninth Annual Conference of the Microbeam Analysis Soc., Ottawa, Canada, July 22-26, 1974, 50A.
12. Hernandez, R., Lanusse, P., Slodzian, G., and Vidal, G., Methods Phys. Anal., (GAMS) 6, 411 (1970).
13. Werner, H. W., De Grefte, H. A. M., and Vandenberg, J., Advances in Mass Spectrometry, Vol. 6, Applied Publishers, England, 673 (1974).

14. Palmberg, P. W., 21st National Symposium of the Amer. Vac. Soc., Anaheim, California, October 1974. Paper to be published in J. of Vac. Sci. Tech. (Special Issue).
15. Morabito, J. M., Surface Physics, McGraw-Hill Yearbook of Science and Technology (1975)—in press.
16. Slodzian, G., paper presented at the Conf. on Analytical Chem. and Applied Spectroscopy, Cleveland, Ohio, March 1973.
17. Brandis, E. K., Proc. of Ninth Annual Conf. of the Microbeam Analysis Soc., Ottawa, Canada, July 22-26, 1974, 45A.
18. Slodzian, G., paper to be published in Sur. Sci. (1975) and presented June 1974, at the Conference on Surface Properties of Materials, U. of Missouri, Rolla.
19. Heavens, O. S., Hass, G. and Thun, R. E., Eds., Physics of Thin Films, Academic Press, Inc., New York, 2, 193 (1964).
20. Tolansky, S., Surface Microtopography, Interscience Publishers, Inc., New York, 1960.
21. Dahlgren, S. D., and McClanahan, E. D., J. of Appl. Phys. 43, 1514 (1972).
22. Schulz, F., Wittmaack, K., and Maul, K., J. Rad. Effects 18, 211 (1973).
23. Lewis, R. K., Morabito, J. M., and Tsai, J. C. C., Phys. Lett. 23, 260 (1973).
24. Tsai, J. C. C., and Morabito, J. M., Sur. Sci. 44, 247 (1974).
25. Evans, C. A., Jr. and Pemsler, J. P., Anal. Chem. 42, 1130 (1970).
26. Blanchard, B., Hilleret, N., Quoirin, J. B., Conf. on Analytical Chem. and Applied Spectroscopy, Cleveland, Ohio, Paper 171, 131 (1973).
27. Evans, C. A., 21st National Symposium of the Amer. Vac. Soc., Anaheim, California, October 1974. Paper to be published in J. of Vac. Sci. Tech. (Special Issue).
28. Palmberg, P. W., J. Vac. Sci. Tech. 10, 274 (1973).
29. Andrews, J. M., and Morabito, J. M., to be published.
30. Chou, N. J., VanderMeulen, Y. J., Hammer, R., and Cahill, J., Appl. Phys. Lett. 24, 200 (1974).
31. Narusawa, R., Komiya, S., and Hiraki, A., Appl. Phys. Lett. 22, 389 (1973).

32. Slodzian, G., Rev. Phys. Appl., 3(4), 360 (1968).
33. Morabito, J. M., and Lewis, R. K., Anal. Chem. 45, 869 (1973).
34. Lindhard, J., Scharff, M., Schiott, A., Mat. Fys. Medd., Dan Vid Selsk, 33, 1 (1973).
35. Bonis, M., Blanchard, B., DeBrebisson, M., Hilleret, N., and Monnier, J., Electrochem. Soc. Meeting, Miami, Florida, Abstract 266, p. 658.
36. Ziegler, J. F., Cole, G. W., and Baglin, J. E. E., IBM Research Report, RC 3643, December 7, 1971.
37. Tsai, J. C. C., Morabito, J. M., and Lewis, R. K., Ion Implantation in Semiconductors and Other Materials edited by B. L. Crowder, Plenum Press, New York, New York, 89 (1973).
38. Newsham, I. G., Hogue, J. V., and Sandstrom, D. R., J. Vac. Sci. Tech., 9, 597 (1972).
39. Werner, H. W., Advances in Applied Spectroscopy, Plenum Press, New York, 7a, 239 (1969).
40. Andersen, C. A., and Hinthorne, J. R., Anal. Chem. 45, 1421 (1973).
41. Schroer, J. M., Sur. Sci. 34, 571 (1973).
42. Werner, H. W., Theoretical and Experimental Aspects of Secondary Ion Mass Spectrometry, Vacuum - in press (1974).
43. Carter, G., Enrico Fermi Summer School Paper, 1973, in print.
44. Morabito, J. M., J. Vac. Sci. Technol. 11, 297 (1974).
45. Brunauer, S., Emmett, P. H., and Teller, E., J. Am. Chem. Soc. 60, 309 (1938).
46. Werner, H. W., Philips Research Laboratories, Eindhoven, The Netherlands. Private communication.
47. Morabito, J. M., and Tsai, J. C. C., Surf. Sci. 33, 422 (1972).
48. Tsai, J. C. C., and Morabito, J. M., Proc. of IVth International Conf. on Ion Implantation in Semiconductors and Other Materials, Japan, 1974 (to be published).
49. Morabito, J. M., Anal. Chem. 46, 189 (1974).
50. Croset, M., International Meeting of Chemical Analysis by Charged Particle Bombardment, Namur, September 5-8, 1971.

51. Heinrich, K. F. J., and Myklebust, R. L., Proc. of 8th National Conference on Electron Probe Analysis, New Orleans, Louisiana, 1973, 3A.
52. Palmberg, P. W., Anal. Chem. 45, 549 (1973).
53. Shimizu, H., Ono, M., and Nakayama, K., Surface Sci. 36 17 (1973).
54. Thomas, J. H., and Morabito, J. M., Sur. Sci. 41, 629 (1974).
55. Castaing, R., These de Doctorat, Universite de Paris (1951), Publication Onera (1955).
56. Weber, R. E., and Johnson, A. L., J. Appl. Phys. 40, 314 (1969).
57. Grant, J. T., and Haas, T. W., Sur. Sci. 44, 617 (1974).
58. From a plot of escape depth values prepared literature by J. C. Tracy, General Motors Research Laboratories (1973).
59. Meyer, F., and Vrakking, J. J., Sur. Sci. 33, 221 (1972).
60. Rudge, M. R. H., and Schwartz, S. B., Proc. Phys. Soc. (London) 88, 563 (1966).
61. Palmberg, P. W., Riach, G. E., Weber, R. E., and MacDonald, N. C., Handbook of Auger Electron Spectroscopy, Physical Electronics Industries, Minn., 3 (1972).
62. The Cu₂O single crystal was supplied by H. Bennett, National Bureau of Standards, Washington, D. C.
63. Blanchard, G., Hilleret, N., and Monnier, J., Material Res. Bull. 6, 1283 (1971).

- Analytical accuracy 96,156
- Applications
- Cosmochemistry 135-178
 - Depth profiling 21,179-190,191-224
 - Geochemistry 135-178
 - Geochemical surface analysis 171
 - Geochronology 167-171
 - Isotope ratio analysis 165
 - Light element geochemistry 165
 - Surface analysis 171,191-224
 - Trace element geochemistry 160-165
- Auger Electron Spectroscopy 191-224
- Auger images 197
- CARISMA computer program 79-120
- Chemical effect 187
- Cosmochemistry 135-178
- Comparison of ion spectra 69-78
- Depth profiling 179-190,191-224
- Instrumental effects 181
 - Ion-matrix effects 185
- Detectability limits 217-219
- Duoplasmatron 6
- Empirical quantitation 129-134
- Geochemical applications 135-178
- Geochemical surface analysis 171
- Geochronology 167-171
- High Mass Resolution SIMS 63-68
- Interference correction 145,193
- Interlaboratory analysis comparison 103,156
- Ion beam parameters 20,21,51-54
- Ion collection efficiency 33-62

Ion emission models, secondary 121
Ion energy loss with depth 113-115
Ion images 130,197
Ion luminescence 28
Ion microscope 2,33-62
 Objective lens 34,39
 Emission lens 34
 Transfer optics 44
Ion microprobe 1-32
 AEI 11,63-68
 ARL IMMA 8
 COALA 22,23,24
 Drummond and Long 10
 Goutte 17
 Herzog and Viehbock 5
 Hitachi IMA 12,18
 Krohn and Ringo 18
 Liebl and Herzog 6
 Long 9
 Rüdenauer and Steiger 28
 UMPA 13,13,17
 VARIAN 15
Ion Sources 26
Ion Spectra
 Argon source 7
 Labradorite 65,66,67
 Shape in ion microscope 75
 Zirconolite 143
Isotope studies 135,165
Knock-on 186
Local analysis 20,53
Local Thermal Equilibrium 79-120
Minimum analyzed volume 14,60,203
Molecular ions 126
Non-conducting samples 140
Optical emission 95

Recoil implantation 186

Relative elemental sensitivity factors 131

Resolution, mass 63

Richardson's equation 91

Saha - Eggert ionization equation 80,123

Secondary ion emission models 121-127

- Andersen and Hinthorne 79-120,123
- Benninghoven 125
- Joyes 125
- Jurela 123
- MacDonald 125
- Plog 126
- Rüdenauer 125
- Schroerer 124
- Sroubek 124
- van der Weg 125
- Werner 126

Secondary ion energy distribution 108

Secondary ion properties 34,43,54,55,82-86,108,142

Sensitivity factors 131

Surface analysis 171,191-224

Temperature - electron density 91-98

Thermal equilibrium 79

Thermal spike 109

Trace elements 160

Transmission 54,64

Useful ion yield 14,60,23

Vacuum requirements 202

Volume of analysis 14,60,203

U.S. DEPT. OF COMM. BIBLIOGRAPHIC DATA SHEET	1. PUBLICATION OR REPORT NO. NBS SP-427	2. Gov't Accession No.	3. Recipient's Accession No.
4. TITLE AND SUBTITLE Secondary Ion Mass Spectrometry, Proceedings of a Workshop on Secondary Ion Mass Spectrometry and Ion Microprobe Mass Analysis		5. Publication Date October 1975	
		6. Performing Organization Code	
7. AUTHOR(S) K. F. J. Heinrich and D. E. Newbury		8. Performing Organ. Report No.	
9. PERFORMING ORGANIZATION NAME AND ADDRESS NATIONAL BUREAU OF STANDARDS DEPARTMENT OF COMMERCE WASHINGTON, D.C. 20234		10. Project/Task/Work Unit No.	
		11. Contract/Grant No.	
12. Sponsoring Organization Name and Complete Address (Street, City, State, ZIP) Same as No. 9.		13. Type of Report & Period Covered	
		14. Sponsoring Agency Code	
15. SUPPLEMENTARY NOTES Library of Congress Catalog Card Number: 75-619223			
16. ABSTRACT (A 200-word or less factual summary of most significant information. If document includes a significant bibliography or literature survey, mention it here.) This book is the formal report of the Workshop on Secondary Ion Mass Spectrometry (SIMS) and Ion Microprobe Mass Analysis held at the National Bureau of Standards in September 1974. Invited and contributed papers cover a range of topics in the SIMS field: design of SIMS instrumentation; factors affecting secondary ion collection; techniques of reducing secondary ion mass spectra to yield quantitative compositional information; comparisons of SIMS with Auger electron spectroscopy (AES); techniques of obtaining elemental depth profiles and the instrumental and physical factors affecting such profiles; and applications of SIMS to the study of geological samples. The papers include both tutorial reviews and detailed reports on current research in SIMS. The volume should be of interest to all workers in the SIMS and surface analysis fields.			
17. KEY WORDS (six to twelve entries; alphabetical order; capitalize only the first letter of the first key word unless a proper name; separated by semicolons) Auger electron spectroscopy; elemental depth profiling; ion microprobe mass analysis; ion optics; local thermal equilibrium (LTE); mineral analysis; secondary ion mass spectrometry (SIMS); surface analysis.			
18. AVAILABILITY <input checked="" type="checkbox"/> Unlimited <input type="checkbox"/> For Official Distribution. Do Not Release to NTIS <input checked="" type="checkbox"/> Order From Sup. of Doc., U.S. Government Printing Office Washington, D.C. 20402, SD Cat. No. C13, 10:427 <input type="checkbox"/> Order From National Technical Information Service (NTIS) Springfield, Virginia 22151		19. SECURITY CLASS (THIS REPORT) UNCLASSIFIED	21. NO. OF PAGES 230
		20. SECURITY CLASS (THIS PAGE) UNCLASSIFIED	22. Price \$3.00

Get
a line on
science and
technology.
Subscribe to

DIMENSIONS



Whether you're in business, or a teacher, scientist, or consumer, you'll want to keep up with the latest developments in science and technology. DIMENSIONS/NBS, the monthly magazine from the Commerce Department's National Bureau of Standards, can help keep you informed. Every day at NBS, one of the nation's largest research laboratories, scientists seek new answers to a host of national problems, including energy conservation, product safety, metric conversion, and pollution abatement. Their findings, reported each month in DIMENSIONS/NBS, have a direct impact on our daily lives.

Subscription price: \$9.45 per year.
Order prepaid from the
Superintendent of Documents,
U.S. Government Printing Office,
Washington, D.C. 20402
SD Catalog No. C13.13

NBS TECHNICAL PUBLICATIONS

PERIODICALS

JOURNAL OF RESEARCH reports National Bureau of Standards research and development in physics, mathematics, and chemistry. It is published in two sections, available separately:

• **Physics and Chemistry (Section A)**

Papers of interest primarily to scientists working in these fields. This section covers a broad range of physical and chemical research, with major emphasis on standards of physical measurement, fundamental constants, and properties of matter. Issued six times a year. Annual subscription: Domestic, \$17.00; Foreign, \$21.25.

• **Mathematical Sciences (Section B)**

Studies and compilations designed mainly for the mathematician and theoretical physicist. Topics in mathematical statistics, theory of experiment design, numerical analysis, theoretical physics and chemistry, logical design and programming of computers and computer systems. Short numerical tables. Issued quarterly. Annual subscription: Domestic, \$9.00; Foreign, \$11.25.

DIMENSIONS/NBS (formerly Technical News Bulletin)—This monthly magazine is published to inform scientists, engineers, businessmen, industry, teachers, students, and consumers of the latest advances in science and technology, with primary emphasis on the work at NBS. The magazine highlights and reviews such issues as energy research, fire protection, building technology, metric conversion, pollution abatement, health and safety, and consumer product performance. In addition, it reports the results of Bureau programs in measurement standards and techniques, properties of matter and materials, engineering standards and services, instrumentation, and automatic data processing.

Annual subscription: Domestic, \$9.45; Foreign, \$11.85.

NONPERIODICALS

Monographs—Major contributions to the technical literature on various subjects related to the Bureau's scientific and technical activities.

Handbooks—Recommended codes of engineering and industrial practice (including safety codes) developed in cooperation with interested industries, professional organizations, and regulatory bodies.

Special Publications—Include proceedings of conferences sponsored by NBS, NBS annual reports, and other special publications appropriate to this grouping such as wall charts, pocket cards, and bibliographies.

Applied Mathematics Series—Mathematical tables, manuals, and studies of special interest to physicists, engineers, chemists, biologists, mathematicians, computer programmers, and others engaged in scientific and technical work.

National Standard Reference Data Series—Provides quantitative data on the physical and chemical properties of materials, compiled from the world's literature and critically evaluated. Developed under a world-wide

program coordinated by NBS. Program under authority of National Standard Data Act (Public Law 90-396).

NOTE: At present the principal publication outlet for these data is the Journal of Physical and Chemical Reference Data (JPCRD) published quarterly for NBS by the American Chemical Society (ACS) and the American Institute of Physics (AIP). Subscriptions, reprints, and supplements available from ACS, 1155 Sixteenth St. N. W., Wash. D. C. 20056.

Building Science Series—Disseminates technical information developed at the Bureau on building materials, components, systems, and whole structures. The series presents research results, test methods, and performance criteria related to the structural and environmental functions and the durability and safety characteristics of building elements and systems.

Technical Notes—Studies or reports which are complete in themselves but restrictive in their treatment of a subject. Analogous to monographs but not so comprehensive in scope or definitive in treatment of the subject area. Often serve as a vehicle for final reports of work performed at NBS under the sponsorship of other government agencies.

Voluntary Product Standards—Developed under procedures published by the Department of Commerce in Part 10, Title 15, of the Code of Federal Regulations. The purpose of the standards is to establish nationally recognized requirements for products, and to provide all concerned interests with a basis for common understanding of the characteristics of the products. NBS administers this program as a supplement to the activities of the private sector standardizing organizations.

Federal Information Processing Standards Publications (FIPS PUBS)—Publications in this series collectively constitute the Federal Information Processing Standards Register. Register serves as the official source of information in the Federal Government regarding standards issued by NBS pursuant to the Federal Property and Administrative Services Act of 1949 as amended, Public Law 89-306 (79 Stat. 1127), and as implemented by Executive Order 11717 (38 FR 12315, dated May 11, 1973), and Part 6 of Title 15 CFR (Code of Federal Regulations).

Consumer Information Series—Practical information, based on NBS research and experience, covering areas of interest to the consumer. Easily understandable language and illustrations provide useful background knowledge for shopping in today's technological marketplace.

NBS Interagency Reports (NBSIR)—A special series of interim or final reports on work performed by NBS for outside sponsors (both government and non-government). In general, initial distribution is handled by the sponsor; public distribution is by the National Technical Information Service (Springfield, Va. 22161) in paper copy or microfiche form.

Order NBS publications (except NBSIR's and Bibliographic Subscription Services) from: Superintendent of Documents, Government Printing Office, Washington, D.C. 20402.

BIBLIOGRAPHIC SUBSCRIPTION SERVICES

The following current-awareness and literature-survey bibliographies are issued periodically by the Bureau: Cryogenic Data Center Current Awareness Service

A literature survey issued biweekly. Annual subscription: Domestic, \$20.00; foreign, \$25.00.

Liquefied Natural Gas. A literature survey issued quarterly. Annual subscription: \$20.00.

Superconducting Devices and Materials. A literature

survey issued quarterly. Annual subscription: \$20.00. Send subscription orders and remittances for the preceding bibliographic services to National Technical Information Service, Springfield, Va. 22161.

Electromagnetic Metrology Current Awareness Service Issued monthly. Annual subscription: \$100.00 (Special rates for multi-subscriptions). Send subscription order and remittance to Electromagnetics Division, National Bureau of Standards, Boulder, Colo. 80302.

U.S. DEPARTMENT OF COMMERCE
National Bureau of Standards
Washington, D.C. 20234

OFFICIAL BUSINESS

Penalty for Private Use, \$300

POSTAGE AND FEES PAID
U.S. DEPARTMENT OF COMMERCE
COM-215

SPECIAL FOURTH-CLASS RATE
BOOK

